2016

A Cartesian Cut-Stencil Method for the Finite Difference Solution of PDEs in Complex Domains

Mohammadali Esmaeilzadeh
University of Windsor

A Cartesian Cut-Stencil Method for the Finite Difference Solution of PDEs in Complex Domains

By

Mohammadali Esmaeilzadeh

A Dissertation
Submitted to the Faculty of Graduate Studies
Through the Department of Mechanical, Automotive and Materials Engineering
in Partial Fulfillment of the Requirements for
the Degree of Doctor of Philosophy
at the University of Windsor

Windsor, Ontario, Canada

2016

A Cartesian Cut-Stencil Method for the Finite Difference Solution of PDEs in Complex Domain

by

Mohammadali Esmaeilzadeh

APPROVED BY:

H. Yang, External Examiner
Bombardier Aerospace, Montreal

M. Monfared
Department of Mathematics & Statistics

J. Defoe
Department of Mechanical, Automotive & Materials Engineering

O. Iqbal
Department of Mechanical, Automotive & Materials Engineering

N. Zamani
Department of Mechanical, Automotive & Materials Engineering

R. Barron, Co-Advisor
Department of Mechanical, Automotive & Materials Engineering

R. Balachandar, Co-Advisor
Department of Mechanical, Automotive & Materials Engineering

26 May 2016

AUTHOR'S DECLARATION of ORIGINALITY

I hereby certify that I am the sole author of this thesis and that no part of this thesis has been published or submitted for publication.

I certify that, to the best of my knowledge, my thesis does not infringe upon anyone's copyright nor violate any proprietary rights and that any ideas, techniques, quotations, or any other material from the work of other people included in my thesis, published or otherwise, are fully acknowledged in accordance with the standard referencing practices. Furthermore, to the extent that I have included copyrighted material that surpasses the bounds of fair dealing within the meaning of the Canada Copyright Act, I certify that I have obtained a written permission from the copyright owner(s) to include such material(s) in my thesis and have included copies of such copyright clearances to my appendix.

I declare that this is a true copy of my thesis, including any final revisions, as approved by my thesis committee and the Graduate Studies office, and that this thesis has not been submitted for a higher degree to any other University or Institution.

ABSTRACT

A new finite difference formulation, referred to as the Cartesian cut-stencil finite difference method (FDM), for discretization of partial differential equations (PDEs) in any complex physical domain is proposed in this dissertation. The method employs unique localized 1-D quadratic transformation functions to map non-uniform (uncut or cut) physical stencils to a uniform computational stencil. The transformation functions are uniquely determined by the coordinates of the points on the physical stencil. In its basic formulation, 2nd-order central differencing is used to approximate derivatives in the transformed PDEs. The resulting finite difference equations can be solved by classical iterative methods.

In the case of a boundary node with a Dirichlet boundary condition, the prescribed value can be used directly in the calculations on the corresponding stencil adjacent to the boundary. However, for Neumann boundary nodes, discretization of the normal derivative in the Neumann condition is accomplished using one-sided approximations, producing an approximate value for the solution variable at the boundary. Then, the cut-stencil method allows stencils adjacent to boundaries to be treated in the same way as interior stencils, thus enabling finite difference calculations on arbitrarily complex domains.

This new formulation can be combined with the higher-order compact Padé-Hermitian method to produce higher-order cut-stencil schemes. Three different Cartesian cut-stencil formulations based on local 4th-order approximations are proposed and analyzed. It has been shown that global 4th-order accuracy can be achieved when the same order of accuracy is implemented at Neumann boundaries.

Comparison of numerical results for some manufactured problems with the exact solution verifies the capability of the cut-stencil method to deal with PDEs in regular and irregular shaped domains. Cartesian cut-stencil FDM solutions are also obtained for some classical engineering benchmark problems, including Prandtl's stress function, steady or unsteady heat conduction and flow in a lid-driven cavity.

This dissertation demonstrates that the Cartesian cut-stencil finite difference method has many desirable features of a high-end numerical simulation code including simplicity in formulation, meshing and coding, higher-order accuracy, high-fidelity solutions, reliable error estimator, applicable in different science and engineering fields, and can solve complicated nonlinear PDEs in complex geometries.

DEDICATION

This thesis is dedicated, in loving memory, to my father, Mohammadjavad, who passed away on September 23, 2014, while I was in the middle of my Ph.D. program. The importance of his desire to see me graduate is clear for me, but I, unfortunately, could not get the chance to share this news with him. His continuous support in all aspects of my life, along with his beautiful warm heart, made him my hero and role model. I am forever indebted to his efforts and kindness. His memory will be with me in every moment of my life.

ACKNOWLEDGEMENTS

TABLE of CONTENTS

LIST of TABLES

LIST of FIGURES

NOMENCLATURE

Symbol	Definition
A, B, L, R	Auxilliary nodes on 5+4-point physical stencil
a, b, l, r	Auxilliary nodes on 5+4-point computational stencil
a_p, a_w, a_e, a_s, a_e	Coefficients in FD equation at interior node P
c_x, c_y	Courant numbers
$\mathcal{C}$	Coefficient in second-order wave equation
d_x, d_y	Diffusion numbers
e	Difference between exact and numerical solution
G, g	Functions in Neumann boundary condition
G	Modulus of elasticity in shear
$\hbar$	Mesh size
$\hbar_c$	Coarse mesh size
$\hbar_f$	Fine mesh size
$\hbar_1$	Sides of a rectangular cell
$\hbar_2$	Diagonal of a rectangular cell
I	Moment of inertia
J	Jacobian of transformation
k, l	Parameters to switch between backward to forward differencing
L_c	Characteristic length
M	Total number of nodes for a grid
$\hat{n} = (n_x, n_y)$	Unit normal vector at the boundary
P, Q	Convection coefficients
P, W, S, E, N	Nodes on physical 5-point stencil
P, w, s, e, n	Nodes on generic computational 5-point stencil
p	Pressure
q	Order of discretization error
r	Refinement factor
Re	Reynolds number
S, s	Source terms
T	Temperature (dimensional)
t	Time

$\mathcal{U}, \mathcal{V}$	X- and Y-components of velocity (dimensional)
U_{ref}	Reference velocity
u, v	x- and y-components of velocity (non-dimensional)
X, Y	Cartesian coordinates (dimensional)
x, y	Cartesian coordinates (non-dimensional)

Greek letters

α, β	Parameters for finite differencing schemes for convective terms
γ	Cell aspect ratio ($\Delta x / \Delta y$)
Δt	Time step
Δt_{Max}	Maximum allowable time step
$\Delta x, \Delta y$	Increments in x and y
$\delta_{k\xi,P}^c$	Difference operator, approximation of $\partial_{k\xi}\big|_P$
$\partial_{k\xi}\big|_P$	Derivative operator for k^{th}-derivative with respect to ξ
η	Computational stencil axis
θ	Angle of twist of a bar
Θ	Temperature (non-dimensional)
ν	Diffusion coefficient, thermal diffusivity
ξ	Computational stencil axis
ρ	Density
σ	Relaxation parameter
ϑ	Poisson's ratio, kinematic viscosity
ϕ	Governing function, Prandtl's stress function
$\phi_{exc.}$	Exact solution
Ψ	Streamfunction (dimensional)
ψ	Streamfunction (non-dimensional)
Ω_z	Z-component of vorticity vector (dimensional)
ω	z-component of vorticity (non-dimensional)

LIST of ABBREVIATIONS

Abbreviation	Definition
PDEs	Partial differential equation(s)
FDM	Finite difference method
TFDM	Traditional finite difference method
FVM	Finite volume method
FEM	Finite element method
SOR	Successive over-relaxation
SUR	Successive under-relaxation
P-J	Point-Jacobi iterative method
HO	Higher-order
HOC	Higher order compact
HO-FDM1	Higher-order Cartesian cut-stencil finite difference method 1
HO cut-stencil FDM1	Higher-order Cartesian cut-stencil finite difference method 1
HO-FDM2	Higher-order Cartesian cut-stencil finite difference method 2
HO cut-stencil FDM2	Higher-order Cartesian cut-stencil finite difference method 2
1(2)-D	One (two) dimensional
LTE	Local truncation error
FTCS	Forward in time and central in space
MMS	Method of manufactured solutions
RMS	Root mean square error
Rel.	Relative (e.g. relative error)
Abs.	Absolute (e.g. absolute error)

CHAPTER 1

INTRODUCTION to PARTIAL DIFFERENTIAL EQUATIONS and NUMERICAL METHODS

1.1 Objective of the Chapter

The main goal of this thesis is to develop a new computational algorithm for the numerical solution of partial differential equations (PDEs) based on the finite difference method (FDM). This new approach will be referred to throughout this thesis as the Cartesian cut-stencil finite difference method, or cut-stencil method for brevity. The immediate question that arises is: Why develop a new FDM? The traditional FDM (TFDM) is a simple, powerful method for approximating the solution of PDEs, but it becomes prohibitively complicated when dealing with highly geometrically complex domains. The Cartesian cut-stencil method retains the simplicity and power of the traditional FDM while simultaneously providing a natural mechanism for handling complex boundaries. Additionally, as will become apparent, this new FDM exhibits many other important benefits such as (i) classical grid generation associated with traditional FD formulations is avoided; (ii) precise expressions for the local truncation (discretization) error can be developed, providing a reliable evaluation of numerical error and a criterion for mesh adaptivity, (iii) mesh files only need to contain simple nodal coordinate and connectivity information, and normal vectors only at boundary points, (iv) significant reduction in the use of low-order interpolations, which leads to more accuracy, (v) amenable to the development of higher-order schemes, and (vi) greater global order of accuracy is possible because near-boundary nodes can be treated in the same way and to the same order as interior nodes, thereby not degrading the overall accuracy.

The complexity of PDEs or a set of PDEs, which normally are formulated to model real physical phenomena in engineering and science, prohibits development of analytical solutions. Consequently, numerical methods are applied to obtain approximate solutions to these PDEs [1]. The possibility of application to any type of domain, ease of implementation to define the mathematical and numerical model of the problem and potential of extending the method to higher-order approximations can be considered as other necessary features of any modern numerical method.

Numerical methods for solution of PDEs in most fields of engineering are categorized with three well-known mesh-based methods, namely, finite difference method (FDM), finite volume method (FVM) and finite element method (FEM). Each of these three methods possesses their own inherent advantages and limitations when applied for solutions of PDEs.

The main objectives of this chapter are to present some basic definitions, concepts and mathematical manipulations which are widely used in FDM, to highlight key differences between FDM and FVM and to assess the current state-of-the-art with respect to these discretization procedures.

1.2 Partial Differential Equations

The general second-order linear PDE in two space dimensions can be expressed as

$$A(x,y,t)\emptyset_t + B(x,y,t)\emptyset_{xx} + C(x,y,t)\emptyset_{yy} + D(x,y,t)\emptyset_x + E(x,y,t)\emptyset_y + F(x,y,t)\emptyset = S(x,y,t) \quad (1.1)$$

where x, y and t are the independent variables, the unknown function $\emptyset$ and the coefficients A, B, C, D, E, F and source term S are functions of the independent variables only. For most PDEs, when the exact (analytical) solution is not easy to derive, a numerical method is used to approximate the continuous dependent variable with discrete variables and the approximation procedure is executed on a computer through the solution of a system of algebraic equations [2]. The order of a PDE is determined by the order of the highest derivative in the PDE. Second-order PDEs, which are common in engineering applications and are the type of PDEs discussed in this research, are classified as elliptic, parabolic or hyperbolic. The Poisson equation $\nabla^2\emptyset = F(x,y)$ is an example of an elliptic equation and the unsteady heat conduction equation in two spatial dimensions, $\frac{\partial \emptyset}{\partial t} = K\nabla^2\emptyset$ introduces an example of a parabolic equation. The first-order wave equation defined by $\frac{\partial \emptyset}{\partial t} + a\frac{\partial \emptyset}{\partial x} + b\frac{\partial \emptyset}{\partial y} = 0$ is a PDE of the hyperbolic type.

1.3   Finite Difference Method: Basic Definitions, Strengths, Limitations

The finite difference method approximates differential equations by replacing the derivatives by the difference of the solution at discrete nodes in the domain of interest. This discretization procedure leads to a system of algebraic equations which are solved after imposing the given boundary conditions. The results of this process give the value of the governing function(s) at each node of the solution domain [3].

The FDM is considered to be simple in concept but it has traditionally only been applicable for uniform and rectangular meshes [3], and may encounter serious difficulties for complex domains, particularly at nodes near boundaries [4]. Fortunately, structured body-fitted curvilinear grids and multiblock techniques have allowed researchers to develop FDM to solve PDEs in complicated domains [5-9]. The initial step in using body-fitted curvilinear coordinates is the transformation of the irregular physical domain and governing equation(s) into a rectangular domain with a logical (structured) grid. The governing equations are also transformed from the physical to computational domain [6]. Unfortunately, generating a body-fitted grid system in highly complex domains is very labour-intensive and may be impractical from a cost perspective. The multiblock technique can alleviate some of these issues, but is somewhat difficult to implement and may require considerable experience to generate good quality grid systems. Nevertheless, the simplicity of FDM provides the possibility of extension to higher-order accurate approximations, development of good error estimates, analysis of the stability of a numerical scheme and reduction of the overall cost of the computation. Thus, FD is a popular discretization procedure for academic research codes, but generally not used for industrial applications, many of which involve highly complex geometries.

FVM and FEM do not suffer from the grid limitations of the FDM and can handle complex domains since these methods can be formulated for a wide variety of mesh cells or elements such as tetrahedral, hexahedral, polyhedral, prismatic and hybrid. But they are not completely exempt from their own difficulties. Development of higher-order schemes is problematic, e.g., for triangular control volumes in FVM, second-order discretization is difficult to achieve [10]. Additionally, the FVM suffers from lack of an accurate definition of derivatives in the event that the mesh is not orthogonal and equally spaced. The absence of a weak formulation, as in FEM, to

convert higher-order derivatives into lower ones, makes the FVM more compatible for flow problems which are not dominated by viscous effects. The functional values or fluxes for cells located on curved boundaries, or for curved grid lines, are often represented by piecewise constant or linear functions in FVM. Although more accurate implementation for curved boundary cells or curved grid lines can be defined, it is a rather difficult task in FVM [11]. Most extrapolation techniques, which are heavily used in cell-centred FVM, lead to lower accuracy at boundary nodes than at internal nodes [12]. Numerical studies can be found in the literature that combine both FVM and FEM (referred to as FEVM) to exploit the merits of each method, particularly in fluid mechanics [13-15]. The cell-centred FVM was used in [13, 14] and the cell-vertex FVM was used in the hybrid FEVM in [15].

The creation of these types of hybrid numerical methods illustrate how, even though FVM is popular in Computational Fluid Dynamic (CFD) commercial software, it may not be able to cover a variety of problems without difficulties. So, any new numerical algorithm/formulation should be assessed in the context of facilitating the previous version of a numerical method of the same type. The focus of this thesis is the development of a FD-based method for solution of PDEs that retains all the advantages, and overcomes some of the main weaknesses, of current methods.

1.3.1 Discretization of Derivatives in FDM

The principles and details of FDM are explained in many texts, e.g., cf. [1, 16, 17]. For our purpose, a brief overview of the main FDM concepts and general governing procedure of this numerical method to achieve an approximate solution, relevant to the research described in this thesis, are addressed. An understanding of these fundamental topics is beneficial for later comparison with the same topics that will be discussed in the context of the cut-stencil finite difference formulation which is the primary object of this research.

The general formulation for Taylor's series expansion, for a single-valued function $\phi(x)$, at point $(x + \Delta x)$, is given by

$$\phi(x + \Delta x) = \emptyset(x) + \sum_{n=1}^{\infty} \frac{(\Delta x)^n}{n!} \frac{\partial^n \emptyset}{\partial x^n} \tag{1.2}$$

Similar approximations using Taylor's series expansion can be derived by replacing Δx with the distance from other points to point x. By combining the Taylor's series at different points and retaining expansion of the infinite series to a certain order of derivatives, one can approximate the derivatives of $\emptyset$ at point x with different order of Δx.

To illustrate the use of FD approximations, consider an elliptic PDE commonly encountered in computational mechanics (solid, fluid and heat transfer). Steady-state heat conduction, potential flow around a body, Prandlt's stress function in an arbitrary bar and the streamfunction-vorticity formulation of the Navier-Stokes equations are some problems that are defined by elliptic PDEs. The 2nd-order accurate approximation of the elliptic Poisson equation $\nabla^2 \emptyset = F(x, y)$ at an arbitrary node (i, j) of the uniform grid system shown in Figure 1.1 is written as

$$\frac{\emptyset_{(i-1,j)} - 2\emptyset_{(i,j)} + \emptyset_{(i+1,j)}}{(\Delta x)^2} + \frac{\emptyset_{(i,j-1)} - 2\emptyset_{(i,j)} + \emptyset_{(i,j+1)}}{(\Delta y)^2} = F(x_i, y_j) \tag{1.3}$$
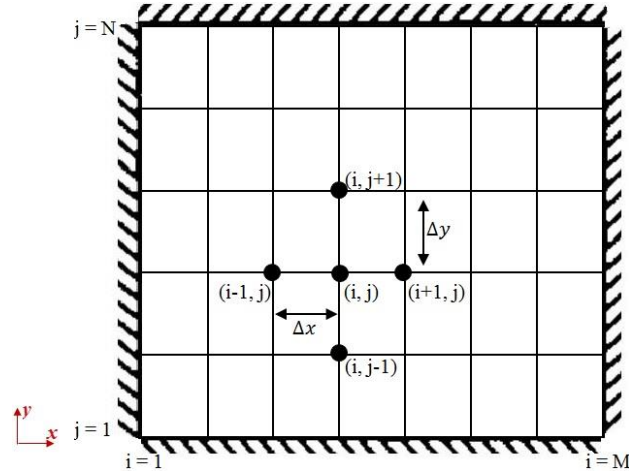
Figure 1.1: Uniform grid system used for solution of Poisson equation

The grid points used in this finite difference approximation of the Poisson equation at point (i, j), illustrated in Figure 1.1, constitute a five-point stencil. This stencil is the basic one for the cut-stencil FDM which will be discussed in Chapter 2. The solution of the Poisson equation in the grid system of Figure 1.1, in the event of Dirichlet boundary conditions, requires the solution to a system on (M-2)(N-2) algebraic equations. This system of equations can be cast into a matrix form $A\vec{\Phi} = \vec{b}$, in which A is the matrix of coefficients, $\vec{\Phi}$ is the vector of unknowns $\phi_{(i,j)}$ and $\vec{b}$ is the vector which incorporates the boundary values and the right hand side for each equation.

The solution algorithms for matrix equations are divided into two main approaches, namely direct and iterative methods. Cramer's rule, Gaussian elimination and LU-decomposition are well-known direct methods to solve a system of linear equations. Details for these direct solution algorithms can be found in Leslie and McAvaney [18] and in many textbooks on numerical linear algebra. Direct methods generally suffer from some disadvantages, especially when the matrices are not simple tridiagonal ones, and may not be computationally efficient. Additionally, the computational storage is huge especially for large size problems that are common in computational mechanics. Accumulation of round-off errors during the arithmetic calculations may also produce poor solutions and consequently a concerted effort should be made to reduce these errors [19, 20]. Due to these limitations, and non-linear coefficients for most PDEs of practical interest, direct methods, generally, are not used in the computational mechanics field. The following section presents a brief introduction to iterative methods which have been employed throughout this thesis to solve PDEs using the Cartesian cut-stencil FDM.

1.3.2 Iterative Solution Algorithms

Iterative methods initiate the solution procedure with an initial guess. The first guess is improved through a finite sequence of logical iterations to approach the exact solution. The pre-defined convergence criteria can control the trend of the iterations [21]. Some of the familiar iterative methods are the Point-Jacobi method, Gauss-Seidel method and Successive over-relaxation (under-relaxation) method (SOR or SUR). The main developments of iterative solution algorithms, over more than a century, have been outlined in Saad and van der Vorst [22]. In the solution for most of the manufactured problems presented in Chapter 3 and the practical problems from different fields in Chapter 4, the Point-Jacobi (P-J) scheme is used to generate the cut-stencil

FD solution to the PDEs. The cut-stencil FD solution for the streamfunction-vorticity formulation of the Navier-Stokes equation is presented in Chapter 5 by using the SUR method depending on the mesh size and Reynolds number. Thus, a brief explanation of these schemes is addressed here. Equation (1.3) is rewritten as

$$\emptyset_{(i-1,j)} + \emptyset_{(i+1,j)} - 2(1 + \gamma^2)\emptyset_{(i,j)} + \gamma^2(\emptyset_{(i,j-1)} + \emptyset_{(i,j+1)}) = (\Delta x)^2 f(x_i, y_j) \qquad (1.4.1)$$

in which γ denotes $\Delta x/\Delta y$. Assuming that $\emptyset_{(i,j)}$ is known at a current iteration level k, i.e., $\emptyset_{(i,j)}^k$ is known, the new value of the dependent variable at new iteration level $k + 1$ at node (i, j) is calculated from

$$\emptyset_{(i,j)}^{k+1} = \frac{\emptyset_{(i-1,j)}^k + \emptyset_{(i+1,j)}^k + \gamma^2(\emptyset_{(i,j-1)}^k + \emptyset_{(i,j+1)}^k) - (\Delta x)^2 F(x_i, y_j)}{2(1 + \gamma^2)} \qquad (1.4.2)$$

The iterative formulation (1.4.2) is known as the Point-Jacobi method, which is regarded as the simplest iterative formulation. It is noted that P-J retains all values of the dependent variable from the old level of iteration until the calculation at level $k + 1$ ends.

The point successive (under or over) relaxation version for calculation of the dependent variable at node (i, j) is expressed as

$$\emptyset_{(i,j)}^{k+1} = (1 - \sigma)\emptyset_{(i,j)}^k + \frac{\sigma[\emptyset_{(i-1,j)}^{k+1} + \emptyset_{(i+1,j)}^k + \gamma^2(\emptyset_{(i,j-1)}^{k+1} + \emptyset_{(i,j+1)}^k) - (\Delta x)^2 F(x_i, y_j)]}{2(1 + \gamma^2)} \qquad (1.4.3)$$

In point successive relaxation methods, the updated values of the dependent variable at neighboring nodes are immediately used for calculation of the dependent variable at node (i, j). The parameter σ in equation (1.4.3) is referred to as the relaxation parameter and the Gauss-Seidel method is recovered when $\sigma = 1$. The converged solution is obtained by implementing the condition $0 < \sigma < 2$. The rate of convergence may be accelerated by changing the value of σ. Computing an optimum value of relaxation parameter requires a procedure to solve an eigenvalue problem and it can only be applied to some limited cases, depending on the mesh scheme and type of boundary conditions. Some analytical suggestions and discussions for finding σ_{opt} are available in numerical analysis literature [17, 23, 24].

1.3.3   Ghost Node Method for Neumann Boundary Condition Treatment in TFDM

The Neumann boundary condition is based on specification of the derivative, usually the first derivative of the dependent variable rather than on the value of the dependent variable itself. So the values of the dependent variable ϕ are unknowns and a special numerical scheme is needed to approximate the values of ϕ on the Neumann type of boundaries. It is common in traditional FDM (TFDM) to employ the ghost node (ghost cell) technique to write the differencing approximation for Neumann boundary nodes. Figure 1.2 illustrates a grid system with a Neumann condition imposed on the lower boundary, where $G(x, y)$ is the prescribed value of the derivative normal to the boundary, i.e., the first derivative of the dependent variable is known for all boundary nodes $(i, 1)$ where i = 1, 2, …, M. The ghost node method inserts a fictitious node outside the domain, along the normal vector to the boundary, adjacent to node $(i, 1)$, and at the same distance, Δy, as the first interior node in the domain.
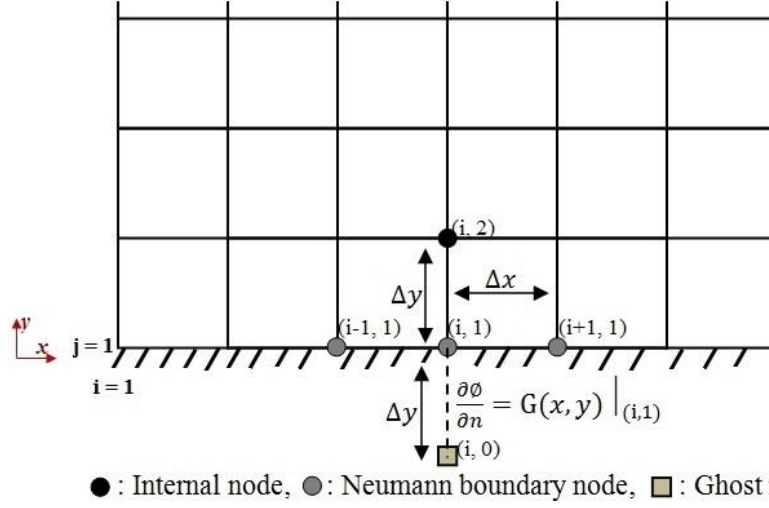
Figure 1.2: Schematic of grid system showing ghost node for approximation of imposed Neumann condition on the lower boundary

The 2nd-order central differencing approximation for the first derivative in the Neumann condition can be written using the fictitious node $(i, 0)$. It is worth pointing out that in the grid system of Figure 1.2, values of ϕ at all the nodes located along the grid line $j = 1$ are unknown. To simplify the discussion, without losing generality, it is assumed that the outward normal vector to the boundary line, depicted in Figure 1.2, has a negative component along the y- direction, i.e., $\hat{n} = -\hat{\jmath}$, where $\hat{\jmath}$ is the unit normal along the y-axis in the Cartesian coordinate system. Then, the Neumann condition can be approximated as

$$\frac{\partial \phi}{\partial y}\bigg|_{(i,1)} = \frac{\phi_{(i,2)} - \phi_{(i,0)}}{2(\Delta y)} = -G(x,y)\big|_{(i,1)} \tag{1.5.1}$$

Using the same central differencing format as for the interior nodes, the governing equation (Poisson equation) at a typical boundary node $(i, 1)$ with Neumann condition is given by

$$\frac{\phi_{(i-1,1)} - 2\phi_{(i,1)} + \phi_{(i+1,1)}}{(\Delta x)^2} + \frac{2\phi_{(i,2)} - 2\phi_{(i,1)} + 2(\Delta y)G|_{(i,1)}}{(\Delta y)^2} = F(x_i, y_1) \tag{1.5.2}$$

where equation (1.5.1) has been used to eliminate the value of ϕ at the ghost node $(i, 0)$. Similar to the case of Dirichlet boundary conditions, any of the iterative methods can be employed to solve for the unknowns, including those at the discrete points along the lower boundary.

The ghost node technique requires inclusion of the boundary unknowns in the solution vector and special entries in the expanded coefficient matrix of the linear system. In this thesis, to avoid this additional complexity, one-sided differencing approximations are employed in the cut-stencil FDM when a Neumann condition is imposed on any boundaries of the domain of interest. The details of this approach and more discussion related to the Neumann boundary condition are presented in Chapter 2.

1.4   Transformation of PDEs

As mentioned above, the TFDM is primarily employed for the numerical approximation of PDEs within regular shaped domains with a uniform grid system. In the case of irregular shaped domains, transformation of the physical domain (*x-y* space) to a regular (mostly rectangular shape) computational domain ($\xi - \eta$ space) is required. To accomplish this transformation, two main categories of approaches have been developed; algebraic methods and partial differential equation methods. Each has its own advantages and drawbacks [25]. The conformal mapping technique that is based on complex variables is an alternative method to generate a grid, but is restricted to 2-D applications [17]. A 2-D physical grid transformation to a computational one is illustrated in Figure 1.3.
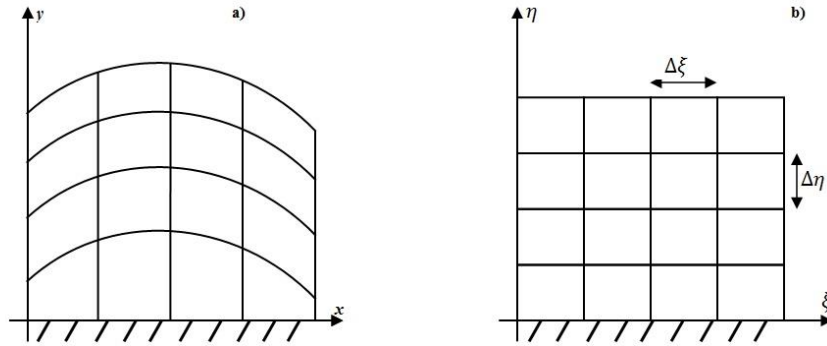
Figure 1.3: Sample of a 2-D grid transformation, a) physical domain, and b) computational domain

Besides generating the grid for the domain of interest, the parameters that determine the quality of the generated grid, such as smoothness, skewness and orthogonality must be examined to ensure the appropriate level of accuracy for the solution of the mapped equations [26]. In fact, grid generation plays a significant role in yielding an accurate solution of e.g., flow passing bodies with irregular and complex shapes. It is known that the computed values and the solution properties are affected by the metrics of the generated grid [27]. Algebraic grid generation, the simplest and fastest technique [17, 28], cannot guarantee the orthogonality of the generated grid [29]. Orthogonality of the grid is associated with a number of advantages such as less number of terms in the transformed equations and more accurate interpolations. Additionally, the numerical accuracy of differencing schemes is higher and implementation of boundary conditions is carried out in a simpler way on an orthogonal grid [30, 31].

This implies that besides the computational and human effort that must be devoted to the grid generation procedure, each method may suffer from its own inherent difficulties. On the other hand, the Cartesian cut-stencil FDM, even in cases of complex and irregular shaped domains, does not depend on the grid generation in its formal and classical definition. This feature originates from a localized mapping of each physical stencil which may have uniform or non-uniform arm lengths. The details of the localized mapping will be presented in Chapter 2.

The remaining material of this section illustrates the transformation of a model governing PDE, the convection-diffusion equation $\nabla^2 \emptyset + P \frac{\partial \emptyset}{\partial x} + Q \frac{\partial \emptyset}{\partial y} = F(x,y)$, and introduces the mapped form of the equation as employed in TFDM. The following expressions and discussions are presented

to reveal the differences between equation transformation in TFDM and in the Cartesian cut-stencil FDM, which will be introduced in Chapter 2. Consider the transformation functions $\xi = \xi(x, y)$ and $\eta = \eta(x, y)$ which, under the assumption that the Jacobian $J = \frac{\partial(x,y)}{\partial(\xi,\eta)}$ is non-zero, uniquely map points from the x-y plane to points in the ξ-η plane. Using the chain rule for partial differentiation, the first derivative operators can be expressed as:

$$\frac{\partial}{\partial x} = \xi_x \frac{\partial}{\partial \xi} + \eta_x \frac{\partial}{\partial \eta}, \qquad \frac{\partial}{\partial y} = \xi_y \frac{\partial}{\partial \xi} + \eta_y \frac{\partial}{\partial \eta} \tag{1.6.1}$$

where ξ_x and ξ_y denote the partial derivatives $\frac{\partial \xi}{\partial x}$ and $\frac{\partial \xi}{\partial y}$ respectively, and similarly for η_x and η_y. The second derivative operators are transformed in the same fashion as:

$$\frac{\partial^2}{\partial x^2} = \xi_{xx} \frac{\partial}{\partial \xi} + \xi_x \left[\xi_x \frac{\partial^2}{\partial \xi^2} + \eta_x \frac{\partial^2}{\partial \xi \partial \eta} \right] + \eta_{xx} \frac{\partial}{\partial \eta} + \eta_x \left[\xi_x \frac{\partial^2}{\partial \xi \partial \eta} + \eta_x \frac{\partial^2}{\partial \eta^2} \right] \tag{1.6.2}$$

$$\frac{\partial^2}{\partial y^2} = \xi_{yy} \frac{\partial}{\partial \xi} + \xi_y \left[\xi_y \frac{\partial^2}{\partial \xi^2} + \eta_y \frac{\partial^2}{\partial \xi \partial \eta} \right] + \eta_{yy} \frac{\partial}{\partial \eta} + \eta_y \left[\xi_y \frac{\partial^2}{\partial \xi \partial \eta} + \eta_y \frac{\partial^2}{\partial \eta^2} \right] \tag{1.6.3}$$

The transformed model equation, from physical domain (space) to computational domain (space), using equations (1.6.1)-(1.6.3), can be expressed in the form

$$\begin{aligned} \xi_{xx} \frac{\partial \emptyset}{\partial \xi} &+ \xi_x \left[\xi_x \frac{\partial^2 \emptyset}{\partial \xi^2} + \eta_x \frac{\partial^2 \emptyset}{\partial \xi \partial \eta} \right] + \eta_{xx} \frac{\partial \emptyset}{\partial \eta} + \eta_x \left[\xi_x \frac{\partial^2 \emptyset}{\partial \xi \partial \eta} + \eta_x \frac{\partial^2 \emptyset}{\partial \eta^2} \right] + \xi_{yy} \frac{\partial \emptyset}{\partial \xi} \\ &+ \xi_y \left[\xi_y \frac{\partial^2 \emptyset}{\partial \xi^2} + \eta_y \frac{\partial^2 \emptyset}{\partial \xi \partial \eta} \right] + \eta_{yy} \frac{\partial \emptyset}{\partial \eta} + \eta_y \left[\xi_y \frac{\partial^2 \emptyset}{\partial \xi \partial \eta} + \eta_y \frac{\partial^2 \emptyset}{\partial \eta^2} \right] \\ &+ P \left[\xi_x \frac{\partial \emptyset}{\partial \xi} + \eta_x \frac{\partial \emptyset}{\partial \eta} \right] + Q \left[\xi_y \frac{\partial \emptyset}{\partial \xi} + \eta_y \frac{\partial \emptyset}{\partial \eta} \right] = f(\xi, \eta) \end{aligned} \tag{1.6.4}$$

From advanced calculus, one can write relationships between the metrics of the transformation:

$$\xi_x = J^{-1} y_\eta, \quad \xi_y = -J^{-1} x_\eta, \quad \eta_x = -J^{-1} y_\xi, \quad \eta_y = J^{-1} x_\xi \tag{1.6.5}$$

The application of such 2-D transformation functions has been discussed extensively in numerical studies of grid generation methods [32-35].

The comparison of the transformed form of the model equation, stated in (1.6.4), and the equation obtained using the specific transformation functions of the cut-stencil FDM, which will be discussed in Chapter 2, shows the obvious simplicity of the Cartesian cut-stencil FDM. The main reason for the simplicity of the mapped model equations in the Cartesian cut-stencil FD formulation arises from independent 1-D transformation equations which exhibit the necessary features of the localized mapping of each stencil.

1.5   Cartesian Grid

Cartesian grids have been employed in many numerical studies of computational mechanics and specifically in CFD [36-39]. One of the main advantages associated with this type of grid is the relatively simple procedure for the grid generation and hence the time to mesh an irregular shaped

domain is not significant [39]. Additionally, no metric terms are needed [37], and this grid system does not suffer from the difficulties of interpolations which are normally associated with body-fitted grid schemes [37, 40].

The type of grid that is used in the cut-stencil FD solution to PDEs is the Cartesian grid system. A Cartesian grid generator[1] has been developed to meet the necessary grid requirements for the Cartesian cut-stencil FDM. Figure 1.4 illustrates the Cartesian grid system for an arbitrary body, created by the Cartesian grid generation software.

●: Internal node, ◔: Boundary node, ▢: External node
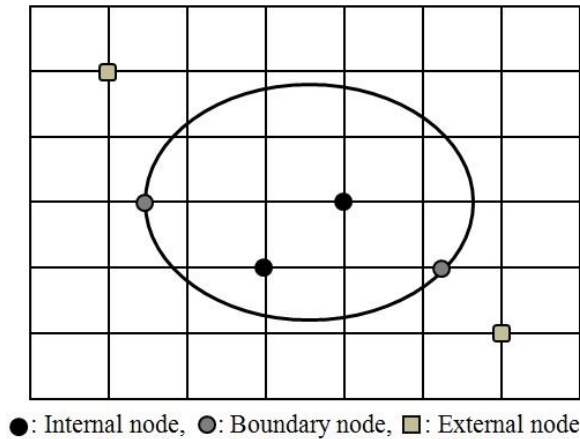
Figure 1.4: Schematic of Cartesian grid system for an arbitrary body

The outputs of the Cartesian grid generator can be summarized as follows:
- (x, y) coordinate of all internal nodes and assignment of a corresponding node identification number
- (x, y) coordinate of all external nodes and assignment of a corresponding node identification number
- (x, y) coordinate of all boundary nodes and assignment of corresponding node identification numbers for each type of boundary node
- the connectivity associated with each 5-point stencil
- the components of the normal vector at each boundary node

All the above-mentioned features are saved in text format files, which can be read by the Cartesian cut-stencil FDM computer code that has been written for this thesis. Due to the solver-dominated context of this research rather than the grid generator used for this purpose, further details of the grid generation software are not discussed.

1.6   Finite Volume Method: Basic Definition and Fundamentals

The vast majority of commercial CFD packages are FV-based. This popularity can be attributed to fewer limitations of FVM with respect to irregular domains. This section of Chapter 1 presents a standard calculation procedure in FVM to highlight the differences between FVM and FDM.

The Laplace equation $\nabla^2 \emptyset = 0$ is studied as the model equation. Figure 1.5 shows the schematic of a typical control volume ABCD which is used to solve the model equation in a complex domain using FVM.

---

[1]) The Cartesian grid generation code was written by J.W. Toth, under the supervision of Dr. R. Barron.
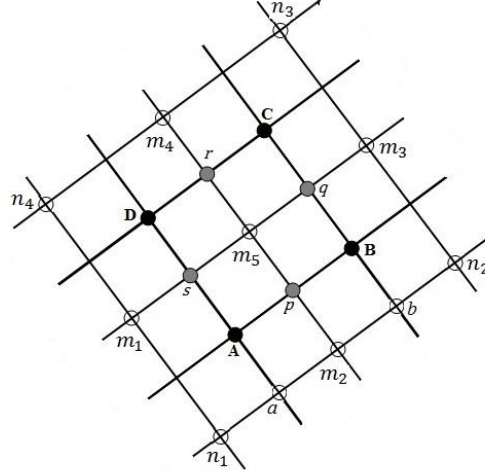
● : Grid nodes of the control volume (CV), ● : Mid-node of CV segments,
○ : Centroid-node of CV

Figure 1.5: Schematic of control volume used for FVM solution to Laplace equation

The integral form of the model equation over the control volume is stated as $\iint_{ABCD} \left(\frac{\partial^2 \emptyset}{\partial x^2} + \frac{\partial^2 \emptyset}{\partial y^2} \right) dxdy = 0$. Applying Green's theorem, this area integral can be written as a line integral, replacing the Laplace equation by

$$\oint \left(\frac{\partial \emptyset}{\partial x} dy - \frac{\partial \emptyset}{\partial y} dx \right) = 0 \tag{1.7.1}$$

Equation (1.7.1) is then approximated as follows. The integral over each face of the control volume ABCD is approximated by the length of each segment times the value of the derivatives at the midpoint of the same segment. The line integration in equation (1.7.1) is expressed in the approximate form

$$\frac{\partial \emptyset}{\partial x} \Big|_p (\Delta y_{AB}) - \frac{\partial \emptyset}{\partial y} \Big|_p (\Delta x_{AB}) + \frac{\partial \emptyset}{\partial x} \Big|_q (\Delta y_{BC}) - \frac{\partial \emptyset}{\partial y} \Big|_q (\Delta x_{BC}) + \frac{\partial \emptyset}{\partial x} \Big|_r (\Delta y_{CD})$$
$$- \frac{\partial \emptyset}{\partial y} \Big|_r (\Delta x_{CD}) + \frac{\partial \emptyset}{\partial x} \Big|_s (\Delta y_{DA}) - \frac{\partial \emptyset}{\partial y} \Big|_s (\Delta x_{DA}) = 0 \tag{1.7.2}$$

One approach to calculate the derivatives in equation (1.7.2), e.g., at the midpoint p, is to assign the average of the derivatives over the control volume which shares the same midpoint, as written in equations (1.7.3) and (1.7.4). In these equations, $\mathcal{S}$ stands for the area of the control volume specified by the subscript.

$$\frac{\partial \emptyset}{\partial x} \Big|_p \simeq \frac{1}{\mathcal{S}_{abqs}} \oint \emptyset dy \simeq \frac{1}{\mathcal{S}_{abqs}} \left[\emptyset_{m_2}(\Delta y_{ab}) + \emptyset_B(\Delta y_{bq}) + \emptyset_{m_5}(\Delta y_{qs}) + \emptyset_A(\Delta y_{sa}) \right] \tag{1.7.3}$$

$$\frac{\partial \emptyset}{\partial y} \Big|_p \simeq \frac{-1}{\mathcal{S}_{abqs}} \oint \emptyset dx \simeq \frac{1}{\mathcal{S}_{abqs}} \left[\emptyset_{m_2}(\Delta x_{ab}) + \emptyset_B(\Delta x_{bq}) + \emptyset_{m_5}(\Delta x_{qs}) + \emptyset_A(\Delta x_{sa}) \right] \tag{1.7.4}$$

A similar procedure can be employed to approximate the derivatives at other midpoints of each segment. Furthermore, it is assumed that the value at corner nodes, such as A, is approximated by averaging the values of the four neighboring nodes, i.e.,

$$\emptyset_A = \frac{\emptyset_{n_1} + \emptyset_{m_2} + \emptyset_{m_5} + \emptyset_{m_1}}{4} \qquad (1.7.5)$$

These approximations yield a set of linear equations for the dependent variables. The iterative schemes described above can be applied to solve this system of linear equations. More details about how FVM can be applied for different types of mesh topologies, as well as different interpolation and approximation schemes used in this numerical method, are addressed in some numerical texts, e.g., [41, 42].

The analysis, as stated above, shows the higher demand of calculations and requirements of interpolation schemes and approximations associated with FVM. Involvement of more grid nodes to increase the accuracy of the interpolation should be viewed in the context of more complexity associated with FVM. Providing a FD-based algorithm that can solve PDEs while enjoying key features of FVM, especially FVM's flexibility in handling irregular shaped domains, would constitute significant advancement in numerical methods for PDEs. This is the primary goal of this thesis.

1.7 Thesis Layout

The thesis is arranged as follows:

- The fundamental concepts and the mathematical manipulations of the Cartesian cut-stencil FDM are presented in Chapter 2. The transformation functions used, the mapped format of model equations, boundary condition implementations, higher-order accurate formulations and unsteady formulations are also addressed in Chapter 2.
- Verification of the proposed cut-stencil algorithm using the results of a number of manufactured problems in different types of physical domains is presented in Chapter 3. This chapter includes a brief summary of the method of manufactured solutions and its applications, especially in code verification. Also, Chapter 3 covers the definitions of local truncation error and formal order of accuracy, and results for these parameters are presented for the manufactured problems.
- The application of the Cartesian cut-stencil FDM for solution of PDEs arising in advanced elasticity and heat transfer are discussed in Chapter 4. These problems mostly are offered in irregular shaped domains which normally create limitations for the traditional finite difference method.
- The study of the streamfunction-vorticity formulation of the Navier-Stokes equations is the main subject of Chapter 5. The Cartesian cut-stencil FD formulation for the coupled non-linear streamfunction and vorticity equations and corresponding results of lid-driven cavity flow in different shapes of domain are presented in this chapter. Since this problem has been addressed as a benchmark flow problem in many numerical studies, Chapter 5 can also be seen in the context of application of the Cartesian cut-stencil FDM to solve complex fluid flow problems.
- Concluding remarks and suggestions for future work constitute Chapter 6, and Appendices are the final sections of the thesis.

CHAPTER 2

FUNDAMENTALS and FORMULATIONS of CARTESIAN CUT-STENCIL FINITE DIFFERENCE METHOD

2.1 Objective of the Chapter

Chapter 2 considers the fundamentals and basic governing formulations of the Cartesian cut-stencil FDM. Boundary condition implementation, unsteady formulation and higher-order schemes and associated equations of the cut-stencil FDM are discussed and their mathematical concepts are addressed in this chapter. To simplify the discussions, without missing the general concepts, Chapter 2 employs the convection-diffusion equation as the model equation since is often used to develop and demonstrate the utility of new numerical algorithms/formulations. In other words, researchers commonly use the convection-diffusion equation to develop and test the key features of the finite difference (FD), finite volume (FV) and finite element (FE) methods [42-47].

2.2 Model Equation and General Transformation Functions

The linear second-order PDE (1.1) is also referred to as the 2-D unsteady convection-diffusion equation and serves as the model equation for this thesis. It can be rewritten in the form

$$\frac{\partial \emptyset}{\partial t} = v\nabla^2\emptyset + P\frac{\partial \emptyset}{\partial x} + Q\frac{\partial \emptyset}{\partial y} + S \tag{2.1}$$

The coefficients P, Q and the source term S are assumed to be independent of the solution $\phi(x, y, t)$. The diffusion coefficient v is considered as constant.

Consider the general 1-D transformation functions $x = x(\xi)$ and $y = y(\eta)$. In this case, the derivative operators given by (1.6.1)–(1.6.3) reduce to

$$\frac{\partial}{\partial x} = \frac{d\xi}{dx}\frac{\partial}{\partial \xi}, \qquad \frac{\partial}{\partial y} = \frac{d\eta}{dy}\frac{\partial}{\partial \eta} \tag{2.2.1}$$

$$\frac{\partial^2}{\partial x^2} = \left(\frac{d\xi}{dx}\right)^2\frac{\partial^2}{\partial \xi^2} + \frac{d^2\xi}{dx^2}\frac{\partial}{\partial \xi}, \qquad \frac{\partial^2}{\partial y^2} = \left(\frac{d\eta}{dy}\right)^2\frac{\partial^2}{\partial \eta^2} + \frac{d^2\eta}{dy^2}\frac{\partial}{\partial \eta} \tag{2.2.2}$$

Using equations (1.6.5) and $J = x'y'$, where $x' \equiv \frac{dx}{d\xi}, y' \equiv \frac{dy}{d\eta}$, these operators become

$$\frac{\partial}{\partial x} = \frac{1}{x'}\frac{\partial}{\partial \xi}, \qquad \frac{\partial}{\partial y} = \frac{1}{y'}\frac{\partial}{\partial \eta} \tag{2.3.1}$$

$$\frac{\partial^2}{\partial x^2} = \frac{1}{(x')^2}\frac{\partial^2}{\partial \xi^2} - \frac{x''}{(x')^3}\frac{\partial}{\partial \xi}, \qquad \frac{\partial^2}{\partial y^2} = \frac{1}{(y')^2}\frac{\partial^2}{\partial \eta^2} - \frac{y''}{(y')^3}\frac{\partial}{\partial \eta} \tag{2.3.2}$$

As indicated above, the transformation Jacobian is $J = x'y'$ and, as long as the transformation functions $x(\xi)$ and $y(\eta)$ have non-zero derivatives with respect to ξ and η, respectively, the Jacobian will be non-zero. Reducing or eliminating the possibility of zero values for the transformation Jacobian is considered as a superior quality for any proposed transformation functions [48], and the transformation used in this thesis is chosen to ensure a non-zero Jacobian.

2.3 Arbitrary Domains and Cartesian Grid

As discussed in Chapter 1 and also referencing the vast literature on numerical simulations for real-world applications, the need to solve PDEs in arbitrary domains with irregular (non-rectangular) complex boundaries is obvious [47-51].

Figure 2.1 illustrates an arbitrarily shaped domain, Ω, on which the PDEs are to be solved, and a 2-D Cartesian grid system which may, in general, have non-uniform spacing between grid lines. The nodes of the grid that are located inside the domain are referred to as active nodes and each active node has a 5-point stencil associated with it.

Some of the 5-point stencils are cut by the boundary of the domain Ω and, as labelled in Figure 2.1, are referred to as "cut-stencils". For any cut-stencil, at least one of the end-nodes on the stencil lies on the boundary. Also, if none of the arms of a stencil are cut by the boundary of Ω, this type of stencil is called an "uncut-stencil". In the case of a non-uniform Cartesian grid, or when any arm(s) of a 5-point stencil are cut by the boundary of Ω, the length of each arm may have different values.
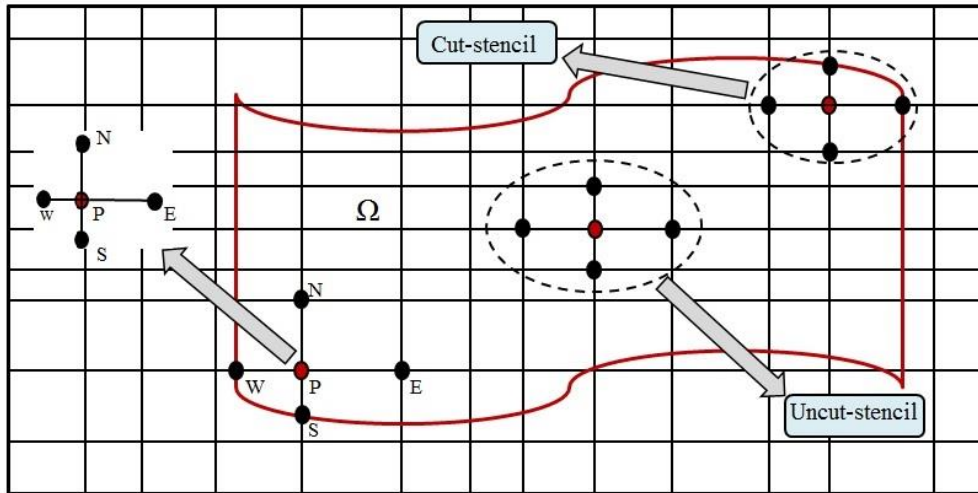
Figure 2.1: Arbitrary complex domain with Cartesian grid and cut-stencils

2.4 Quadratic Form of the Transformation Functions

The core idea of this thesis is to map any 5-point stencil in the physical domain to a generic computational $\xi - \eta$ stencil. In particular, the transformation functions $x(\xi)$ and $y(\eta)$ are chosen to have a quadratic form with respect to ξ and η, respectively. The general forms of these quadratic functions are

$$x = x(\xi) = a_2\xi^2 + a_1\xi + a_0, \quad y = y(\eta) = b_2\eta^2 + b_1\eta + b_0 \tag{2.4}$$

These two quadratic functions are the transformation functions which are used in the Cartesian cut-stencil finite difference (FDM). This transformation is applied at every active node P which is located at the centre of a 5-point stencil shown in Figure 2.1. For each 5-point stencil, the coefficients a_i and b_i can be expressed in terms of the coordinates of the nodes on the stencil.

2.4.1   Mapping of an Arbitrary 5-point Stencil

Figure 2.2 illustrates the mapping of an arbitrary FD stencil centred at an active node P with different arm lengths to a generic uniform computational stencil with all arms of length one.
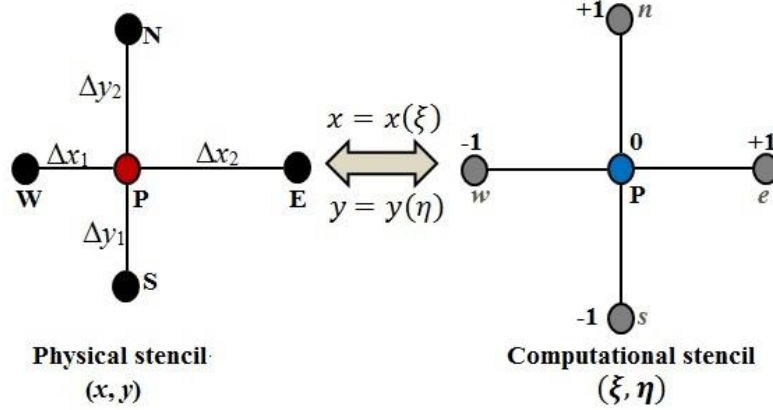
Figure 2.2: Mapping from an arbitrary physical stencil to a generic computational stencil in 2-D

The coefficients a_i and b_i in equations (2.4) are determined uniquely by requiring that the central node P is mapped to the point $\xi = 0, \eta = 0$, and the stencil endpoints W, S, E and N are mapped to (-1,0), (0,-1), (1,0) and (0,1) on the computational stencil, respectively. These conditions lead to:

$$a_2 = \frac{1}{2}(x_W + x_E) - x_P, a_1 = \frac{1}{2}(x_E - x_W), a_0 = x_P \tag{2.5.1}$$

$$b_2 = \frac{1}{2}(y_S + y_N) - y_P, b_1 = \frac{1}{2}(y_N - y_S), b_0 = y_P \tag{2.5.2}$$

By substituting the coefficients from equations (2.5.1) and (2.5.2) into equations (2.4), the first and second derivatives of the quadratic functions $x(\xi)$ and $y(\eta)$ can be calculated analytically in terms of the physical coordinates of the nodes on the stencil. These derivatives, evaluated at node P of the physical FD stencil, are:

$$x'_P = \frac{dx}{d\xi}\Big|_{@P,\xi=0} = a_1 = \frac{1}{2}(x_E - x_W) \tag{2.6.1}$$

$$x''_P = \frac{d^2x}{d\xi^2}\Big|_{@P,\xi=0} = 2a_2 = (x_E + x_W) - 2x_P \tag{2.6.2}$$

$$y'_P = \frac{dy}{d\eta}\Big|_{@P,\eta=0} = b_1 = \frac{1}{2}(y_N - y_S) \tag{2.6.3}$$

$$y''_P = \frac{d^2y}{d\eta^2}\Big|_{@P,\eta=0} = 2b_2 = (y_N + y_S) - 2y_P \tag{2.6.4}$$

It can be concluded from equations (2.6.2) and (2.6.4) that x'' and y'' are both zero if the physical stencil is uniform and, in this event, equations (2.6.1) and (2.6.3) imply that $x' = \Delta x$ and $y' = \Delta y$.

Both uncut and cut stencils are mapped to the uniform 5-point computational stencil. The schematic of this mapping is presented in Figure 2.3. The only difference between cut and uncut

14

stencils is that a cut-stencil includes one or more boundary nodes at which a Dirichlet or Neumann boundary condition will be applied.
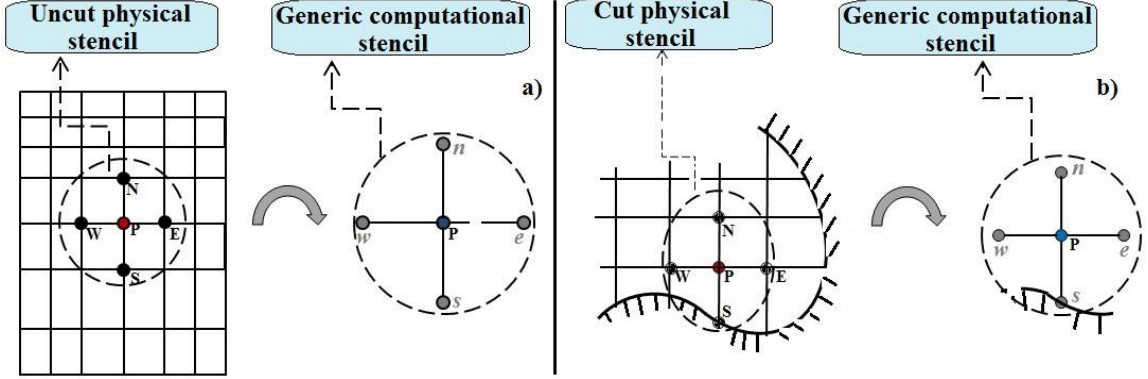
Figure 2.3: Mapping of (a) uncut physical stencil, and (b) cut physical stencil, to a uniform computational stencil

2.4.2 Transformation and Discretization of the Model Convection-Diffusion Equation

The transformation to the uniform computational stencil allows 2nd-order accuracy for the discretization of the derivatives in the model equations. Therefore, the first and second derivatives of the solution variable $\emptyset$ can be approximated using 3-point central differencing with equally spaced neighbouring nodes on the computational stencil. Using equations (2.3.1) and (2.3.2), the cut-stencil formulation can easily be applied to the diffusion-convection equation (2.1). For steady convection-diffusion, the transformed governing equation is

$$v\left[\frac{1}{(x')^2}\frac{\partial^2\emptyset}{\partial\xi^2} - \frac{x''}{(x')^3}\frac{\partial\emptyset}{\partial\xi} + \frac{1}{(y')^2}\frac{\partial^2\emptyset}{\partial\eta^2} - \frac{y''}{(y')^3}\frac{\partial\emptyset}{\partial\eta}\right] + \frac{P}{x'}\frac{\partial\emptyset}{\partial\xi} + \frac{Q}{y'}\frac{\partial\emptyset}{\partial\eta} = s(\xi,\eta) \qquad (2.7)$$

It is well-known that central differencing of the convective terms, particularly in equations with non-linear convective coefficients, may not model the physics of the problem correctly and may, therefore, produce an incorrect solution, or no solution at all. So, in general, upwind differencing is also recommended for discretization of the convective terms to overcome this issue [52-56].

To accommodate these possible options, parameters α and β can be introduced to produce a 1st-order forward ($\alpha = \beta = $ -1), 2nd-order central ($\alpha = \beta = 0$) or 1st-order backward ($\alpha = \beta = 1$) differencing scheme in the x- and y-directions for the convective terms, respectively. Then, equation (2.7) is written in discretized form at the point P, located at the centre of the computational stencil, as:

$$v\left[\frac{\phi_w - 2\phi_P + \phi_e}{(x'_P)^2} - \frac{x''_P(\phi_e - \phi_w)}{2(x'_P)^3} + \frac{\phi_s - 2\phi_P + \phi_n}{(y'_P)^2} - \frac{y''_P(\phi_n - \phi_s)}{2(y'_P)^3}\right] +$$

$$\frac{P[-(1+\alpha)\phi_w + 2\alpha\phi_P + (1-\alpha)\phi_e]}{2x'_P} + \frac{Q[-(1+\beta)\phi_s + 2\beta\phi_P + (1-\beta)\phi_n]}{2y'_P} = s_P \qquad (2.8)$$

Equation (2.8) can be cast in the standard form

$$a_P\phi_P + a_w\phi_w + a_e\phi_e + a_s\phi_s + a_n\phi_n = s_P \qquad (2.9)$$

where the coefficients are defined as:

$$a_{\mathrm{p}} = -v\left(\frac{2}{(x'_{\mathrm{P}})^2} + \frac{2}{(y'_{\mathrm{P}})^2}\right) + \left(\frac{\alpha P}{x'_{\mathrm{P}}} + \frac{\beta Q}{y'_{\mathrm{P}}}\right) \tag{2.10.1}$$

$$a_w = v\left(\frac{1}{(x'_{\mathrm{P}})^2} + \frac{x''_{\mathrm{P}}}{2(x'_{\mathrm{P}})^3}\right) + \left(\frac{-P(1+\alpha)}{2x'_{\mathrm{P}}}\right) \tag{2.10.2}$$

$$a_e = v\left(\frac{1}{(x'_{\mathrm{P}})^2} - \frac{x''_{\mathrm{P}}}{2(x'_{\mathrm{P}})^3}\right) + \left(\frac{P(1-\alpha)}{2x'_{\mathrm{P}}}\right) \tag{2.10.3}$$

$$a_s = v\left(\frac{1}{(y'_{\mathrm{P}})^2} + \frac{y''_{\mathrm{P}}}{2(y'_{\mathrm{P}})^3}\right) + \left(\frac{-Q(1+\beta)}{2y'_{\mathrm{P}}}\right) \tag{2.10.4}$$

$$a_n = v\left(\frac{1}{(y'_{\mathrm{P}})^2} - \frac{y''_{\mathrm{P}}}{2(y'_{\mathrm{P}})^3}\right) + \left(\frac{Q(1-\beta)}{2y'_{\mathrm{P}}}\right) \tag{2.10.5}$$

Equation (2.9) can be solved using standard iterative procedures discussed in Chapter 1, such as Jacobi, Gauss-Seidel or successive over-relaxation (SOR) methods, repeatedly sweeping through all active nodes in the mesh.

2.5   Treatment of Boundary Nodes and Conditions

The treatment of boundary nodes in the Cartesian cut-stencil FD method is based on the type of boundary condition imposed at the node, which may be either a Dirichlet or Neumann boundary condition. In the case of a Dirichlet boundary node, since the boundary condition gives a known value of the solution, this value can be used directly in the calculations on the corresponding stencil adjacent to the boundary. Hence, the discussion in this section focuses on a scheme for Neumann boundary condition implementation in the cut-stencil FDM. This scheme uses a one-sided approximation for the derivatives in the Neumann condition.

The Neumann boundary condition $\frac{\partial \emptyset}{\partial n}\big|_{\mathrm{B}} = G(x_{\mathrm{B}}, y_{\mathrm{B}})$ specifies the value $G(x_{\mathrm{B}}, y_{\mathrm{B}})$ of the normal derivative of the solution variable $\emptyset$ at a point B on a boundary curve S, as illustrated in Figure 2.4. From vector calculus, the normal derivative of a function at a point B on the curve S can be written as:

$$\left[n_x\frac{\partial \emptyset}{\partial x} + n_y\frac{\partial \emptyset}{\partial y}\right]_{\mathrm{B}} = G(x_{\mathrm{B}}, y_{\mathrm{B}}) \tag{2.11}$$

The unit vector $\hat{n}$ denotes the outward unit normal vector to S and the components of the normal vector along x- and y-directions are n_x and n_y, respectively.
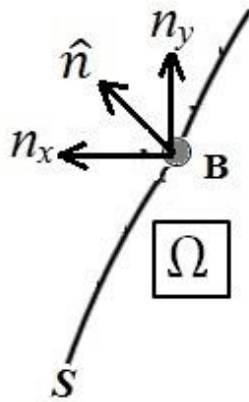
Figure 2.4: Boundary curve and normal vector at specific point

To simplify the discussion, consider a straight line boundary W with a Neumann condition at boundary node B, with corresponding equally-spaced Cartesian grid lines, as depicted in Figure 2.5. It is assumed that for all the nodes along boundary W, the Neumann function G is a prescribed function of the (x, y) coordinate of each point. The outward normal vector at point B is along the negative x-direction, i.e., $\hat{n} = (-1,0)$, and therefore equation (2.11) reduces to $-\frac{\partial \emptyset}{\partial x}\big|_B = G(x_B, y_B)$. Initially, the traditional FD notation is used to write the differencing approximation of the first derivatives and for this purpose, it is assumed that point B has the node indices (i, j).
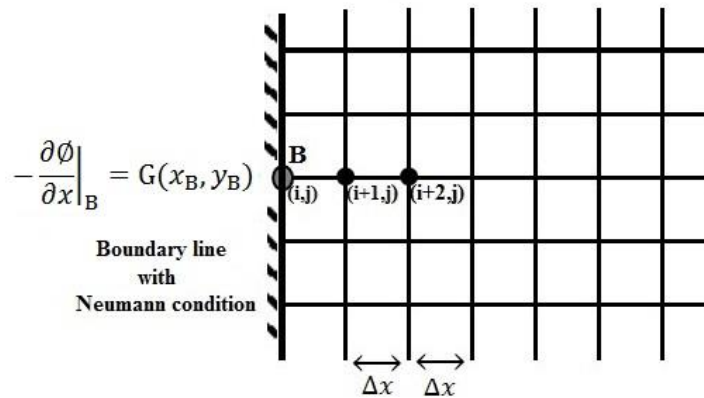
Figure 2.5: Uniform Cartesian grid used for one-sided differencing of Neumann boundary condition (TFD notation)

One-sided 2nd-order accurate differencing is used to approximate the first derivative at point B. This method of approximation uses the nodes inside the domain of interest, unlike the ghost node method which introduces one node from outside the domain to define the difference approximation. Although there are no mathematical issues with the ghost node method, there may be a physical issue hidden in this method for real engineering problems. The ghost node method assumes that the ghost node, which is designed outside the domain and adjacent to the boundary line or node with Neumann boundary condition, carries the same properties as the nodes inside the domain of interest [57, 58]. However, the ghost node may require special treatment in order to

properly respect the different physics because they are located outside the domain, which may be surrounded by another medium and with a different set of governing equations.

Using standard one-sided 2nd-order accurate differencing, the Neumann condition (2.11) becomes

$$\frac{\partial \emptyset}{\partial x}\Big|_B = \frac{-3\emptyset_{(i,j)} + 4\emptyset_{(i+1,j)} - \emptyset_{(i+2,j)}}{2(\Delta x)} = -G(x_B, y_B) \qquad (2.12)$$

which can be rearranged to find the unknown boundary value at point (i,j) based on the value of neighbouring internal nodes and the value of the Neumann boundary function G:

$$\emptyset_{(i,j)} = \frac{4\emptyset_{(i+1,j)} - \emptyset_{(i+2,j)} + 2(\Delta x)G(x_B, y_B)}{3} \qquad (2.13)$$

Analogous to the TFDM, the Cartesian cut-stencil formulation for Neumann boundary nodes is illustrated in Figure 2.6(b). In Figure 2.6(a), the boundary line with the Neumann boundary condition may be located adjacent to a uniform or non-uniform physical grid. The boundary node W, in the physical domain, is a Neumann boundary node.
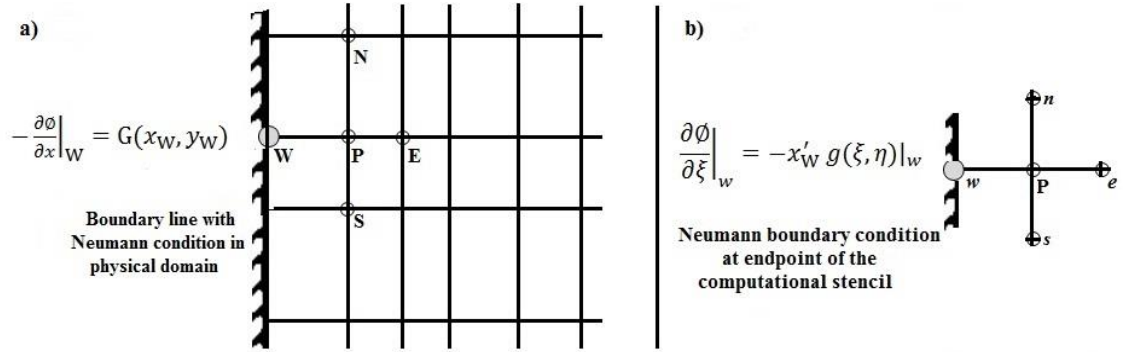
Figure 2.6: Sample grid used for one-sided differencing of Neumann boundary condition (cut-stencil FD notation)

Since the computational stencil in Figure 2.6(b) is uniform, the 3-point approximation in equation (2.12) can be applied. Using the cut-stencil FD formulation and notation, the unknown boundary value at point w in the computational stencil can be obtained as:

$$\frac{1}{x_W'}\frac{\partial \emptyset}{\partial \xi}\Big|_w = \frac{-3\emptyset_w + 4\emptyset_P - \emptyset_e}{2(x_W')} \qquad (2.14.1)$$

$$\emptyset_w = \frac{4\emptyset_P - \emptyset_e + 2(x_W')g(\xi,\eta)|_w}{3} \qquad (2.14.2)$$

In the cut-stencil FDM and corresponding codes, the calculations using one of the iterative schemes is done to find the value of governing function ϕ, at point P of each stencil. Referring to the concept of cut-stencil FD reveals that each endpoint of a stencil centred at point P, as long as it is not a boundary node, can be the centre point of another cut-stencil. This concept is shown schematically in Figure 2.7 which illustrates two five-point stencils in the vicinity of each other. In Figure 2.7(a) the points with subscript 1 (in red) are endpoints of the physical five-point stencil located at point P which is also depicted with subscript 1 (in red). The point W_1 (in red) is also a

centre point P, shown with subscript 2 (in blue), of a physical stencil with endpoints shown with subscript 2 (in blue). It is clear from Figure 2.7(a) that P_1 (in red) is the centre point of a stencil and simultaneously is the east point for another stencil for which the point P_2 (in blue) is the centre point. Figure 2.7(b) conveys the same concept for two computational stencils with the same subscript (color) labelling.
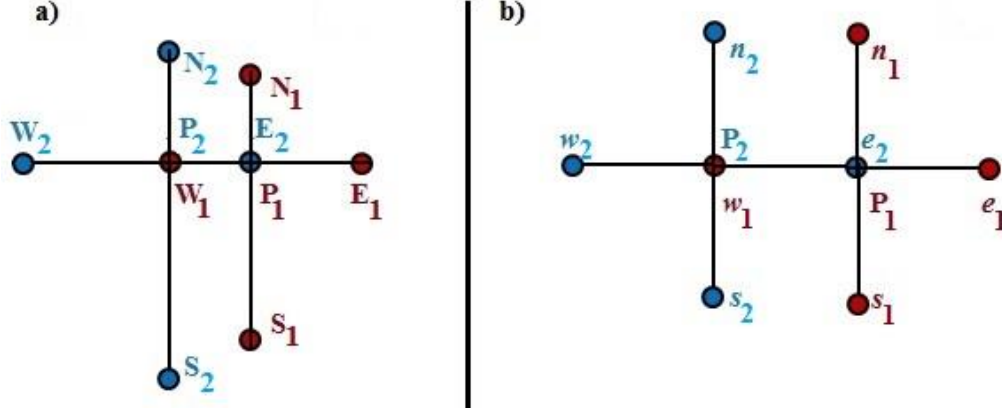
Figure 2.7: Illustration of two five-point stencils in neighbouring a) physical stencils, b) generic computational stencils

Now consider an interior active node P which is adjacent to the Neumann boundary, as shown in Figure 2.6(b). Replacing $\emptyset_w$ in equation (2.9) with the expression in (2.14.2) will change the coefficients written in equations (2.10.1 – 2.10.5). In the event that the Neumann boundary node lies at the west node of a stencil, the coefficients and right hand side in the finite difference equation at interior node P are:

$$a_\mathrm{p} = \nu\left(\frac{-2}{3(x'_\mathrm{P})^2} + \frac{-2}{(y'_\mathrm{P})^2} + \frac{2x''_\mathrm{P}}{3(x'_\mathrm{P})^3}\right) + \left(\frac{(\alpha-2)P}{3x'_\mathrm{P}} + \frac{\beta Q}{y'_\mathrm{P}}\right) \tag{2.15.1}$$

$$a_w = 0 \tag{2.15.2}$$

$$a_e = \nu\left(\frac{2}{3(x'_\mathrm{P})^2} - \frac{2x''_\mathrm{P}}{3(x'_\mathrm{P})^3}\right) + \left(\frac{P(2-\alpha)}{3x'_\mathrm{P}}\right) \tag{2.15.3}$$

$$a_s = \nu\left(\frac{1}{(y'_\mathrm{P})^2} + \frac{y''_\mathrm{P}}{2(y'_\mathrm{P})^3}\right) + \left(\frac{-Q(1+\beta)}{2y'_\mathrm{P}}\right) \tag{2.15.4}$$

$$a_n = \nu\left(\frac{1}{(y'_\mathrm{P})^2} - \frac{y''_\mathrm{P}}{2(y'_\mathrm{P})^3}\right) + \left(\frac{Q(1-\beta)}{2y'_\mathrm{P}}\right) \tag{2.15.5}$$

$$\text{RHS} = s_\mathrm{P} + \nu\left[-\frac{x''_\mathrm{P}}{3(x'_\mathrm{P})^3}x'_\mathrm{W}g|_w - \frac{2}{3(x'_\mathrm{P})^2}x'_\mathrm{W}g|_w\right] + \left[\frac{P(1+\alpha)}{3x'_\mathrm{P}}x'_\mathrm{W}g|_w\right] \tag{2.15.6}$$

A similar procedure can be used to derive new sets of coefficients and expressions for the right hand side of equation (2.9) in the case of a Neumann boundary condition at other endpoints of the stencil.

To illustrate the procedure when two endpoints of a five-point stencil have a Neumann condition, Figures 2.8(a) and (b) show a stencil centred at point P where both west and north endpoints have Neumann conditions.
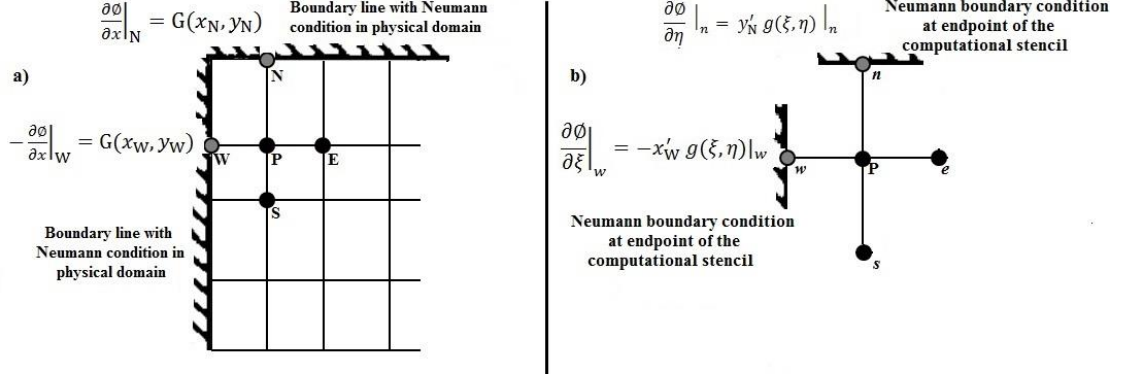
Figure 2.8: Sample of five-point stencil with Neumann conditions at two endpoints

Following the same procedure used to approximate the first derivative at point w as proposed in equation (2.14.1), the difference approximation for the first derivative at point n yields

$$\frac{1}{y_N'}\frac{\partial\emptyset}{\partial\eta}\Big|_n = \frac{3\emptyset_n - 4\emptyset_P + \emptyset_s}{2(y_N')} = g(\xi,\eta)|_n \tag{2.16.1}$$

$$\emptyset_n = \frac{4\emptyset_P - \emptyset_s + 2(y_N')g(\xi,\eta)|_n}{3} \tag{2.16.2}$$

In this case, by substituting the values of $\emptyset_w$ and $\emptyset_n$ from equations (2.14.2) and (2.16.2) respectively, in the discrete form (2.9) of the convection-diffusion equation, the coefficients and right hand side of (2.9) can be written as:

$$a_\mathrm{p} = \nu\left(\frac{-2}{3(x_P')^2} + \frac{-2}{3(y_P')^2} + \frac{2x_P''}{3(x_P')^3} - \frac{2y_P''}{3(y_P')^3}\right) + \left(\frac{(\alpha-2)P}{3x_P'} + \frac{(\beta-2)Q}{3y_P'}\right) \tag{2.17.1}$$

$$a_w = 0 \tag{2.17.2}$$

$$a_e = \nu\left(\frac{2}{3(x_P')^2} - \frac{2x_P''}{3(x_P')^3}\right) + \left(\frac{P(2-\alpha)}{3x_P'}\right) \tag{2.17.3}$$

$$a_s = \nu\left(\frac{2}{3(y_P')^2} + \frac{2y_P''}{3(y_P')^3}\right) + \left(\frac{-Q(2+\beta)}{3y_P'}\right) \tag{2.17.4}$$

$$a_n = 0 \tag{2.17.5}$$

$$\mathrm{RHS} = s_P + \nu\left[-\frac{x_P''}{3(x_P')^3}x_W'g|_w - \frac{2}{3(x_P')^2}x_W'g|_w + \frac{y_P''}{3(y_P')^3}y_N'g|_n - \frac{2}{3(y_P')^2}y_N'g|_n\right]$$
$$+ \left[\frac{P(1+\alpha)}{3x_P'}x_W'g|_w\right] - \left[\frac{Q(1-\beta)}{3y_P'}y_N'g|_n\right] \tag{2.17.6}$$

2.5.1 Implementation for Curved Boundaries with Neumann Condition

The concepts and approximations discussed in connection with Neumann boundary conditions has, thus far, been limited to consideration of a straight boundary line as shown in Figures 2.6 and 2.8 to simplify the explanation of boundary nodes and conditions implementation. In reality, the boundaries of a complex domain may be any type of arbitrary curve. This fact, along with a Cartesian grid system, as the grid system used in the Cartesian cut-stencil FDM, may create two types of boundary nodes, referred to in this dissertation as "regular boundary nodes" and "irregular boundary nodes".

Figure 2.9 illustrates an arbitrary domain Ω and a Cartesian grid, similar to Figure 2.1. As can be seen from Figure 2.9, both a horizontal and a vertical grid line may pass through some boundary nodes. This type of boundary node is called a "regular boundary node". At a regular boundary node with a Neumann boundary condition, the data required for constructing one-sided difference formulas in both $\xi -$ and $\eta -$ directions are available.

If only one horizontal grid line or one vertical grid line passes through a boundary node, this type of boundary node is called an "irregular boundary node". For any irregular boundary node with a Neumann condition placed at an endpoint of any stencil, the data for a one-sided approximation in either $\xi -$ or $\eta -$ direction is available, but not in both directions. In this case, a weighted average method has been used to provide the conditions for the differencing approximation in the direction with missing data. The concepts and equations associated with these two types of boundary nodes are considered in the following sections.
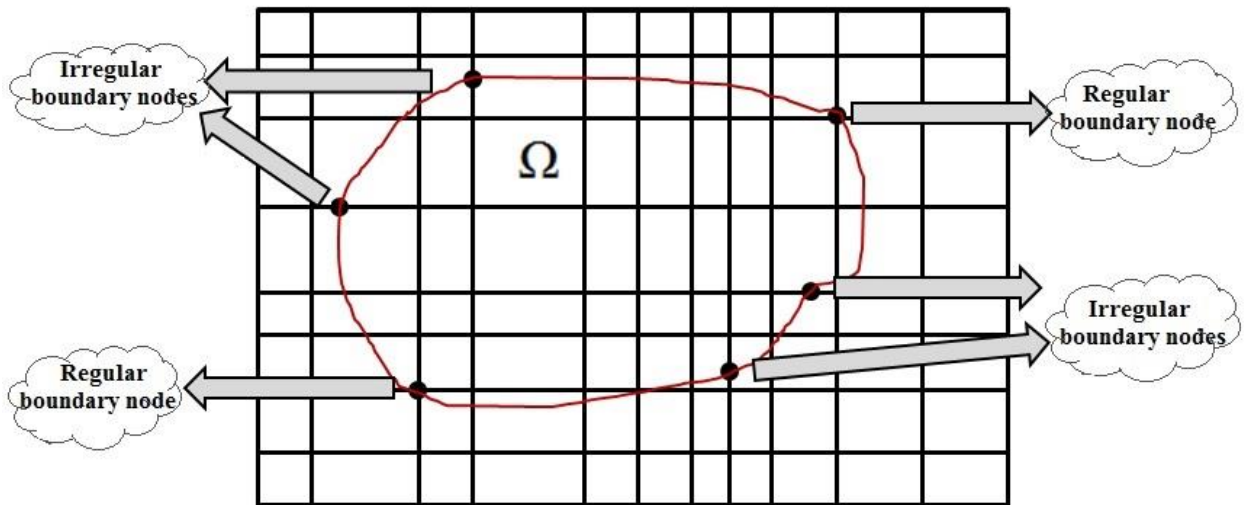
Figure 2.9: Illustration of regular and irregular boundary nodes

2.5.2 Treatment of Regular Boundary Nodes

As noted above, discretization of the first derivatives in the given Neumann condition, in both *x*- and *y*-directions, or correspondingly with respect to ξ and η, are required. Without loss of generality, assume that the boundary node lies at the west endpoint W, located on a curved boundary shown in Figure 2.10, for which the *y*-component of the normal vector is negative, i.e., $n_y < 0$. W is the west endpoint of the physical stencil associated with an internal node P which is adjacent to the boundary, and assume that a Neumann condition is imposed at node W. Boundary node W in Figure 2.10 is a regular boundary node.
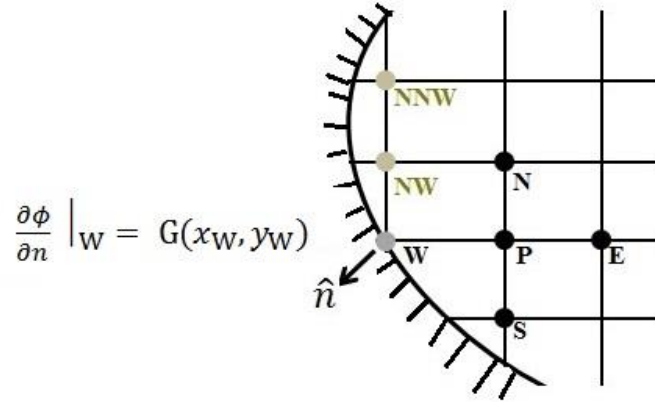
Figure 2.10: Regular boundary node at west node of physical stencil with $n_y < 0$

Since both vertical and horizontal grid lines pass through node W, in general, enough nodes and corresponding ϕ values are available to construct the one-sided 2nd-order approximation for the first derivatives of ϕ. Applying the Neumann boundary condition (2.11) at node W, mapping to the computational stencil and using 2nd-order approximations for the derivatives, the boundary condition at W, when $n_y < 0$, can be written as:

$$\frac{\partial \emptyset}{\partial n}\Big|_{W} = \left[\frac{n_x}{x'}\frac{\partial \emptyset}{\partial \xi} + \frac{n_y}{y'}\frac{\partial \emptyset}{\partial \eta}\right]_{W}$$

$$\approx \left(\frac{n_x}{x'}\right)_{W}\left[\frac{-3\emptyset_w + 4\emptyset_P - \emptyset_e}{2}\right] + \left(\frac{n_y}{y'}\right)_{W}\left[\frac{-3\emptyset_w + 4\emptyset_{nw} - \emptyset_{nnw}}{2}\right] = g|_w \tag{2.18}$$

where *nw* and *nnw* refer to the north-west and north-north-west nodes relative to node P. The sign of one of the components of the normal vector to the curve at the boundary node with Neumann condition determines whether to use the backward or forward differencing scheme along that direction. For a west boundary node the sign of n_x is always negative (or zero) while the n_y component of the normal vector could be negative, as shown in Figure 2.10, or positive as depicted in Figure 2.11. To be precise, if the normal vector at the west boundary node with Neumann condition has a negative *y*-component (Figure 2.10), the forward differencing scheme is used to approximate the derivatives in both $\xi -$ and $\eta -$ directions. Figure 2.11 presents the case of west boundary node when $n_y > 0$, for which forward differencing is used to approximate $\frac{\partial \emptyset}{\partial \xi}$ and backward differencing is used for $\frac{\partial \emptyset}{\partial \eta}$, yielding
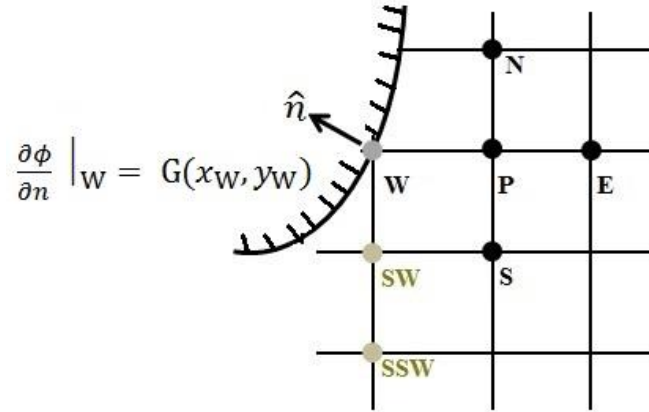
Figure 2.11: Regular node at west boundary node of physical stencil with $n_y > 0$

$$\frac{\partial \emptyset}{\partial n}\Big|_w = \left[\frac{n_x}{x'}\frac{\partial \emptyset}{\partial \xi} + \frac{n_y}{y'}\frac{\partial \emptyset}{\partial \eta}\right]_w$$

$$\approx \left(\frac{n_x}{x'}\right)_w\left[\frac{-3\emptyset_w + 4\emptyset_P - \emptyset_e}{2}\right] + \left(\frac{n_y}{y'}\right)_w\left[\frac{3\emptyset_w - 4\emptyset_{sw} + \emptyset_{ssw}}{2}\right] = g|_w \qquad (2.19)$$

To further clarify the concept, consider the case of a regular boundary node with Neumann boundary condition at the south of an internal node P. The sign of n_y is always negative in this case, as illustrated in Figures 2.12 and 2.13, which means that forward differencing should be used for $\frac{\partial \emptyset}{\partial \eta}$. However, for the ξ-derivative, forward or backward differencing is used depending on whether $n_x < 0$ (Figure 2.12) or $n_x > 0$ (Figure 2.13), respectively.
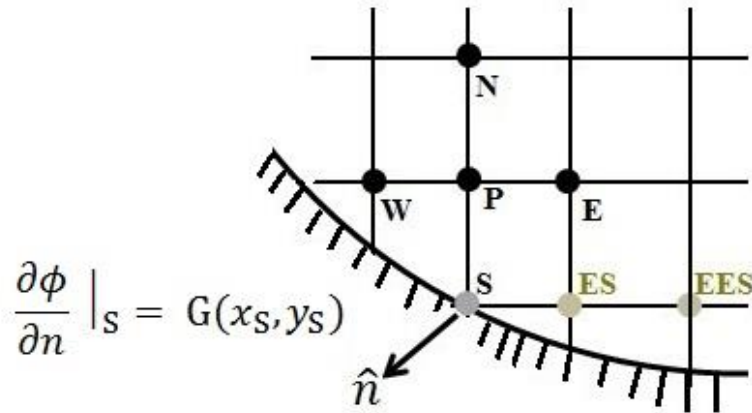
Figure 2.12: Regular node at south boundary node of physical stencil with $n_x < 0$
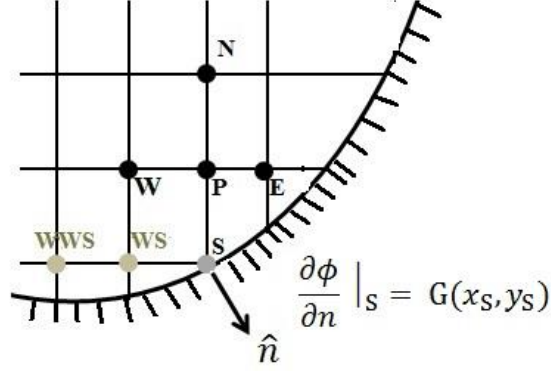
Figure 2.13: Regular node at south boundary node of physical stencil with $n_x > 0$

Thus, for south boundary nodes with Neumann conditions,

$$\frac{\partial \emptyset}{\partial n}\Big|_S = \left[\frac{n_x}{x'}\frac{\partial \emptyset}{\partial \xi} + \frac{n_y}{y'}\frac{\partial \emptyset}{\partial \eta}\right]_S$$

$$\approx \left(\frac{n_x}{x'}\right)_S \left[\frac{-3\emptyset_s + 4\emptyset_{es} - \emptyset_{ees}}{2}\right] + \left(\frac{n_y}{y'}\right)_S \left[\frac{-3\emptyset_s - 4\emptyset_P + \emptyset_n}{2}\right] = g|_s \qquad \text{if } n_x < 0 \quad (2.20.1)$$

$$\frac{\partial \emptyset}{\partial n}\Big|_S = \left[\frac{n_x}{x'}\frac{\partial \emptyset}{\partial \xi} + \frac{n_y}{y'}\frac{\partial \emptyset}{\partial \eta}\right]_S$$

$$\approx \left(\frac{n_x}{x'}\right)_S \left[\frac{3\emptyset_s - 4\emptyset_{ws} + \emptyset_{wws}}{2}\right] + \left(\frac{n_y}{y'}\right)_S \left[\frac{-3\emptyset_s - 4\emptyset_P + \emptyset_n}{2}\right] = g|_s \qquad \text{if } n_x > 0 \quad (2.20.2)$$

For other boundary nodes at the north and east of an internal node P with Neumann conditions, similar conditions are valid with one of the components of the normal vector at the boundary node determining the differencing scheme. Table 2.1 gives a summary of the appropriate differencing scheme based on the sign of the components of the normal vector at boundary nodes at the west, south, east and north.

Boundary node on a curved boundary	Sign of x-component of normal vector	Sign of y-component of normal vector	Differencing scheme along ξ-direction	Differencing scheme along η-direction
West	Negative	Negative or positive	Forward	Forward or backward
South	Negative or positive	Negative	Forward or backward	Forward
East	Positive	Negative or positive	Backward	Forward or backward
North	Negative or positive	Positive	Forward or backward	Backward

Table 2.1: Summary of the sign of normal vector components and corresponding differencing schemes for boundary nodes on curved boundaries

2.5.3   Treatment of Irregular Boundary Nodes

The discussion for boundary nodes on curved boundaries, so far, has dealt with the treatment of the regular type of boundary nodes at the west, south, east or north. The treatment of irregular type of boundary nodes, as identified in Figure 2.9, will be discussed in this section. Recall that grid lines do not intersect at an irregular boundary node, so there is either a horizontal grid line or a vertical grid line emanating from the boundary node, but not both. Some representative schematics of this situation are illustrated in Figures 2.14, 2.15 and 2.16. Consequently, there are no internal nodes along one of the grid line directions from the boundary node. For example, considering boundary node E in Figure 2.14, the condition for constructing a differencing scheme along the horizontal grid line is available, while it is not possible to write the differencing scheme along the vertical direction. In general, for any irregular boundary node, this problem is resolved by inserting an imaginary line emanating in the appropriate direction from the boundary node and imaginary nodes are defined as shown in Figures 2.14-2.16. The dashed lines and the nodes labelled by * are fictitious lines and nodes, respectively.
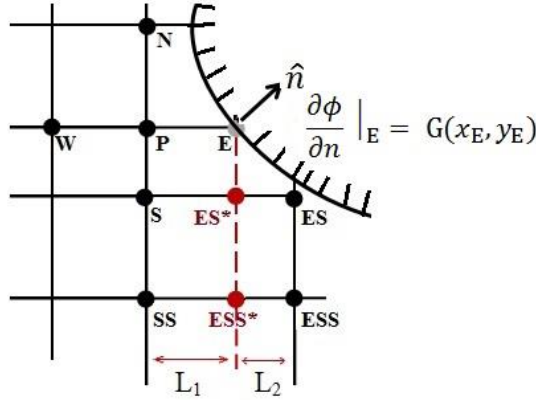
Figure 2.14: Irregular node at east boundary node of physical stencil with $n_y > 0$

Then, formulas that were derived for regular boundary nodes can be modified to treat irregular boundary nodes. It is simply a matter of replacing the off-stencil nodal values, such as $\emptyset_{nw}$ and $\emptyset_{nnw}$ in equation (2.18) by the values at the fictitious nodes, i.e., $\emptyset_{nw*}$ and $\emptyset_{nnw*}$. However, these nodes are not real nodes and the corresponding values are not part of the unknowns in the solution procedure. These fictitious nodal values must be defined in terms of the values at the actual nodes of the Cartesian mesh.

To accomplish this, a distance weighted average method is applied to evaluate the values at the fictitious nodes. The averaging can be explained by referring to Figure 2.14. For the irregular boundary node at the east of internal node P, L_1 is the distance between nodes S or SS and E, and L_2 is the distance between nodes ES or ESS and E. The values at the fictitious nodes ES* and ESS*, or equivalently at *es** and *ess** on the computational stencil, are evaluated by weighted average equations as follows:

$$\emptyset_{es*} = \frac{\dfrac{\emptyset_s}{L_1} + \dfrac{\emptyset_{es}}{L_2}}{\dfrac{1}{L_1} + \dfrac{1}{L_2}} = \frac{L_2\emptyset_s + L_1\emptyset_{es}}{L_1 + L_2} \tag{2.21.1}$$

$$\emptyset_{ess*} = \frac{\dfrac{\emptyset_{ss}}{L_1} + \dfrac{\emptyset_{ess}}{L_2}}{\dfrac{1}{L_1} + \dfrac{1}{L_2}} = \frac{L_2\emptyset_{ss} + L_1\emptyset_{ess}}{L_1 + L_2} \tag{2.21.2}$$

Similar expressions can be derived for other cases where the irregular boundary node lies on the west, south or north endpoint of the stencil. Once these fictitious values have been computed, the Neumann boundary conditions corresponding to Figures 2.14, 2.15 and 2.16 are written respectively as:

$$\frac{\partial \emptyset}{\partial n}\bigg|_E = \left[\frac{n_x}{x'}\frac{\partial \emptyset}{\partial \xi} + \frac{n_y}{y'}\frac{\partial \emptyset}{\partial \eta}\right]_E$$
$$\approx \left(\frac{n_x}{x'}\right)_E \left[\frac{3\emptyset_e - 4\emptyset_P + \emptyset_w}{2}\right] + \left(\frac{n_x}{y'}\right)_E \left[\frac{3\emptyset_e - 4\emptyset_{es*} + \emptyset_{ess*}}{2}\right] = g|_e \tag{2.22.1}$$

$$\frac{\partial \phi}{\partial n}\Big|_E = \left[\frac{n_x}{x'}\frac{\partial \phi}{\partial \xi} + \frac{n_y}{y'}\frac{\partial \phi}{\partial \eta}\right]_E$$

$$\approx \left(\frac{n_x}{x'}\right)_E \left[\frac{3\phi_e - 4\phi_P + \phi_w}{2}\right] + \left(\frac{n_y}{y'}\right)_E \left[\frac{-3\phi_e + 4\phi_{en^*} - \phi_{enn^*}}{2}\right] = g|_e \qquad (2.22.2)$$

$$\frac{\partial \phi}{\partial n}\Big|_N = \left[\frac{n_x}{x'}\frac{\partial \phi}{\partial \xi} + \frac{n_y}{y'}\frac{\partial \phi}{\partial \eta}\right]_N$$

$$\approx \left(\frac{n_x}{x'}\right)_N \left[\frac{-3\phi_n + 4\phi_{ne^*} - \phi_{nee^*}}{2}\right] + \left(\frac{n_y}{y'}\right)_N \left[\frac{3\phi_n - 4\phi_P + \phi_s}{2}\right] = g|_n \qquad (2.22.3)$$
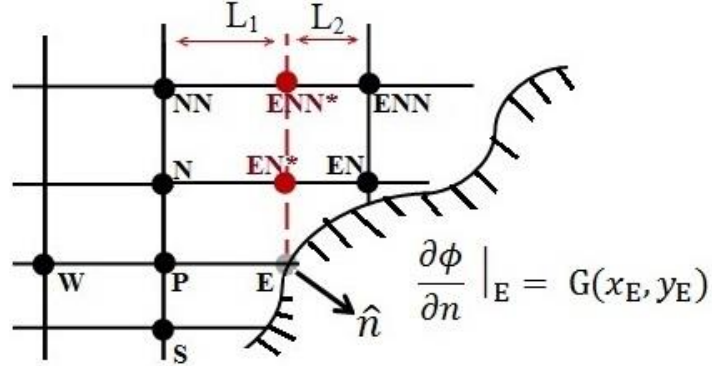
Figure 2.15: Irregular node at east boundary node of physical stencil with $n_y < 0$
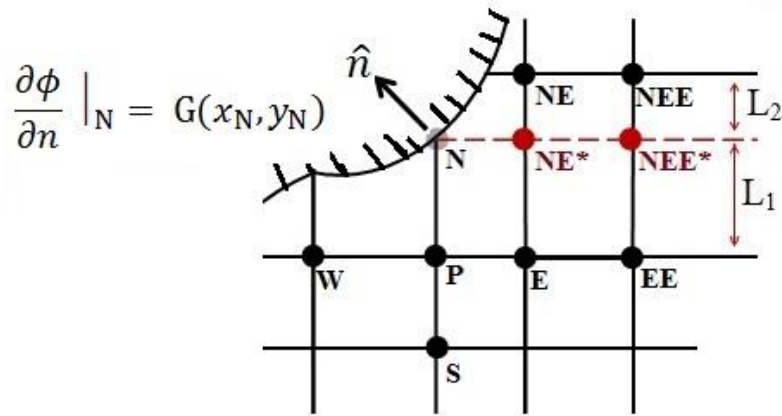
Figure 2.16: Irregular node at north boundary node of physical stencil with $n_x < 0$

The details of Neumann boundary condition treatment at any boundary node on any curved boundary have been discussed in this section. Figures 2.10-2.16, along with the corresponding equations (2.18), (2.19), (2.20) and (2.22), consider representative cases of regular and irregular boundary nodes. Since the values of ϕ at the boundary nodes are required in the solution algorithm, these equations are rearranged to produce an explicit expression for the unknown value at a Neumann boundary node. For example, the value at the irregular boundary node with Neumann condition at the east of internal node P, as depicted in Figure 2.15, is obtained using equation (2.22.2) in the following form:

$$\emptyset_e = \left(\frac{3}{2}\left(\left(\frac{n_x}{x'}\right)_E - \left(\frac{n_y}{y'}\right)_E\right)\right)^{-1}\left[g|_e + 2\left(\frac{n_x}{x'}\right)_E \emptyset_P - \frac{1}{2}\left(\frac{n_x}{x'}\right)_E \emptyset_w - 2\left(\frac{n_y}{y'}\right)_E \emptyset_{en^*}\right.$$
$$\left. + \frac{1}{2}\left(\frac{n_y}{y'}\right)_E \emptyset_{enn^*}\right] \tag{2.22.4}$$

The expression in equation (2.22.4) conveys the same concept as discussed in implementation of the Neumann boundary condition on a straight boundary and stated, e.g., in equation (2.14.2). A new set of coefficients in the finite difference equation for an internal node P, when a Neumann boundary node is located at one (or more) of the endpoints of its stencil, can be derived, similar to coefficients for a straight boundary given by equations (2.17.1-2.17.6).

The concept of common nodes in neighbouring 5-point stencils has been mentioned in preceding sections and illustrated in Figure 2.7. Any regular boundary node on curved boundaries, which is located at the endpoint of more than one 5-point stencil, may have Dirichlet or Neumann boundary conditions. In fact, the concept of common nodes is applicable for treatment of regular boundary nodes.

To simplify the discussion of common nodes, the study here is limited to one case with Neumann condition boundary node since the procedure is the same for other cases and can also cover the boundary node with a Dirichlet condition. It is assumed that regular node B on the curved boundary, as presented in Figure 2.17, has the Neumann boundary condition. The node B is located at the west end node and north end node of arbitrary internal nodes P_W and P_N, respectively.
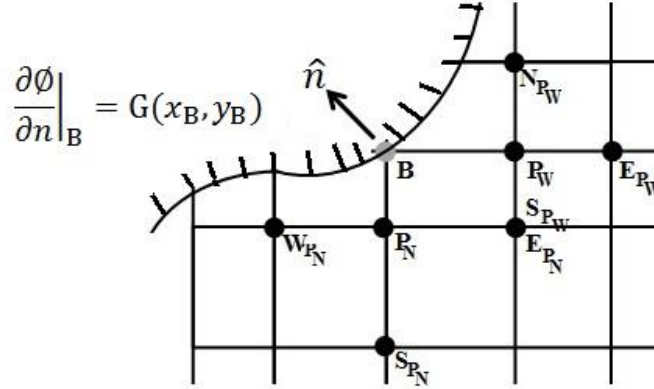
Figure 2.17: Illustration of a regular boundary node with Neumann condition at the endpoints of two 5-point stencils

The differencing along the $\xi-$ direction is performed using forward differencing and backward differencing is used for differencing along the $\eta-$ direction. The difference approximation of the Neumann condition at regular boundary node B, as indicated in Figure 2.17, is written as:

$$\left.\frac{\partial\emptyset}{\partial n}\right|_B = \left[\frac{\hat{n}_x}{x'_B}\frac{\partial\emptyset}{\partial\xi} + \frac{\hat{n}_y}{y'_B}\frac{\partial\emptyset}{\partial\eta}\right]_E$$

$$\approx \left(\frac{n_x}{x'}\right)_E\left[\frac{-3\emptyset_B + 4\emptyset_{P_W} - \emptyset_{E_{P_W}}}{2}\right] + \left(\frac{n_y}{y'}\right)_E\left[\frac{3\emptyset_B - 4\emptyset_{P_N} + \emptyset_{S_{P_N}}}{2}\right] = G(x,y)\left.\right|_B \tag{2.23}$$

Equation (2.23) is similar to equation (2.19) for a regular boundary node at west node with $\hat{n}_y > 0$, and restated here by considering the values of the governing function from two neighbouring 5-point stencils. The condition illustrated in Figure 2.17 is applicable for any other combinations of identical Neumann boundary nodes as the common endpoint of two 5-point stencils.

2.6   Higher-Order Differencing

The order of discretization is one of the primary criteria used to assess the accuracy of a solution in a FD method. Higher-order methods (higher than 2) have generated intense interest in recent years in many application areas such as compressible and incompressible flow, computational aeroacoustics, geodynamic simulations, simulations in aerospace and other fields [59-63]. Clearly, a wider stencil typically used to achieve a higher-order discretization can offer more accurate solution of the governing PDEs for points in the domain interior, but this approach fails at near-boundary nodes, where lower-order schemes have to be implemented. Furthermore, wider stencils cannot be easily accommodated in complex domains and they lead to more matrix calculations [64, 65]. As an alternative, the compact Padé-Hermitian formulation, which uses a narrower stencil, has been used in many studies to propose higher-order formulations for the solution of PDEs, e.g. [64, 66-68].

Undoubtedly, one of the main purposes of applying any higher-order formulation to the solution of PDEs is to obtain more accurate solutions compared to a lower-order formulation with the same size of mesh. So, in this research two main formulations, categorized as higher-order, have been proposed and investigated. These two formulations, which lead to more accurate solutions for "manufactured" problems and real physical problems, are referred to as 5+4-point cut-stencil and higher-order (HO) compact cut-stencil FD. The details of the formulations for each main higher-order scheme and combinations of these higher-order schemes with the cut-stencil FDM are studied in this chapter. Consideration of the real order of accuracy for the higher-order formulations and the corresponding results will be investigated later, especially in Chapter 3.

The cut-stencil FDM, due to its simplicity, is well-suited for extension to higher-order formulations. The localized treatment of the physical stencil provides a simple framework for development of higher-order schemes. Furthermore, programming the higher-order formulations in complicated domains is possible with any type of boundary conditions and arbitrarily complex boundaries. The main aim in the development of higher-order methods proposed in this dissertation is to keep the size of stencil and number of nodes in each stencil as the original 5-point stencil of the cut-stencil FDM, as depicted in Figure 2.2. Accordingly, the values of the governing function and its derivatives used to construct the higher-order methods are all expressed in terms of only the five points of the main stencil of the cut-stencil FDM. That is to say, the values and derivatives of the governing function at the nodes of the 5-point stencil are used explicitly in the higher-order formulations. However, it is worth noting that the values of the governing function at some neighbouring nodes outside the 5-point stencil may be used to approximate the derivatives in the HO compact formulations of the cut-stencil FDM, particularly near the boundary. This fact will be clearer when the formulation of each HO scheme is considered.

2.6.1 5+4-point (4 Auxiliary Nodes) Stencil Formulation

The main issue associated with using higher-order formulation with a wider stencil, e.g. 9-point stencil, becomes apparent in differencing at the nodes near the boundaries [17]. Figure 2.18 shows a sample 9-point stencil in the physical domain with TFD labelling which can be used to approximate first and second derivatives with 4th-order of accuracy.
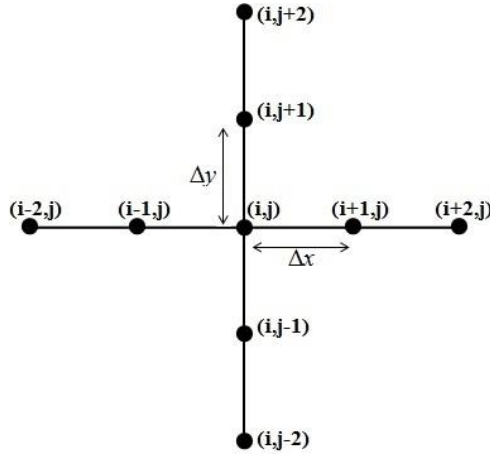
Figure 2.18: Sample of 9-point stencil with TFD notation used for 4th-order approximation

Standard 5-point (in each direction) central differencing produces 4th-order approximations given by equations (2.24) for first and second derivatives at node (i,j) using the stencil shown in Figure 2.18. Obviously, the width and height of the 9-point stencil used to construct the differencing expressions are twice as large compared to the 5-point stencil. Thus, in the event that the point (i,j) is neighbouring to a boundary in any direction, equations (2.24) cannot be applied to find a 4th-order accurate solution at point (i,j). The usual remedy for this issue is to use 3-point 2nd-order accurate approximations for nodes located next to boundaries, or construct an upwind differencing formulation with the same higher-order approximation as interior nodes, which also requires a wider stencil in one or two directions.

$$\frac{\partial \emptyset}{\partial x}\Big|_{(i,j)} = \frac{\emptyset_{(i-2,j)} - 8\emptyset_{(i-1,j)} + 8\emptyset_{(i+1,j)} - \emptyset_{(i+2,j)}}{12\Delta x} \tag{2.24.1}$$

$$\frac{\partial^2 \emptyset}{\partial x^2}\Big|_{(i,j)} = \frac{-\emptyset_{(i-2,j)} + 16\emptyset_{(i-1,j)} - 30\emptyset_{(i,j)} + 16\emptyset_{(i+1,j)} - \emptyset_{(i+2,j)}}{12(\Delta x)^2} \tag{2.24.2}$$

$$\frac{\partial \emptyset}{\partial y}\Big|_{(i,j)} = \frac{\emptyset_{(i,j-2)} - 8\emptyset_{(i,j-1)} + 8\emptyset_{(i,j+1)} - \emptyset_{(i,j+2)}}{12\Delta y} \tag{2.24.3}$$

$$\frac{\partial^2 \emptyset}{\partial y^2}\Big|_{(i,j)} = \frac{-\emptyset_{(i,j-2)} + 16\emptyset_{(i,j-1)} - 30\emptyset_{(i,j)} + 16\emptyset_{(i,j+1)} - \emptyset_{(i,j+2)}}{12(\Delta y)^2} \tag{2.24.4}$$

In this thesis, to overcome the problem of reduced accuracy near the boundary while still preserving the goal of the cut-stencil method not to use points outside the 5-point stencil, a 9-point stencil is created by inserting four auxiliary points along the arms of the original 5-point stencil. Figure 2.19 illustrates physical and computational stencils which are made by adding one node at the midpoint of each arm of the computational stencil, shown in Figure 2.2, and

corresponding location on the arms of the physical stencil, i.e., at *l*, *r*, *b* and *a* corresponding to ξ, η values of (-½, 0), (½, 0), (0, -½) and (0, ½) respectively.
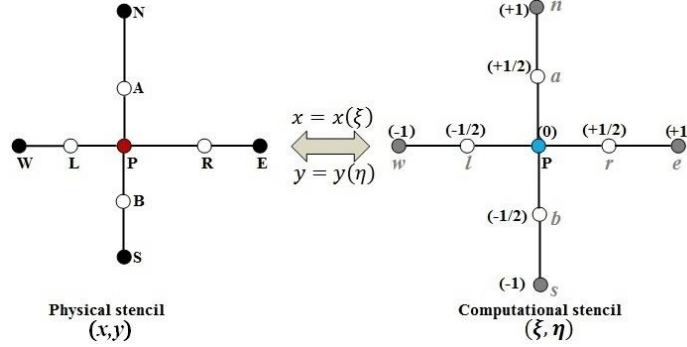
Figure 2.19: Illustration of physical and computational 5+4-point (4 auxiliary nodes) stencils

The same quadratic functions in equation (2.4), which map an arbitrary physical 5-point stencil to a uniform computational 5-point stencil, are used for the process of mapping the 5+4-point physical stencil to a uniform 5+4-point computational stencil, as shown in Figure 2.19. As mentioned before, the auxiliary nodes *l*, *r*, *a* and *b* are the midpoints on the arms of the computational stencil. Under the quadratic mapping, these midpoints on the arms of the computational stencil do not map to midpoints on the physical stencil, unless the physical stencil is uniform. The value of ξ and η and the corresponding expressions for the *x*- and *y*-coordinates of the four auxiliary nodes on the physical stencil are summarized in Table 2.2.

Node	ξ	η	*x*-coordinate	*y*-coordinate
L	$-1/2$	0	$\frac{3}{4}x_P + \frac{3}{8}x_W - \frac{1}{8}x_E$	y_P
R	$+1/2$	0	$\frac{3}{4}x_P - \frac{1}{8}x_W + \frac{3}{8}x_E$	y_P
B	0	$-1/2$	x_P	$\frac{3}{4}y_P + \frac{3}{8}y_S - \frac{1}{8}y_N$
A	0	$+1/2$	x_P	$\frac{3}{4}y_P - \frac{1}{8}y_S + \frac{3}{8}y_N$

Table 2.2: Expressions for *x*- and *y*-coordinates of four auxiliary nodes on the physical stencil used in the 5+4-point cut-stencil formulation

The computational stencil in Figure 2.19 provides the opportunity to write 4th-order differencing expressions for first and second derivatives at point P, by taking into account that $\Delta\xi$ and $\Delta\eta$ are both equal to 1/2. Analogous to equations (2.24), these 4th-order accurate approximations at point P on the computational stencil are:

$$\frac{\partial \emptyset}{\partial \xi}\bigg|_P = \frac{\emptyset_w - 8\emptyset_l + 8\emptyset_r - \emptyset_e}{12\Delta\xi}\bigg|_{\Delta\xi=1/2} \tag{2.25.1}$$

$$\frac{\partial^2 \emptyset}{\partial \xi^2}\bigg|_P = \frac{-\emptyset_w + 16\emptyset_l - 30\emptyset_P + 16\emptyset_r - \emptyset_e}{12(\Delta\xi)^2}\bigg|_{\Delta\xi=1/2} \tag{2.25.2}$$

$$\frac{\partial \emptyset}{\partial \eta}\bigg|_P = \frac{\emptyset_s - 8\emptyset_b + 8\emptyset_a - \emptyset_n}{12\Delta\eta}\bigg|_{\Delta\eta=1/2} \tag{2.25.3}$$

$$\frac{\partial^2 \emptyset}{\partial \eta^2}\bigg|_{\text{P}} = \frac{-\emptyset_s + 16\emptyset_b - 30\emptyset_{\text{P}} + 16\emptyset_a - \emptyset_n}{12(\Delta\eta)^2\big|_{\Delta\eta=1/2}} \tag{2.25.4}$$

Then, the discrete form of the model equation, e.g. $\nabla^2\emptyset = F(x, y)$, in the cut-stencil FD formulation using 4$^{\text{th}}$-order approximation for the derivatives at node P can be written as:

$$\frac{1}{(x'_{\text{P}})^2}\left[\frac{-\emptyset_w + 16\emptyset_l - 30\emptyset_{\text{P}} + 16\emptyset_r - \emptyset_e}{3}\right] - \frac{x''_{\text{P}}}{(x'_{\text{P}})^3}\left[\frac{\emptyset_w - 8\emptyset_l + 8\emptyset_r - \emptyset_e}{6}\right]$$
$$+\frac{1}{(y'_{\text{P}})^2}\left[\frac{-\emptyset_s + 16\emptyset_b - 30\emptyset_{\text{P}} + 16\emptyset_a - \emptyset_n}{3}\right] - \frac{y''_{\text{P}}}{(y'_{\text{P}})^3}\left[\frac{\emptyset_s - 8\emptyset_b + 8\emptyset_a - \emptyset_n}{6}\right] = f_{\text{P}} \tag{2.26}$$

Equation (2.26) can be cast in the standard form:

$$a_{\text{p}}\phi_{\text{p}} + a_w\phi_w + a_e\phi_e + a_s\phi_s + a_n\phi_n + a_l\phi_l + a_r\phi_r + a_a\phi_a + a_b\phi_b = f_{\text{P}} \tag{2.27}$$

where the coefficients are given by:

$$a_{\text{p}} = -\frac{10}{(x'_{\text{P}})^2} - \frac{10}{(y'_{\text{P}})^2} \tag{2.28.1}$$

$$a_w = -\frac{1}{3(x'_{\text{P}})^2} - \frac{x''_{\text{P}}}{6(x'_{\text{P}})^3} \tag{2.28.2}$$

$$a_e = -\frac{1}{3(x'_{\text{P}})^2} + \frac{x''_{\text{P}}}{6(x'_{\text{P}})^3} \tag{2.28.3}$$

$$a_s = -\frac{1}{3(y'_{\text{P}})^2} - \frac{y''_{\text{P}}}{6(y'_{\text{P}})^3} \tag{2.28.4}$$

$$a_n = -\frac{1}{3(y'_{\text{P}})^2} + \frac{y''_{\text{P}}}{6(y'_{\text{P}})^3} \tag{2.28.5}$$

$$a_l = \frac{16}{3(x'_{\text{P}})^2} + \frac{4x''_{\text{P}}}{3(x'_{\text{P}})^3} \tag{2.28.6}$$

$$a_r = \frac{16}{3(x'_{\text{P}})^2} - \frac{4x''_{\text{P}}}{3(x'_{\text{P}})^3} \tag{2.28.7}$$

$$a_b = \frac{16}{3(y'_{\text{P}})^2} + \frac{4y''_{\text{P}}}{3(y'_{\text{P}})^3} \tag{2.28.8}$$

$$a_a = \frac{16}{3(y'_{\text{P}})^2} - \frac{4y''_{\text{P}}}{3(y'_{\text{P}})^3} \tag{2.28.9}$$

It is beneficial to emphasize that the 5+4-point stencil scheme uses the same 5-point stencil as the original stencil of the cut-stencil FDM which was used to evaluate the PDEs with 2$^{\text{nd}}$-order accuracy. Thus, the 5+4-point stencil can be applied to achieve higher-order accuracy at all nodes in the mesh without requiring special formulas for stencils that are adjacent to boundaries.

2.6.1.1 Evaluation of Metrics at Auxiliary Nodes of 5+4-point Stencil Formulation

Metrics used in the FD solutions at the four auxiliary nodes on a computational stencil can be written in terms of coordinates of the 5+4-point stencil similar to the metrics of the 5-point stencil scheme as presented in equations (2.6). Figure 2.20 shows a 5+4-point stencil containing four

stencils at the auxiliary nodes. The dash lines in Figure 2.20 show the horizontal or vertical arms of the stencils at the auxiliary nodes, while the solid lines are the arms of the original 5-point stencil.
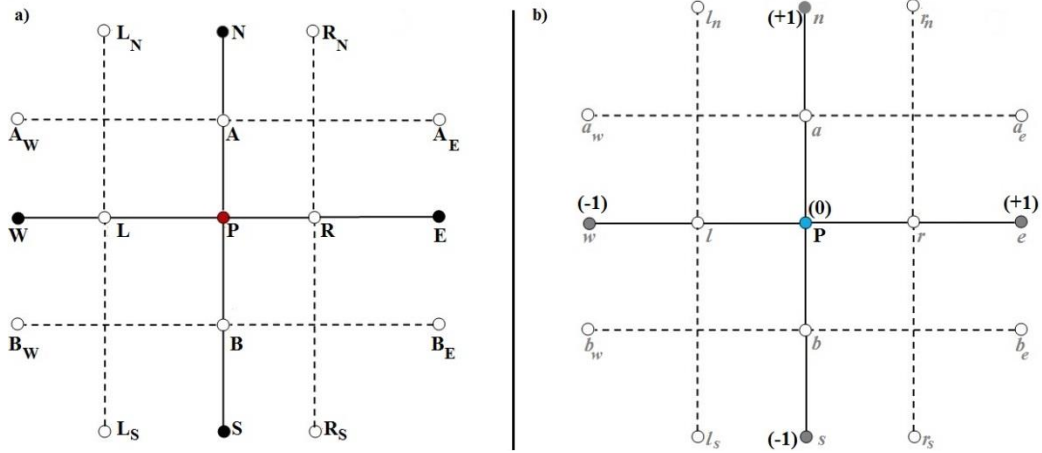
Figure 2.20: 5+4-point main stencil along with four 5-point stencils at the auxiliary nodes, a) physical illustration, b) computational illustration

At first, consider the stencil centred at the auxiliary node L with endpoints at W, L_S, P and L_N. This stencil is mapped to a 5-point computational stencil with all arms of length one using the quadratic transformation functions $x(\xi)$ and $y(\eta)$ defined in equation (2.4). The schematic of this mapping is shown in Figure 2.21.
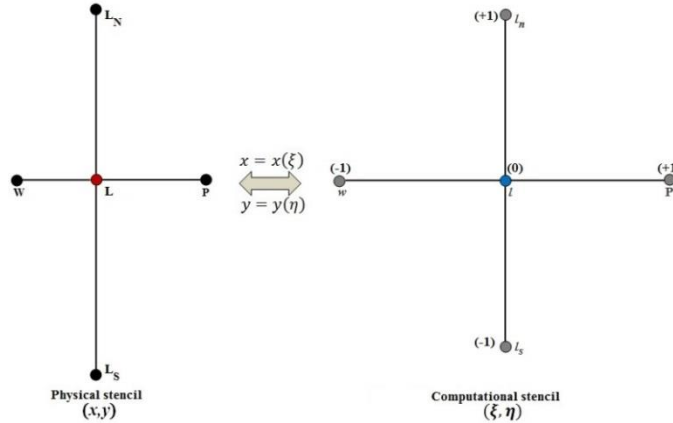
Figure 2.21: Mapping from 5-point physical stencil located at auxiliary node L to a uniform 5-point computational stencil centred at auxiliary node l

The coefficients of the quadratic transformation functions $x(\xi)$ and $y(\eta)$ that map the physical stencil to the uniform computational stencil are found in terms of the coordinates of nodes W, L, P, L_N and L_S, as explained in previous sections. The metrics at auxiliary node L are given by:

$$x_L' = \frac{1}{2}(x_P - x_W) \tag{2.29.1}$$

$$x_L'' = x_W - 2x_L + x_P \tag{2.29.2}$$

$$y_L' = \frac{1}{2}\left(y_{L_N} - y_{L_S}\right) \tag{2.29.3}$$

$$y_L'' = y_{L_S} - 2y_L + y_{L_N} \tag{2.29.4}$$

where expressions for x_L, y_L, etc., are given in Table 2.2 in terms of the endpoints of the original 5-point stencil. Similarly, from the schematic of the 5-point physical stencil centred at the auxiliary node B and the corresponding uniform computational stencil depicted in Figure 2.22, the metrics at B are given by:
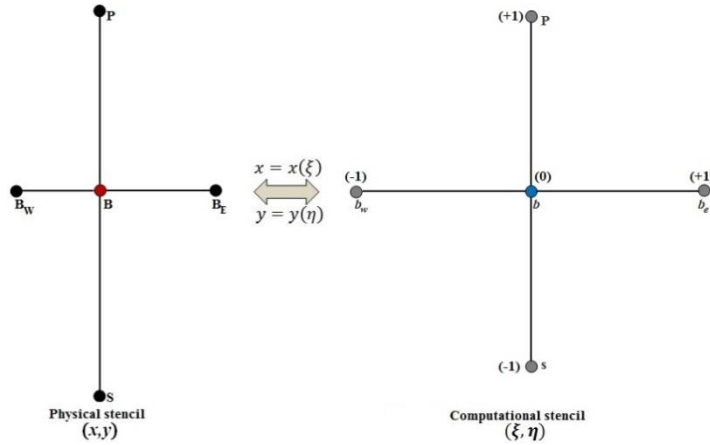
Figure 2.22: Mapping from 5-point physical stencil located at auxiliary node B to a uniform 5-point computational stencil centred at auxiliary node b

$$x_B' = \frac{1}{2}\left(x_{B_E} - x_{B_W}\right) \tag{2.30.1}$$

$$x_B'' = x_{B_W} - 2x_B + x_{B_E} \tag{2.30.2}$$

$$y_B' = \frac{1}{2}\left(y_P - y_S\right) \tag{2.30.3}$$

$$y_B'' = y_S - 2y_B + y_P \tag{2.30.4}$$

Noting that $y_L = y_R = y_P$ and $x_B = x_A = x_P$, the expressions used to calculate the metrics at the four auxiliary nodes have been summarized in Table 2.3.

Node	x'	x''	y'	y''
L	$\frac{1}{2}(x_P - x_W)$	$x_W - 2x_L + x_P$	y_P'	y_P''
R	$\frac{1}{2}(x_E - x_P)$	$x_P - 2x_R + x_E$	y_P'	y_P''
B	x_P'	x_P''	$\frac{1}{2}(y_P - y_S)$	$y_S - 2y_B + y_P$
A	x_P'	x_P''	$\frac{1}{2}(y_N - y_P)$	$y_P - 2y_A + y_N$

Table 2.3: Metrics at four auxiliary nodes in 5+4-point stencil formulation

2.6.1.2 Evaluation of the Governing Function at Auxiliary Nodes in the 5+4-point Stencil Formulation

As written in equations (2.27), to find the solution at an internal node P, the values of the function $\emptyset$ at the four auxiliary nodes are required. The values of the function $\emptyset$ at these auxiliary nodes are expressed by 2nd-order accurate approximations. Referring to Figure 2.20 reveals that the conditions to write the 2nd-order accurate approximation for the first and second derivatives at the auxiliary nodes l, r, a and b are available. To simplify the discussion, consider the model Poisson equation $\nabla^2\emptyset = F(x, y)$. Then, for example, using 3-point central differencing, the discrete form of the model equation in the cut-stencil FD formulation at auxiliary node L is:

$$\frac{1}{(x'_L)^2}[\phi_w - 2\phi_l + \phi_P] - \frac{x''_L}{2(x'_L)^3}[\phi_P - \phi_w]$$
$$+ \frac{1}{(y'_L)^2}[\phi_{l_s} - 2\phi_l + \phi_{l_n}] - \frac{y''_L}{2(y'_L)^3}[\phi_{l_n} - \phi_{l_s}] = f_l \tag{2.31}$$

Rewriting equation (2.31) and collecting the same terms yields the explicit form of equation (2.31) for $\emptyset_l$:

$$\left(\frac{-2}{(x'_L)^2} + \frac{-2}{(y'_L)^2}\right)\emptyset_l$$
$$= f_l - \left(\frac{1}{(x'_L)^2} + \frac{x''_L}{2(x'_L)^3}\right)\emptyset_w - \left(\frac{1}{(x'_L)^2} - \frac{x''_L}{2(x'_L)^3}\right)\emptyset_P \tag{2.32.1}$$
$$- \left(\frac{1}{(y'_L)^2} + \frac{y''_L}{2(y'_L)^3}\right)\emptyset_{l_s} - \left(\frac{1}{(y'_L)^2} - \frac{y''_L}{2(y'_L)^3}\right)\emptyset_{l_n}$$

It is worth mentioning that the nodes l_s and l_n are the images of the L nodes on the physical stencils centred at nodes S and N, respectively. This connectivity between nodes in the cut-stencil FD formulation and the corresponding solver codes was previously explained and depicted in Figure 2.7 for the 5-point stencil formulation. The values of function $\emptyset$ at the auxiliary nodes are updated at each iteration when the standard iterative procedure sweeps through all nodes in the mesh. The explicit expressions for the value of $\emptyset$ at the other auxiliary nodes, similar to equation (2.32.1) for $\emptyset_l$, can be written as:

$$\left(\frac{-2}{(x'_R)^2} + \frac{-2}{(y'_R)^2}\right)\emptyset_r = f_r - \left(\frac{1}{(x'_R)^2} + \frac{x''_R}{2(x'_R)^3}\right)\emptyset_P - \left(\frac{1}{(x'_R)^2} - \frac{x''_R}{2(x'_R)^3}\right)\emptyset_e -$$
$$\left(\frac{1}{(y'_R)^2} + \frac{y''_R}{2(y'_R)^3}\right)\emptyset_{r_s} - \left(\frac{1}{(y'_R)^2} - \frac{y''_R}{2(y'_R)^3}\right)\emptyset_{r_n} \tag{2.32.2}$$

$$\left(\frac{-2}{(x'_B)^2} + \frac{-2}{(y'_B)^2}\right)\emptyset_b = f_b - \left(\frac{1}{(x'_B)^2} + \frac{x''_B}{2(x'_B)^3}\right)\emptyset_{bw} - \left(\frac{1}{(x'_B)^2} - \frac{x''_B}{2(x'_B)^3}\right)\emptyset_{be} -$$
$$\left(\frac{1}{(y'_B)^2} + \frac{y''_B}{2(y'_B)^3}\right)\emptyset_s - \left(\frac{1}{(y'_B)^2} - \frac{y''_B}{2(y'_B)^3}\right)\emptyset_P \tag{2.32.3}$$

$$\left(\frac{-2}{(x'_A)^2} + \frac{-2}{(y'_A)^2}\right)\emptyset_a = f_a - \left(\frac{1}{(x'_A)^2} + \frac{x''_A}{2(x'_A)^3}\right)\emptyset_{aw} - \left(\frac{1}{(x'_A)^2} - \frac{x''_A}{2(x'_A)^3}\right)\emptyset_{ae} -$$
$$\left(\frac{1}{(y'_A)^2} + \frac{y''_A}{2(y'_A)^3}\right)\emptyset_P - \left(\frac{1}{(y'_A)^2} - \frac{y''_A}{2(y'_A)^3}\right)\emptyset_n \tag{2.32.4}$$

The metrics at the auxiliary nodes appearing in equations (2.32) were introduced in Table 2.3. It is important to mention that the 5+4-point stencil formulation and corresponding calculations described above can be applied to any uncut or cut-stencil, as long as the stencil does not intersect with a curved or oblique boundary. Figure 2.23 presents two samples of cut-stencils for which the 5+4-point stencil formulation must be modified to be applicable. These stencils are characterized by an oblique straight or curved boundary line passing from one node of the stencil.
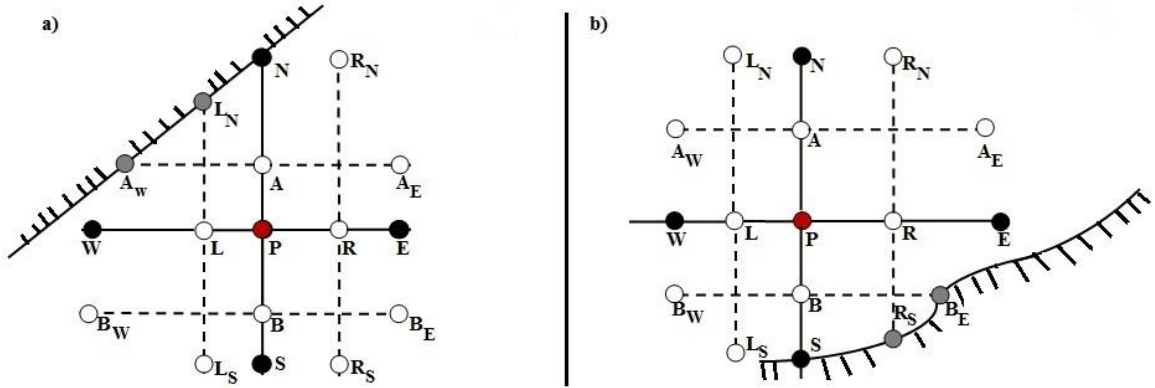
Figure 2.23: Cut-stencils not directly applicable to the 5+4-point cut-stencil formulation, a) intersection with straight oblique boundary line, b) intersection with curved boundary line

As Figure 2.23(a) shows, the stencil at the internal node P is cut by a straight oblique boundary line at node N. In this event the y-coordinate of the node L_N and node N are not the same so y'_L, which is normally calculated as $\frac{1}{2}(y_{L_N} - y_{L_S})$, is not equal to y'_P. This issue also occurs for the x-coordinate of A_w, which does not have the same value as the x-coordinate of node W, meaning that x'_A and x'_P are not equal to each other. Figure 2.23(b) looks at another sample of a stencil for internal node P, cut by a curved boundary at node S. The y-coordinate of R_S and S are different and consequently y'_R and y'_P are different. In the same way, x'_B and x'_P are not equal due to different values for the x-coordinates of nodes B_E and E.

The 5+4-point higher-order cut-stencil formulation has been implemented to analyse and demonstrate the potential of the cut-stencil FDM to generate more accurate solutions to PDEs compared to the 5-point 2nd-order scheme with the same mesh size. The results of applying both the 5+4-point and 5-point cut-stencil schemes to "manufactured" problems are compared and the real order of this method is discussed in Chapter 3.

2.6.2 Higher-Order (HO) Padé-Hermitian Compact Cut-Stencil FD Formulation

The compact FD formulation, as mentioned earlier, has been considered extensively in numerical studies for the solution of PDEs as well as in real physical problems [64, 66-72].

As a general definition, it can be said that the classical Padé-Hermitian compact finite difference technique treats the governing function and its derivatives as unknowns and a linear combination of the function values and the derivatives of the function, typically first and second derivatives, are used to obtain a higher-order solution of the PDE [66, 72-74].

The compact Padé-Hermitian finite difference technique has been used in this research to develop a higher-order formulation of the cut-stencil FD method. The localized treatment of the physical stencil provides a simple framework for development of higher-order schemes. Furthermore, it

supports the possibility of programming the higher-order formulation in highly complex domains with any type of boundary conditions. The 4th-order compact Padé-Hermitian finite differencing approximations have been used to construct the combination of higher-order compact (HOC) scheme and the cut-stencil FDM in this study. To achieve this purpose, the discussion continues with the general description and formulation of the HOC scheme using Padé-Hermitian finite differencing approximations in TFD notation.

2.6.2.1 Approximation of First Derivatives in Compact Padé-Hermitian Finite Differencing

To initially simplify the concept, consider a one-dimensional uniform mesh with spacing Δx and let $\emptyset$ be a function of independent variable x. A family of approximations of the first derivative of $\emptyset$ at node x_i is given by the expression:

$$a_9\emptyset_{i-2}'+a_7\emptyset_{i-2} + a_5\emptyset_{i-1}'+a_3\emptyset_{i-1}+\emptyset_i'+a_1\emptyset_i+a_2\emptyset_{i+1} + a_4\emptyset_{i+1}'+a_6\emptyset_{i+2} + a_8\emptyset_{i+2}' = O(\Delta x^k) \qquad (2.33)$$

Taking different values for the coefficients a_i in equation (2.33) yields different orders of accuracy for approximation of $\emptyset_i'$ [75]. The essence of HO compact formulations is to use the narrowest possible stencil in approximation of the derivatives. Furthermore, in HO formulation of the cut-stencil FDM, to avoid any special formulas or stencils for internal nodes in the neighborhood of a boundary, all the approximation expressions in this research are written with at most one node in each direction adjacent to node i in TFDM (or node P in the cut-stencil FD method). Thus, the coefficients a_6, a_7, a_8 and a_9 are chosen as zero in equation (2.33), and the first derivative is approximated by an expression of the form:

$$a_5\emptyset_{i-1}'+ a_3\emptyset_{i-1} + \emptyset_i'+ a_1\emptyset_i + a_2\emptyset_{i+1} + a_4\emptyset_{i+1}' = O(\Delta x^k) \qquad (2.34.1)$$

The parameter k in equation (2.34.1) is introduced to identify the order of accuracy for the approximation of $\emptyset_i'$. The coefficients a_j (j = 1,2,3,4,5) and k are calculated by expanding each term in (2.34.1) in Taylor's series about x_i. Table 2.4 is a convenient way to organize the terms in the Taylor's series expansion which is used to find the coefficients and order of accuracy for equation (2.34.1).

	$\emptyset_i$	$\emptyset_i'$	$\emptyset_i''$	$\emptyset_i'''$	$\emptyset_i^{(4)}$	$\emptyset_i^{(5)}$
$\emptyset_i'$	0	1	0	0	0	0
$a_1\emptyset_i$	a_1	0	0	0	0	0
$a_2\emptyset_{i+1}$	a_2	$a_2(\Delta x)$	$a_2(\Delta x)^2/2!$	$a_2(\Delta x)^3/3!$	$a_2(\Delta x)^4/4!$	$a_2(\Delta x)^5/5!$
$a_3\emptyset_{i-1}$	a_3	$a_3(-\Delta x)$	$a_3(-\Delta x)^2/2!$	$a_3(-\Delta x)^3/3!$	$a_3(-\Delta x)^4/4!$	$a_3(-\Delta x)^5/5!$
$a_4\emptyset_{i+1}'$	0	a_4	$a_4(\Delta x)$	$a_4(\Delta x)^2/2!$	$a_4(\Delta x)^3/3!$	$a_4(\Delta x)^4/4!$
$a_5\emptyset_{i-1}'$	0	a_5	$a_5(-\Delta x)$	$a_5(-\Delta x)^2/2!$	$a_5(-\Delta x)^3/3!$	$a_5(-\Delta x)^4/4!$
$\sum$	0	0	0	0	0	$O(\Delta x^k)$

Table 2.4: Taylor's series expansion used to derive the first derivative approximation in HOC finite difference method

The five coefficients a_j are calculated from the system of five linear equations formed by summing the 2nd to 6th columns of Table 2.4 to zero, giving the values:

$$a_5 = 1/4, \quad a_3 = 3/4(\Delta x), \quad a_1 = 0, \quad a_2 = -3/4(\Delta x), \quad a_4 = 1/4 \qquad (2.34.2)$$

Substituting the coefficients from equation (2.34.2) in the last column of Table 2.4 reveals that k = 4 which means that the approximation proposed in equation (2.34.1) has 4th-order accuracy. The last column of Table 2.4 also provides the expression for the local truncation error (LTE) for this difference approximation, which will be discussed in more details in the section on LTE in Chapter 3. Using the coefficients listed in (2.34.2), the explicit expression for the 4th-order accurate approximation for $\emptyset_i'$, known as the standard central 4th-order Padé approximation and widely used in numerical studies and various applications, e.g. [64, 66, 74, 76], is:

$$\emptyset_i' = \frac{3(\emptyset_{i+1} - \emptyset_{i-1})}{4(\Delta x)} - \frac{\emptyset_{i+1}' + \emptyset_{i-1}'}{4} + O(\Delta x^4) \tag{2.35}$$

2.6.2.2 Approximation of Second Derivatives in Compact Padé-Hermitian Finite Differencing

The same procedure as above can be used to derive a higher-order approximation for the second derivative of $\emptyset$ at node i. In this case, $\emptyset_i''$ is written as a linear combination of $\emptyset$ and $\emptyset''$ at the nodes i-1, i and i+1, i.e.,

$$b_5\emptyset_{i-1}'' + b_3\emptyset_{i-1} + \emptyset_i'' + b_1\emptyset_i + b_2\emptyset_{i+1} + b_4\emptyset_{i+1}'' = O(\Delta x^k) \tag{2.36.1}$$

The coefficients in equation (2.36.1) are calculated from a system of five linear equations which are constructed by summing the 2nd to 6th columns of Table 2.5 to zero. The LTE is determined by replacing the value of coefficients b_i in the terms of the last column of Table 2.5.

	$\emptyset_i$	$\emptyset_i'$	$\emptyset_i''$	$\emptyset_i'''$	$\emptyset_i^{(4)}$	$\emptyset_i^{(5)}$	$\emptyset_i^{(6)}$
$\emptyset_i''$	0	0	1	0	0	0	0
$b_1\emptyset_i$	b_1	0	0	0	0	0	0
$b_2\emptyset_{i+1}$	b_2	$b_2(\Delta x)$	$b_2(\Delta x)^2/2!$	$b_2(\Delta x)^3/3!$	$b_2(\Delta x)^4/4!$	$b_2(\Delta x)^5/5!$	$b_2(\Delta x)^6/6!$
$b_3\emptyset_{i-1}$	b_3	$b_3(-\Delta x)$	$b_3(-\Delta x)^2/2!$	$b_3(-\Delta x)^3/3!$	$b_3(-\Delta x)^4/4!$	$b_3(-\Delta x)^5/5!$	$b_3(-\Delta x)^6/6!$
$b_4\emptyset_{i+1}''$	0	0	b_4	$b_4(\Delta x)$	$b_4(\Delta x)^2/2!$	$b_4(\Delta x)^3/4!$	$b_4(\Delta x)^4/4!$
$b_5\emptyset_{i-1}''$	0	0	b_5	$b_5(-\Delta x)$	$b_5(-\Delta x)^2/2!$	$b_5(-\Delta x)^3/4!$	$b_5(-\Delta x)^4/4!$
$\sum$	0	0	0	0	0	0	$O(\Delta x^k)$

Table 2.5: Taylor's series expansion used to derive the second derivative approximation in HOC finite difference method

Solving the resulting linear equations yields the coefficients for the 4th-order accurate approximation for $\emptyset_i''$:

$$b_5 = 1/10, \quad b_3 = -6/5(\Delta x)^2, \quad b_1 = 12/5(\Delta x)^2, \quad b_2 = -6/5(\Delta x)^2, \quad b_4 = 1/10 \tag{2.36.2}$$

which produces the commonly used explicit form of equation (2.36.1) for the 4th-order accurate approximation of the second derivative [64, 66, 74, 76]:

$$\emptyset_i'' = \frac{6(\emptyset_{i+1} - 2\emptyset_i + \emptyset_{i-1})}{5(\Delta x)^2} - \frac{\emptyset_{i+1}'' + \emptyset_{i-1}''}{10} + O(\Delta x^4) \tag{2.37.1}$$

An alternative 4th-order approximation for $\emptyset_i''$ can be formulated by expressing $\emptyset_i''$ as a linear combination of $\emptyset$ and $\emptyset'$ at the nodes i-1, i and i+1. Proceeding as above gives the 4th-order approximation:

$$\emptyset_i'' = \frac{2(\emptyset_{i+1} - 2\emptyset_i + \emptyset_{i-1})}{(\Delta x)^2} + \frac{\emptyset_{i-1}' - \emptyset_{i+1}'}{2(\Delta x)} + O(\Delta x^4) \qquad (2.37.2)$$

The higher-order Cartesian cut-stencil finite difference formulation based on approximating $\emptyset_i''$ using (2.37.1) will be referred to as HO-FDM1 in subsequent sections, and that based on (2.37.2) will be denoted by HO-FDM2.

2.6.3 Comparison of the Stencil of Higher-Order Compact (Implicit) and Explicit Finite Difference Methods

To simplify the discussion, HO approximations for first and second derivatives were developed for a 1-D uniform mesh in the previous sections. These 1-D results can be easily extended for a 2-D non-uniform Cartesian mesh and provide a higher (hereon, 4th-order) approximation in both the *x* and *y* directions. The compact finite difference method is also introduced in the literature as an "implicit" scheme due to the use of nodal and derivative values to evaluate the derivatives of the governing function. On the other hand, the normal FD approximation, which uses only nodal function values for evaluation of the derivatives of the function, is called an "explicit" scheme [64]. The compact FD method can provide a more accurate solution compared to the explicit FD scheme with the same size of stencil. Figure 2.24 shows the stencils which are used for 4th-order accurate approximation of the first and second derivatives at node (i,j) in both implicit and explicit FD schemes, in a uniform mesh with spacing Δx and Δy in the *x* and *y* directions, respectively.
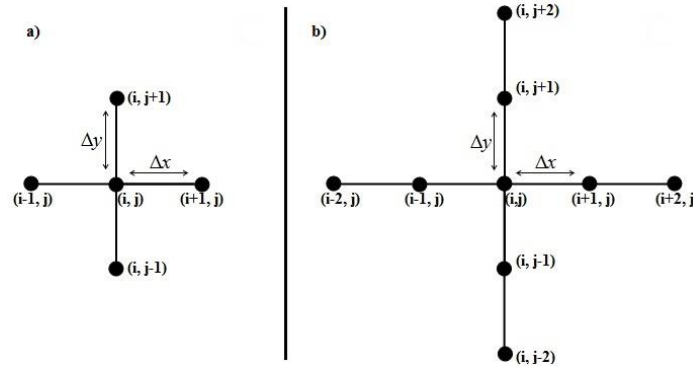
Figure 2.24: Comparison of the stencil for 4th-order accurate approximations, a) compact FD (implicit) scheme, b) explicit FD scheme

It can be seen from Figure 2.24 that the stencil for a 4th-order accurate approximation using the explicit FD scheme is twice as wide as the stencil used for the 4th-order accurate approximation in the compact FD scheme. The 5-point stencil, as indicated in Figure 2.24(a), also represents the 5-point stencil of the Cartesian cut-stencil FDM. Thus, higher-order approximations for the first and second derivatives for 2-D Cartesian cut-stencils can be achieved using the 5-point stencil.

2.6.4 Higher-Order Cut-Stencil Finite Difference Method (HO Cut-Stencil FDM) for Convection-Diffusion Equation

The simple but efficient localized treatment of a physical stencil in the Cartesian cut-stencil FDM provides the capability to combine this FD scheme with HOC FD schemes. The 4th-order Padé-Hermitian approximations for first and second derivatives, as addressed in equations (2.35, 2.37.1 or 2.37.2), are used to write globally 4th-order expressions for the derivatives in the model equations in the cut-stencil FDM formulations.

Two different 4th-order approximations for second derivatives were proposed in equations (2.37.1) and (2.37.2), and the off-centre derivatives in each of these two expressions are different. So, the higher-order cut-stencil finite difference method 1 (HO cut-stencil FDM1) and the higher-order cut-stencil finite difference method 2 (HO cut-stencil FDM2) are developed based on equations (2.37.1) and (2.37.2), respectively.

For convenience, the mapped form of the 2-D steady convection-diffusion equation (2.7) is rewritten below as equation (2.38).

$$ v\left[\frac{1}{(x')^2}\frac{\partial^2\emptyset}{\partial\xi^2} - \frac{x''}{(x')^3}\frac{\partial\emptyset}{\partial\xi} + \frac{1}{(y')^2}\frac{\partial^2\emptyset}{\partial\eta^2} - \frac{y''}{(y')^3}\frac{\partial\emptyset}{\partial\eta}\right] + \frac{P}{x'}\frac{\partial\emptyset}{\partial\xi} + \frac{Q}{y'}\frac{\partial\emptyset}{\partial\eta} = s(\xi,\eta) \tag{2.38} $$

As seen in (2.38), the diffusive part of the convection-diffusion equation contains first and second derivatives, while the convective part involves only first derivatives. Since the diffusive derivatives are always approximated by central differences, equations (2.35) and either (2.37.1) or (2.37.2) can be applied to achieve 4th-order accuracy. There is more flexibility in the choice of scheme used for the convective terms in (2.38). Besides the central scheme (2.35), an upwinding scheme is often used to correctly capture the physics, especially in convection-dominated flows, as well as stabilize the numerical solution. Thus, different schemes for upwind differencing of convection terms have been proposed and discussed in numerical studies of this model equation [17, 77-82].

Following the same procedure used to derive the compact Padé-Hermitian approximations (2.35), (2.37.1) and (2.37.2), higher-order upwind formulas can be obtained for the first-order convective derivatives. For example, 2nd-order accurate backward and forward approximations for the first derivative are respectively given by,

$$ \emptyset'_i = \frac{2(\emptyset_i - \emptyset_{i-1})}{(\Delta x)} - \emptyset'_{i-1} + O(\Delta x^2) \tag{2.39.1} $$

and

$$ \emptyset'_i = \frac{2(\emptyset_{i+1} - \emptyset_i)}{(\Delta x)} - \emptyset'_{i+1} + O(\Delta x^2) \tag{2.39.2} $$

It is worth noting that the higher-order approximations (2.35), (2.37.1), (2.37.2), (2.39.1) and (2.39.2) are symbolically written for the variable x, but they can be similarly written for any arbitrary variable, e.g. ξ or η. A summary of the higher-order discretizations of the transformed convection-diffusion equation used in this thesis, taking into account the compact central and upwind schemes above, is represented by the following:

$$v\left[\underbrace{\frac{1}{(x')^2}\frac{\partial^2 \emptyset}{\partial \xi^2}}_{\substack{\text{approximate} \\ \text{by eq. (2.37.1)} \\ \text{or (2.37.2)}}} - \underbrace{\frac{x''}{(x')^3}\frac{\partial \emptyset}{\partial \xi}}_{\substack{\text{approximate} \\ \text{by eq. (2.35)}}} + \underbrace{\frac{1}{(y')^2}\frac{\partial^2 \emptyset}{\partial \eta^2}}_{\substack{\text{approximate} \\ \text{by eq. (2.37.1)} \\ \text{or (2.37.2)}}} - \underbrace{\frac{y''}{(y')^3}\frac{\partial \emptyset}{\partial \eta}}_{\substack{\text{approximate} \\ \text{by eq. (2.35)}}}\right]$$

$$+ \quad P\underbrace{\frac{1}{x'}\frac{\partial \emptyset}{\partial \xi}}_{\substack{\text{approximate} \\ \text{by eq. (2.35) } or \\ \text{(2.39.1) } or \text{ (2.39.2)}}} + \quad Q\underbrace{\frac{1}{y'}\frac{\partial \emptyset}{\partial \eta}}_{\substack{\text{approximate} \\ \text{by eq. (2.35) } or \\ \text{(2.39.1) } or \text{ (2.39.2)}}} \quad = s(\xi,\eta) \tag{2.40}$$

HO-FDM1 utilizes equations (2.37.1) to discretize the second-order derivatives in the diffusion terms of equation (2.40). When central differencing (2.35) is implemented for the convective derivatives, the scheme is fully 4th-order accurate and the resulting finite difference equation is:

$$\begin{aligned}
&\frac{v}{(x'_P)^2}\left[\frac{6\phi_w - 12\phi_P + 6\phi_e}{5} - \frac{1}{10}\left(\frac{\partial^2 \emptyset}{\partial \xi^2}\Big|_w + \frac{\partial^2 \emptyset}{\partial \xi^2}\Big|_e\right)\right] \\
&- \frac{vx''_P}{(x'_P)^3}\left[\frac{3\phi_e - 3\phi_w}{4} - \frac{1}{4}\left(\frac{\partial \emptyset}{\partial \xi}\Big|_w + \frac{\partial \emptyset}{\partial \xi}\Big|_e\right)\right] \\
&+ \frac{v}{(y'_P)^2}\left[\frac{6\phi_s - 12\phi_P + 6\phi_n}{5} - \frac{1}{10}\left(\frac{\partial^2 \emptyset}{\partial \eta^2}\Big|_s + \frac{\partial^2 \emptyset}{\partial \eta^2}\Big|_n\right)\right] \\
&- \frac{vy''_P}{(y'_P)^3}\left[\frac{3\phi_n - 3\phi_s}{4} - \frac{1}{4}\left(\frac{\partial \emptyset}{\partial \eta}\Big|_s + \frac{\partial \emptyset}{\partial \eta}\Big|_n\right)\right] \\
&+ P\frac{1}{x'_P}\left[\frac{3\phi_e - 3\phi_w}{4} - \frac{1}{4}\left(\frac{\partial \emptyset}{\partial \xi}\Big|_w + \frac{\partial \emptyset}{\partial \xi}\Big|_e\right)\right] \\
&+ Q\frac{1}{y'_P}\left[\frac{3\phi_n - 3\phi_s}{4} - \frac{1}{4}\left(\frac{\partial \emptyset}{\partial \eta}\Big|_s + \frac{\partial \emptyset}{\partial \eta}\Big|_n\right)\right] = s_P
\end{aligned} \tag{2.41}$$

In this case, the coefficients and right hand side in the standard equation (2.9) become:

$$a_p = -\frac{12v}{5}\left(\frac{1}{(x'_P)^2} + \frac{1}{(y'_P)^2}\right) \tag{2.42.1}$$

$$a_w = \frac{6v}{5(x'_P)^2} + \frac{3vx''_P}{4(x'_P)^3} - \frac{3P}{4x'_P} \tag{2.42.2}$$

$$a_e = \frac{6v}{5(x'_P)^2} - \frac{3vx''_P}{4(x'_P)^3} + \frac{3P}{4x'_P} \tag{2.42.3}$$

$$a_s = \frac{6v}{5(y'_P)^2} + \frac{3vy''_P}{4(y'_P)^3} - \frac{3Q}{4y'_P} \tag{2.42.4}$$

$$a_n = \frac{6v}{5(y'_P)^2} - \frac{3vy''_P}{4(y'_P)^3} + \frac{3Q}{4y'_P} \tag{2.42.5}$$

$$\text{RHS} = s_P - \left[-\frac{\nu}{10(x_P')^2}\left(\frac{\partial^2 \emptyset}{\partial \xi^2}\Big|_w + \frac{\partial^2 \emptyset}{\partial \xi^2}\Big|_e\right) + \frac{\nu x_P''}{4(x_P')^3}\left(\frac{\partial \emptyset}{\partial \xi}\Big|_w + \frac{\partial \emptyset}{\partial \xi}\Big|_e\right)\right.$$

$$\left. -\frac{\nu}{10(y_P')^2}\left(\frac{\partial^2 \emptyset}{\partial \eta^2}\Big|_s + \frac{\partial^2 \emptyset}{\partial \eta^2}\Big|_n\right) + \frac{\nu y_P''}{4(y_P')^3}\left(\frac{\partial \emptyset}{\partial \eta}\Big|_s + \frac{\partial \emptyset}{\partial \eta}\Big|_n\right)\right. \tag{2.42.6}$$

$$\left. -\frac{P}{4x_P'}\left(\frac{\partial \emptyset}{\partial \xi}\Big|_w + \frac{\partial \emptyset}{\partial \xi}\Big|_e\right) - \frac{Q}{4y_P'}\left(\frac{\partial^2 \emptyset}{\partial \eta^2}\Big|_s + \frac{\partial^2 \emptyset}{\partial \eta^2}\Big|_n\right)\right]$$

Similarly, for HO-FDM2, if backward differencing (equation (2.39.1)) is used for the convective terms in (2.40), the finite difference form of the convection-diffusion equation (2.38) is:

$$\frac{\nu}{(x_P')^2}\left[(2\phi_w - 4\phi_P + 2\phi_e) + \frac{1}{2}\left(\frac{\partial \emptyset}{\partial \xi}\Big|_w - \frac{\partial \emptyset}{\partial \xi}\Big|_e\right)\right]$$

$$-\frac{\nu x_P''}{(x_P')^3}\left[\frac{3\phi_e - 3\phi_w}{4} - \frac{1}{4}\left(\frac{\partial \emptyset}{\partial \xi}\Big|_w + \frac{\partial \emptyset}{\partial \xi}\Big|_e\right)\right]$$

$$+\frac{\nu}{(y_P')^2}\left[(2\phi_s - 4\phi_P + 2\phi_n) + \frac{1}{2}\left(\frac{\partial \emptyset}{\partial \eta}\Big|_s - \frac{\partial \emptyset}{\partial \eta}\Big|_n\right)\right] \tag{2.43}$$

$$-\frac{\nu y_P''}{(y_P')^3}\left[\frac{3\phi_n - 3\phi_s}{4} - \frac{1}{4}\left(\frac{\partial \emptyset}{\partial \eta}\Big|_s + \frac{\partial \emptyset}{\partial \eta}\Big|_n\right)\right]$$

$$+P\frac{1}{x_P'}\left[2\phi_P - 2\phi_w - \frac{\partial \emptyset}{\partial \xi}\Big|_w\right] + Q\frac{1}{y_P'}\left[2\phi_P - 2\phi_s - \frac{\partial \emptyset}{\partial \eta}\Big|_s\right] = s_P$$

and the coefficients and right hand side in the standard equation (2.9) are:

$$a_p = -\left(\frac{4\nu}{(x_P')^2} + \frac{4\nu}{(y_P')^2}\right) + 2\left(\frac{P}{x_P'} + \frac{Q}{y_P'}\right) \tag{2.44.1}$$

$$a_w = \frac{2\nu}{(x_P')^2} + \frac{3\nu x_P''}{4(x_P')^3} - \frac{2P}{x_P'} \tag{2.44.2}$$

$$a_e = \frac{2\nu}{(x_P')^2} - \frac{3\nu x_P''}{4(x_P')^3} \tag{2.44.3}$$

$$a_s = \frac{2\nu}{(y_P')^2} + \frac{3\nu y_P''}{4(y_P')^3} - \frac{2Q}{y_P'} \tag{2.44.4}$$

$$a_n = \frac{2\nu}{(y_P')^2} - \frac{3\nu y_P''}{4(y_P')^3} \tag{2.44.5}$$

$$\text{RHS} = s_P - \left[\frac{\nu}{2(x_P')^2}\left(\frac{\partial \emptyset}{\partial \xi}\Big|_w - \frac{\partial \emptyset}{\partial \xi}\Big|_e\right) + \frac{\nu x_P''}{4(x_P')^3}\left(\frac{\partial \emptyset}{\partial \xi}\Big|_w + \frac{\partial \emptyset}{\partial \xi}\Big|_e\right)\right.$$

$$\left. +\frac{\nu}{2(y_P')^2}\left(\frac{\partial \emptyset}{\partial \eta}\Big|_s - \frac{\partial \emptyset}{\partial \eta}\Big|_n\right) + \frac{\nu y_P''}{4(y_P')^3}\left(\frac{\partial \emptyset}{\partial \eta}\Big|_s + \frac{\partial \emptyset}{\partial \eta}\Big|_n\right)\right. \tag{2.44.6}$$

$$\left. -\frac{P}{x_P'}\frac{\partial \emptyset}{\partial \xi}\Big|_w - \frac{Q}{y_P'}\frac{\partial \emptyset}{\partial \eta}\Big|_s\right]$$

All the terms containing the first and second derivatives at nodes w, e, s and n are transferred to the RHS of the equation, as indicated in equations (2.42.6) and (2.44.6), to form a new RHS. The derivatives of $\emptyset$ at nodes w, e, s and n are updated through the standard iteration scheme for each internal node P.

The derivatives of Ø appearing in equations (2.42.6) and (2.44.6), which must be evaluated at the stencil endpoints, are approximated by central or one-sided 2nd-order approximations based on the location of the node P relative to the boundaries of the domain. An example of the central or one-sided 2nd-order approximation of derivatives at the stencil end nodes is discussed here. Figure 2.25 illustrates an arbitrary 5-point computational stencil centred at node P. The west node *w* is an internal node which is also the centre node of its own 5-point stencil. So, in the scenario shown in Figure 2.25, the west node of node *w* is available, and it might be located on a boundary or lie at another internal node. Figure 2.25 shows the situation when the node to the west of the west node *w* lies on the boundary. In fact, the west node of node *w* can also be referred to as the west node of the west node of node P, which is conveniently denoted by *ww*.

5-point stencil
centred at node P
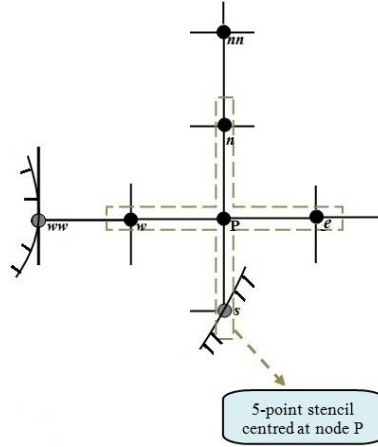
Figure 2.25: Computational stencil for central or one-sided second-order approximations of derivatives at the endpoints of a stencil used in HO-FDM1

For HO-FDM1, the derivatives $\frac{\partial^2 \emptyset}{\partial \xi^2}$ and $\frac{\partial \emptyset}{\partial \xi}$ in (2.42.6) at the endpoint *w* can be approximated with central 2nd-order accuracy, given by,

$$\frac{\partial^2 \emptyset}{\partial \xi^2}\Big|_w = \phi_{ww} - 2\phi_w + \phi_P \tag{2.45.1}$$

$$\frac{\partial \emptyset}{\partial \xi}\Big|_w = \frac{\phi_P - \phi_{ww}}{2} \tag{2.45.2}$$

The south endpoint of the stencil centred in point P shown in Figure 2.25 is located on the boundary. It is assumed that node *nn*, representing the north node of the north node n of node P, is an internal or a boundary node so the value at node *nn* can be used in the calculations. Then, the derivatives $\frac{\partial^2 \emptyset}{\partial \eta^2}$ and $\frac{\partial \emptyset}{\partial \eta}$ at the endpoint *s* can be approximated by one-sided 2nd-order accuracy:

$$\frac{\partial^2 \emptyset}{\partial \eta^2}\Big|_s = 2\phi_s - 5\phi_P + 4\phi_n - \phi_{nn} \tag{2.45.3}$$

$$\frac{\partial \emptyset}{\partial \eta}\Big|_s = \frac{-3\phi_s + 4\phi_P - \phi_n}{2} \tag{2.45.4}$$

In the event that both south and north nodes, or both west and east nodes, are located on the boundary as illustrated for node P in Figure 2.26, the second derivatives at the endpoints in equation (2.42.6) will be approximated by one-sided 1st-order FD expressions.
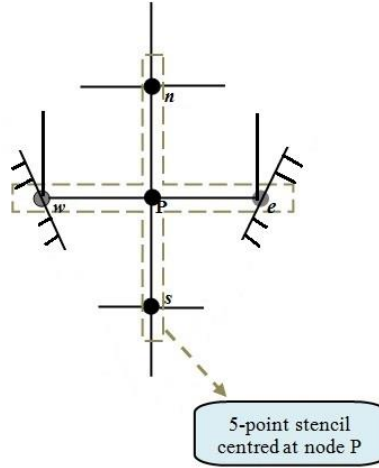
Figure 2.26: Computational stencil for central or one-sided first-order approximations of second derivatives at the endpoints of a stencil used in HO-FDM1

The second derivatives $\frac{\partial^2 \emptyset}{\partial \xi^2}$ at nodes w and e are approximated by the one-sided 1st-order FD expressions given in equations (2.46.1) and (2.46.2), whereas, one-sided 2nd-order accurate approximations can be written for the first derivatives at the same nodes for this condition.

$$\frac{\partial^2 \emptyset}{\partial \xi^2}\Big|_w = \phi_w - 2\phi_P + \phi_e \qquad (2.46.1)$$

$$\frac{\partial^2 \emptyset}{\partial \xi^2}\Big|_e = \phi_w - 2\phi_P + \phi_e \qquad (2.46.2)$$

As mentioned previously, due to the simplicity of the cut-stencil FD formulation, all possible combinations for the location of an internal active node P relative to the boundaries of the domain can be considered and programmed with relative ease. Some of the results, in the form of solutions to "manufactured" problems or real physical problems, e.g. solution to streamfunction-vorticity in lid-driven cavity flow, are presented in the following chapters.

To gain the maximum potential of each grid to find the most accurate solution to the governing PDEs, the first derivatives at endpoints w, e, s and n are approximated by central, one-sided or upwind 4th, 3rd or 2nd-order accurate FD expressions, depending on the locations of the node P.

For HO-FDM2, only the first derivatives at w, e, s and n are needed as seen in equation (2.44.6). Figure 2.27 presents a part of an arbitrary domain and boundary lines which include a 5-point computational stencil, centred at node P, as well as a couple of other nodes, located near to node P, which may be regarded as centre points of other 5-point stencils.
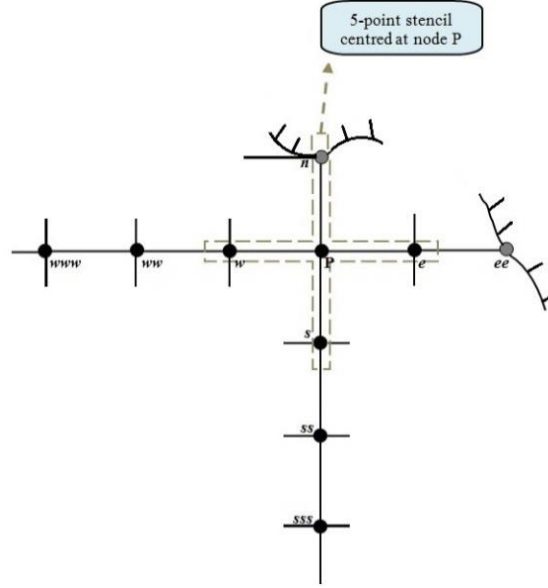
Figure 2.27: Computational stencil for central or upwind 4th-order approximations of first derivatives at the endpoints of a stencil used in HO-FDM2

The location of the node P and its 5-point stencil reveal that central 4th-order accurate approximation (2.24.1) for $\frac{\partial \emptyset}{\partial \xi}$ at endpoint w can be applied, as given by equation (2.47.1). For the 5-point stencil centred at node P shown in Figure 2.27, the values at two nodes on the left side of node w can be used to write the FD expression. In other words, the node www, which is west of west of west of node P, could be an internal node or be located on a boundary.

The derivative $\frac{\partial \emptyset}{\partial \xi}$ at the endpoint e can also be approximated to 4th-order accuracy, given by equation (2.47.2). In this case, the node ee, which can be regarded as the east node of node e from the perspective of the 5-point stencil centred at point e, is located on a boundary of the domain, meaning that only one point at the right side of endpoint e is available.

$$\frac{\partial \emptyset}{\partial \xi}\Big|_w = \frac{\phi_{www} - 8\phi_{ww} + 8\phi_P - \phi_e}{12} \tag{2.47.1}$$

$$\frac{\partial \emptyset}{\partial \xi}\Big|_e = \frac{-\phi_{ww} + 6\phi_w - 18\phi_P + 10\phi_e + 3\phi_{ee}}{12} \tag{2.47.2}$$

The north node of node P, which is indicated by n in Figure 2.27, is located on the boundary and the node sss of node P is taken as an internal or boundary node, so the value of $\emptyset$ at node sss can be used to construct an appropriate FD expression. Therefore, $\frac{\partial \emptyset}{\partial \eta}$ can be approximated to 4th-order accuracy at the north node of node P (node n), based on the location of node P and its corresponding 5-point stencil. Access of the value at node sss also provides the condition needed to write a central 4th-order accurate approximation for $\frac{\partial \emptyset}{\partial \eta}$ at node s. These respective approximations are:

$$\frac{\partial \emptyset}{\partial \eta}\Big|_n = \frac{3\phi_{sss} - 16\phi_{ss} + 36\phi_s - 48\phi_P + 25\phi_n}{12} \tag{2.48.1}$$

$$\frac{\partial \emptyset}{\partial \eta}\Big|_s = \frac{\phi_{sss} - 8\phi_{ss} + 8\phi_P - \phi_n}{12} \tag{2.48.2}$$

Figure 2.28 illustrates an example of a 5-point computational stencil centered at node P for which the location of node P relative to the boundaries provides the conditions for a 3rd-order accurate approximation for some of the derivatives at endpoints appearing in equations (2.42.6) and (2.44.6).
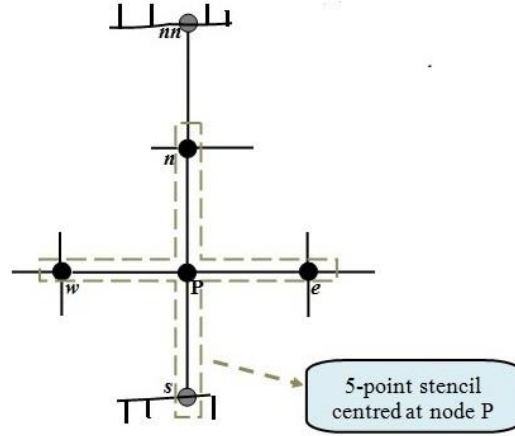
Figure 2.28: Computational stencil for 3rd-order approximations of first derivatives at the endpoints of a stencil used in HO-FDM2

For the 5-point stencil centred at node P shown in Figure 2.28, the south node *s* is located on the boundary, so a one-sided FD expression is applied to approximate $\frac{\partial \emptyset}{\partial \eta}$ at node *s*. Furthermore, the north node of the north node of P (i.e., *nn*) is also a boundary node, which imposes the condition for writing a one-sided FD approximation of $\frac{\partial \emptyset}{\partial \eta}$ at node *s* up to the node *nn*. Using the values of $\emptyset$ at nodes *s*, P, *n* and *nn* to approximate the first derivative at endpoint *s* leads to a 3rd-order accurate FD expression, as written in equation (2.49.1).

The north node of node P (*n*) is located adjacent to the boundary, so the value at the north node of this node (*nn*) can be used to write the FD expression to approximate $\frac{\partial \emptyset}{\partial \eta}$ at node *n*. On the other side of node *n*, the values at nodes P and *s* are available and, in this case, the location of node P and its corresponding 5-point stencil, as illustrated in Figure 2.28, provides enough data to write a 3rd-order accurate approximation for $\frac{\partial \emptyset}{\partial \eta}$ at node *n*, as expressed in equation (2.49.2).

$$\frac{\partial \emptyset}{\partial \eta}\Big|_s = \frac{-11\phi_s + 18\phi_P - 9\phi_n + 2\phi_{nn}}{6} \tag{2.49.1}$$

$$\frac{\partial \emptyset}{\partial \eta}\Big|_n = \frac{\phi_s - 6\phi_P + 3\phi_n + 2\phi_{nn}}{6} \tag{2.49.2}$$

In some situations, according to the location of the node P relative to the boundaries, the derivatives at the endpoints of the stencil appearing in equations (2.42.6) and (2.44.6) may be

approximated by 2nd-order accurate FD expressions. Due to the use of first derivatives to construct the HOC FD formulations, the order of approximation of derivatives never falls below 2nd-order accuracy.

2.6.5   Higher-Order Cut-Stencil Finite Difference Method for Boundaries Nodes

Previous sections have considered the derivations and formulations for higher-order approximation of the solution of PDEs at an arbitrary internal node P and equations with globally 4th-order accurate approximation were presented in equations (2.41) and (2.43). But as mentioned earlier, in the event of a Neumann boundary condition, the values at boundary nodes are also treated as unknown. The 2nd-order accurate approximation scheme was discussed and proposed for the solution at Neumann boundary nodes in Section 2.5.

The Neumann boundary condition is typically given by specification of the normal derivative $\frac{\partial \emptyset}{\partial n}\Big|_B$ at nodes B on the boundary. The cut-stencil FD formula given by equation (2.35), due to its double-sided structure, cannot be applied as a higher-order approximation for the first derivative in the Neumann boundary condition. Normally, in the event of Neumann boundary nodes, the approximation used for these unknown boundary values is considered differently, and this numerical approximation at the boundary nodes may affect the overall accuracy of the solution [83]. It has been common in numerical analyses to use one order of accuracy lower (or the same order, if possible) for approximation of the boundary condition compared to the order of accuracy used for inner nodes [66, 70, 83, 84]. Reasons for using one order lower for boundary condition approximation are related to some concepts such as stability considerations [84] and, as might be expected, using accuracy of more than one order lower will reduced the overall order of accuracy of the solution [85]. Research has shown that a pth-order scheme for the interior nodes along with a (p-1)-order accurate scheme for the boundary nodes approximation can retain the global accuracy of the scheme used at the interior nodes [86]. As an example, 6th-order and 3rd-order accurate approximation schemes for internal nodes and Neumann boundary conditions, respectively, have been shown to produce only a globally 4th-order scheme [87].

In this dissertation a 3rd-order accurate formulation using HOC cut-stencil FDM is proposed for the higher-order differencing approximation at the boundary nodes with Neumann boundary conditions.

To illustrate the concept while keeping the discussion simple, the boundary is taken as a straight line parallel to the *y*-axis, as shown in Figure 2.29, with Neumann condition at the boundary node (i, j), defined by $\frac{\partial \emptyset}{\partial n}\Big|_{(i,j)} = -\frac{\partial \emptyset}{\partial x}\Big|_{(i,j)} = G(x_{(i,j)}, y_{(i,j)})$.

$$\frac{\partial \emptyset}{\partial n}\Big|_{(i,j)} = -\frac{\partial \emptyset}{\partial x}\Big|_{(i,j)} = G(x_{(i,j)}, y_{(i,j)})$$
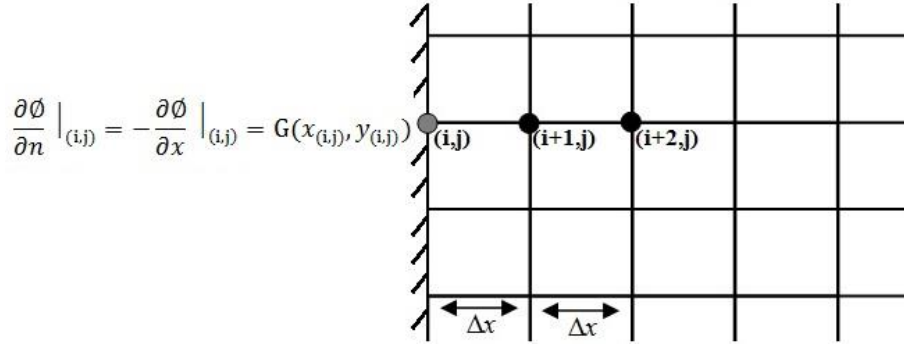
Figure 2.29: Schematic used for higher-order differencing at a boundary node with Neumann condition in TFD notation (in x direction)

One-sided differencing of the first derivative along the normal direction to the boundary line is achieved by expressing $\frac{\partial \emptyset}{\partial x}\Big|_{(i,j)}$ in terms of $\emptyset$–values at (i+1,j) and (i+2,j), and $\frac{\partial \emptyset}{\partial x}\Big|_{(i+1,j)}$. The coefficients are calculated by the same Taylor series procedure as presented earlier, leading to the 3rd-order accurate approximation (in TFD notation),

$$\frac{\partial \emptyset}{\partial x}\Big|_{(i,j)} = \frac{-5\emptyset_{(i,j)} + 4\emptyset_{(i+1,j)} + \emptyset_{(i+2,j)}}{2(\Delta x)} - 2\frac{\partial \emptyset}{\partial x}\Big|_{(i+1,j)} + O(\Delta x^3) \qquad (2.50.1)$$

Similar higher-order finite difference formulas can be derived for other boundary lines and in other coordinate directions, such as alignment with the *y*-axis as illustrated in Figure 2.30. For this boundary node (i,j), the Neumann condition is given by $\frac{\partial \emptyset}{\partial n}\Big|_{(i,j)} = \frac{\partial \emptyset}{\partial y}\Big|_{(i,j)} = G(x_{(i,j)}, y_{(i,j)})$. The derivative in this condition can be approximated with the one-sided formula:

$$\frac{\partial \emptyset}{\partial y}\Big|_{(i,j)} = \frac{5\emptyset_{(i,j)} - 4\emptyset_{(i,j-1)} - \emptyset_{(i,j-2)}}{2(\Delta y)} - 2\emptyset'_{(i,j-1)} + O(\Delta y^3) \qquad (2.50.2)$$
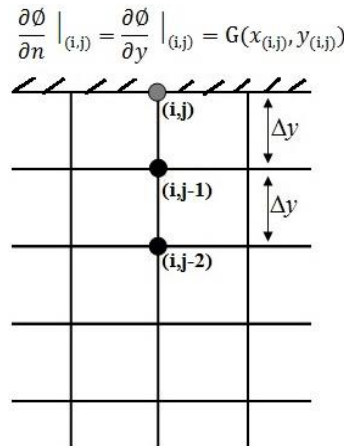
Figure 2.30: Schematic used for higher-order differencing at boundary node with Neumann condition in TFD notation (in y direction)

These 3rd-order accurate expressions in equations (2.50.1) and (2.50.2) have also been proposed in other higher-order finite difference numerical studies [64].

The Cartesian cut-stencil FD formulation equivalent of equations (2.50.1) and (2.50.2) is achieved by referring to an arbitrary 5-point computational stencil centred at node P which includes both a west and north boundary node with Neumann boundary conditions, as shown in Figure 2.31.
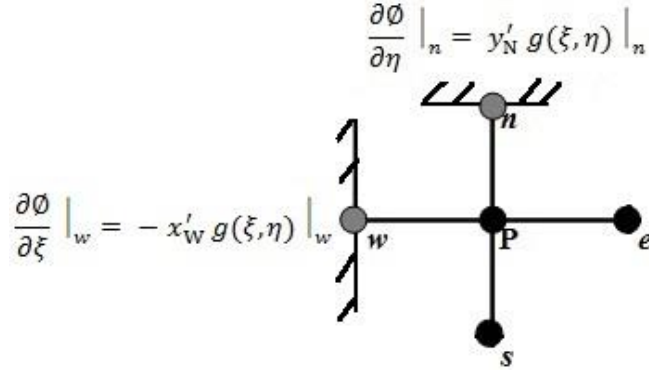
Figure 2.31: Computational stencil for higher-order differencing at boundary nodes with Neumann condition (cut-stencil FD notation)

These approximations are given by:

$$\emptyset_w = \frac{4\emptyset_P + \emptyset_e + 2(x'_W)g|_w}{5} - \frac{4}{5}\frac{\partial\emptyset}{\partial\xi}\Big|_P \qquad (2.51.1)$$

$$\emptyset_n = \frac{4\emptyset_P + \emptyset_s + 2(y'_N)g|_n}{5} + \frac{4}{5}\frac{\partial\emptyset}{\partial\eta}\Big|_P \qquad (2.51.2)$$

The terms $\frac{\partial\emptyset}{\partial\xi}\Big|_P$ and $\frac{\partial\emptyset}{\partial\eta}\Big|_P$ in equations (2.51.1) and (2.51.2) are updated through the standard iterative scheme, using the same equations and conditions as explained for the higher-order accurate approximation at interior nodes.

2.7 Cut-Stencil FD Formulation of Unsteady Model Equation

To gradually convey the essential characteristics of the Cartesian cut-stencil FDM without introducing too much complexity, the formulations and expressions throughout this chapter have thus far been limited to spatial discretization and all the conceptual topics were discussed in the context of the steady formulation of the cut-stencil FDM. This section and corresponding subsections extend the analysis to the unsteady formulation of the Cartesian cut-stencil FDM. The unsteady convection-diffusion equation, introduced in equation (2.1), is broadly applied to describe various phenomena in science and engineering fields [88], such as unsteady Navier-Stokes equations in fluid mechanics, cf. e.g. [89-91], or transient conduction heat transfer, which is modelled by the unsteady diffusion equation. Due to its importance as a model of physical phenomena, solution methods for the unsteady convection-diffusion equation have received much attention in numerical studies, e.g. [49, 88-93].

2.7.1　Explicit Forward in Time and Central in Space (FTCS) Formulation of the Cut-Stencil FDM

In order to simplify the discussion, the unsteady diffusion equation, $\frac{\partial \varnothing}{\partial t} = \nu \nabla^2 \varnothing + S$, is considered and an explicit method is applied to numerically solve this parabolic equation. Although there are many well-established explicit and implicit methods for solving parabolic PDEs, cf. e.g. [94-96], the intent in this research is to investigate the basis and fundamentals of the Cartesian cut-stencil FD algorithm. Therefore, the discussion of the unsteady model equation (diffusion equation) is limited to the forward in time and central in space (FTCS) explicit formulation.

The mapped form of the unsteady diffusion equation is written as:

$$\frac{\partial \varnothing}{\partial t} = \nu \left[\frac{1}{(x')^2}\frac{\partial^2 \varnothing}{\partial \xi^2} - \frac{x''}{(x')^3}\frac{\partial \varnothing}{\partial \xi} + \frac{1}{(y')^2}\frac{\partial^2 \varnothing}{\partial \eta^2} - \frac{y''}{(y')^3}\frac{\partial \varnothing}{\partial \eta} \right] + s \qquad (2.52.1)$$

1st-order forward and 2nd-order central difference schemes are used to approximate the time and space derivatives, respectively. Then, the discrete form of equation (2.52.1), at point P of an arbitrary 5-point stencil, is given by:

$$\frac{\varnothing_P^{n+1} - \varnothing_P^n}{(\Delta t)} = \nu \left[\frac{\varnothing_w^n - 2\varnothing_P^n + \varnothing_e^n}{(x_P')^2} - \frac{x_P''}{(x_P')^3}\frac{\varnothing_e^n - \varnothing_w^n}{2} + \frac{\varnothing_s^n - 2\varnothing_P^n + \varnothing_n^n}{(y_P')^2} - \frac{y_P''}{(y_P')^3}\frac{\varnothing_n^n - \varnothing_s^n}{2} \right] + s_P^n \qquad (2.52.2)$$

The superscript n (recall that subscript n refers to north) and Δt represent time level ($t = t_n$) and time step, respectively. An initial condition, which is the value of the function $\varnothing$ at initial time (t_0), is given along with specified boundary conditions to start the solution procedure. This standard time marching scheme is applied to solve equation (2.52.2). The value of function $\varnothing$ at time level $n + 1$ is computed from the previous time level at which all values of $\varnothing$ are known. The only unknown in equation (2.52.2) is $\varnothing_P^{n+1}$ and clearly this equation can be solved to explicitly provide the value of the unknown [17]. Figure 2.32 illustrates the nodes used in the evaluation of $\varnothing_P^{n+1}$ using the explicit FTCS formulation.
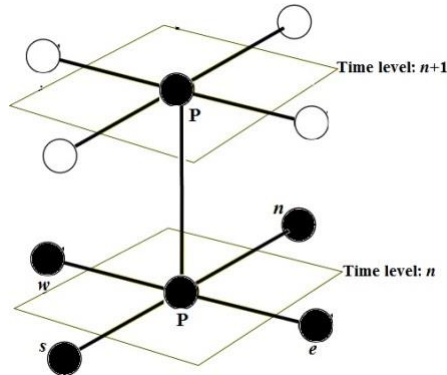
Figure 2.32: Illustration of stencil used for explicit FTCS formulation

The value $\varnothing_P^{n+1}$ is computed from the following form of equation (2.52.2),

$$\varnothing_P^{n+1} = a_P \phi_P^n + a_w \phi_w^n + a_e \phi_e^n + a_s \phi_s^n + a_n \phi_n^n + (\Delta t) S_P^n \qquad (2.53)$$

where the coefficients are given by:

$$a_P^n = -2\nu(\Delta t)\left(\frac{1}{(x_P')^2} + \frac{1}{(y_P')^2}\right) + 1 \qquad (2.53.1)$$

$$a_w^n = \nu(\Delta t)\left(\frac{1}{(x_P')^2} + \frac{x_P''}{2(x_P')^3}\right) \qquad (2.53.2)$$

$$a_e^n = \nu(\Delta t)\left(\frac{1}{(x_P')^2} - \frac{x_P''}{2(x_P')^3}\right) \qquad (2.53.3)$$

$$a_s^n = \nu(\Delta t)\left(\frac{1}{(y_P')^2} + \frac{y_P''}{2(y_P')^3}\right) \qquad (2.53.4)$$

$$a_n^n = \nu(\Delta t)\left(\frac{1}{(y_P')^2} - \frac{y_P''}{2(y_P')^3}\right) \qquad (2.53.5)$$

Explicit discretization of the unsteady convection-diffusion equation yields an algorithm that is easy to implement for unsteady problems involving heat diffusion [97], but it may suffer from numerical instability and show oscillatory solutions for large values of time step since this method is conditionally stable. Stable solution of the FTCS formulation is achieved by satisfying the stability requirements which are discussed in the following section.

2.7.1.1 Stability Analysis for FTCS Formulation of Cut-Stencil FDM

The stability requirements for the unsteady convection-diffusion equation have been addressed in many numerical analysis and CFD textbooks, as well as numerous journal papers, e.g. [17, 57, 58, 98, 99]. Analysis of the stability conditions for 2-D convection-diffusion, even in TFDM, is relatively complicated and this task is beyond the main purpose of this research which is focused on proving the feasibility and showing the potential of the Cartesian cut-stencil FD formulation for the solution of PDEs on complex domains. Thus, the approach taken here is to find similarities or analogies between the stability conditions for the 2-D convection-diffusion equation in TFDM and the cut-stencil FD formulation, mostly with reference to the unsteady diffusion equation as the model equation.

Many researchers have proposed stability criteria for the multidimensional unsteady convection-diffusion equation for different FD approaches [99, 100]. Beckers [99] analysed stability criteria for the explicit formulation of the general convection-diffusion equation (2.54.1) by considering the amplification factor in the von Neumann method. All convection and diffusion coefficients in (2.54.1) were assumed to be constant. The discrete finite difference approximation of equation (2.54.1), as addressed in [99], is stated in equation (2.54.2).

$$\frac{\partial \emptyset}{\partial t} + U\frac{\partial \emptyset}{\partial x} + V\frac{\partial \emptyset}{\partial y} = \kappa\frac{\partial^2 \emptyset}{\partial x^2} + \mu\frac{\partial^2 \emptyset}{\partial y^2} \qquad (2.54.1)$$

$$\emptyset_{i,j}^{n+1} = \emptyset_{i,j}^n - \frac{U(\Delta t)}{2(\Delta x)}\left(\emptyset_{i+1,j}^n - \emptyset_{i-1,j}^n\right) - \frac{V(\Delta t)}{2(\Delta y)}\left(\emptyset_{i,j+1}^n - \emptyset_{i,j-1}^n\right) +$$
$$\frac{\kappa(\Delta t)}{(\Delta x)^2}\left(\emptyset_{i-1,j}^n - 2\emptyset_{i,j}^n + \emptyset_{i+1,j}^n\right) + \frac{\mu(\Delta t)}{(\Delta y)^2}\left(\emptyset_{i,j-1}^n - 2\emptyset_{i,j}^n + \emptyset_{i,j+1}^n\right) \qquad (2.54.2)$$

The physical parameters, which convey the definition of Courant and diffusion numbers as defined in Beckers [99], are defined by:

$$c_x = \frac{U(\Delta t)}{(\Delta x)}, \qquad c_y = \frac{V(\Delta t)}{(\Delta y)}, \qquad d_x = \frac{\kappa(\Delta t)}{(\Delta x)^2}, \qquad d_y = \frac{\mu(\Delta t)}{(\Delta y)^2} \qquad (2.54.3)$$

Beckers [99] derived two general stability conditions for the explicit FTCS formulation of equation (2.54.1) and stated that these two conditions are sufficient conditions for the stability of the numerical algorithm. The two sufficient stability criteria, as proposed by Beckers [99], are:

$$d_x + d_y \leq \frac{1}{2} \Rightarrow \left(\frac{\kappa}{(\Delta x)^2} + \frac{\mu}{(\Delta y)^2}\right)(\Delta t) \leq \frac{1}{2} \qquad (2.55.1)$$

$$\frac{(c_x)^2}{d_x} + \frac{(c_y)^2}{d_y} \leq 2 \Rightarrow \left(\frac{U^2}{\kappa} + \frac{V^2}{\mu}\right)(\Delta t) \leq 2 \qquad (2.55.2)$$

Similar conditions as equations (2.55.1) and (2.55.2) were proposed by Chan [101] for the 1-D convection-diffusion model equation, which can be written as $\frac{\partial \emptyset}{\partial t} = a\frac{\partial \emptyset}{\partial x} + b\frac{\partial^2 \emptyset}{\partial x^2}$. Chan [101] showed that the maximum allowable time step for stability of the FTCS formulation of the 1-D model equation is given by $(\Delta t)_{Max} \leq Min(\frac{2b}{a^2}, \frac{(\Delta x)^2}{2b})$. Thompson et al. [102] also used von Neumann stability analysis to analyse the stability criteria for the FTCS algorithm of 2-D unsteady convection-diffusion equation and concluded the same conditions as written in equations (2.55.1) and (2.55.2).

It is possible to draw an analogy between Beckers' model convection-diffusion equation (2.54.1) and the cut-stencil FD equation for diffusion (2.52.1). Identifying the parameters in (2.54.1) as

$$\kappa = \frac{\nu}{(x'_P)^2}, \qquad \mu = \frac{\nu}{(y'_P)^2}, \qquad U = \frac{\nu x''_P}{(x'_P)^3}, \qquad V = \frac{\nu y''_P}{(y'_P)^3} \qquad (2.56)$$

leads to the following stability conditions in the Cartesian cut-stencil FDM notation for a 5-point stencil centred at node P,

$$\nu\left(\frac{1}{(x'_P)^2} + \frac{1}{(y'_P)^2}\right)(\Delta t) \leq \frac{1}{2} \qquad (2.57.1)$$

$$\nu\left(\frac{(x''_P)^2}{(x'_P)^4} + \frac{(y''_P)^2}{(y'_P)^4}\right)(\Delta t) \leq 2 \qquad (2.57.2)$$

The conditions given by equations (2.57.1) and (2.57.2) should be satisfied for each stencil and the maximum allowable time step which can fulfil the stability requirement on the whole domain is obtained through this consideration. This situation is similar to that which occurs in TFDM when finite differencing is applied for approximation of equations with variable coefficients or on non-uniform meshes, where the stability criteria should be considered and satisfied at very node of the solution field [102, 103]. It is worth mentioning that in the event of a uniform mesh, the metrics x'' and y'' are both zero and only the first stability condition, as written in equation (2.57.1), should be considered and checked for each stencil.

The results for the unsteady formulation of the cut-stencil FDM using "manufactured" problems and examining the proposed stability criteria, similar to steady formulations of the cut-stencil FDM, will be discussed in Chapter 3.

2.7.2 Cut-Stencil FDM Formulation for Second-Order Wave Equation

The second-order wave equation is a hyperbolic equation that can be applied to model different phenomena such as vibrations of a thin membrane [50, 104] or the model equation for an acoustic wave [105]. The solution of the second-order wave equation needs two sets of initial conditions which are usually expressed as the initial value, i.e. the value of the governing function at initial time (t_0), and the first temporal derivative of the governing function at the initial time. The model second-order wave equation, which may include a source term S, is represented by:

$$\frac{\partial^2 \emptyset}{\partial t^2} = C^2 \nabla^2 \emptyset + S = C^2 \left[\frac{\partial^2 \emptyset}{\partial x^2} + \frac{\partial^2 \emptyset}{\partial y^2} \right] + S \qquad (2.58.1)$$

where C^2 is taken to be constant. The mapped form of (2.58.1) is:

$$\frac{\partial^2 \emptyset}{\partial t^2} = C^2 \left[\frac{1}{(x')^2} \frac{\partial^2 \emptyset}{\partial \xi^2} - \frac{x''}{(x')^3} \frac{\partial \emptyset}{\partial \xi} + \frac{1}{(y')^2} \frac{\partial^2 \emptyset}{\partial \eta^2} - \frac{y''}{(y')^3} \frac{\partial \emptyset}{\partial \eta} \right] + s \qquad (2.58.2)$$

and applying central 2nd-order accurate finite difference expressions to approximate both the time and space derivatives, the discrete form of equation (2.58.2), at point P of an arbitrary 5-point stencil, is:

$$\frac{\emptyset_P^{n-1} - 2\emptyset_P^n + \emptyset_P^{n+1}}{(\Delta t)^2} = C^2 \left[\frac{\emptyset_w^n - 2\emptyset_P^n + \emptyset_e^n}{(x'_P)^2} - \frac{x''_P}{(x'_P)^3} \frac{\emptyset_e^n - \emptyset_w^n}{2} + \frac{\emptyset_s^n - 2\emptyset_P^n + \emptyset_n^n}{(y'_P)^2} - \frac{y''_P}{(y'_P)^3} \frac{\emptyset_n^n - \emptyset_s^n}{2} \right] + S_P^n \quad (2.58.3)$$

Rearrangement of equation (2.58.3) gives the direct formulation to calculate the unknown $\emptyset_P^{n+1}$ as shown in equation (2.58.4). The solution for $\emptyset_P^{n+1}$ needs the value of the function from two previous time steps; therefore, as mentioned before, two initial conditions are defined for the second-order wave equation.

$$\begin{aligned} \emptyset_P^{n+1} = C^2 (\Delta t)^2 &\left[\left(\frac{-2}{(x'_P)^2} + \frac{-2}{(y'_P)^2} \right) \phi_P^n + \left(\frac{1}{(x'_P)^2} + \frac{x''_P}{2(x'_P)^3} \right) \phi_w^n + \left(\frac{1}{(x'_P)^2} - \frac{x''_P}{2(x'_P)^3} \right) \phi_e^n \right. \\ &\left. + \left(\frac{1}{(y'_P)^2} + \frac{y''_P}{2(y'_P)^3} \right) \phi_s^n + \left(\frac{1}{(y'_P)^2} - \frac{y''_P}{2(y'_P)^3} \right) \phi_e^n \right] + 2\emptyset_P^n - \emptyset_P^{n-1} + (\Delta t)^2 S_P^n \end{aligned} \qquad (2.58.4)$$

The method used to discretize the first-order temporal derivative at the initial time, e.g. with either 1st- or 2nd-order accuracy, provides a different set of coefficients than in equation (2.58.4) and, consequently, can change the accuracy of the solution. The details of this matter are discussed in the following sections. Similar to other model equations already discussed, the discrete form of the second-order wave equation, as written in equation (2.58.3) or (2.58.4), can be cast in the standard format similar to equation (2.53).

2.7.2.1 1$^{\text{st}}$-Order Accurate Approximation for First Temporal Derivative at Initial Time for Second-Order Wave Equation

The two initial conditions for the mapped form of the model second-order wave equation at an arbitrary internal or boundary node $\mathcal{P}$ are defined as $\emptyset(\mathcal{P}, t_0) = \emptyset_0$ and $\left.\frac{\partial \emptyset}{\partial t}\right|_{(\mathcal{P}, t_0)} = g_0$. For the first scheme used, the temporal derivative at t_0 is approximated by a 1$^{\text{st}}$-order accurate approximation in time, as shown in equation (2.59.1).

$$\left.\frac{\partial \emptyset}{\partial t}\right|_{(\mathcal{P}, t_0)} = \frac{\emptyset_{\mathcal{P}}^{t_0} - \emptyset_{\mathcal{P}}^{t_0 - \Delta t}}{(\Delta t)} = g_0 \tag{2.59.1}$$

For notational convenience, $\emptyset_{\mathcal{P}}^{t_0 - \Delta t}$, $\emptyset_{\mathcal{P}}^{t_0}$ and $\emptyset_{\mathcal{P}}^{t_0 + \Delta t}$ are represented by $\emptyset_{\mathcal{P}}^{-1}$, $\emptyset_{\mathcal{P}}^{0}$ and $\emptyset_{\mathcal{P}}^{1}$, respectively. The function g_0 in equation (2.59.1) is a known function which is taken from the exact solution in "manufactured" problems, or from the physics of the problem; therefore, $\emptyset_{\mathcal{P}}^{-1}$ can be calculated from equation (2.59.1), given by:

$$\emptyset_{\mathcal{P}}^{-1} = \emptyset_{\mathcal{P}}^{0} - (\Delta t)g_0 \tag{2.59.2}$$

The value of $\emptyset_{\mathcal{P}}^{-1}$ from equation (2.59.2) is substituted into equation (2.58.4), giving modified coefficients for the standard form of equation (2.58.4) for an arbitrary internal point $\mathcal{P}$ of a 5-point stencil and which are used for calculation of the function at the first time step (when superscript $n = 0$). These coefficients are given in equations (2.60.1) to (2.60.5). The source term for $n = 0$ is evaluated by $(\Delta t)^2 s_{\mathcal{P}}^{0} + (\Delta t)g_0$.

$$a_{\mathcal{P}}^{0} = -2C^2(\Delta t)^2 \left(\frac{1}{(x_{\mathcal{P}}')^2} + \frac{1}{(y_{\mathcal{P}}')^2}\right) + 1 \tag{2.60.1}$$

$$a_w^{0} = C^2(\Delta t)^2 \left(\frac{1}{(x_{\mathcal{P}}')^2} + \frac{x_{\mathcal{P}}''}{2(x_{\mathcal{P}}')^3}\right) \tag{2.60.2}$$

$$a_e^{0} = C^2(\Delta t)^2 \left(\frac{1}{(x_{\mathcal{P}}')^2} - \frac{x_{\mathcal{P}}''}{2(x_{\mathcal{P}}')^3}\right) \tag{2.60.3}$$

$$a_s^{0} = C^2(\Delta t)^2 \left(\frac{1}{(y_{\mathcal{P}}')^2} + \frac{y_{\mathcal{P}}''}{2(y_{\mathcal{P}}')^3}\right) \tag{2.60.4}$$

$$a_n^{0} = C^2(\Delta t)^2 \left(\frac{1}{(y_{\mathcal{P}}')^2} - \frac{y_{\mathcal{P}}''}{2(y_{\mathcal{P}}')^3}\right) \tag{2.60.5}$$

The coefficients for subsequent time steps (when superscript $n \geq 1$) are directly achieved from rearrangement of equation (2.58.4) and are expressed in equations (2.61.1) to (2.61.5). The source term for $n \geq 1$ is evaluated by $(\Delta t)^2 S_{\text{P}}^{n} - \emptyset_{\text{P}}^{n-1}$ where the term $\emptyset_{\text{P}}^{n-1}$ is calculated from the last time step.

$$a_{\text{P}}^{n} = -2C^2(\Delta t)^2 \left(\frac{1}{(x_{\text{P}}')^2} + \frac{1}{(y_{\text{P}}')^2}\right) + 2 \tag{2.61.1}$$

$$a_w^n = \mathcal{C}^2 (\Delta t)^2 \left(\frac{1}{(x_P')^2} + \frac{x_P''}{2(x_P')^3} \right) \tag{2.61.2}$$

$$a_e^n = \mathcal{C}^2 (\Delta t)^2 \left(\frac{1}{(x_P')^2} - \frac{x_P''}{2(x_P')^3} \right) \tag{2.61.3}$$

$$a_s^n = \mathcal{C}^2 (\Delta t)^2 \left(\frac{1}{(y_P')^2} + \frac{y_P''}{2(y_P')^3} \right) \tag{2.61.4}$$

$$a_n^n = \mathcal{C}^2 (\Delta t)^2 \left(\frac{1}{(y_P')^2} - \frac{y_P''}{2(y_P')^3} \right) \tag{2.61.5}$$

2.7.2.2 2nd-Order Accurate Approximation for First Temporal Derivative at Initial Time for Second-Order Wave Equation

The temporal derivative at initial time at an arbitrary node $\mathcal{P}$ can be approximated to 2nd-order accuracy using central differencing:

$$\left. \frac{\partial \emptyset}{\partial t} \right|_{(\mathcal{P}, t_0)} = \frac{\emptyset_{\mathcal{P}}^{t_0 + \Delta t} - \emptyset_{\mathcal{P}}^{t_0 - \Delta t}}{2(\Delta t)} = g_0 \tag{2.62.1}$$

Using the same notation as above for $\emptyset_{\mathcal{P}}^{t_0 - \Delta t}$ and $\emptyset_{\mathcal{P}}^{t_0 + \Delta t}$, the value of $\emptyset_{\mathcal{P}}^{-1}$ is calculated from equation (2.62.1) as:

$$\emptyset_{\mathcal{P}}^{-1} = \emptyset_{\mathcal{P}}^{1} - 2(\Delta t) g_0 \tag{2.62.2}$$

Substitution of $\emptyset_{\mathcal{P}}^{-1}$ from equation (2.62.2) into (2.58.4) gives the coefficients of the standard form of equation (2.58.4) at node $\mathcal{P}$ of an arbitrary 5-point stencil at the first time step ($n = 0$), expressed in equations (2.63.1) to (2.63.5). The source term expression when $n = 0$ is written as $0.5(\Delta t)^2 S_P^0 + (\Delta t) g_0$.

$$a_{\mathcal{P}}^0 = -\mathcal{C}^2 (\Delta t)^2 \left(\frac{1}{(x_{\mathcal{P}}')^2} + \frac{1}{(y_{\mathcal{P}}')^2} \right) + 1 \tag{2.63.1}$$

$$a_w^0 = 0.5 \mathcal{C}^2 (\Delta t)^2 \left(\frac{1}{(x_{\mathcal{P}}')^2} + \frac{x_{\mathcal{P}}''}{2(x_{\mathcal{P}}')^3} \right) \tag{2.63.2}$$

$$a_e^0 = 0.5 \mathcal{C}^2 (\Delta t)^2 \left(\frac{1}{(x_{\mathcal{P}}')^2} - \frac{x_{\mathcal{P}}''}{2(x_{\mathcal{P}}')^3} \right) \tag{2.63.3}$$

$$a_s^0 = 0.5 \mathcal{C}^2 (\Delta t)^2 \left(\frac{1}{(y_{\mathcal{P}}')^2} + \frac{y_{\mathcal{P}}''}{2(y_{\mathcal{P}}')^3} \right) \tag{2.63.4}$$

$$a_n^0 = 0.5 \mathcal{C}^2 (\Delta t)^2 \left(\frac{1}{(y_{\mathcal{P}}')^2} - \frac{y_{\mathcal{P}}''}{2(y_{\mathcal{P}}')^3} \right) \tag{2.63.5}$$

The coefficients for the other time steps ($n \geq 1$) for this method are the same as the previous scheme shown in equations (2.61.1)-(2.61.5).

2.7.2.3 Stability Analysis for Cut-Stencil Formulation of Second-Order Wave Equation

The stability condition for the model equation (2.58.3) is discussed only for a uniform physical mesh, implying that x'' and y'' both are zero. The discussion begins with the TFD formulation for the discrete form of equation (2.58.1):

$$\frac{\emptyset_{(i,j)}^{n-1} - 2\emptyset_{(i,j)}^{n} + \emptyset_{(i,j)}^{n+1}}{(\Delta t)^2} = \mathcal{C}^2 \left[\frac{\emptyset_{(i-1,j)}^{n} - 2\emptyset_{(i,j)}^{n} + \emptyset_{(i+1,j)}^{n}}{(\Delta x)^2} + \frac{\emptyset_{(i,j-1)}^{n} - 2\emptyset_{(i,j)}^{n} + \emptyset_{(i,j+1)}^{n}}{(\Delta y)^2} \right] + s_{(i,j)}^{n} \qquad (2.64)$$

The Fourier component is defined by $\emptyset_{(i,j)}^{n} = \Phi^n e^{I\theta_x i} e^{I\theta_y j}$ where the parameters θ_x and θ_y are phase angles, Φ stands for the Fourier amplitude and $I = \sqrt{-1}$. Substituting the Fourier component into equation (2.64) and simplification of the resulting expression produces the equation

$$\Phi^2 - 2 \left[1 - \left(\frac{\mathcal{C}(\Delta t)}{(\Delta x)} \right)^2 (1 - \cos \theta_x) - \left(\frac{\mathcal{C}(\Delta t)}{(\Delta y)} \right)^2 (1 - \cos \theta_y) \right] \Phi + 1 = 0 \qquad (2.65.1)$$

To satisfy the stability requirement, the absolute value of both roots of the quadratic equation (2.65.1) should be less than unity. In this event, the term inside the brackets (in equation (2.65.1)) needs to satisfy the following condition:

$$-1 \leq \left[1 - \left(\frac{\mathcal{C}(\Delta t)}{(\Delta x)} \right)^2 (1 - \cos \theta_x) - \left(\frac{\mathcal{C}(\Delta t)}{(\Delta y)} \right)^2 (1 - \cos \theta_y) \right] \leq 1 \qquad (2.65.2)$$

The most severe condition occurs when the values of $\cos \theta_x$ and $\cos \theta_y$ are both equal to -1, and this leads to the stability condition for the difference form of the 2-D second-order wave equation, written as:

$$\left(\frac{\mathcal{C}(\Delta t)}{(\Delta x)} \right)^2 + \left(\frac{\mathcal{C}(\Delta t)}{(\Delta y)} \right)^2 \leq 1 \Rightarrow \mathcal{C}^2 \left(\frac{1}{(\Delta x)^2} + \frac{1}{(\Delta y)^2} \right) (\Delta t)^2 \leq 1 \qquad (2.65.3)$$

Correspondence between equation (2.61.1) and the cut-stencil form of the 2-D second-order wave equation for a uniform physical mesh gives the following stability condition for each computational stencil, centred at node P:

$$\mathcal{C}^2 \left(\frac{1}{(x'_P)^2} + \frac{1}{(y'_P)^2} \right) (\Delta t)^2 \leq 1 \Rightarrow (\Delta t) \leq \frac{1}{\mathcal{C} \sqrt{\left(\frac{1}{(x'_P)^2} + \frac{1}{(y'_P)^2} \right)}} \qquad (2.65.4)$$

2.8 Chapter Summary

Generally speaking, the details of several mathematical formulations of the Cartesian cut-stencil FDM were presented in this chapter. The systematic development of this new numerical

formulation, beginning from the particular transformation functions (1-D quadratic functions) and the metrics of this transformation, was discussed. The uniform arms of the generic computational stencil provide the conditions for 2nd-order accurate approximations for the derivatives in the mapped form of the convection-diffusion equation, which is taken as the model equation. The mathematical formulations are developed using the same 5-point stencil for all cut and uncut stencils to cast the discretized form of the governing equation in the standard iterative form (equation (2.9)). The details of extension of the cut-stencil FDM from its basic 2nd-order accurate formulation to higher-order accurate approximation were addressed in this chapter. The higher-order formulations include a 5+4-point stencil scheme which is constructed by adding 4 fictitious nodes to the 5-point stencil, and two families of compact Padé-Hermitian schemes using only the 5-point stencil. The implementation of boundary conditions was considered and the formulation for higher-order accurate approximation of unknown boundary values was presented. The formulation of unsteady model equations using the Cartesian cut-stencil FDM and corresponding stability criteria were also discussed in this chapter.

CHAPTER 3

CARTESIAN CUT-STENCIL FDM SOLUTIONS to MANUFACTURED PROBLEMS

3.1   Objective of the Chapter

Verification of the Cartesian cut-stencil FDM formulated in Chapter 2 will be undertaken in this chapter by employing the method of manufactured solutions (MMS). This chapter concentrates on verification of the cut-stencil method by computer implementation of the equations, schemes and methods proposed in Chapter 2 and presenting the solutions of a number of manufactured problems. A computer code has been written for this purpose. The problems in this chapter include the solution of PDEs on different shapes of domains and specific aspects of the cut-stencil FDM, such as 2nd-order accurate formulation, treatment of boundary conditions and HO methods. The unsteady formulation and the proposed stability criteria are also discussed through these manufactured problems. The manufactured problems, as discussed in this chapter, all have analytical solutions which are defined by mathematical functions such as trigonometric or logarithmic functions. Due to the fact that verification of methods (or codes) is a purely mathematical procedure, it is not necessary to choose problems with exact physical meaning [106, 107]. One can say that verification reflects the solution of the PDE and does not deal with any real physics of the problem that may be associated with that PDE [108].

3.2   Definition of Method (Code) Verification

Researchers have made a distinction between calculation verification and code verification [109]. Roache [107] states that calculation verification is associated with estimation of errors, while code verification studies error evaluation which is devised from a benchmark problem for which the solution is known. The difference between calculation and code verification has been widely discussed in the literature [106, 107, 109, 110, 111, 112]. In this dissertation, verification conveys a more general meaning. The goal of presenting the numerical solution to the sample problems in this chapter is to survey the correctness of the proposed algorithms, formulations and schemes for the solution of PDEs. In other words, the verification process contained herein means assessing the correctness of the numerical solution to the equations, which can alternatively be expressed as correct numerical analysis [112]. In this context, verification aims at testing the accurate implementation for solution of a mathematical model [113]. Thus, the efforts of this chapter in terms of verification procedure is to show that the equations are solved correctly [114, 115, 116].

3.2.1   Method of Manufactured Solutions (MMS)

The method of manufactured solutions (MMS) is regarded as an efficient tool for the verification procedure [108, 109, 114, 117, 118]. As mentioned above, the verification process is a purely mathematical exercise; therefore, the proposed manufactured problems do not need a realistic physical interpretation [117]. However, from the perspective of subsequent applications, one should chose or design manufactured problems that exhibit some of the key characteristics of real-world problems of current interest, cf. e.g. [119]. The MMS technique constructs the exact solution to a PDE or set of PDEs and, in general, if the manufactured solution does not satisfy the governing equation(s), source terms can be defined to correct the imbalance. These source terms

are determined by substituting the manufactured solution into the model PDE(s) [106], and is then applied within the solver (or code) [110]. The boundary conditions may be Dirichlet, Neumann, etc., and are defined from the manufactured solution by applying the solution on the boundaries of the domain [107]. The discrete form of the modified model equation(s) (governing equation(s)) is solved numerically and the solution is compared to the exact solution of the manufactured problem [110, 120].

This procedure has been used for the sample problems defined throughout this chapter, and begins with definition of a manufactured problem, followed by its exact solution $\emptyset_{exact}$, where $\emptyset$ is a function of independent variables x and y for solution to steady equations and x, y and t for solution to unsteady problems. The first and second derivatives of function $\emptyset$ with respect to independent variables ξ and η in the computational stencil are calculated analytically and the source term is obtained from substitution of analytical derivatives into the corresponding PDE. After this mathematical manipulation, the discrete form of the manufactured equation gives the coefficients already defined in Chapter 2, such as equations (2.10) for the 2nd-order accurate solution. The boundary conditions are similarly taken from $\emptyset_{exact}$ and solution of the discrete form of the manufactured equation provides the Cartesian cut-stencil FD solution which can be compared to $\emptyset_{exact}$ at each node.

3.3   Local Truncation Error (LTE)

The local truncation error (LTE) in FDM, also referred to as discretization error, reveals how well the continuous differential equation is approximated by the discrete difference equation [58, 121]. In absence of the exact solution to the governing model equation, the LTE can be used to examine the accuracy of the differencing formulation. Additionally, the region of the domain with the largest value of LTE can be refined to reduce the overall error of the differencing method used. In other words, LTE can be used as a criterion for grid adaptation [122, 123, 124].

The LTE is associated with the difference between the differential equation and the proposed differencing scheme. For example, for a 2nd-order accurate approximation of the second derivative of a 1-D function $\emptyset$, the mathematical definition of LTE, in TFD notation, is:

$$\text{LTE}_{(i)} = \frac{\partial^2 \emptyset}{\partial x^2}\bigg|_{(i)} - \frac{\emptyset_{(i-1)} - 2\emptyset_{(i)} + \emptyset_{(i+1)}}{(\Delta x)^2} \qquad (3.1.1)$$

Note that, for later convenience when presenting the LTE for 2-D problems, the partial derivative notation has been used here, rather than the ordinary derivative $\frac{d^2\emptyset}{dx^2}$. The concept of the modified PDE can be exploited to determine the LTE using Taylor series expansions to convert the difference expression back to the continuous derivative form. This procedure is illustrated for the 2nd-order approximation of $\frac{\partial^2 \emptyset}{\partial x^2}$ written in equation (3.1.1):

$$\text{LTE}_{(i)} = \frac{\partial^2 \emptyset}{\partial x^2}\bigg|_{(i)} - \frac{1}{(\Delta x)^2} \left\{ \left[\emptyset_{(i)} - \frac{(\Delta x)}{1!}\frac{\partial \emptyset}{\partial x}\bigg|_{(i)} + \frac{(\Delta x)^2}{2!}\frac{\partial^2 \emptyset}{\partial x^2}\bigg|_{(i)} - \right. \right.$$
$$\left. \frac{(\Delta x)^3}{3!}\frac{\partial^3 \emptyset}{\partial x^3}\bigg|_{(i)} + \frac{(\Delta x)^4}{4!}\frac{\partial^4 \emptyset}{\partial x^4}\bigg|_{(i)} + \cdots \right] - 2\emptyset_{(i)} + \left[\emptyset_{(i)} + \frac{(\Delta x)}{1!}\frac{\partial \emptyset}{\partial x}\bigg|_{(i)} + \right. \qquad (3.1.2)$$
$$\left. \left. \frac{(\Delta x)^2}{2!}\frac{\partial^2 \emptyset}{\partial x^2}\bigg|_{(i)} + \frac{(\Delta x)^3}{3!}\frac{\partial^3 \emptyset}{\partial x^3}\bigg|_{(i)} + \frac{(\Delta x)^4}{4!}\frac{\partial^4 \emptyset}{\partial x^4}\bigg|_{(i)} + \cdots \right] \right\}$$

Cancelling out terms and rearranging equation (3.1.2) gives

$$\text{LTE}_{(i)} = -\frac{(\Delta x)^2}{12}\frac{\partial^4 \emptyset}{\partial x^4}\Big|_{(i)} - \frac{(\Delta x)^4}{360}\frac{\partial^6 \emptyset}{\partial x^6}\Big|_{(i)} + \cdots \qquad (3.1.3)$$

The leading term of equation (3.1.3) includes $(\Delta x)^2$ which conveys the 2nd-order accuracy of the approximation. The other terms appearing after the leading term are suppressed and the LTE is evaluated as:

$$\text{LTE}_{(i)} = -\frac{(\Delta x)^2}{12}\frac{\partial^4 \emptyset}{\partial x^4}\Big|_{(i)} \qquad (3.1.4)$$

The Cartesian cut-stencil FD formulation of the model expression in equation (3.1.1) on a 3-point computational stencil (since 1-D) centred at node P is obtained after mapping the second derivative $\frac{\partial^2 \emptyset}{\partial x^2}$ to $\frac{1}{(x_P')^2}\frac{\partial^2 \emptyset}{\partial \xi^2} - \frac{x_P''}{(x_P')^3}\frac{\partial \emptyset}{\partial \xi}$ as discussed in Chapter 2, e.g. in equation (2.7). This expression includes first and second derivatives which are normally approximated by 2nd-order accuracy using central differencing. Following the same procedure as above, the LTE in the transformed system is defined by:

$$\text{LTE}_{(P)} = \frac{1}{(x_P')^2}\frac{\partial^2 \emptyset}{\partial \xi^2}\Big|_P - \frac{x_P''}{(x_P')^3}\frac{\partial \emptyset}{\partial \xi}\Big|_P - \left\{\frac{\emptyset_w - 2\emptyset_P + \emptyset_e}{(x_P')^2} - \frac{x_P''}{(x_P')^3}\frac{\emptyset_e - \emptyset_w}{2}\right\} \qquad (3.2.1)$$

Since $\Delta \xi = 1$ on the computational stencil, the Taylor series expansion of the finite difference portion of (3.2.1) leads to:

$$\begin{aligned}
\text{LTE}_{(P)} = &\frac{1}{(x_P')^2}\frac{\partial^2 \emptyset}{\partial \xi^2}\Big|_P - \frac{x_P''}{(x_P')^3}\frac{\partial \emptyset}{\partial \xi}\Big|_P - \Bigg\{\frac{1}{(x_P')^2}\Bigg[\left(\emptyset_P - \frac{\partial \emptyset}{\partial \xi}\Big|_P + \frac{1}{2!}\frac{\partial^2 \emptyset}{\partial \xi^2}\Big|_P - \frac{1}{3!}\frac{\partial^3 \emptyset}{\partial \xi^3}\Big|_P + \\
&\frac{1}{4!}\frac{\partial^4 \emptyset}{\partial \xi^4}\Big|_P + \cdots\right) - 2\emptyset_P + \left(\emptyset_P + \frac{\partial \emptyset}{\partial \xi}\Big|_P + \frac{1}{2!}\frac{\partial^2 \emptyset}{\partial \xi^2}\Big|_P + \frac{1}{3!}\frac{\partial^3 \emptyset}{\partial \xi^3}\Big|_P + \frac{1}{4!}\frac{\partial^4 \emptyset}{\partial \xi^4}\Big|_P + \cdots\right)\Bigg] - \\
&\frac{x_P''}{2(x_P')^3}\Bigg[\left(\emptyset_P + \frac{\partial \emptyset}{\partial \xi}\Big|_P + \frac{1}{2!}\frac{\partial^2 \emptyset}{\partial \xi^2}\Big|_P + \frac{1}{3!}\frac{\partial^3 \emptyset}{\partial \xi^3}\Big|_P + \frac{1}{4!}\frac{\partial^4 \emptyset}{\partial \xi^4}\Big|_P + \cdots\right) - \left(\emptyset_P - \frac{\partial \emptyset}{\partial \xi}\Big|_P + \\
&\frac{1}{2!}\frac{\partial^2 \emptyset}{\partial \xi^2}\Big|_P - \frac{1}{3!}\frac{\partial^3 \emptyset}{\partial \xi^3}\Big|_P + \frac{1}{4!}\frac{\partial^4 \emptyset}{\partial \xi^4}\Big|_P + \cdots\right)\Bigg]\Bigg\}
\end{aligned} \qquad (3.2.2)$$

The final expression for the LTE is obtained after some algebraic manipulation as:

$$\text{LTE}_P = -\frac{1}{12(x_P')^2}\frac{\partial^4 \emptyset}{\partial \xi^4}\Big|_P + \frac{x_P''}{6(x_P')^3}\frac{\partial^3 \emptyset}{\partial \xi^3}\Big|_P \qquad (3.2.3)$$

This procedure can be extended to construct the expression for the LTE for the $\eta -$ direction and, eventually, the LTE expression for the 2-D diffusion equation $v\left[\frac{\partial^2 \emptyset}{\partial x^2} + \frac{\partial^2 \emptyset}{\partial y^2}\right] = S(x, y)$ in the cut-stencil FD formulation is achieved. The LTE expression for 2nd-order accurate approximation of the 2-D diffusion equation in the cut-stencil FD formulation, at the central node P of a 5-point stencil, is:

$$\text{LTE}_P^{5-\text{pt stencil}} = v\left[\frac{-1}{12}\left(\frac{1}{(x_P')^2}\frac{\partial^4 \emptyset}{\partial \xi^4}\Big|_P + \frac{1}{(y_P')^2}\frac{\partial^4 \emptyset}{\partial \eta^4}\Big|_P\right) + \frac{1}{6}\left(\frac{x_P''}{(x_P')^3}\frac{\partial^3 \emptyset}{\partial \xi^3}\Big|_P + \frac{y_P''}{(y_P')^3}\frac{\partial^3 \emptyset}{\partial \eta^3}\Big|_P\right)\right] \qquad (3.2.4)$$

Similarly, the expression for calculation of the LTE for the 2-D convection-diffusion equation $\nu\nabla^2\emptyset + P\frac{\partial\emptyset}{\partial x} + Q\frac{\partial\emptyset}{\partial y} = S(x,y)$, which depends on whether central or backward/forward differencing is used for the convective terms, can be defined for the cut-stencil FDM. Using the parameters α and β defined in Section 2.4.2, which yield the backward, forward or central differencing of the convective terms, the LTE for the convection-diffusion equation can be written as:

$$\text{LTE}_{\text{P}}^{5-\text{pt stencil}} = \nu\left[\frac{-1}{12}\left(\frac{1}{(x_{\text{P}}')^2}\frac{\partial^4\emptyset}{\partial\xi^4}\Big|_{\text{P}} + \frac{1}{(y_{\text{P}}')^2}\frac{\partial^4\emptyset}{\partial\eta^4}\Big|_{\text{P}}\right) + \frac{1}{6}\left(\frac{x_{\text{P}}''}{(x_{\text{P}}')^3}\frac{\partial^3\emptyset}{\partial\xi^3}\Big|_{\text{P}} + \right.\right.$$
$$\left.\left.\frac{y_{\text{P}}''}{(y_{\text{P}}')^3}\frac{\partial^3\emptyset}{\partial\eta^3}\Big|_{\text{P}}\right)\right] - \left[\frac{1}{6}\left(\frac{P}{x_{\text{P}}'}\frac{\partial^3\emptyset}{\partial\xi^3}\Big|_{\text{P}} + \frac{Q}{y_{\text{P}}'}\frac{\partial^3\emptyset}{\partial\eta^3}\Big|_{\text{P}}\right)\right] \qquad \text{(central)}$$

(3.2.5.1)

$$\text{LTE}_{\text{P}}^{5-\text{pt stencil}} = \nu\left[\frac{-1}{12}\left(\frac{1}{(x_{\text{P}}')^2}\frac{\partial^4\emptyset}{\partial\xi^4}\Big|_{\text{P}} + \frac{1}{(y_{\text{P}}')^2}\frac{\partial^4\emptyset}{\partial\eta^4}\Big|_{\text{P}}\right) + \frac{1}{6}\left(\frac{x_{\text{P}}''}{(x_{\text{P}}')^3}\frac{\partial^3\emptyset}{\partial\xi^3}\Big|_{\text{P}} + \right.\right.$$
$$\left.\left.\frac{y_{\text{P}}''}{(y_{\text{P}}')^3}\frac{\partial^3\emptyset}{\partial\eta^3}\Big|_{\text{P}}\right)\right] + \left[\frac{1}{2}\left(\frac{P\alpha}{x_{\text{P}}'}\frac{\partial^2\emptyset}{\partial\xi^2}\Big|_{\text{P}} + \frac{Q\beta}{y_{\text{P}}'}\frac{\partial^2\emptyset}{\partial\eta^2}\Big|_{\text{P}}\right)\right] \text{(backward: } \alpha = \beta = 1, \text{ forward: } \alpha = \beta = -1\text{)}$$

(3.2.5.2)

Expressions for the LTE can also be derived for other formulations of the cut-stencil FDM such as the 5+4-point (4 fictitious nodes) stencil, HO-FDM1 and HO-FDM2.

For the 5+4-point stencil formulation, the general approach outlined above is used, noting that in this formulation $\Delta\xi$ and $\Delta\eta$ are both equal to 0.5. Using equations (2.24.1) and (2.24.2), the TFD expressions for the LTE for the 4$^{\text{th}}$-order accurate approximations of $\frac{\partial^2\emptyset}{\partial x^2}$ and $\frac{\partial\emptyset}{\partial x}$ at point (i), in which $\emptyset$ is assumed as a 1-D function, are respectively:

$$\text{LTE}_{(i)} = \frac{(\Delta x)^4}{90}\frac{\partial^6\emptyset}{\partial x^6}\Big|_{(i)} \qquad (3.3.1)$$

$$\text{LTE}_{(i)} = \frac{(\Delta x)^4}{30}\frac{\partial^5\emptyset}{\partial x^5}\Big|_{(i)} \qquad (3.3.2)$$

On the computational stencil, the difference between the continuous and discrete representation for the Laplacian $\nabla^2\emptyset$ and for the LTE, using the 5+4-point stencil formulation, are:

$$\text{LTE}_{(\text{P})} = \left[\frac{1}{(x_{\text{P}}')^2}\frac{\partial^2\emptyset}{\partial\xi^2}\Big|_{\text{P}} - \frac{x_{\text{P}}''}{(x_{\text{P}}')^3}\frac{\partial\emptyset}{\partial\xi}\Big|_{\text{P}} + \frac{1}{(y_{\text{P}}')^2}\frac{\partial^2\emptyset}{\partial\eta^2}\Big|_{\text{P}} - \frac{y_{\text{P}}''}{(y_{\text{P}}')^3}\frac{\partial\emptyset}{\partial\eta}\Big|_{\text{P}}\right] -$$
$$\left\{\left[\frac{1}{(x_{\text{P}}')^2}\left(\frac{-\emptyset_w + 16\emptyset_l - 30\emptyset_{\text{P}} + 16\emptyset_r - \emptyset_e}{3}\right) - \frac{x_{\text{P}}''}{(x_{\text{P}}')^3}\left(\frac{\emptyset_w - 8\emptyset_l + 8\emptyset_r - \emptyset_e}{6}\right)\right] + \right.$$
$$\left. + \frac{1}{(y_{\text{P}}')^2}\left(\frac{-\emptyset_s + 16\emptyset_b - 30\emptyset_{\text{P}} + 16\emptyset_a - \emptyset_n}{3}\right) - \frac{y_{\text{P}}''}{(y_{\text{P}}')^3}\left(\frac{\emptyset_s - 8\emptyset_b + 8\emptyset_a - \emptyset_n}{6}\right)\right\}$$

(3.4.1)

$$\text{LTE}_{\text{P}}^{5+4-\text{pt stencil}} = \left[\frac{1}{1440}\left(\frac{1}{(x_{\text{P}}')^2}\frac{\partial^6\emptyset}{\partial\xi^6}\Big|_{\text{P}} + \frac{1}{(y_{\text{P}}')^2}\frac{\partial^6\emptyset}{\partial\eta^6}\Big|_{\text{P}}\right) - \frac{1}{480}\left(\frac{x_{\text{P}}''}{(x_{\text{P}}')^3}\frac{\partial^5\emptyset}{\partial\xi^5}\Big|_{\text{P}} + \right.\right.$$
$$\left.\left.\frac{y_{\text{P}}''}{(y_{\text{P}}')^3}\frac{\partial^5\emptyset}{\partial\eta^5}\Big|_{\text{P}}\right)\right]$$

(3.4.2)

The LTEs for the higher-order methods introduced in Chapter 2, HO-FDM1 and HO-FDM2, are developed using the same definitions and procedures as above. As mentioned in Chapter 2, the LTE expressions of each of the compact differencing schemes for the first and second derivatives can be derived by inserting the coefficients of each method into the last column of the corresponding Taylor tables, i.e. Tables 2.4 and 2.5. This mathematical manipulation, for example

in the last column of Table 2.4, leads to the LTE for the compact 4th-order accurate approximation of the first derivative of a 1-D function ϕ as $\frac{1}{120}(\Delta x)^4 \frac{\partial^5 \phi}{\partial x^5}$, as found in the literature [76].

The general expression for the LTE in the cut-stencil FD formulation HO-FDM1 for the 2-D Laplacian is given by (cf., equation (2.41)):

$$
\begin{aligned}
\text{LTE}_{(P)} = \nu \Bigg\{ &\left[\frac{1}{(x'_P)^2} \frac{\partial^2 \phi}{\partial \xi^2} \Big|_P - \frac{x''_P}{(x'_P)^3} \frac{\partial \phi}{\partial \xi} \Big|_P + \frac{1}{(y'_P)^2} \frac{\partial^2 \phi}{\partial \eta^2} \Big|_P - \frac{y''_P}{(y'_P)^3} \frac{\partial \phi}{\partial \eta} \Big|_P \right] - \\
&\left[\frac{1}{(x'_P)^2} \left(\frac{6\phi_w - 12\phi_P + 6\phi_e}{5} - \frac{1}{10}\left(\frac{\partial^2 \phi}{\partial \xi^2} \Big|_w + \frac{\partial^2 \phi}{\partial \xi^2} \Big|_e \right) \right) - \frac{x''_P}{(x'_P)^3} \left(\frac{3\phi_e - 3\phi_w}{4} - \right. \right. \\
&\left. \frac{1}{4}\left(\frac{\partial \phi}{\partial \xi} \Big|_w + \frac{\partial \phi}{\partial \xi} \Big|_e \right) \right) + \frac{1}{(y'_P)^2} \left(\frac{6\phi_s - 12\phi_P + 6\phi_n}{5} - \frac{1}{10}\left(\frac{\partial^2 \phi}{\partial \eta^2} \Big|_s + \frac{\partial^2 \phi}{\partial \eta^2} \Big|_n \right) \right) - \\
&\left. \left. \frac{y''_P}{(y'_P)^3} \left(\frac{3\phi_n - 3\phi_s}{4} - \frac{1}{4}\left(\frac{\partial \phi}{\partial \xi} \Big|_s + \frac{\partial \phi}{\partial \xi} \Big|_n \right) \right) \right] \right\}
\end{aligned}
\tag{3.5}
$$

Additional convective terms can be added to this equation and rearranging the mathematical expression resulting from the Taylor series expansions yields the LTE for the 4th-order accurate approximation of the derivatives in the mapped form of the 2-D convection-diffusion equation using HO-FDM1:

$$
\begin{aligned}
\text{LTE}_P^{\text{HO-FDM1}} = \nu \Bigg[&\frac{1}{200}\left(\frac{1}{(x'_P)^2} \frac{\partial^6 \phi}{\partial \xi^6} \Big|_P + \frac{1}{(y'_P)^2} \frac{\partial^6 \phi}{\partial \eta^6} \Big|_P \right) - \frac{1}{120}\left(\frac{x''_P}{(x'_P)^3} \frac{\partial^5 \phi}{\partial \xi^5} \Big|_P + \right. \\
&\left. \frac{y''_P}{(y'_P)^3} \frac{\partial^5 \phi}{\partial \eta^5} \Big|_P \right) \Bigg] + \frac{1}{120}\left(\frac{P}{x'_P} \frac{\partial^5 \phi}{\partial \xi^5} \Big|_P + \frac{Q}{y'_P} \frac{\partial^5 \phi}{\partial \eta^5} \Big|_P \right) \quad \text{(central)}
\end{aligned}
\tag{3.6.1}
$$

$$
\begin{aligned}
\text{LTE}_P^{\text{HO-FDM1}} = \nu \Bigg[&\frac{1}{200}\left(\frac{1}{(x'_P)^2} \frac{\partial^6 \phi}{\partial \xi^6} \Big|_P + \frac{1}{(y'_P)^2} \frac{\partial^6 \phi}{\partial \eta^6} \Big|_P \right) - \frac{1}{120}\left(\frac{x''_P}{(x'_P)^3} \frac{\partial^5 \phi}{\partial \xi^5} \Big|_P + \right. \\
&\left. \frac{y''_P}{(y'_P)^3} \frac{\partial^5 \phi}{\partial \eta^5} \Big|_P \right) \Bigg] + \frac{1}{6}\left(\frac{P}{x'_P} \frac{\partial^3 \phi}{\partial \xi^3} \Big|_P + \frac{Q}{y'_P} \frac{\partial^3 \phi}{\partial \eta^3} \Big|_P \right) \quad \text{(upwind)}
\end{aligned}
\tag{3.6.2}
$$

The LTE expression for the HO-FDM2 formulation uses the left hand side of equation (2.42). Since the only difference between the cut-stencil methods HO-FDM1 and HO-FDM2 is related to the finite difference approximation of second derivatives, the first derivative approximations used for equation (3.5.1) remain unchanged in the corresponding HO-FDM2 equation. Thus, to construct the LTE expression for the 2-D convection-diffusion equation using HO-FDM2, it can be shown that only the coefficient $\frac{1}{200}$ in equations (3.6.1) and (3.6.2) should be replaced by $\frac{1}{360}$.

3.3.1 Temporal Local Truncation Error for FTCS Formulation

The previous derivations for the LTE considered only steady formulations and consequently discussed only the spatial LTE. For unsteady formulations, the LTE depends upon both the spatial and temporal discretizations. The temporal truncation error has been employed in numerical studies for different purposes, such as adaptive time-stepping by controlling the temporal truncation error [125]. The main time-dependent cut-stencil FD formulation in Chapter 2 dealt with the unsteady diffusion equation and its FTCS discretization.

The time derivative in FTCS is approximated by 1st-order accuracy, so the error should be truncated at the term which is $O(\Delta t)$. The basic definition used for the spatial LTE is also applied for the temporal LTE, i.e.,

$$\text{LTE}_P^n = \frac{\partial \emptyset_P^n}{\partial t} - \left\{ \frac{\emptyset_P^{n+1} - \emptyset_P^n}{(\Delta t)} \right\} \tag{3.7.1}$$

Using the Taylor series about t_n in equation (3.7.1) gives the final expression for the temporal LTE for the unsteady diffusion equation:

$$\text{LTE}_P^n = -\frac{(\Delta t)}{2} \frac{\partial^2 \emptyset_P^n}{\partial t^2} \tag{3.7.2}$$

The total LTE for the unsteady diffusion equation is the sum of the spatial LTE (3.2.4) and the temporal LTE (3.7.2). Similar results are obtained for the unsteady convection-diffusion equation.

3.3.2   Procedure for Calculation of Spatial Local Truncation Error (LTE)

As shown in equations (3.2.4), (3.2.5.1), (3.2.5.2), (3.4.2), (3.6.1) and (3.6.2), there are second, third, fourth, fifth and sixth derivatives in the expressions for the LTE depending on the particular cut-stencil formulation used. The flexibility and simplicity of the localized treatment of each 5-point physical stencil in the Cartesian cut-stencil FDM give the facility to calculate these higher-order derivatives. One of the main factors to construct all the equations in this research is an attempt to define and construct the basic form of all FD approximations within a 5-point stencil. This feature avoids any problems in dealing with the nodes located near the boundaries. The procedure for calculation of derivatives in the LTE expressions is organized as described in the following.

At first, after completion of the solution algorithm, the value at each node is used to approximate the second derivative at all nodes in the domain including all active nodes and boundary nodes which have a Neumann condition, using central or one-sided forward/backward 2nd-order accurate differencing schemes for internal or boundary nodes, respectively. Then, similarly, 2nd-order differencing formulas are applied to approximate the third through sixth derivatives for all nodes from the values of the second derivative.

This procedure for evaluation of the terms in the LTE can be conveniently described by introducing difference operators as approximations to differential operators. In general, the differential operator representing the kth-derivative with respect to ξ, $\partial_{k\xi}\big|_P$, is approximated to 2nd-order accuracy by the difference operator $\delta_{k\xi,P}^c$, i.e., $\partial_{k\xi}\big|_P = \delta_{k\xi,P}^c + O(\Delta \xi^2)$, where the superscript c denotes 3-point central differencing, the subscript $k\xi$ refers to the order of derivative in the ξ − direction and the operator is applied at point P. A similar expression can be written for differentiation with respect to η, simply by replacing ξ with η. Further, when the difference operator operates on a function $\emptyset(\xi, \eta)$ at a point P, we use the notation $\delta_{k\xi,P}^c \emptyset = \emptyset_P^{(k\xi)}$. Then, all higher-order differences can be expressed in terms of the 2nd-order difference. For example, $\delta_{3\xi,P}^c \emptyset = \delta_{1\xi,P}^c \emptyset_P^{(2\xi)}$, $\delta_{4\xi,P}^c \emptyset = \delta_{2\xi,P}^c \emptyset_P^{(2\xi)}$, $\delta_{5\xi,P}^c \emptyset = \delta_{1\xi,P}^c \emptyset_P^{(4\xi)} = \delta_{1\xi,P}^c (\delta_{2\xi,P}^c \emptyset_P^{(2\xi)})$, etc. Denoting the identity operator by $\delta_{0\xi,P}^c$, these differences can be computed recursively as follows:

$$\partial_{k\xi}\big|_{\mathrm{P}} \approx \delta^{c}_{k\xi,\mathrm{P}} = \begin{cases} \delta^{c}_{1\xi,\mathrm{P}}\big(\delta^{c}_{(k-1)\xi,\mathrm{P}}\big), & \text{if } k \text{ is odd} \\ \delta^{c}_{2\xi,\mathrm{P}}\big(\delta^{c}_{(k-2)\xi,\mathrm{P}}\big), & \text{if } k \text{ is even} \end{cases} \tag{3.8.1}$$

Using (3.8.1), the various formulas for the LTE derived above can be expressed in their finite difference form. For example, for the 2$^{\text{nd}}$-order 5-point cut-stencil LTE, equation (3.2.4) at any internal point P can be written as:

$$\mathrm{LTE}^{\mathbf{5-point\ stencil}}_{\mathrm{P}} \approx$$

$$\nu\left\{\frac{-1}{12}\left[\frac{1}{(x'_{\mathrm{P}})^2}\big(\delta^{c}_{4\xi,\mathrm{P}}\emptyset_{\mathrm{P}}\big) + \frac{1}{(y'_{\mathrm{P}})^2}\big(\delta^{c}_{4\eta,\mathrm{P}}\emptyset_{\mathrm{P}}\big)\right] + \right.$$

$$\frac{1}{6}\left[\frac{x''_{\mathrm{P}}}{(x'_{\mathrm{P}})^3}\big(\delta^{c}_{3\xi,\mathrm{P}}\emptyset_{\mathrm{P}}\big) + \frac{y''_{\mathrm{P}}}{(y'_{\mathrm{P}})^3}\big(\delta^{c}_{3\eta,\mathrm{P}}\emptyset_{\mathrm{P}}\big)\right]\right\} \approx \nu\left\{\frac{-1}{12}\left[\frac{1}{(x'_{\mathrm{P}})^2}\big(\delta^{c}_{2\xi,\mathrm{P}}\emptyset^{(2\xi)}_{\mathrm{P}}\big) + \right.\right. \tag{3.8.2}$$

$$\left.\left.\frac{1}{(y'_{\mathrm{P}})^2}\big(\delta^{c}_{2\eta,\mathrm{P}}\emptyset^{(2\eta)}_{\mathrm{P}}\big)\right] + \frac{1}{6}\left[\frac{x''_{\mathrm{P}}}{(x'_{\mathrm{P}})^3}\big(\delta^{c}_{1\xi,\mathrm{P}}\emptyset^{(2\xi)}_{\mathrm{P}}\big) + \frac{y''_{\mathrm{P}}}{(y'_{\mathrm{P}})^3}\big(\delta^{c}_{1\eta,\mathrm{P}}\emptyset^{(2\eta)}_{\mathrm{P}}\big)\right]\right\}$$

Expressions similar to equation (3.8.2) can be constructed to calculate the value of the LTE for other formulations of the Cartesian cut-stencil FDM, and at Neumann boundary nodes if necessary, which shows the potential of this method in the calculation of complicated PDEs formulas in any arbitrary irregular shaped domain. The values and trends of the LTE will be studied for the solution of different sample problems in later chapters.

3.4   Verification of Formal Accuracy of the Numerical Scheme

Computational efforts to find the numerical solution of PDEs in all fields of engineering are normally associated with some sources of errors [126]. The determination of a formal or global order of accuracy compared to a local order of accuracy for the method used is an underlying challenge for any discretization scheme [127]. In other words, it must be considered how well the theoretical order of discretization matches with the actual order of accuracy from the numerical solution [128, 129]. So, examination of the "real" order of accuracy for schemes used to find the numerical solution of PDEs has been a topic of discussion in the literature. In most cases, systematic grid refinement along with root mean square (RMS) error are applied to observe the real order of accuracy for the numerical simulation [58, 69, 130, 131].

To develop a computational procedure for the real (formal or global) order of accuracy, it is assumed that the numerical solution and exact solution of the PDE(s) at arbitrary node P in the domain of interest are represented by $\emptyset_{num.}$ and $\emptyset_{exc.}$, respectively. The difference between these two solutions gives the error $\mathrm{e} = \emptyset_{exc.} - \emptyset_{num.}$. Referring to the concept of truncation error reveals that for finite differencing on a mesh of constant spacing $\hbar$, the error term $\mathrm{e} \propto \hbar^{q}$, where q means the order of the leading term of the truncation error. Then, the RMS error for a grid of M nodes is defined as [130, 132]:

$$\mathrm{RMS} = \sqrt{\frac{\sum_{i=1}^{M}\mathrm{e}^2}{M}} \tag{3.9.1}$$

The proportional relation between the error e, the mesh size $\hbar$ and the order of the leading term of the truncation error implies that equation (3.9.1) can be written as RMS $\propto \hbar^{q}$. The definition of

error e and RMS error can be applied for two successively refined meshes, where the mesh size of the coarse and fine mesh and the factor of refinement are introduced by $\hbar_c$, $\hbar_f$ and $r = \hbar_c/\hbar_f$. One can write the ratio of RMS errors for coarse and fine mesh as $\frac{\text{RMS}_c}{\text{RMS}_f} = (\frac{\hbar_c}{\hbar_f})^q$. Then, taking the natural log on both sides, this equality gives the order of accuracy of the numerical solution for these two levels of grids [109, 116, 129, 130, 131, 133]. The slope of the line plotted from $\log(\text{RMS})$ versus $\log(\hbar)$ for a series of successive refinements reveals the formal order of accuracy q that has been used in numerical analysis to observe the global order of accuracy for the chosen discretization method [130, 131, 132], i.e.,

$$q = \frac{\log\left(\frac{\text{RMS}_c}{\text{RMS}_f}\right)}{\log\left(\frac{\hbar_c}{\hbar_f}\right)} \tag{3.9.2}$$

3.5   Cut-Stencil FDM Solution to Sample Problems Using MMS

The remaining sections of this chapter are devoted to the Cartesian cut-stencil FD solution of several sample problems using MMS. The rationale for selecting the specific sample problems is to evaluate various aspects of the cut-stencil FD method in the solution of PDEs, including the level of accuracy and potential for future applications. The list of all problems considered in this chapter is provided in Appendix I.

3.5.1   Problem 1: Solution of Poisson Equation on a Square Domain with Dirichlet Boundary Conditions Using the 2nd-Order 5-point Cut-Stencil Formulation

The purpose of this first problem is to validate the basic concept of the Cartesian cut-stencil method, without introducing the complexities associated with an irregular domain, Neumann boundary conditions, higher-order accuracy or convection effects. Problem 1 considers the 5-point stencil solution of the manufactured Poisson equation, given in equation (3.10.1), on a square domain $0 \le x, y \le 1.0$. The exact solution of this problem is written in equation (3.10.2).

$$\nabla^2 \emptyset = -\left[2 + \frac{\pi^2}{4}x(1-x)\right] \cos\left(\frac{\pi}{2}y\right) \tag{3.10.1}$$

$$\emptyset_{exc.} = x(1-x) \cos\left(\frac{\pi}{2}y\right) \tag{3.10.2}$$

Several uniform grids with different number of nodes varying from 25 to 4225 have been used for comparison of the results from the 2nd-order 5-point stencil formulation, based on equation (2.9) and coefficients given in (2.10), with the exact solution. Dirichlet boundary conditions for this problem are taken from the exact solution.

The average and maximum values of the relative errors, the maximum of the absolute values of LTE and the RMS error for each mesh studied are reported in Table 3.1. Equation (3.2.4) was used to calculate the LTE at every internal node for each grid size. The mapped form of equation (3.10.1) was discretized and solved iteratively at all internal nodes P and the solution was regarded as converged when the absolute difference between two successive iterations fell below 10^{-12} at all internal nodes.

# of nodes	Mesh size (h)	Rel. error (%) Avg.	Rel. error (%) Max.	Max |LTE|	RMS error
25	0.250	0.17472	0.21425	5.525E-3	1.43E-4
36	0.200	0.10927	0.13716	3.896E-3	9.54E-5
81	0.125	0.04120	0.05432	1.817E-3	3.97E-5
121	0.100	0.02605	0.03481	1.200E-3	2.60E-5
289	0.0625	0.00999	0.01362	4.847E-4	1.05E-5
441	0.050	0.00636	0.00872	3.126E-4	6.80E-6
1089	0.03125	0.00246	0.00340	1.232E-4	2.70E-6
1681	0.025	0.00156	0.00216	7.899E-5	1.73E-6
4225	0.015625	0.00052	0.00071	3.092E-5	5.96E-7

Table 3.1: Relative error, LTE and RMS results for Problem 1

It is clear from the data in Table 3.1 that the average and maximum relative errors are reduced monotonically as the number of nodes is increased. The maximum values of |LTE| and RMS error follow the same trend. Figure 3.1 shows the plot of log(RMS) versus the $\log(h)$ for all cases in Table 3.1. The slope of the line in this figure verifies that the 2nd-order 5-point formulation has close to real 2nd-order accuracy for the cut-stencil FD solution to PDE (3.10.1).
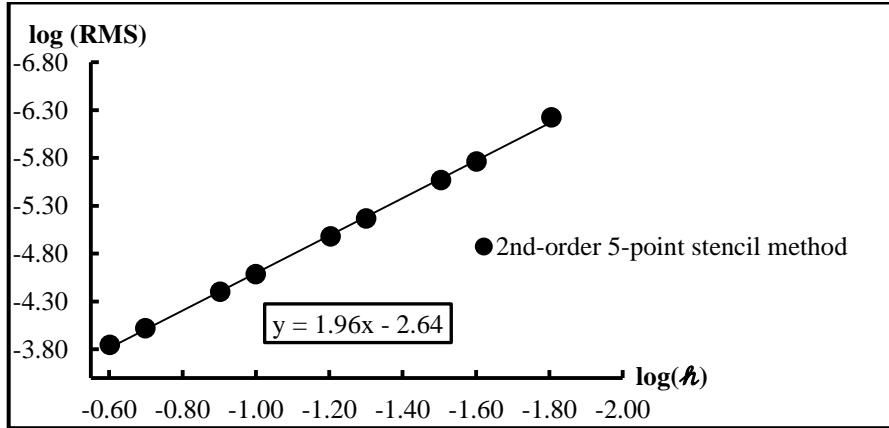
Figure 3.1: Verification plot for global order of accuracy for Problem 1

3.5.2 Problem 2: Solution of Poisson Equation on a Square Domain a with Neumann Boundary Condition Using the 2nd-Order 5-point Cut-Stencil Formulation

This problem considers another Poisson equation on the same domain used in Problem 1, but with Neumann boundary conditions taken from the exact solution. The designed Poisson equation and corresponding exact solution for this problem are, respectively,

$$\nabla^2 \emptyset = \frac{\pi^2}{4}(1-x)e^{\frac{\pi}{2}y} - 2\pi y \cos(\pi xy) - \pi^2[x^2 + y^2]\sin(\pi xy)(1-x) \qquad (3.11.1)$$

$$\emptyset_{exc.} = \left[e^{\frac{\pi}{2}y} + \sin(\pi xy) - 1\right](1-x) \qquad (3.11.2)$$

The Neumann condition is applied on the west boundary of the domain, that is, the line $x = 0$. Several uniform grids from 36 to 40401 nodes are used to consider average and maximum values of the relative errors for internal nodes as well as for the boundary nodes located on the west boundary. The results are given in Table 3.2. The RMS error and maximum |LTE| for each grid

are also available in the same table. The iterative procedure satisfied the convergence criterion when the absolute difference between the numerical values at each internal node from two successive iterations fell below 10^{-12}.

The study of relative errors for both internal and boundary nodes reveals the decreasing trend of all the error measures as the grid is refined.

On the computational stencil, the normal derivative $\frac{-1}{x_W'}\frac{\partial \emptyset}{\partial \xi}$ in the Neumann boundary condition on the west boundary is approximated by the one-sided 2nd-order accurate approximation given in equation (2.14.1). The unknown values at Neumann boundary nodes are calculated by equation (2.14.2).

# of nodes	Mesh size ($\hbar$)	Rel. error at internal nodes (%)		Rel. error at boundary nodes (%)		Max |LTE|	RMS error
		Avg.	Max.	Avg.	Max.		
36	0.200	1.10267	1.80647	1.70934	2.11168	1.792E-1	1.00E-2
81	0.125	0.50360	0.99674	0.86532	1.11474	1.248E-1	5.00E-3
121	0.100	0.33774	0.71200	0.59416	0.78114	9.319E-2	3.40E-3
289	0.0625	0.14100	0.32606	0.25466	0.34638	4.472E-2	1.43E-3
441	0.050	0.09216	0.21965	0.16756	0.23066	3.072E-2	9.37E-4
1089	0.03125	0.03712	0.09246	0.06804	0.09537	1.380E-2	3.78E-4
1681	0.025	0.02399	0.06062	0.04407	0.06215	9.499E-3	2.44E-4
4225	0.015625	0.00947	0.02443	0.01747	0.02481	4.458E-3	9.65E-5
6561	0.0125	0.00601	0.01561	0.01115	0.01580	3.169E-3	6.16E-5
10201	0.010	0.00367	0.00956	0.00693	0.00966	2.281E-3	3.84E-5
15876	0.008	0.00190	0.00492	0.00388	0.00496	1.662E-3	2.19E-5
25921	0.00625	0.00154	0.00407	0.00285	0.00409	1.187E-3	1.57E-5
40401	0.005	0.00071	0.00184	0.00148	0.00185	8.866E-4	8.36E-6

Table 3.2: Relative error and LTE results for Problem 2 (west Neumann boundary condition)

Figure 3.2 illustrates the real order of accuracy analysis for the PDE (3.11.1) with Neumann condition defined for the west boundary. The slope of the line in Figure 3.2 indicates almost 2nd-order of accuracy for the global order of accuracy for this problem, confirming that the approximation scheme proposed for the Neumann boundary condition does not degrade the global order of accuracy.
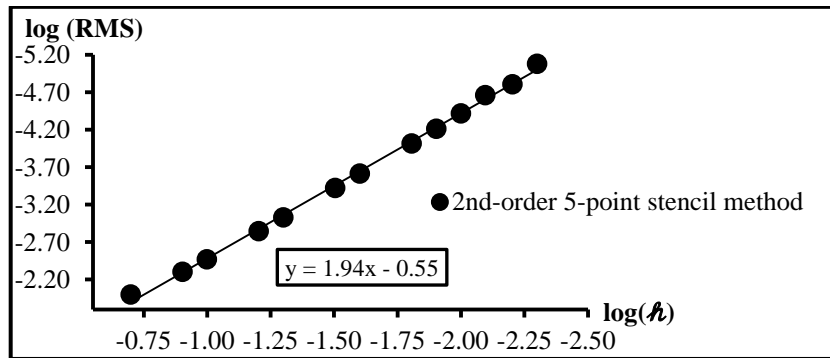
Figure 3.2: Verification plot for global order of accuracy for Problem 2 (west Neumann condition)

This problem is also studied when a Neumann condition is applied to the north boundary, which is the line $y = 1$. Using the same uniform grids as used for the west Neumann condition, the accuracy of the cut-stencil FDM solution is assessed by comparison to the exact solution, as well as verification of the global order of accuracy for this boundary condition. The Neumann condition on the computational stencil contains the derivative $\frac{1}{y'_N}\frac{\partial \emptyset}{\partial \eta}$ which is approximated by the one-sided 2nd-order accurate approximation (2.16.1). The unknown at boundary nodes in this condition are calculated by equation (2.16.2). Similar to Table 3.2, the average and maximum absolute error for internal and Neumann boundary nodes are given in Table 3.3, which also reports the maximum |LTE| error for the north Neumann condition of this problem.

# of nodes	Mesh size ($\hbar$)	Rel. error at internal nodes (%)		Rel. error at boundary nodes (%)		Max |LTE|	RMS error
		Avg.	Max.	Avg.	Max.		
36	0.200	1.79278	2.57979	2.30457	3.15756	1.644E-1	2.05E-2
81	0.125	0.70872	1.12180	0.93710	1.37625	1.130E-1	8.28E-3
121	0.100	0.45575	0.74638	0.60613	0.90162	8.239E-2	5.35E-3
289	0.0625	0.17972	0.31185	0.24052	0.36065	3.921E-2	2.12E-3
441	0.050	0.11549	0.20491	0.15482	0.23208	2.737E-2	1.36E-3
1089	0.03125	0.04544	0.08386	0.06106	0.09129	1.211E-2	5.37E-4
1681	0.025	0.02916	0.05467	0.03922	0.05855	8.102E-3	3.44E-4
4225	0.015625	0.01144	0.02199	0.01541	0.02298	3.444E-3	1.35E-4
6561	0.0125	0.00733	0.01422	0.00988	0.01474	2.298E-3	8.66E-5
10201	0.010	0.00470	0.00918	0.00633	0.00945	1.540E-3	5.55E-5
15876	0.008	0.00300	0.00591	0.00406	0.00605	1.037E-3	3.55E-5
25921	0.00625	0.00184	0.00364	0.00248	0.00371	6.760E-4	2.17E-5
40401	0.005	0.00089	0.00199	0.00141	0.00202	4.632E-4	1.19E-5

Table 3.3: Relative error and LTE results for Problem 2 (north Neumann boundary condition)

The trend of the variation of relative error and LTE in Table 3.3 shows monotonic reduction of these errors as the grid becomes finer. The slope of the line in Figure 3.3 indicates the 2nd-order accurate approximation for this condition, suggesting that the proposed differencing for a Neumann condition on the north boundary retains the global order of solution as 2nd-order accurate.
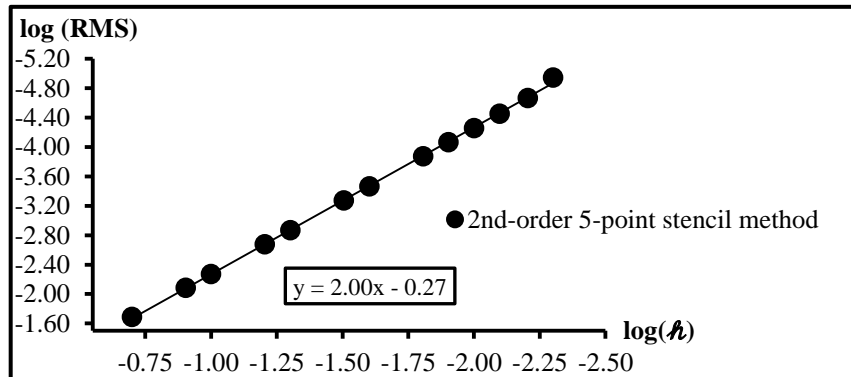
Figure 3.3: Verification plot for global order of accuracy for Problem 2 (north Neumann condition)

3.5.3 Problem 3: Solution of Poisson Equation on a Square Domain with Combination of Neumann Conditions on More Than One Boundary Using 2nd-Order 5-point Cut-Stencil Formulation

This problem examines the level of solution accuracy for a Poisson equation, solved by the cut-stencil FDM when Neumann conditions are imposed on two boundaries of the domain. In this problem, similar to the previous problems, the 2nd-order 5-point cut-stencil formulation is used to solve the discrete form (2.9) and (2.10) of the mapped equations. The domain is a unit square. The manufactured Poisson equation and exact solution for Problem 3 are, respectively:

$$\nabla^2 \emptyset = 2e^{(x+y)} + e^x[1 - 4\pi^2 y^2] \cos(\pi y^2) - 2\pi e^x \sin(\pi y^2) \qquad (3.12.1)$$

$$\emptyset_{exc.} = \left[e^{(x+y)} + e^x \cos(\pi y^2)\right] \qquad (3.12.2)$$

At first, the Neumann condition is defined for both west and east boundaries. The mapped form of the Neumann condition at each node on the west and east boundaries involve the derivatives $\frac{-1}{x'_W} \frac{\partial \emptyset}{\partial \xi}$ and $\frac{1}{x'_E} \frac{\partial \emptyset}{\partial \xi}$, respectively, which are approximated by (2.14.1) and an analogous expression for the east boundary. The average and maximum of relative error for internal and Neumann boundary nodes, maximum |LTE| and the value of RMS error for a group of uniform grids, varying from 36 to 25921 nodes, are shown in Table 3.4.

# of nodes	Mesh size ($\hbar$)	Rel. error at internal nodes (%)		Rel. error at boundary nodes (%)		Max |LTE|	RMS error
		Avg.	Max.	Avg.	Max.		
36	0.200	4.37072	6.61387	4.46633	7.50956	3.700	1.38E-1
81	0.125	1.52419	2.64016	1.55552	2.86833	2.142	5.32E-2
121	0.100	0.94236	1.73628	0.96170	1.85995	1.458	3.41E-2
289	0.0625	0.35109	0.68212	0.35836	0.71372	6.098E-1	1.34E-2
441	0.050	0.22146	0.43812	0.22607	0.45460	3.983E-1	8.61E-3
1089	0.03125	0.08475	0.17281	0.08653	0.17698	1.610E-1	3.39E-3
1681	0.025	0.05389	0.11090	0.05502	0.11306	1.042E-1	2.17E-3
4225	0.015625	0.02085	0.04363	0.02129	0.04417	5.241E-2	8.52E-4
6561	0.0125	0.01330	0.02799	0.01359	0.02827	3.692E-2	5.46E-4
10201	0.010	0.00867	0.01794	0.00867	0.01809	2.540E-2	3.50E-4
15876	0.008	0.00542	0.01150	0.00554	0.01157	1.717E-2	2.24E-4
25921	0.00625	0.00331	0.00703	0.00338	0.00707	1.098E-2	1.37E-4

Table 3.4: Relative error and LTE results for Problem 3 (west & east Neumann boundary conditions)

The results summarized in Table 3.4 show a good level of accuracy since simulations with two Neumann conditions mean the presence of unknown values on the two boundaries, giving a maximum error of almost 6.6% on the coarsest (36 nodes) grid size. The reduction in average and maximum error and LTE at internal nodes and Neumann boundary nodes can be observed as the mesh becomes finer. This study also can show the accuracy of the proposed FD formulation for a Neumann condition imposed on the east boundary. Figure 3.4 plots the variation of RMS error versus cell size for PDE (3.12.1) with Neumann condition on the west and east. The slope of the

line in this figure verifies the 2nd-order accurate approximation of the proposed 5-point 2nd-order accurate cut-stencil FDM for this boundary value problem.
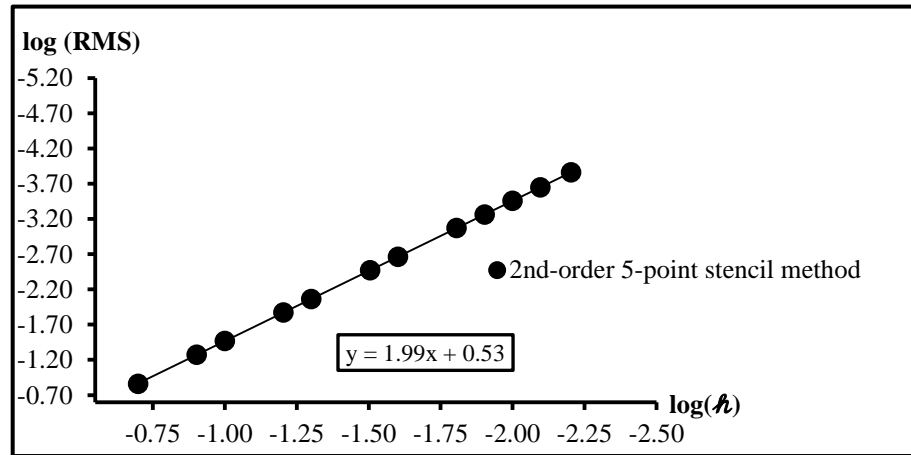
Figure 3.4: Verification plot for global order of accuracy for Problem 3 (west and east Neumann condition)

Another combination of Neumann conditions, including imposed Neumann conditions on the west and south boundaries, for the Poisson equation (3.12.1) is further investigated. Similar to other studies, the average and maximum of the relative error at both internal and boundary nodes and LTE at internal nodes are given in Table 3.5 for this case. The maximum relative errors on the coarsest grid (36 nodes) are slightly higher compared to other cases but this appears to be due to the quality of mesh since these maxima on the second grid studied (81 nodes) are much closer to the values given in Table 3.4 for the same mesh.

# of nodes	Mesh size (h)	Rel. error at internal nodes (%)		Rel. error at boundary nodes (%)		Max |LTE|	RMS error
		Avg.	Max.	Avg.	Max.		
36	0.200	5.66892	9.09079	9.00580	11.53584	3.617	1.71E-1
81	0.125	1.75116	3.18228	2.58816	3.53430	2.088	5.43E-2
121	0.100	1.02614	1.96135	1.46737	2.12589	1.433	3.24E-2
289	0.0625	0.34718	0.73587	0.46577	0.77334	6.030E-1	1.13E-2
441	0.050	0.21103	0.46393	0.27570	0.48280	3.951E-1	7.00E-3
1089	0.03125	0.07599	0.17732	0.09474	0.18178	1.606E-1	2.59E-3
1681	0.025	0.04727	0.11279	0.05789	0.11506	1.040E-1	1.63E-3
4225	0.015625	0.01763	0.04351	0.02095	0.04406	5.165E-2	6.21E-4
6561	0.0125	0.01105	0.02763	0.01293	0.02791	3.640E-2	3.92E-4
10201	0.010	0.00682	0.01735	0.00777	0.01749	2.504E-2	2.44E-4
15876	0.008	0.00434	0.01111	0.00492	0.01118	1.694E-2	1.56E-4

Table 3.5: Relative error and LTE results for Problem 3 (west & south Neumann boundary conditions)

The solution of Problem 3, when Neumann conditions are imposed on both the west and south boundaries, is verified to be a 2nd-order accurate approximation as depicted by the slope of the line in Figure 3.5.
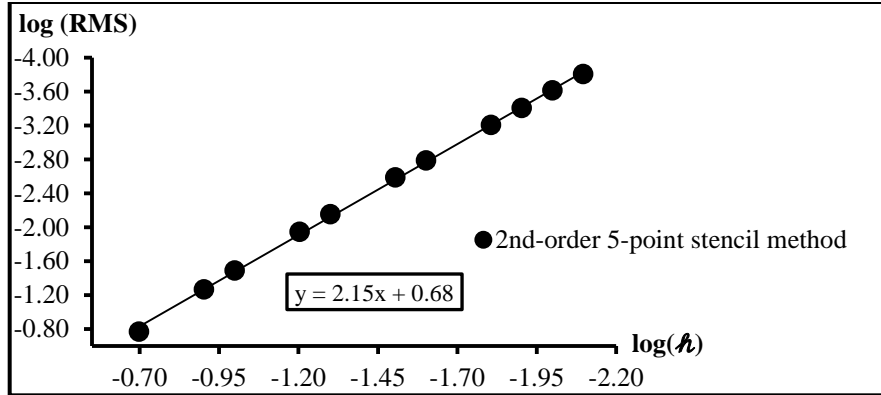
Figure 3.5: Verification plot for global order of accuracy for Problem 3 (west and south Neumann condition)

The variation of the maximum relative error for internal and boundary nodes for both combinations of Neumann boundaries studied in this problem (west-east & west-south) for different cell sizes ($\hbar$) is plotted in Figure 3.6. This plot shows that the level of error for each cell size and for each combination of Neumann condition is almost the same and the only difference between these two combinations occurs for the coarsest grids.
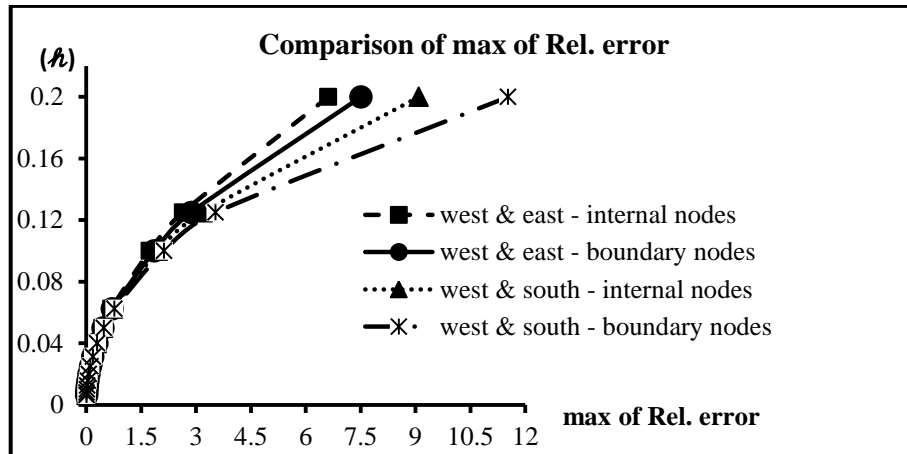
Figure 3.6: Variation of maximum relative error of internal and boundary nodes for different cell sizes (combination of Neumann boundary conditions)

The first three problems have considered the cut-stencil FD solution of the steady diffusion equation using 5-point 2nd-order accurate approximation to write the difference expression for the discretized form of the PDE. Neumann boundary conditions were imposed on different boundaries and the proposed cut-stencil FD formulation for each case was tested. The trends of relative error and LTE confirm mesh convergence to the correct solution.

3.5.4   Problem 4: Solution of Convection-Diffusion Equation on Rectangular Domain Using 2nd-Order 5-point Cut-Stencil Formulation

The Cartesian cut-stencil FD solution of a manufactured convection-diffusion equation which was formulated on the computational stencil in equation (2.9), is discussed in this problem. The convection coefficients P and Q are assumed as independent of the variables x and y. The

manufactured PDE and the exact solution are stated in equations (3.13.1) and (3.13.2). The rectangular domain $0 \leq x \leq 2, 0 \leq y \leq 1$ along with a set of uniform grids are defined to compute the cut-stencil FD solution to the PDE (3.13.1). The cell dimensions in this problem have different value in each direction, with constant aspect ratio 2:1. In the event of different grid spacing in each direction, e.g. $\hbar_x$ and $\hbar_y$, the cell size used to verify the real order of accuracy can be defined in terms of the sides of the rectangular cell and given by $\hbar_1 = \sqrt{\hbar_x \hbar_y}$, or expressed as the diagonal of the rectangular cell which is given by $\hbar_2 = \sqrt{\hbar_x^2 + \hbar_y^2}$ [133].

$$\nu \nabla^2 \emptyset + P \frac{\partial \emptyset}{\partial x} + Q \frac{\partial \emptyset}{\partial y} = \nu e^y + P \left[\frac{\pi}{5} \left(e^{\frac{\pi}{5}x} \cos(\frac{\pi}{5}y) - e^{\frac{\pi}{5}y} \sin(\frac{\pi}{5}x) \right) \right] +$$
$$Q \left[e^y + \frac{\pi}{5} \left(e^{\frac{\pi}{5}y} \cos(\frac{\pi}{5}x) - e^{\frac{\pi}{5}x} \sin(\frac{\pi}{5}y) \right) \right] \tag{3.13.1}$$

$$\emptyset_{exc.} = e^{\frac{\pi}{5}x} \cos\left(\frac{\pi}{5}y\right) + e^{\frac{\pi}{5}y} \cos\left(\frac{\pi}{5}x\right) + e^y \tag{3.13.2}$$

Table 3.6 gives the average and maximum of relative error and maximum |LTE| for the cut-stencil FD solution of equation (3.13.1) when $\nu = 1$ and $P = Q = 0.02$. These values were chosen to ensure the problem does not show convection-dominated behaviour and a diagonally dominant condition occurs [134]. In this case, divergence of the solution can be avoided when the central differencing scheme is applied for approximation of the convection terms to solve the PDE. The data in Table 3.6 are obtained from central difference approximation for both the diffusion and convection terms in equation (3.13.1), indicating that $\alpha = \beta = 0$ in equation (2.8) and therefore in the coefficients defined in equations (2.10). All boundary conditions for data reported in Table 3.6 are considered as Dirichlet, taken from the exact solution.

# of nodes	Mesh size		Rel. error (%)		Max	RMS
	$\hbar_x$	$\hbar_y$	Avg.	Max.	|LTE|	error
36	0.40	0.20	0.02355	0.03281	1.436E-2	7.36E-4
121	0.20	0.10	0.00515	0.00858	4.146E-3	2.07E-4
441	0.10	0.05	0.00119	0.00216	1.106E-3	5.46E-5
1681	0.05	0.025	0.00028	0.00054	2.856E-4	1.40E-5
6561	0.025	0.0125	0.00007	0.00013	7.265E-5	3.32E-6

Table 3.6: Relative error and LTE results for Problem 4 with Dirichlet boundary conditions
($\nu = 1$, $P = Q = 0.02$, $\alpha = \beta = 0$)

Equation (3.2.5.1) was used to calculate the LTE at internal nodes for the cases reported in Table 3.6. The real order of accuracy for this problem from the grids and RMS errors in Table 3.6 was investigated using both the sides and diagonal of rectangular cell definitions for the cell size. As seen in Figure 3.7, both cell size definitions give the same order of accuracy, verifying the 2nd-order accuracy for the proposed cut-stencil FD central differencing for diffusion and convection terms.
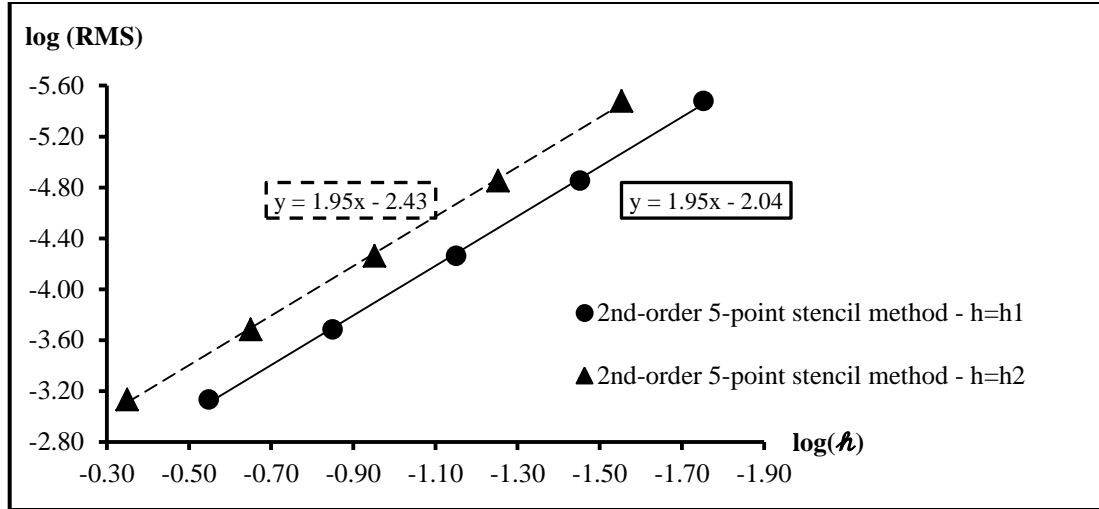
Figure 3.7: Verification plot for global order of accuracy for Problem 4, Dirichlet boundaries
$(\nu = 1, \ P = Q = 0.02, \ \alpha = \beta = 0)$

The PDE (3.13.1) was also solved with Neumann boundary conditions, taken from the exact solution, imposed on both the east and north boundaries. The diffusion and convection coefficients are the same as used for the Dirichlet boundary condition problem and central differencing was also applied for approximation of the convective terms. The same mesh sizes as indicated in Table 3.6 were used for this case. The average and maximum of relative errors for both internal nodes and Neumann boundary nodes and the maximum |LTE| for internal nodes, are recorded in Table 3.7.

# of nodes	Mesh size		Rel. error at internal nodes (%)		Rel. error at boundary nodes (%)		Max |LTE|	RMS error
	$\hbar_x$	$\hbar_y$	Avg.	Max.	Avg.	Max.		
36	0.4	0.2	0.54221	1.06456	0.93555	1.32602	1.501E-2	3.28E-2
121	0.2	0.1	0.13684	0.32096	0.23740	0.35740	4.294E-3	8.67E-3
441	0.1	0.05	0.03456	0.08816	0.06010	0.09302	1.392E-3	2.22E-3
1681	0.05	0.025	0.00870	0.02311	0.01515	0.02374	5.836E-4	5.59E-4
6561	0.025	0.0125	0.00218	0.00592	0.00381	0.00600	2.620E-4	1.40E-4

Table 3.7: Relative error and LTE results for Problem 4 with east and north Neumann boundary conditions $(\nu = 1, \ P = Q = 0.02, \ \alpha = \beta = 0)$

The real order of the solution for this case was considered using both definitions of the cell size $\hbar$, as shown by the slopes of the lines in Figure 3.8. This proves that the 2nd-order accurate approximation for the Neumann boundary nodes can preserve the real 2nd-order accuracy of the solution for the convection-diffusion equation.
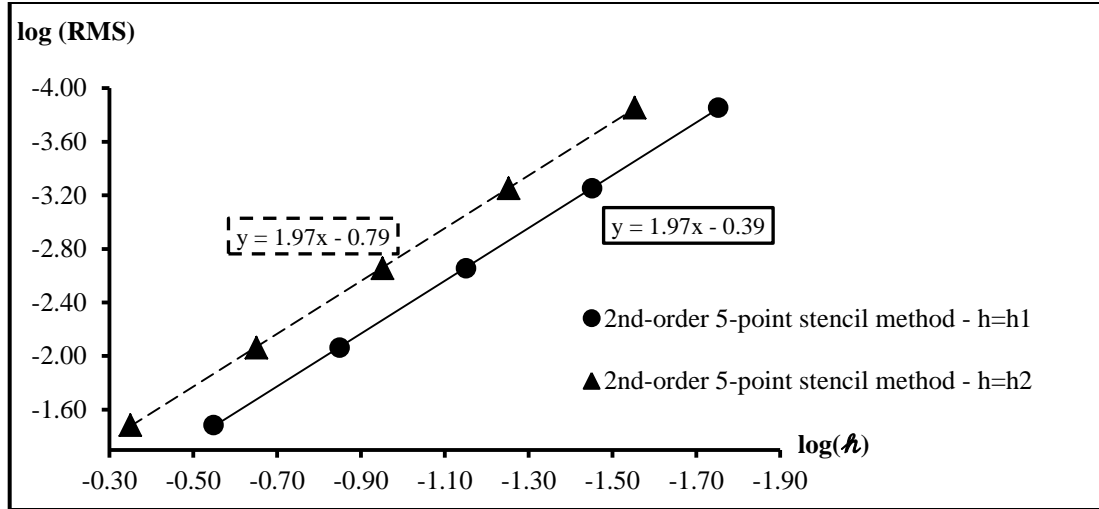
Figure 3.8: Verification plot for global order of accuracy for Problem 4, Neumann boundary conditions on east and north ($\nu = 1$, $P = Q = 0.02$, $\alpha = \beta = 0$)

The solution of PDE (3.13.1) using an upwind differencing scheme for the convection terms is now studied. The diffusion coefficient and convective velocities are set the same as those used for data in Table 3.6. To select upwind differencing for the convection terms the parameters α and β are both set equal to -1. In this event, the convection terms are approximated by 1st-order of accuracy while 2nd-order accurate approximations are used for the diffusion terms. Maximum and average relative error and maximum LTE are shown in Table 3.8, when the boundaries of the domain have Dirichlet conditions taken from the exact solution.

# of	Mesh size		Rel. error (%)		Max	RMS
nodes	h_x	h_y	Avg.	Max.	|LTE|	error
36	0.40	0.20	0.03027	0.04182	1.791E-2	9.48E-4
121	0.20	0.10	0.00810	0.01347	6.702E-3	3.26E-4
441	0.10	0.05	0.00255	0.00463	2.622E-3	1.18E-4
1681	0.05	0.025	0.00093	0.00178	1.108E-3	4.64E-5
6561	0.025	0.0125	0.00038	0.00075	5.011E-4	1.97E-5

Table 3.8: Relative error and LTE results for Problem 4 with Dirichlet boundary conditions ($\nu = 1$, $P = Q = 0.02$, $\alpha = \beta = -1$)

Comparison of the data in Tables 3.6 and 3.8 shows the reduction of accuracy when an upwind scheme is applied for differencing of convective terms, but the average values of the maximum relative error are still at an acceptable level of accuracy even for the coarsest mesh. The LTE, as given in Table 3.8, is calculated from equation (3.2.5.2). It can also be seen that, for each case, the maximum LTE is higher in Table 3.8 compared to the similar case of Table 3.6.

The real order of the method, based on the data in Table 3.8, can be observed in the plot of Figure 3.9. The slope of lines in this figure shows the reduction of order of accuracy, to 1.4th-order compared to almost 2nd-order (1.95th-order) of accuracy in Figure 3.7.
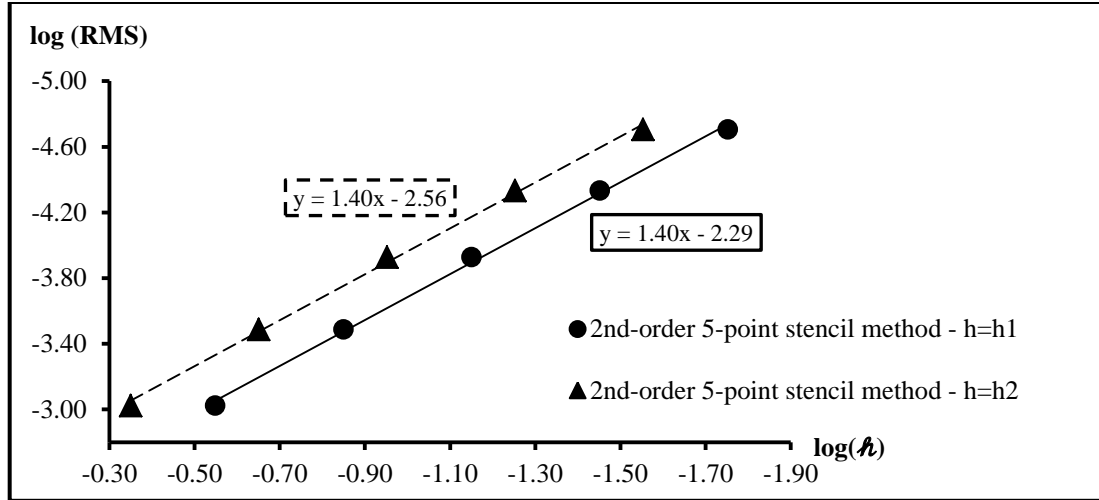
Figure 3.9: Verification plot for global order of accuracy for Problem 4, Dirichlet boundaries
($\nu = 1,\ P = Q = 0.02,\ \alpha = \beta = -1$)

The upwind discretization of the convection terms is applied for the cut-stencil FD solution of Problem 4 with a stronger convection-dominated condition. Thus, for this purpose, the diffusion coefficient is changed to $\nu = 0.08$ and the convective velocities are set to $P = Q = 1.0$. This case is solved with both central and upwind differencing of the convection terms, corresponding to $\alpha = \beta = 0$ and $\alpha = \beta = -1$, respectively, Results are listed in Table 3.9.

# of nodes	Mesh size		Rel. error (%)				Max |LTE|		RMS error	
			Central*		Upwind**					
	$\hbar_x$	$\hbar_y$	Avg.	Max.	Avg.	Max.	Central	Upwind	Central	Upwind
36	0.4	0.2	0.36293	0.89480	1.66534	2.54793	8.187E-2	2.078E-1	1.15E-2	5.11E-2
121	0.2	0.1	0.07366	0.15903	0.82823	1.54014	2.988E-2	1.308E-1	2.89E-3	3.20E-2
441	0.1	0.05	0.01558	0.03499	0.41161	0.84448	3.032E-3	7.432E-2	7.03E-4	1.80E-2
1681	0.05	0.025	0.00781	0.09251	0.20400	0.43797	1.454E-3	4.015E-2	5.58E-4	9.51E-3
6561	0.025	0.0125	0.03926	0.44697	0.08558	0.19686	2.439E-3	2.102E-2	3.16E-3	4.29E-3
*: $\alpha = \beta = 0$, **: $\alpha = \beta = -1$										

Table 3.9: Relative error and LTE results for Problem 4 with Dirichlet boundary conditions
($\nu = 0.08,\ P = Q = 1,\ \alpha = \beta = 0, -1$)

The upwind scheme in Table 3.9 shows higher values of maximum relative error compared to the central difference formulation for the first grid studied, but the grid of 6561 nodes produces a relatively higher value of maximum error when central differencing is applied. Additionally, examination of the results for the central scheme reveals oscillation in the solution, as has also been mentioned in the literature, e.g. [134]. It is clear from the solution with the central difference scheme, from the grid of 1681 nodes, that the maximum relative error increases as the mesh become finer. This kind of behaviour also occurs in the trend of the maximum LTE for the central difference scheme.

The real order of accuracy of this problem, from the upwind data in Table 3.9, can be observed in Figure 3.10. The more convection-dominated behaviour of the problem and the use of a 1st-order accurate approximation for the convection terms provide a solution with less than 1st-order

accuracy, as shown by the slopes of the lines. This condition of accuracy less than unity has been addressed in other numerical studies for convection-dominated problems, e.g. [134, 135].
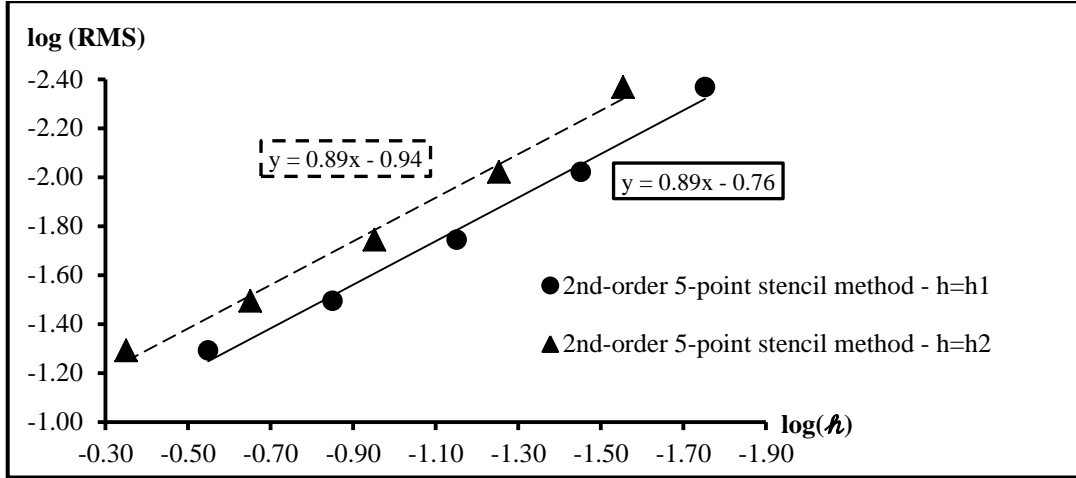
Figure 3.10: Verification plot for global order of accuracy for Problem 4, Dirichlet boundaries
$(\nu = 0.08, \ P = Q = 1, \ \alpha = \beta = -1)$

3.5.5 Problem 5: 2nd-Order 5-point Cut-Stencil FD Solution of Laplace Equation on an Arbitrary, Irregular Shaped Domain

The previous problems were set up to validate some important aspects of the cut-stencil FD formulation. Due to the regular shape of the previous domains, i.e., rectangles or squares, and the use of Cartesian grids, the conditions for constructing cut stencils did not occur. The strength of the Cartesian cut-stencil method lies in its ability to handle arbitrarily irregular shaped domains, as will be discussed in this problem.

The domain for this problem, depicted in Figure 3.11, is a cut-away section of the square $0 \leq x, y \leq 2$. The 2nd-order 5-point cut-stencil FDM solution to the following manufactured problem for the Laplace equation is studied. The PDE and corresponding exact solution, which is used to set the boundary conditions, are respectively:

$$\nabla^2 \emptyset = 0 \tag{3.14.1}$$

$$\emptyset_{exc.} = \ e^{\frac{\pi}{5}x} \ cos\left(\frac{\pi}{5}y\right) + e^{\frac{\pi}{5}y} \ cos\left(\frac{\pi}{5}x\right) \tag{3.14.2}$$

Several uniform grids with number of nodes as shown in Table 3.10 were designed to test the accuracy of the solution, compared to the exact solution, in the irregular domain which includes several cut stencils. The number of active nodes listed in Table 3.10 is the sum of all internal nodes, corner nodes and boundary nodes of each grid. As illustrated in Figure 2.1, when a Cartesian grid is overlayed on an irregular shaped domain, a number of nodes will be located outside the domain. Thus, if the solution of the PDE(s) is intended for internal nodes and correspondingly for the boundary nodes, the nodes located outside the domain do not take part in the solution process. As an example, for the first case in Table 3.10, a Cartesian grid system with nine nodes in both the x and y direction was designed, creating a total of 81 nodes, of which only 71 are active nodes.
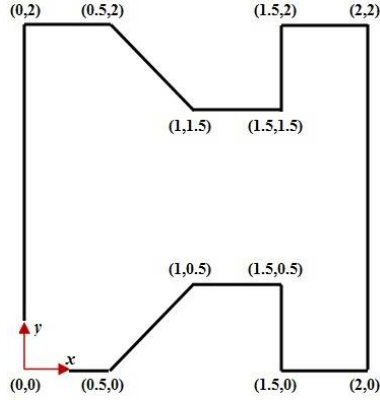
Figure 3.11: Irregular shaped domain used for Problem 5

The FD equation (2.9) with coefficients (2.10), with $P = Q = 0$ and $s_p = 0$, was solved with Dirichlet boundary conditions specified from the exact solution. The values of average and maximum relative error, and the RMS error, are reported in Table 3.10. The results in Table 3.10 also show the facility of calculating the relatively complicated high-order derivative expressions for the LTE on irregular domains. As seen in Table 3.10, all measures of the error show a reduction as the grid become finer. These results demonstrate the capability of the Cartesian cut-stencil FD method to deal with the solution of PDEs on irregular domains with cut stencils.

# of active nodes	Mesh size h	Rel. error (%)		Max |LTE|	RMS error
		Avg.	Max.		
71	0.250	0.01419	0.02465	1.698E-2	3.20E-4
245	0.125	0.00314	0.00629	1.701E-3	8.89E-5
905	0.0625	0.00073	0.00159	5.475E-4	2.34E-5
3473	0.03125	0.00018	0.00040	2.174E-4	5.99E-6
8531	0.020	0.00007	0.00016	1.342E-4	2.48E-6

Table 3.10: Relative error, RMS error and maximum LTE for Problem 5 (Laplace equation, Dirichlet boundary conditions)

Equation (3.14.1) was also solved on the same domain shown in Figure 3.11 when Neumann conditions, taken from the exact solution, were imposed on both the west and east boundaries, correspond to the lines $x = 0$ and $x = 2$, respectively. Results for this simulation are shown in Table 3.11.

# of active nodes	Mesh size (h)	Rel. error at internal nodes (%)		Rel. error at boundary nodes (%)		Max |LTE|	RMS error
		Avg.	Max.	Avg.	Max.		
71	0.25	0.06650	0.25652	0.20899	0.39927	1.287E-2	4.23E-3
245	0.125	0.01829	0.08643	0.04877	0.10567	5.717E-3	1.05E-3
905	0.0625	0.00474	0.02464	0.01179	0.02720	3.069E-3	2.62E-4
3473	0.03125	0.00120	0.00656	0.00290	0.00689	1.794E-3	6.55E-5
8531	0.020	0.00050	0.00275	0.00118	0.00283	1.299E-3	2.68E-5

Table 3.11: Relative error, RMS error and maximum LTE for Problem 5 (Laplace equation, Neumann boundary conditions)

The slopes of the lines in Figure 3.12 indicate the real order of accuracy for the solution of equation (3.14.1) for the cases in Tables 3.10 and 3.11. Solution to this sample problem confirms 2nd-order accuracy of the 5-point cut-stencil formulation for problems with cut stencils on irregular domains.

log (RMS)

y = 1.93x - 2.32

● 2nd-order 5-point stencil method - Dirichlet boundaries

▲ 2nd-order 5-point stencil method - Neumann boundary condition, west & east

y = 2.00x - 1.17

log($\hbar$)
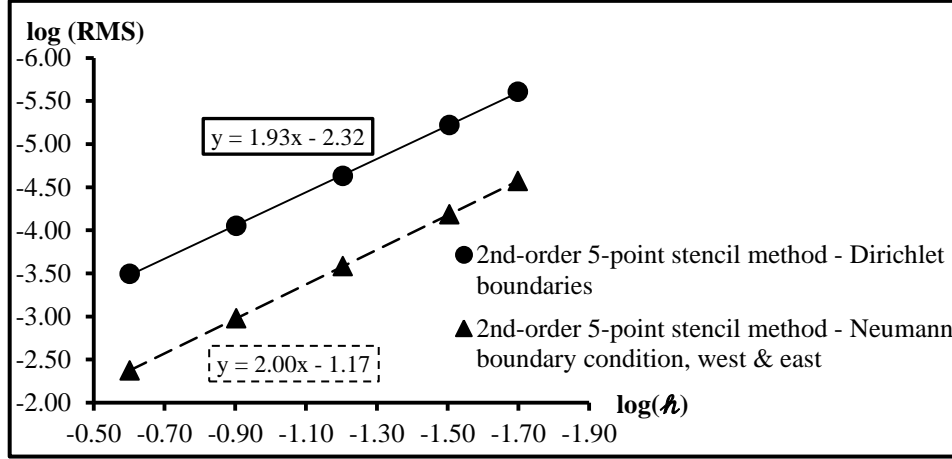
Figure 3.12: Verification of global order of accuracy for Problem 5 (Laplace equation)

3.5.6   Problem 6: 2nd-Order 5-point Cut-Stencil FD Solution of Convection-Diffusion Equation on an Arbitrary, Irregular Shaped Domain

The next manufactured problem studies the solution of the convection-diffusion equation, as written in equation (3.15.1), on the irregular shaped domain illustrated in Figure 3.13. The variables x and y both lie in the range of 0 to 1 and the domain is constructed by cutting the corners with straight lines and circles. A non-uniform Cartesian mesh comprised of 242 active nodes was designed for this case study. The exact solution for the PDE (3.15.1) is given in equation (3.15.2).

$$\nu\nabla^2\emptyset + P\frac{\partial\emptyset}{\partial x} + Q\frac{\partial\emptyset}{\partial y} = \nu\left[\frac{2e^{(x+y)}}{(e^x+e^y)^2} - \pi^2\big(sin(\pi x) + sin(\pi y)\big)\right] +$$
$$P\left[\frac{e^x}{e^x+e^y} + \pi\,cos(\pi x)\right] + Q\left[\frac{e^y}{e^x+e^y} + \pi\,cos(\pi y)\right] \tag{3.15.1}$$
$$\emptyset_{exc.} = \ln(e^x + e^y) + sin(\pi x) + sin(\pi y) \tag{3.15.2}$$

Several cut-stencils and regular and irregular boundary nodes are located along the angular cuts (denoted by L1 and L2) and circular cuts (denoted by C1 and C2) which are shown in Figure 3.13. The equations of the angular cuts and the centres (c) and radii (R) of the circular cuts have been presented in the figure.

Equation (3.15.1) was solved with different values of convection and diffusion coefficients, as well as parameters α and β. Recall that values of 0, 1, -1 for α and β refer to central or one-sided differencing of the convective derivatives. The boundary conditions were set as Dirichlet or Neumann, specified from the exact solution. The average and maximum relative errors are reported in Table 3.12. The west and east boundaries correspond to the lines $x = 0$ and $x = 1$, respectively, and similarly the lines $y = 0$ and $y = 1$ are the south and north boundaries in the irregular shaped domain.
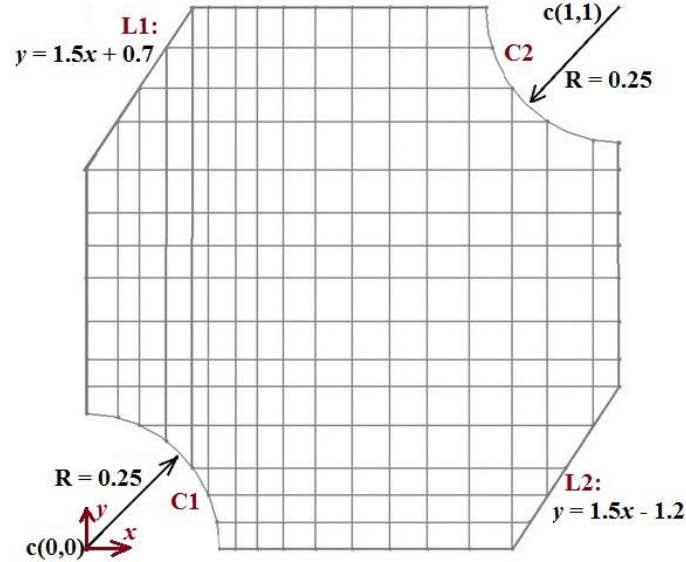
Figure 3.13: Irregular shaped domain with non-uniform grid and cut-stencils for Problem 5 (convection-diffusion equation)

Boundary conditions	Equation and parameter settings	Rel. error at internal nodes (%)		Rel. error at boundary nodes (%)	
		Avg.	Max.	Avg.	Max.
Dirichlet (all)	Diffusion $v = 1, P = Q = 0$	0.31084	0.52722	-	-
	Convection-diffusion $v = 1, P = Q = 0.5, \alpha = \beta = 0$	0.14130	0.25729	-	-
	Convection-diffusion $v = 1, P = Q = 0.5, \alpha = \beta = 1$	0.44059	0.78755	-	-
	Convection-diffusion $v = 1, P = Q = 0.1, \alpha = \beta = -1$	0.15329	0.31141	-	-
	Convection-diffusion $v = 0.56, P = Q = 0.85, \alpha = \beta = 0$	0.21070	0.56273	-	-
	Convection-diffusion $v = 0.56, P = Q = 0.85, \alpha = \beta = 1$	0.74734	1.49210	-	-
	Convection-diffusion $v = 0.56, P = Q = 0.85, \alpha = \beta = -1$	1.03642	1.86091	-	-
Neumann (west & east)	Diffusion $v = 1, P = Q = 0$	0.47863	0.85479	0.81303	1.02782
	Convection-diffusion $v = 1, P = Q = 0.5, \alpha = \beta = 0$	0.25921	0.80933	0.57358	1.00876
	Convection-diffusion $v = 1, P = Q = 0.5, \alpha = \beta = 1$	0.62952	1.05336	0.90517	1.19316
	Convection-diffusion $v = 0.56, P = Q = 0.85, \alpha = \beta = -1$	1.17832	2.55259	1.58426	2.81464
Neumann (south & north)	Diffusion $v = 1, P = Q = 0$	0.50949	0.87893	0.77585	1.08362
	Convection-diffusion $v = 1, P = Q = 0.5, \alpha = \beta = 1$	0.68114	1.26248	0.90804	1.49146
	Convection-diffusion $v = 0.56, P = Q = 0.85, \alpha = \beta = -1$	1.35184	2.63517	1.26932	2.80636

Table 3.12: Relative error results for Problem 6 (convection-diffusion equation)

The results shown in Table 3.12 reveal the capability of the 2nd-order 5-point Cartesian cut-stencil FD formulation (2.8) for the convection-diffusion equation to solve the PDE in an irregular shaped domain with cut-stencils created by cutting the domain with angular or circular cuts. The proposed one-sided 2nd-order accurate approximations for derivatives at the Neumann boundary nodes, e.g. equations (2.19) and (2.20) for regular boundary nodes and (2.22) for irregular boundary nodes, have been implemented in these calculations. The results for the convection-diffusion cases show smaller values for the average and maximum relative error when using $\alpha = \beta = 0$ which is associated with 2nd-order central differencing of the convective terms, compared to the one-sided 1st-order accurate approximation of these terms.

3.5.7 Problem 7: Comparison of 5-point 2nd-Order and 5+4-point Stencil Formulations of Cut-Stencil FDM to Solution of Poisson Equation in a Rectangular Domain

Problems 1 to 6 considered the solutions of several PDEs using the 2nd-order 5-point stencil formulation of the cut-stencil FDM and through each of these problems one or more aspects of the formulation were investigated. The schematic of the 5+4-point stencil of the cut-stencil FDM is illustrated in Figure 2.19, and the discrete form of the diffusion equation on the computational stencil is given by equation (2.26). The purpose of this problem is to test the capability of the 5+4-point formulation to solve PDEs and compare the results to the 2nd-order 5-point cut-stencil solution using the same size of mesh. To achieve this purpose a manufactured diffusion equation, as written in equation (3.16.1), is solved using both the 2nd-order 5-point cut-stencil and the 5+4-point cut-stencil formulations. The exact solution of equation (3.16.1) is given by equation (3.16.2). The domain is a rectangle with $0 \leq x \leq 1$ and $0 \leq y \leq 0.5$.

$$\nabla^2 \emptyset = e^{x+y}[\ (\ (1 - \pi^2)sin(\pi x) + 2\pi \, cos(\pi x) \ ) \, sin(\pi y)$$
$$+ (\ (1 - \pi^2)sin(\pi y) + 2\pi \, cos(\pi y) \ ) \, sin(\pi x) \ ] \tag{3.16.1}$$
$$\emptyset_{exc.} = \ sin(\pi x) \, sin(\pi y) \, e^{x+y} \tag{3.16.2}$$

The average and maximum relative error, the RMS error and maximum |LTE| of the cut-stencil FDM, using 2nd-order 5-point stencil and 5+4-point stencil formulations, are compared in Table 3.13, for several uniform grids. The local truncation error is calculated by equations (3.2.4) and (3.4.2) for the 2nd-order 5-point stencil and the 5+4-point stencil schemes, respectively. The boundary conditions, for data reported in Table 3.13, are considered as Dirichlet conditions taken from the exact solution.

As seen from the trend of data, for both methods the average and maximum relative errors, the RMS error and the absolute LTE are reduced as the number of nodes is increased. Additionally, for all of these error measures, the 5+4-point stencil formulation, for each grid studied, produces a relatively smaller error compared to the 2nd-order 5-point stencil method. One should note, in particular, that the maximum |LTE| when the 5+4-point stencil method is applied is about two orders of magnitude smaller than the |LTE| from the 2nd-order 5-point stencil method.

Figure 3.14 demonstrates the ratio of maximum relative error of the 2nd-order 5-point stencil to the 5+4-point stencil versus the cell size $\hbar$. This ratio varies between 2.20 and 2.30 for all grid sizes and expresses the fact that the maximum error of the 5+4-point stencil solution is smaller than half of the maximum error of the 2nd-order 5-point stencil solution for each grid size.

# of nodes	Mesh size $\hbar$	Method	Rel. error (%)		Max |LTE|	RMS error
			Avg.	Max.		
45	0.125	2nd-order 5-point stencil	0.23863	0.79483	3.834E-1	1.35E-3
		5+4-point stencil	0.10603	0.34644	4.317E-3	6.07E-4
153	0.0625	2nd-order 5-point stencil	0.06677	0.28577	1.378E-1	3.81E-4
		5+4-point stencil	0.03004	0.12730	1.256E-3	1.73E-4
561	0.03125	2nd-order 5-point stencil	0.01753	0.08428	3.824E-2	1.00E-4
		5+4-point stencil	0.00794	0.03794	3.271E-4	4.56E-5
2145	0.015625	2nd-order 5-point stencil	0.00448	0.02282	1.010E-2	2.57E-5
		5+4-point stencil	0.00204	0.01034	8.375E-5	1.17E-5

Table 3.13: Comparison of results for 2nd-order 5-point stencil and 5+4-point cut-stencil formulations for Problem 6 (Dirichlet boundary condition)
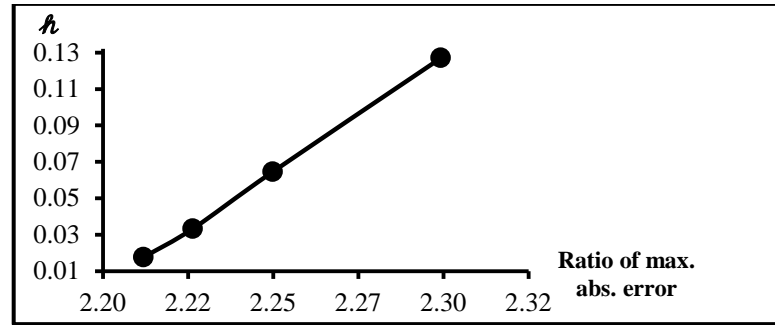
Figure 3.14: Ratio of maximum absolute error of 2nd-order 5-point stencil to 5+4-point stencil methods vs. $\hbar$ for Problem 7 (Dirichlet boundary conditions)

The solution of (3.16.1), using both the 5-point and 5+4-point methods, is further studied when the boundary conditions on the west and east boundaries are replaced by Neumann conditions taken from the exact solution. The error measures presented in previous tables for Neumann conditions, such as Tables 3.2-3.5, are addressed in Table 3.14. The exact solution at all boundary nodes is zero so the absolute error, which is defined as the absolute difference between the numerical and exact solutions, is reported in this table. The reducing trend of the absolute and relative errors the RMS error and LTE, as the meshes become finer, can be seen from the data.

# of nodes	Mesh size ($\hbar$)	Method	Rel. error at internal nodes (%)		Abs. error at boundary nodes		Max |LTE|	RMS error
			Avg.	Max.	Avg.	Max.		
45	0.125	M$_{5\text{-point}}$*	0.98880	3.40496	0.02815	0.04121	4.174E-1	1.25E-2
		M$_{5+4\text{-point}}$**	0.45226	1.73230	0.01954	0.02821	5.285E-3	8.02E-3
153	0.0625	M$_{5\text{-point}}$	0.38289	2.47035	0.00684	0.01296	1.587E-1	3.28E-3
		M$_{5+4\text{-point}}$	0.12107	0.68935	0.00344	0.00654	2.028E-3	1.39E-3
561	0.03125	M$_{5\text{-point}}$	0.13648	1.57240	0.00168	0.00360	4.960E-2	8.41E-4
		M$_{5+4\text{-point}}$	0.02641	0.24786	0.00054	0.00117	7.955E-4	2.11E-4
2145	0.015625	M$_{5\text{-point}}$	0.04532	0.88386	0.00042	0.00095	1.581E-2	2.14E-4
		M$_{5+4\text{-point}}$	0.00517	0.07236	0.00008	0.00018	3.471E-4	3.12E-5
*: M$_{5\text{-point stencil}}$: 2nd-order 5-point stencil, **:M$_{5+4\text{-point stencil}}$: 5+4-point stencil								

Table 3.14: Comparison of results for 2nd-order 5-point cut-stencil and 5+4-point cut-stencil formulations for Problem 7 (west and east Neumann boundary conditions)

The real order of the method for the solution of equation (3.16.1) using the 2nd-order 5-point stencil and 5+4-point stencil formulations of the cut-stencil FDM have been verified in the plot of Figure 3.15. The slopes of the lines indicate almost 2nd-order and 2.7th-order accuracy for the 2nd-order 5-point stencil and 5+4-point stencil formulations, respectively. Although 4th-order accurate finite difference formulas have been applied for approximation of first and second derivatives at node P on the computational stencil in the 5+4-point stencil formulation, the 2nd-order accurate approximation of the first and second derivatives at the four auxiliary nodes *l*, *r*, *a* and *b*, which were discussed in Chapter 2, reduces the global order of accuracy of the solution to 2.7.
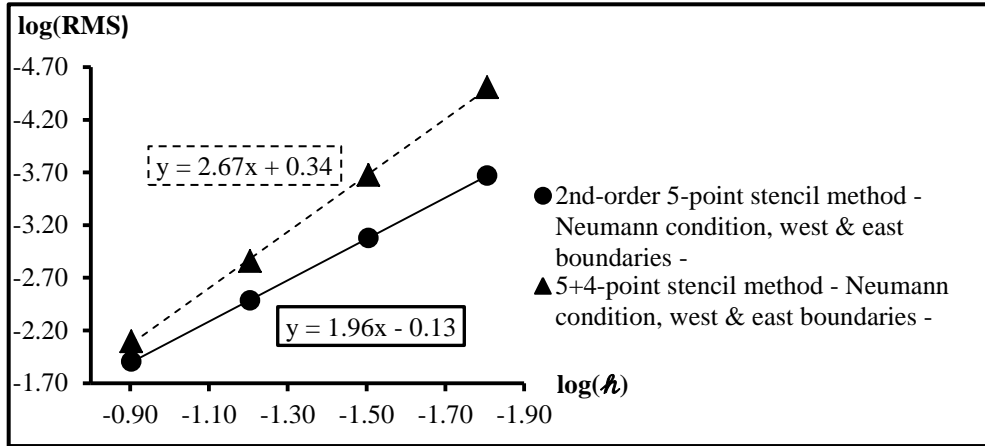
Figure 3.15: Verification plot for global order of accuracy for Problem 7 (west and east Neumann boundary condition)

The absolute error along the vertical and horizontal centrelines of the domain for Neumann boundary conditions on west and east is plotted for grids of 153 and 2145 nodes in Figures 3.16. The difference in level for the absolute error along these centrelines, indicating the accuracy of the solutions from the two methods, is significant. This matter is especially apparent along the horizontal centreline where the solutions at the end nodes, corresponding to the west and east boundaries, should be zero. Clearly, the 5+4-point method gives a more accurate prediction at these Neumann boundaries, and shows much greater accuracy than the 5-point method, particularly as the mesh is refined. This is due to the fact that the 5+4-point method uses 4th-order accurate expressions for the derivatives, even for those near the boundaries.
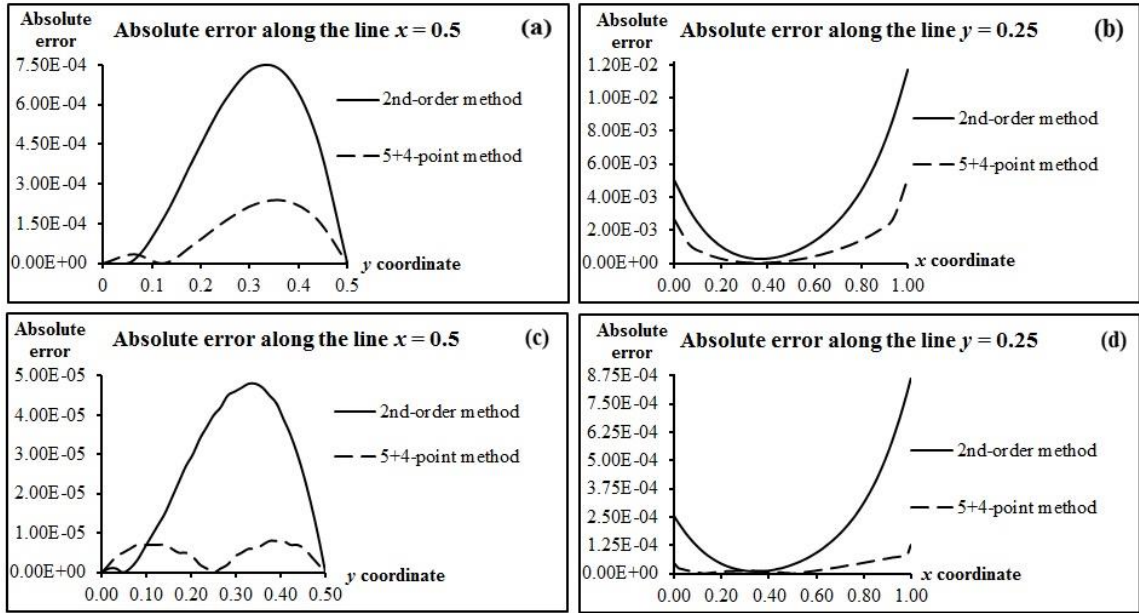
Figure 3.16: Comparison of absolute errors along centrelines of domain of Problem 7 (Neumann conditions on west and east boundaries), (a,b) 153 nodes, (c,d) 2145 nodes

3.5.8 Problem 8: HO Cut-Stencil FDM1 Solution of PDEs in Rectangular and Irregular Shaped Domains

The higher-order method HO cut-stencil FDM1, which was introduced in Chapter 2, is considered for the solution of three manufactured problems in this section. The discrete form of the convection-diffusion equation, using HO cut-stencil FDM1, was presented in equation (2.41). Comparison of the accuracy of solutions to the manufactured problems, predicted by the schemes of 2nd-order 5-point cut-stencil, 5+4-point cut-stencil and HO cut-stencil FDM1, is studied in this problem. Furthermore, the capability of applying this method to irregular shaped domains to solve PDEs with more accuracy is illustrated.

Problem 8.1: First, to make a comparison among the various cut-stencil FD schemes, the same manufactured diffusion equation defined for Problem 7, i.e., equation (3.16.1), is considered here. The same domain and grid sizes are used to solve the PDE using HO cut-stencil FDM1 and the results are recorded in Table 3.15.

# of nodes	Mesh size h	Rel. error (%)		Max $|LTE|$	RMS error
		Avg.	Max.		
45	0.125	0.19197	0.63831	2.713E-2	1.01E-3
153	0.0625	0.01521	0.08919	7.816E-3	7.43E-5
561	0.03125	0.00215	0.00859	2.026E-3	1.49E-5
2145	0.015625	0.00072	0.00296	5.140E-04	4.73E-6

Table 3.15: HO cut-stencil FDM1 solution to Problem 8.1 (Poisson equation, Dirichlet boundary conditions)

Comparing the data in Table 3.15 with that in Table 3.13 reveals that for all grid sizes, the errors produced by HO-FDM1 are much smaller than the errors produced by the 2nd-order 5-point cut-

stencil method, and that the difference becomes more pronounced as the number of nodes increases. Except for the grid of 45 nodes (coarsest grid), FDM1 yields average and maximum relative errors and RMS errors that are smaller compared to the 5+4-point stencil formulation. The ratio of maximum relative error of the 2nd-order 5-point stencil to HO cut-stencil FDM1 varies between 1.2 and 9.8 or, in other words, the maximum relative error of the cut-stencil FDM1 for this problem is almost one-tenth that of the 2nd-order 5-point stencil method. The comparison of global order of accuracy for the grids used in Tables 3.13 and 3.15 is displayed in Figure 3.17. The slopes of lines suggest nearly 2nd-order accuracy for the 2nd-order 5-point stencil and 5+4-point stencil schemes and 2.55 order of accuracy for the HO cut-stencil FDM1. The 2nd-order accurate approximations to derivatives in both the 5+4-point stencil and HO cut-stencil FDM1 schemes are likely the main reason for the reduced global accuracy. Nevertheless, the comparison of these results clearly reveals a more precise solution to this problem than that predicted by the 2nd-order 5-point stencil formulation. This data provides evidence that, for a specific grid size and with the same boundary conditions, the 5+4-point cut-stencil and HO cut-stencil FDM1 formulations, which have been considered thus far, are able to capture more accurate solutions, which is the main aims of higher-order numerical simulations.
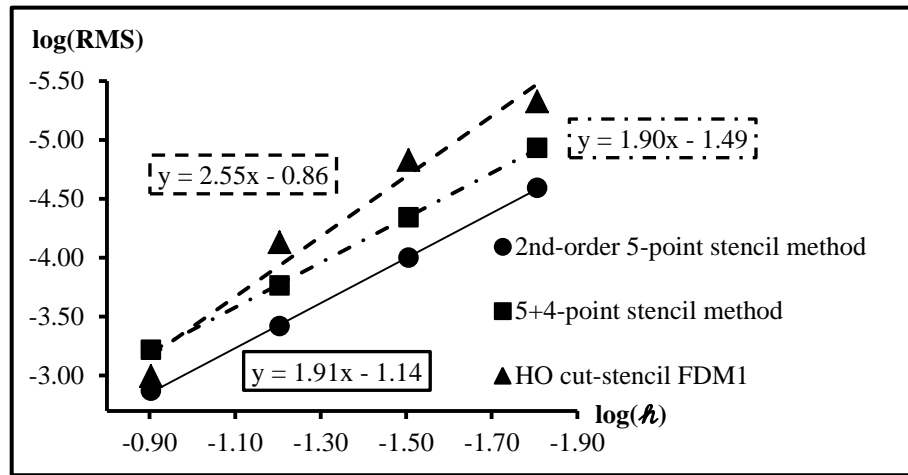
Figure 3.17: Verification plot for global order of accuracy for Problem 8.1 and comparison with Problem 7 (Dirichlet boundary conditions)

Problem 8.2: As mentioned in Chapter 2, the 5+4-point cut-stencil scheme has limitations when applied to stencils which are cut with boundary lines, as illustrated in Figure 2.23. These restrictions for treating the cut stencil with a higher-order formulation are resolved by using HO cut-stencil FDM1, as explained in Chapter 2. To verify that FDM1 can handle boundary cuts which may create regular or irregular boundary nodes, consider the triangular domain shown in Figure 3.18 and the manufactured convection-diffusion equation:

$$\nu\nabla^2\emptyset + P\,\frac{\partial\emptyset}{\partial x} + Q\,\frac{\partial\emptyset}{\partial y} = \nu\left[\frac{2e^{x+y}}{(e^x+e^y)^2} + e^{xy}(x^2+y^2)\right] + P\left[\frac{e^x}{e^x+e^y} + ye^{xy}\right] +$$
$$Q\left[\frac{e^y}{e^x+e^y} + xe^{xy}\right]$$

(3.17.1)

$$\emptyset_{exc.} = \ln(e^x + e^y) + e^{xy}$$

(3.17.2)

Initially, for this problem, consider only diffusion with a source term by setting $v = 1$ and $P = Q = 0$. The results of this study, for several grid sizes with different number of active nodes, are presented in Table 3.16.
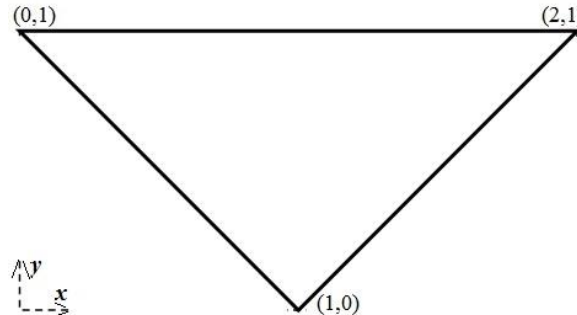
Figure 3.18: Irregular domain illustration for Problem 8.2 (diffusion equation)

The data in Table 3.16 demonstrates a more accurate solution for FDM1 compared to the 2nd-order 5-point cut-stencil method and the LTE also shows smaller values in the event of using HO cut-stencil FDM1.

| # of active nodes | Mesh size $\hbar$ | Method | Rel. error (%) | | Max \|LTE\| | RMS error |
			Avg.	Max.		
81	0.125	2nd-order 5-point stencil	0.00440	0.00947	2.104E-2	1.71E-4
		HO cut-stencil FDM1	0.00143	0.00599	2.047E-3	8.75E-5
121	0.100	2nd-order 5-point stencil	0.00273	0.00606	2.056E-2	1.13E-4
		HO cut-stencil FDM1	0.00050	0.00304	2.001E-3	4.21E-5
289	0.0625	2nd-order 5-point stencil	0.00101	0.00240	1.491E-2	4.60E-5
		HO cut-stencil FDM1	0.00010	0.00064	1.453E-3	7.83E-6
441	0.050	2nd-order 5-point stencil	0.00063	0.00154	1.169E-2	2.99E-5
		HO cut-stencil FDM1	0.00007	0.00029	1.141E-3	4.06E-6
676	0.040	2nd-order 5-point stencil	0.00039	0.00099	8.800E-3	1.92E-5
		HO cut-stencil FDM1	0.00006	0.00015	8.592E-4	2.71E-6
1089	0.03125	2nd-order 5-point stencil	0.00023	0.00060	6.186E-3	1.15E-5
		HO cut-stencil FDM1	0.00005	0.00012	6.044E-4	2.30E-6

Table 3.16: Comparison of results for 2nd-order 5-point stencil and HO-FDM1 5-point stencil formulations for Problem 8.2 (diffusion equation)

Problem 8.3: The convection-diffusion equation (3.17.1) is solved in the irregular shaped domain shown in Figure 3.19. The equation of angular cuts L1 and L2, as well as the centre and radius of the circular cut are indicated in the figure. Results are presented for different values of the diffusion and convection coefficients. The solutions of the 2nd-order 5-point stencil method and HO cut-stencil FDM1 have been compared for two grid sizes of 30 and 100 nodes and the data for all cases are recorded in Table 3.17. The Dirichlet and Neumann boundary conditions are taken from the exact solution which is given in equation (3.17.2). The south and north boundaries correspond to the lines $y = 0$ and $y = 2$ of the domain.
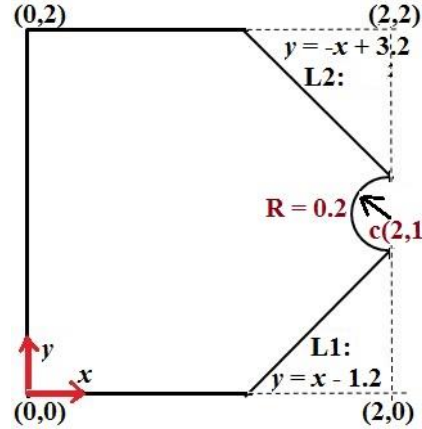
Figure 3.19: Irregular shaped domain for Problem 8.3 (convection-diffusion equation)

It is worth noting that for the cases of the convection-diffusion equation reported in Table 3.17, in event of using the 2nd-order 5-point stencil method, the convection terms are approximated by either globally 2nd- or 1st-order accurate approximations depending on the values of α and β set equal to 0 or 1, respectively. When HO cut-stencil FDM1 is applied, these same terms are approximated by globally 4th- or 2nd-order accuracy by setting the values of α and β to 0 or 1, respectively. Equation (2.41) is used for the 4th-order central approximations of HO cut-stencil FDM1, for the convection-diffusion equation, and a similar equation can be derived for 2nd-order backward differencing. Equation (3.6.2) was used to generate the LTE values for HO cut-stencil FDM1 in Table 3.17.

Boundary Condition	Equation	# of active nodes	Method	Rel. error at internal nodes (%)		Rel. error at boundary nodes (%)		Max |LTE|
				Avg.	Max.	Avg.	Max.	
Dirichlet (all)	Diffusion $\nu = 1$, $P = Q = 0$	30	2nd-order*	0.64561	0.92459	-	-	3.057E-1
			FDM1**	0.41677	0.56799	-	-	3.286E-2
		100	2nd-order	0.13616	0.23759	-	-	2.100E-1
			FDM1	0.01249	0.04393	-	-	1.420E-2
	Convection-diffusion $\nu = 1$, $P = Q = 0.4$, $\alpha = \beta = 1$	30	2nd-order	1.62835	2.46938	-	-	2.369E-0
			FDM1	0.51783	0.81348	-	-	3.008E-1
		100	2nd-order	0.87068	1.54981	-	-	1.778E-0
			FDM1	0.08381	0.16848	-	-	1.406E-1
Neumann (south & north)	Diffusion $\nu = 1$, $P = Q = 0$	30	2nd-order	0.95284	1.67404	0.88935	1.81622	3.640E-1
			FDM1	0.58148	0.91450	0.60508	1.15059	3.674E-2
		100	2nd-order	0.24052	0.55253	0.25834	0.54877	2.698E-1
			FDM1	0.04568	0.15044	0.12631	0.25517	1.901E-2
	Convection-diffusion $\nu = 1$, $P = Q = 0.4$, $\alpha = \beta = 1$	30	2nd-order	2.18574	3.10754	2.39475	3.71635	2.368E-0
			FDM1	0.75474	1.21349	0.67841	1.23137	3.009E-1
		100	2nd-order	1.27602	1.95640	1.28138	1.71908	1.777E-0
			FDM1	0.09651	0.17552	0.13174	0.25075	1.429E-1
*: 2nd-order 5-point stencil, **: HO cut-stencil FDM1								

Table 3.17: Comparison of results for 2nd-order 5-point stencil and the HO cut-stencil FDM1 for Problem 8.3 (convection-diffusion equation)

The data in Table 3.17 clearly shows smaller values for average and maximum absolute error as the mesh is refined from 30 to 100 nodes, which has also been observed in the previous problems and captured here in this irregular shaped domain for both formulations used.

Additionally, for each case in Table 3.17, the average and maximum absolute error and maximum |LTE| for HO cut-stencil FDM1 is smaller than for the 2nd-order 5-point stencil scheme. The capability of the cut-stencil FDM to calculate the relatively complicated expression for LTE in irregular domains can be seen in this problem. In the situation when Neumann boundary conditions are applied with HO cut-stencil FDM1, the boundary nodes are approximated by 3rd-order accuracy as, for example, in the case of north boundary nodes in equation (2.51.2), compared to the 2nd-order accurate approximation for the 2nd-order 5-point stencil scheme.

3.5.9 Problem 9: HO Cut-Stencil FDM2 Solution of PDEs in Rectangular and Irregular Shaped Domains

The HO cut-stencil FDM2, which was discussed in Chapter 2 and described by, e.g., equation (2.43), is studied here for three manufactured problems.

Problem 9.1: The solution obtained from HO-FDM2 and comparison of results with the 2nd-order 5-point cut-stencil scheme, as well as verification of real order of accuracy for the solution of equation (3.18.1), on a square domain $0 \leq x, y \leq 1$, with Dirichlet boundary conditions, are discussed. Equation (3.18.2) gives the exact solution of the Poisson equation (3.18.1).

$$\nabla^2 \emptyset = \frac{2e^{x+y}}{(e^x + e^y)^2} - 2\pi^2 sin(\pi(x + y)) \qquad (3.18.1)$$

$$\emptyset_{exc.} = \ln(e^x + e^y) + sin(\pi(x + y)) \qquad (3.18.2)$$

The solution of equation (3.18.1) was obtained using the 2nd-order 5-point cut-stencil FDM and the HO cut-stencil FDM2 and error results are presented in Table 3.18 for several uniform grids with number of nodes varying from 36 to 2601. The difference in solution accuracy of the 2nd-order 5-point formulation and the HO cut-stencil FDM2 can be seen from comparison of the maximum relative error from both schemes. The ratio of these errors is greater than 5 for the coarsest mesh size (grid of 36 nodes) and reaches to nearly 923 for the finest mesh size (grid of 2601 nodes). This suggests that the HO cut-stencil FDM2 solution to this boundary value problem is more than 900 times more accurate than the 2nd-order 5-point stencil solution. The |LTE| of HO cut-stencil FDM2, as reported in Table 3.18, has been calculated from equation (3.6.1) with the coefficient $\frac{1}{200}$ replaced by $\frac{1}{360}$.

It is worthwhile to investigate the degree of mesh refinement required to achieve the same level of solution accuracy reported for FDM2 on the 2601 node mesh if the 2nd-order 5-point formulation is used. In this event, the average and maximum absolute error for a mesh of 25921 nodes are 0.00089 and 0.00456, respectively, when the 2nd-order 5-point scheme is applied. This mesh size is about 10 times larger than the finest grid in Table 3.18 (2601 nodes) but it is still not able to capture the same level of solution accuracy as the FDM2 5-point stencil formulation. This example reveals one of the most beneficial effects of HO formulations, namely significant reduction of the demand on computational resources and time to achieve a desired level of accuracy.

# of nodes	Mesh size h	Method	Relative error (%)		Max |LTE|	RMS error
			Avg.	Max.		
36	0.200	2nd-order 5-point stencil	0.98341	3.09980	3.646E-1	6.54E-3
		HO cut-stencil FDM2	0.20384	0.59951	1.931E-2	1.44E-3
81	0.125	`2nd-order 5-point stencil	0.35745	1.35536	2.490E-1	2.76E-3
		HO cut-stencil FDM2	0.01403	0.04878	8.950E-3	1.34E-4
121	0.100	2nd-order 5-point stencil	0.22139	0.89497	1.605E-1	1.81E-3
		HO cut-stencil FDM2	0.00650	0.02344	4.977E-3	5.83E-5
289	0.0625	2nd-order 5-point stencil	0.08172	0.35472	6.319E-2	7.31E-4
		HO cut-stencil FDM2	0.00111	0.00465	1.310E-3	1.02E-5
441	0.050	2nd-order 5-point stencil	0.05122	0.22792	4.051E-2	4.74E-4
		HO cut-stencil FDM2	0.00046	0.00201	7.038E-4	4.30E-6
676	0.04	2nd-order 5-point stencil	0.03222	0.14751	2.591E-2	3.06E-4
		HO cut-stencil FDM2	0.00019	0.00085	4.446E-4	1.79E-6
1089	0.03125	2nd-order 5-point stencil	0.01936	0.09001	1.586E-2	1.88E-4
		HO cut-stencil FDM2	0.00007	0.00032	2.686E-4	6.78E-7
1681	0.025	2nd-order 5-point stencil	0.01225	0.05755	1.015E-2	1.21E-4
		HO cut-stencil FDM2	0.00003	0.00012	1.710E-4	2.82E-7
2601	0.020	2nd-order 5-point stencil	0.00777	0.03689	6.499E-3	7.80E-5
		HO cut-stencil FDM2	0.00001	0.00004	1.090E-4	1.36E-7

Table 3.18: Comparison of results for 2nd-order 5-point stencil and HO-FDM2 5-point stencil formulations for Problem 9 (diffusion equation)

The global order of accuracy of these two schemes applied to solve the Poisson equation (3.18.1) has been investigated with the slopes of lines shown in Figure 3.20. These slopes suggest that the 2nd-order 5-point stencil method and the FDM2 5-point stencil formulation have nearly 2nd and 4th-order accuracy, respectively. The effect of the 4th-order accurate approximation of first derivatives in the FDM2 5-point stencil formulation is apparent in successfully retaining a nearly globally 4th-order accurate solution to this problem.
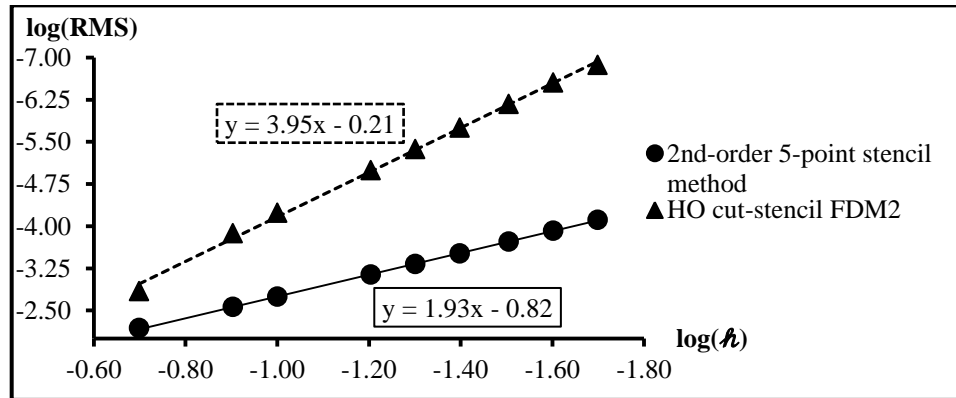
Figure 3.20: Verification plot for global order of accuracy for Problem 9.1 (diffusion equation, Dirichlet boundary conditions)

Problem 9.2: The boundary value problem considered in Problem 8.2 is solved using the FDM2 5-point cut-stencil formulation on the same triangular domain indicated in Figure 3.18. Similar grid sizes, as reported in Table 3.16, are used to generate the solution of equation (3.17.1) for the FDM2 5-point stencil scheme and the results are given in Table 3.19.

# of active nodes	Mesh size $\hbar$	Relative error (%)		Max |LTE|	RMS error
		Avg.	Max.		
81	0.125	0.00062	0.00507	1.288E-3	6.07E-5
121	0.100	0.00020	0.00250	1.259E-3	2.65E-5
289	0.0625	0.00002	0.00050	9.153E-4	3.89E-6
441	0.050	0.00001	0.00022	7.188E-4	1.47E-6
676	0.040	0.00001	0.00010	5.415E-4	5.88E-7

Table 3.19: Errors from HO cut-stencil FDM2 solution for Problem 9.2 on irregular domain – (diffusion equation, Dirichlet boundary conditions)

The comparison of average and maximum relative errors, RMS errors and maximum |LTE| in Table 3.19 to the same values reported in Table 3.16 demonstrates that a more accurate solution to the PDE in equation (3.17.1) is obtained when using HO cut-stencil FDM2. The slopes of lines in Figure 3.21 indicate the real order of solution to equation (3.17.1) for the three schemes of 2nd-order 5-point stencil, FDM1 5-point stencil and FDM2 5-point stencil. The solutions of 2nd-, 3rd- and 4th-order accurate approximations have been captured for each of these three formulations. It should be mentioned that round-off error affects the FDM2 solution after the grid size of 676 nodes, so the solution procedure stopped after this grid size. The lines in Figure 3.21 are plotted for grid sizes with number of nodes varying from 81 to 676.
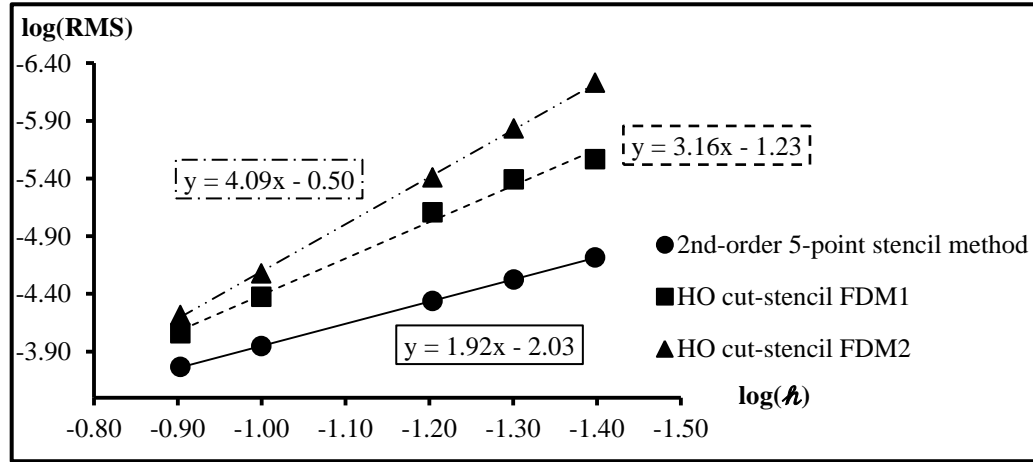
Figure 3.21: Verification plot for global order of accuracy for Problem 9.2 (diffusion equation on irregular domain, Dirichlet boundary conditions)

Problem 9.3: As a further example, the 2nd-order 5-point stencil, FDM1 5-point stencil and FDM2 5-point stencil solutions of a boundary value problem for the convection-diffusion equation (3.19.1) have been compared. The irregular shaped domain for this problem is depicted in Figure 3.22 and the solution is obtained with both Dirichlet and Neumann boundary conditions taken from the exact solution given in (3.19.2).

$$v\nabla^2 \emptyset + P\frac{\partial \emptyset}{\partial x} + Q\frac{\partial \emptyset}{\partial y} = v[e^x + e^y - 2\pi^2 \sin(\pi(x+y))] + P[e^x +$$
$$\pi\cos(\pi(x+y))] + Q[e^y + \pi\cos(\pi(x+y))] \tag{3.19.1}$$

$$\emptyset_{exc.} = e^x + e^y + \sin(\pi(x+y)) \tag{3.19.2}$$
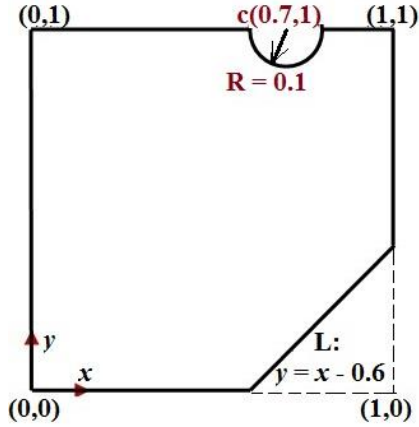
Figure 3.22: Irregular shaped domain for Problem 9.3 (diffusion-convection equation)

Results for the solution of equation (3.19.1) on the domain shown in Figure 3.22, with different values of diffusion and convection coefficients, are given in Table 3.20. In the case of Neumann boundary conditions, the south and east boundaries correspond to the lines $y = 0$ and $x = 1$ of the domain, respectively.

Boundary Condition	Equation	# of active nodes	Method	Relative error at internal nodes (%)		Relative error at boundary nodes (%)		Max |LTE|
				Avg.	Max.	Avg.	Max.	
Dirichlet (all)	Diffusion $v = 1$, $P = Q = 0$	33	2nd-order*	0.26235	0.42925	-	-	3.736E-1
			FDM1**	0.14912	0.29482	-	-	3.488E-2
			FDM2***	0.04646	0.09797	-	-	2.005E-2
		110	2nd-order	0.05470	0.11263	-	-	1.624E-1
			FDM1	0.00552	0.01703	-	-	7.482E-3
			FDM2	0.00144	0.00510	-	-	5.033E-3
	Convection-diffusion $v = 1$, $P = Q = 0.4$, $\alpha = \beta = 1$	33	2nd-order	0.61876	1.10543	-	-	1.238E-0
			FDM1	0.21714	0.42904	-	-	1.676E-1
			FDM2	0.16822	0.30778	-	-	1.631E-1
		110	2nd-order	0.19796	0.45572	-	-	7.315E-1
			FDM1	0.05269	0.11538	-	-	4.381E-2
			FDM2	0.03033	0.06274	-	-	4.297E-2
Neumann (south & east)	Diffusion $v = 1$, $P = Q = 0$	33	2nd-order	0.42684	0.95323	1.04301	2.08495	3.659E-1
			FDM1	0.28756	0.79823	0.86318	1.93104	3.358E-2
			FDM2	0.13960	0.37246	0.65436	0.80764	2.271E-2
		110	2nd-order	0.11622	0.38171	0.33291	0.61565	1.798E-1
			FDM1	0.03512	0.24525	0.20036	0.52703	1.058E-2
			FDM2	0.00805	0.03750	0.04128	0.05510	5.023E-3
	Convection-diffusion $v = 1$, $P = Q = 0.4$, $\alpha = \beta = 1$	33	2nd-order	0.96949	2.05079	2.04092	2.98520	1.275E-0
			FDM1	0.35714	0.84769	0.86845	1.78963	1.687E-1
			FDM2	0.25381	0.62218	0.68507	0.92956	1.627E-1
		110	2nd-order	0.33829	0.84659	0.71262	0.98542	8.037E-1
			FDM1	0.06659	0.20284	0.19017	0.49164	4.385E-2
			FDM2	0.03773	0.07229	0.04526	0.08090	4.297E-2
*: 2nd-order 5-point stencil, **: HO cut-stencil FDM1, ***: HO cut-stencil FDM2								

Table 3.20: Comparison of results for 2nd-order 5-point stencil, HO-FDM1 5-point stencil and HO-FDM2 5-point stencil formulations for Problem 9.3 (convection-diffusion equation)

It can be seen from the data in Table 3.20 that the FDM2 5-point stencil formulation gives the most accurate solution to the problem for all the cases studied. For the convection-diffusion

equation, the same central 2nd-order discretization has been used for the convection terms for both FDM1 and FDM2, although the fundamental difference comes back to using 2nd-order and 4th-order accurate approximations of the derivatives in the equations for these two schemes (cf., (2.41) and (2.43)). The boundary nodes, in the event of Neumann conditions, are approximated by 2nd-order and 3rd-order accurate formulas for the 2nd-order 5-point stencil method and the HO methods, respectively. The comparisons of results for Neumann boundary conditions show no significant change of relative error between 2nd-order 5-point stencil and FDM1 solutions for the diffusion equation. For all cases of Neumann conditions, FDM2 shows significant reduction in error compared to the other formulations.

Problem 9.4: The effect of the order of approximation at Neumann boundary nodes is discussed here through the solution of equation (3.19.1) by setting $v = 1$ and $P = Q = 0$ on a square domain $0 \leq x, y \leq 1$. For this case the Neumann conditions are imposed on both west and east boundaries and several uniform grids are used to generate the data in Table 3.21. The results in this table can be analysed in two manners; the effect of higher-order method used for the solution of the given problem with Neumann boundary conditions and, the effect of order of accuracy used to approximate the unknown solution at Neumann boundary nodes.

Comparison of the solution using the 2nd-order 5-point cut-stencil method to FDM1 shows no significant changes in the results and even for some grid sizes the value of maximum relative error at boundary nodes is higher for the FDM1 solution to the problem. This behaviour indicates that the 2nd-order accurate approximations used for first and second derivatives in the FDM1 formulation cannot preserve the real order of accuracy for cases when Neumann conditions are imposed on the boundaries of the domain.

Table 3.21 also surveys the FDM2 solutions with 2nd- and 3rd-order accurate approximations at the Neumann boundary nodes. The FDM2 solution, when the 3rd-order accurate approximation is applied at Neumann boundary nodes, indicates clear reduction in errors for both internal and boundary nodes, whereas the 2nd-order accurate approximation produces the same level of errors as the 2nd-order 5-point stencil scheme. Referring to the higher-order methods for the boundary nodes, as discussed in Chapter 2, one order of accuracy lower for approximation of derivatives at boundaries nodes, compared to the order used for internal nodes, can still retain the real (formal or global) order of accuracy of the solution for the whole domain. Consequently, the 2nd-order accurate approximation at boundaries nodes reduces the real order of the solution, which can be seen by comparing FDM2 5-point stencil solution along with 2nd-order accurate approximation at boundaries nodes to the solution of the 2nd-order 5-point stencil method for each grid sizes in Table 3.21. However, in the event of using 3rd-order accurate approximation at boundaries nodes, FDM2 captures a significantly more accurate solution than the 2nd-order 5-point cut-stencil method.

The real orders of solutions, addressed in Table 3.21, are shown by the slopes of lines which are plotted in Figure 3.23. These slopes suggest 2nd-order (slope of 2.08) for the 2nd-order 5-point stencil method and 2.23rd-order (slopes of 2.23) for both solutions of FDM1 with 3rd-order accurate approximation at boundaries nodes and FDM2 with 2nd-order accurate approximation at boundaries nodes. Higher than 3rd-order accurate solution is achieved when FDM2 is used along with a 3rd-order accurate approximation at the Neumann boundary nodes. These slopes prove that the more accurate solution, for problems associated with Neumann boundary conditions, is

obtained from higher-order cut-stencil FD formulations when both higher-order approximation for the derivatives in their fundamental formulations (4th-order accurate approximation used in FDM2) and higher-order accurate approximation at nodes located on the Neumann boundaries are implemented.

# of nodes (h)	Method	Order of Neumann boundary approximation	Rel. error at internal nodes (%)		Rel. error at boundary nodes (%)		RMS error
			Avg.	Max.	Avg.	Max.	
36 (0.2)	2nd-order*	2nd	0.55974	1.06083	1.54034	2.94196	3.28E-2
	FDM1**	3rd	0.48355	1.11992	1.70165	3.06855	3.45E-2
	FDM2***	2nd	0.46069	1.14318	1.68671	3.06340	3.45E-2
		3rd	0.32924	0.71648	0.94610	1.27847	1.85E-2
81 (0.125)	2nd-order	2nd	0.20624	0.45617	0.54855	0.94457	1.06E-2
	FDM1	3rd	0.15600	0.54911	0.55253	1.02295	1.05E-2
	FDM2	2nd	0.15421	0.56504	0.54738	1.04010	1.07E-2
		3rd	0.05112	0.15467	0.14746	0.22600	2.91E-3
121 (0.1)	2nd-order	2nd	0.13150	0.35248	0.33663	0.59667	6.45E-3
	FDM1	3rd	0.09336	0.36980	0.33393	0.60816	6.11E-3
	FDM2	2nd	0.09371	0.38986	0.33205	0.61573	6.21E-3
		3rd	0.02280	0.07502	0.06399	0.10165	1.26E-3
289 (0.0625)	2nd-order	2nd	0.05195	0.17459	0.12599	0.24368	2.39E-3
	FDM1	3rd	0.03355	0.16058	0.11943	0.21955	2.05E-3
	FDM2	2nd	0.03439	0.16462	0.11932	0.22390	2.08E-3
		3rd	0.00468	0.01652	0.01242	0.02000	2.43E-4
441 (0.050)	2nd-order	2nd	0.03353	0.12160	0.07971	0.16037	1.52E-3
	FDM1	3rd	0.02102	0.10659	0.07422	0.13677	1.25E-3
	FDM2	2nd	0.02170	0.10826	0.07432	0.13860	1.26E-3
		3rd	0.00230	0.00827	0.00597	0.00966	1.17E-4
1089 (0.03125)	2nd-order	2nd	0.01332	0.05417	0.03070	0.06440	5.93E-4
	FDM1	3rd	0.00802	0.04416	0.02786	0.05182	4.55E-4
	FDM2	2nd	0.00835	0.04397	0.02799	0.05172	4.56E-4
		3rd	0.00054	0.00199	0.00136	0.00218	2.64E-5
1681 (0.025)	2nd-order	2nd	0.00859	0.03620	0.01959	0.04175	3.80E-4
	FDM1	3rd	0.00511	0.02886	0.01760	0.03286	2.85E-4
	FDM2	2nd	0.00533	0.02856	0.01769	0.03258	2.85E-4
		3rd	0.00028	0.00102	0.00068	0.00110	1.33E-5
4225 (0.015625)	2nd-order	2nd	0.00339	0.01518	0.00762	0.01658	1.49E-4
	FDM1	3rd	0.00199	0.01169	0.00676	0.01265	1.08E-4
	FDM2	2nd	0.00208	0.01142	0.00680	0.01241	1.07E-4
		3rd	0.00007	0.00025	0.00016	0.00026	3.19E-6
6561 (0.0125)	2nd-order	2nd	0.00218	0.00994	0.00487	0.01067	9.58E-5
	FDM1	3rd	0.00127	0.00757	0.00430	0.00807	6.82E-5
	FDM2	2nd	0.00133	0.00737	0.00433	0.00787	6.78E-5
		3rd	0.00003	0.00013	0.00008	0.00014	1.63E-6

*: 2nd-order 5-point stencil, **: HO cut-stencil FDM1, ***: HO cut-stencil FDM2

Table 3.21: Comparison of results of different schemes for Problem 9.4 (diffusion equation, different orders used for Neumann boundaries)

The data given in Table 3.21 accompanied by the data in Table 3.20 confirms the capability of the cut-stencil FDM to produce higher-order accurate solution of PDEs in complex irregular shaped

domains when Neumann conditions are imposed on boundaries of the domain. The unique localized treatment of the stencils provides the facility to offer higher-order accurate formulation for boundary nodes without requiring special stencils for the nodes that are located on the boundaries or those adjacent to the boundaries. The real order of FDM2 is also shown in Figure 3.23 when 4th-order accurate approximation is applied for the Neumann boundaries nodes. This also indicates the potential of cut-stencil higher-order formulations to extend the same order of accuracy for internal nodes to the boundaries nodes.
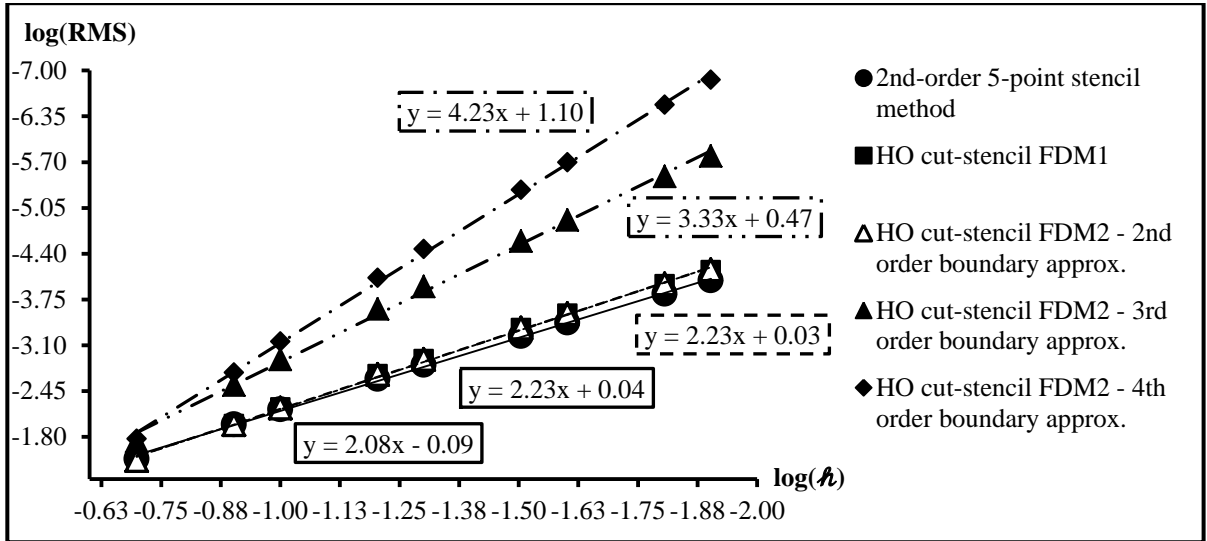
Figure 3.23: Verification plot for global order of accuracy for Problem 9.4 (diffusion equation, Neumann boundary conditions)

3.5.10 Problem 10: Cartesian Cut-Stencil FDM Solutions for Unsteady PDEs on Rectangular and Irregular Shaped Domains

The Cartesian cut-stencil method solutions to unsteady PDEs on a rectangular domain and an irregular shaped domain are studied by designing an unsteady manufactured problem. The results of the spatial and temporal LTEs are presented and the correctness of the proposed stability criteria is tested.

Problem 10.1: The cut-stencil solution to the unsteady diffusion equation $\frac{\partial \emptyset}{\partial t} = \nu \nabla^2 \emptyset$ using the explicit FTCS formulation discussed in Section 2.7, on square domain $0 \leq x, y \leq 1$ is studied. The unsteady diffusion equation considered, and the corresponding exact solution, are given by equations (3.20.1) and (3.20.2), respectively. The initial condition at time $t = 0$ and boundary conditions are taken from the exact solution.

$$\frac{\partial \emptyset}{\partial t} = \frac{1}{16}\left(\frac{\partial^2 \emptyset}{\partial x^2} + \frac{\partial^2 \emptyset}{\partial y^2}\right) \tag{3.20.1}$$

$$\emptyset_{exc.}(x, y, t) = e^{-\frac{\pi^2}{8}t} \sin(\pi x) \sin(\pi y) + x + y \tag{3.20.2}$$

The study begins with a grid size of 121 nodes to check the stability criteria. For this uniform mesh size, $x' = y' = 0.1$ and $x'' = y'' = 0$ at all nodes of the domain. Using these values of

transformation metrics and $v = 1/16$ in the stability criteria expressed by equalities (2.57.1) and (2.57.2), gives the maximum allowable time step as $\Delta t_{Max} = 0.04$. Figure 3.24 indicates the contours of the exact solution (3.20.2) at $t = 5.0$.
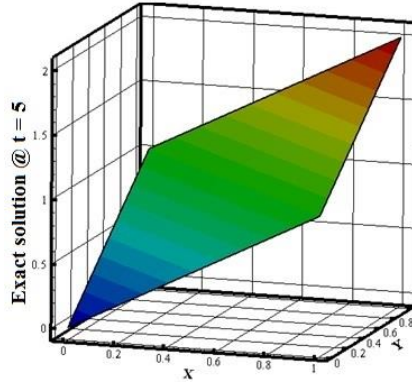
Figure 3.24: Exact solution $\phi(x, y, 5)$ for Problem 10.1 (unsteady diffusion)

Figure 3.25 show the cut-stencil FTCS solutions to equation (3.20.1) at $t = 5.0$ by taking two different time steps of $\Delta t = 0.04$ and $\Delta t = 0.05$. The solution to equation (3.20.1) using $\Delta t = 0.04$, shown in Figure 3.25(a), is stable and qualitatively similar to the exact solution in Figure 3.24. However, the contours in Figure 3.25(b) shows an unstable solution since the time step taken is larger than the maximum allowable time step calculated from the stability criteria. The maximum relative errors at $t = 5.0$ are 0.02338% and 14.25537% for the solutions using $\Delta t = 0.04$ and $\Delta t = 0.05$, respectively.
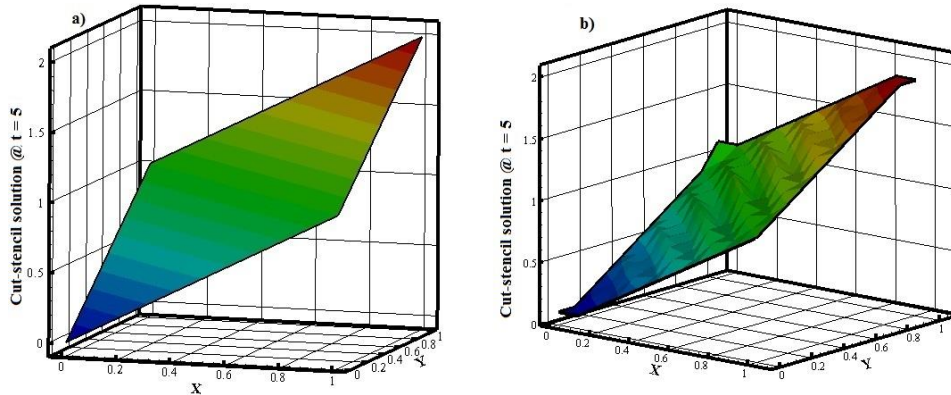
Figure 3.25: Cut-stencil FDM solution at $t = 5.0$ for grid of 121 nodes for Problem 10.1, a) $\Delta t = 0.04$, b) $\Delta t = 0.05$ (unsteady diffusion)

Four uniform grid sizes with different number of nodes varying from 36 to 1681 are used to analyze the cut-stencil FTCS solution to equation (3.20.1) by comparing the average and maximum relative errors, RMS errors and maximum spatial and temporal LTEs at an arbitrary time $t = 1.76$, as given in Table 3.22. The time step for each grid size was chosen as the maximum allowable time step for that grid size. Table 3.22 shows a reducing trend of average and maximum errors as the mesh size becomes finer and accordingly, as the time step size becomes smaller. The maximum value of temporal |LTE| follows the same behaviour as the number of nodes increase, while the spatial |LTE| becomes nearly constant. The comparison of

temporal and spatial |LTE| shows a smaller value for temporal |LTE| since, for a reduction in grid size, the value of time step must be chosen small enough to guarantee the stability criteria is satisfied. The rate of time step reduction is faster than mesh size reduction, e.g. in Table 3.22 the mesh size becomes half between two successive grids while the time step is reduced by a factor of 4 for the same grids. This suggests that the solution is more dependent on the choice of time step rather than mesh size, therefore the maximum spatial |LTE| shows an almost constant trend.

# of Nodes	Mesh size ($\hbar$)	Relative error (%)		Max. spatial |LTE|	Max. temporal |LTE|	RMS error
		Avg.	Max.			
36	0.2	1.01404	1.68829	1.208E-2	1.169E-2	1.05E-2
121	0.1	0.21049	0.41136	1.176E-2	3.452E-3	2.28E-3
441	0.05	0.04786	0.10247	1.174E-2	8.670E-4	5.37E-4
1681	0.025	0.01140	0.02565	1.173E-2	2.169E-4	1.31E-4

Table 3.22: Comparison of relative error, spatial and temporal truncation error and RMS error at $t = 1.76$ for Problem 10.1 (unsteady diffusion)

The spatial and temporal truncation errors, as given in Table 3.22, are calculated using equations (3.2.5.1) and (3.7.2), respectively. Verification of the global order of accuracy for spatial discretization can be observed in Figure 3.26. The slope of the line in this figure confirms the 2nd-order accurate cut-stencil FTCS solution to equation (3.20.1).
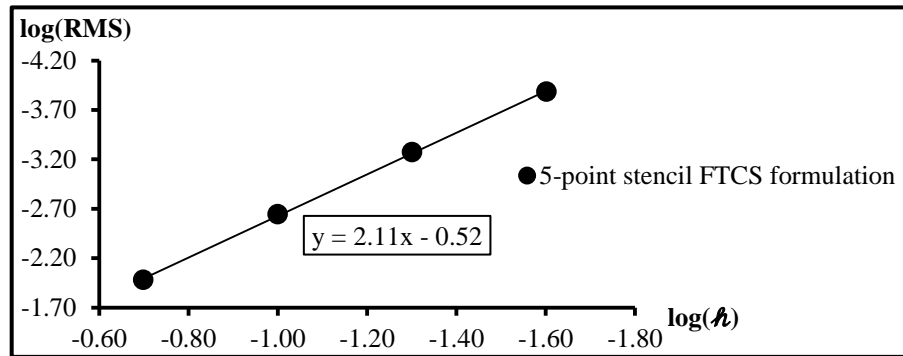
Figure 3.26: Verification plot for global order of accuracy for spatial discretization for Problem 10.1 (unsteady diffusion)

Problem 10.2: The unsteady diffusion equation (3.20.1) is solved in the complex irregular shaped domain illustrated in Figure 3.27, using a grid size of 67 nodes. The stability criteria give the maximum allowable time step as $\Delta t_{Max} = 0.0625$. Similar to solution of equation (3.20.1) in the unit square domain, the exact solution and cut-stencil FTCS solution at $t = 3.0$ using $\Delta t = \Delta t_{Max.}$ and $\Delta t = 0.075$, are presented in Figure 3.28 to verify the proposed stability requirements for an irregular shaped domain.
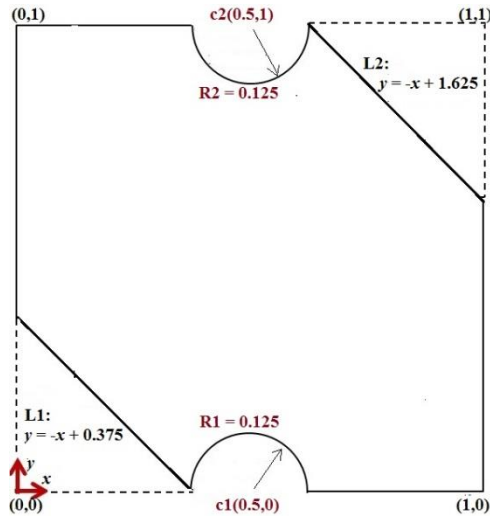
Figure 3.27: Irregular shaped domain for Problem 10.2 (unsteady diffusion)
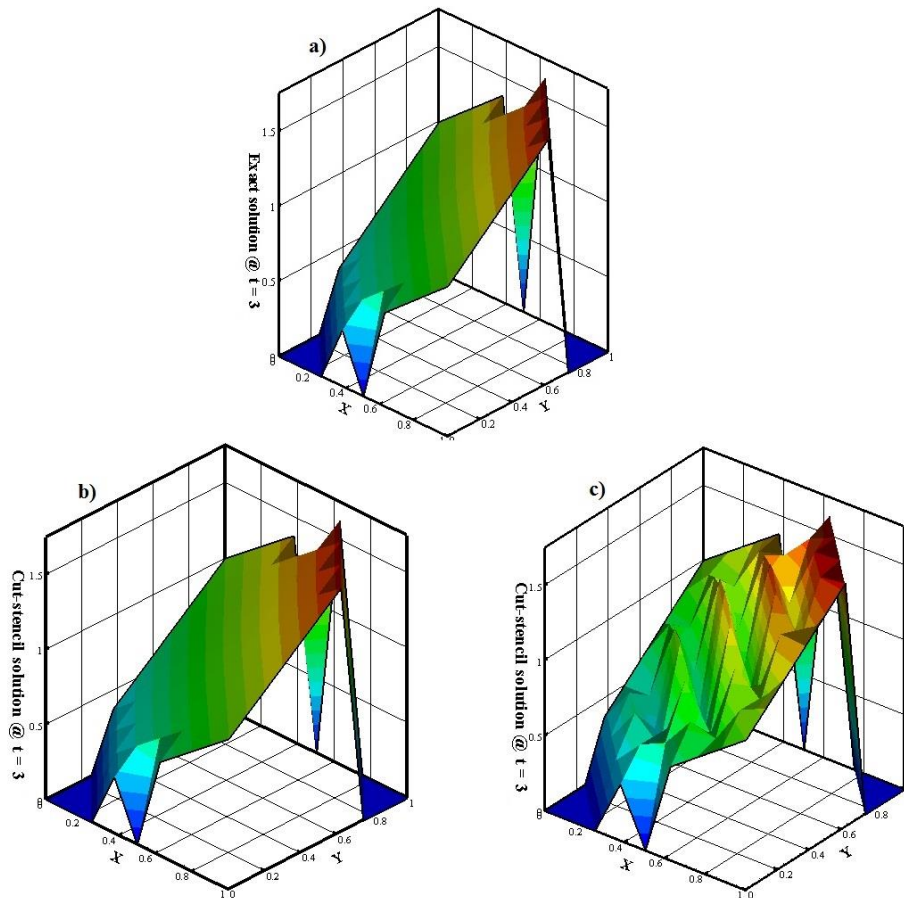
Figure 3.28: Exact and cut-stencil FDM solutions at $t = 3.0$ for grid of 67 nodes for Problem 10.2, a) exact solution, b) $\Delta t = \Delta t_{\text{Max}}$, c) $\Delta t = 0.075$ (unsteady diffusion, irregular domain)

The maximum relative errors for Δt_{Max} and $\Delta t = 0.075$ are equal to 0.16% and 37.95%, respectively. This example shows the capability of the cut-stencil FDM to solve the unsteady

diffusion equation on a complex irregular domain and verifies the accuracy of the proposed stability criteria for the central in space, explicit Euler time marching scheme.

The average and maximum relative errors and maximum spatial and temporal LTEs, for solution of equation (3.20.1) on the irregular shaped domain shown in Figure 3.27, for several sample times using Δt_{Max} as the time step, are presented in Table 3.23.

Time	Relative error (%)		Max. spatial |LTE|	Max. temporal |LTE|
	Avg.	Max.		
1.0	0.38121	0.68863	1.064	1.427E-2
3.5	0.04710	0.09275	1.003	6.029E-4
4.0	0.02699	0.05327	1.002	3.226E-4
8.25	0.00017	0.00034	1.000	1.700E-6
10.5	0.00001	0.00002	1.000	1.000E-7
11.6875	0.00000	0.00000	1.000	0.000
11.75	0.00000	0.00000	1.000	0.000

Table 3.23: Average and relative errors and LTEs at different time with $\Delta t = 0.0625$ for Problem 10.2 (unsteady diffusion, irregular domain)

The data in Table 3.23 shows that the unsteady solution is marching to steady-state condition almost after $t = 10.5$ and, similar to solution of equation (3.20.1) on the unit square domain, the maximum temporal \|LTE\| is relatively smaller than maximum spatial \|LTE\|. Additionally, the variation of spatial \|LTE\| shows an almost constant trend while until time $t = 10.5$, the temporal \|LTE\| is reducing. As the solution reaches the steady-state condition, both LTEs follow a constant trend.

3.5.11 Problem 11: Cut-Stencil FDM Solution for Second-Order Wave Equation on Rectangular and Irregular Shaped Domains

The manufactured problem method is used to test the capability of the cut-stencil FDM to solve the model second-order wave equation (2.58.1) and assess the accuracy of the discretization represented in equation (2.58.3). The stability requirement, as proposed in equation (2.65.4) for this model equation, is discussed through this sample problem. The effects of the two proposed methods of approximating the first time derivative at initial time (for the initial condition), i.e. equations (2.59.1) and (2.62.1), are also investigated.

Problem 11.1: In this example the cut-stencil FD solution to the model equation $\frac{\partial^2 \emptyset}{\partial t^2} = C^2 \nabla^2 \emptyset$ on a unit square domain is proposed. The second-order wave equation and the corresponding exact solution are written in equations (3.21.1) and (3.21.2), respectively. The initial conditions, i.e. including $\emptyset(x, y, t_0)$ and $\frac{\partial \emptyset}{\partial t}\big|_{t_0}$, and boundary conditions are taken from the exact solution when the initial time is set as $t = 0$.

$$\frac{\partial^2 \emptyset}{\partial t^2} = \frac{\partial^2 \emptyset}{\partial x^2} + \frac{\partial^2 \emptyset}{\partial y^2} \tag{3.21.1}$$

$$\emptyset_{exc.}(x, y, t) = sin(0.3\pi x + 0.4\pi y - 0.5\pi t) + 1.1 \tag{3.21.2}$$

Figure 3.29 demonstrates the exact solution and the Cartesian cut-stencil FD solution of equation (3.21.1) at time $t = 0.84$ for two time step sizes of $\Delta t = 0.035$ and $\Delta t = 0.04$ for a grid of 441 nodes. The stability criteria, as addressed in equation (2.65.4), gives the maximum allowable time step as $\Delta t_{Max} = 0.035$ for this grid size. The solution at a time of 0.84 obtained by taking $\Delta t = 0.04$, which exceeds the maximum allowable time step, is clearly unstable. The average and maximum relative errors, for the case of $\Delta t = 0.035$, are equal to 0.005% and 0.015%, respectively. These same errors are greater than 141% and, almost 1357%, for the (unstable) solution using $\Delta t = 0.04$.
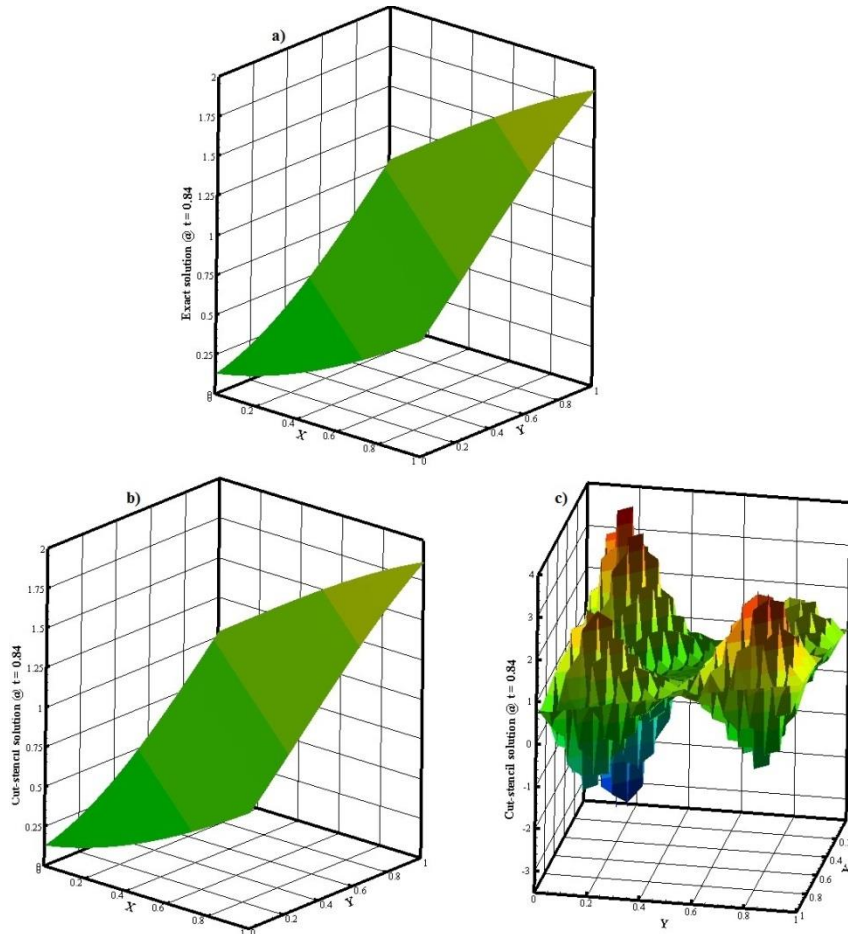
Figure 3.29: Exact and cut-stencil FDM solutions at $t = 0.84$ for grid of 441 nodes for Problem 11.1, a) exact solution, b) $\Delta t = 0.035$, c) $\Delta t = 0.04$

Several uniform grid sizes with number of nodes varying from 81 to 4225 are used to analyze the cut-stencil solution to equation (3.21.1) when a 1st-order accurate approximation and a 2nd-order accurate approximation are applied to approximate the first temporal derivative at initial time. The average and maximum relative error for each grid size and for each approximation scheme are given in Table 3.24, at a time $t = 1.326$. The time step for each grid size was chosen as the maximum allowable time step for grid size studied. The data in Table 3.24 shows significant reduction in the average and maximum relative errors in the event of using the 2nd-order accurate approximation for the temporal derivative at initial time.

# of Nodes	Mesh size ($\hbar$)	Order used for $\left.\dfrac{\partial \emptyset}{\partial t}\right|_{t_0}$	Relative error (%) Avg.	Max.	RMS error at internal nodes
81	0.125	1st-order	2.79269	10.03626	7.66E-3
		2nd-order	0.05158	0.11301	1.64E-4
289	0.0625	1st-order	1.13484	5.20238	3.64E-3
		2nd-order	0.01183	0.03309	4.03E-5
1089	0.03125	1st-order	0.51847	2.84008	1.76E-3
		2nd-order	0.00273	0.00931	9.80E-6
4225	0.015625	1st-order	0.24988	1.47917	8.63E-4
		2nd-order	0.00066	0.00241	2.41E-6

Table 3.24: Comparison of relative and RMS errors at $t = 1.326$ for Problem 11.1 (second-order wave equation)

The real order of the cut-stencil FD solutions to equation (3.21.1) can be observed in the plot of Figure 3.30, for the two methods used for approximation of the temporal derivative at initial time. The slopes of the lines in this figure indicate that the solution is 1st-order or 2nd-order accurate when that order of approximation is applied to approximate the first derivative at initial time. This suggests that the lower order of approximation, used to approximate the first derivative at initial time, propagates through the whole solution for this unsteady equation. On the other hand, when the time derivative at initial time is approximated by a 2nd-order accurate approximation, the overall solution retains its 2nd-order accuracy. Thus, it might be stated that the real order of accuracy for the solution of the unsteady model equation depends strictly on the order of approximation applied at initial time.
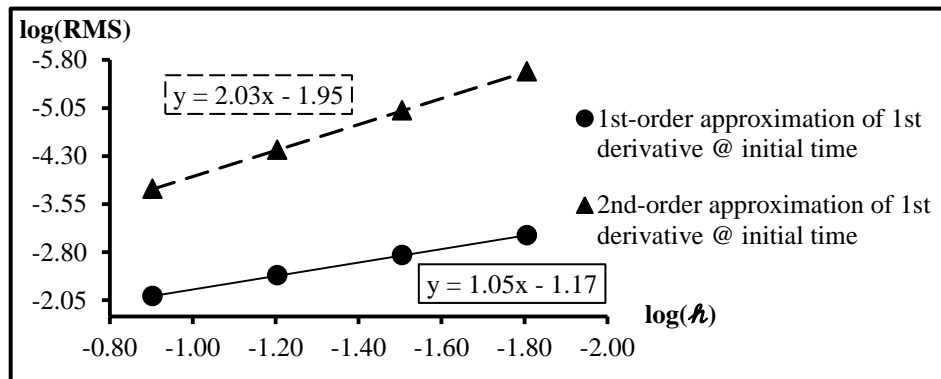
Figure 3.30: Verification plot for global order of accuracy for initial time discretization for Problem 11.1 (second-order wave equation)

Problem 11.2: The Cartesian cut-stencil FD solution of equation (3.21.1) on the irregular shaped domain depicted in Figure 3.31 with 79 nodes is considered in this final problem. The stability criteria produce the maximum allowable time step as $\Delta t_{Max} = 0.142$. At first, the absolute errors (absolute difference between the numerical and exact solution) at the centre point of the domain, where $x = y = 1$, from initial time up to 1.92, for two time steps of $\Delta t = 0.12$ and $\Delta t = 0.16$, have been compared in Figure 3.32.
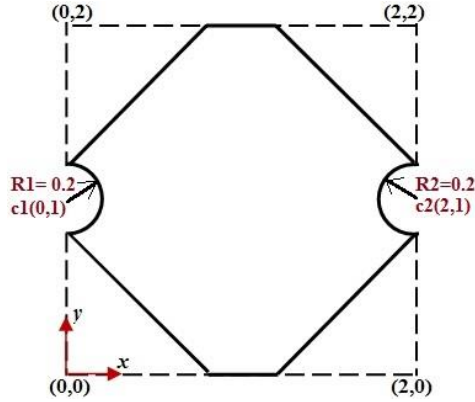
Figure 3.31: Irregular shaped domain for Problem 11.2 (second-order wave equation)

The magnitude of the absolute error for the time step $\Delta t = 0.16$ shows that the solution becomes unbounded, as expected since the time step is larger than the maximum allowable time step for stability. However, by choosing a step almost equal to the maximum allowable time step, the same parameter shows uniform behaviour as the solution proceeds with time.
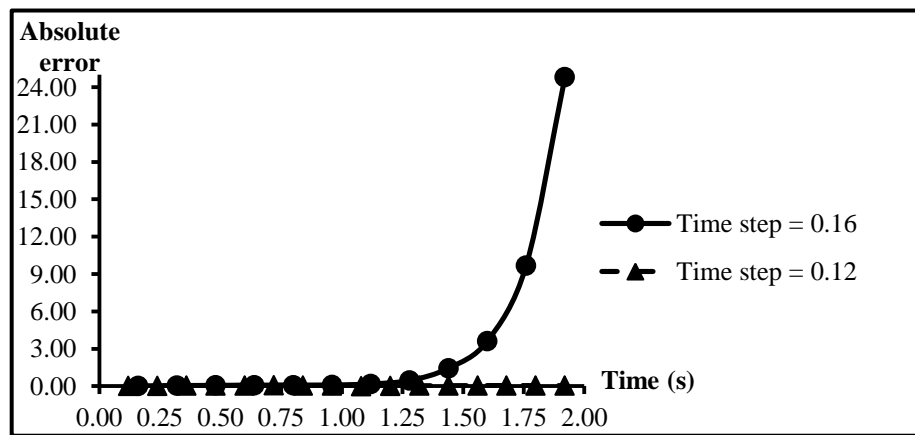
Figure 3.32: Absolute error at midpoint of the domain for two step sizes for Problem 11.2 (wave equation, irregular shaped domain)

The relative error in the cut-stencil FD solutions of equation (3.21.1), at $t = 1.42$, using 1st-order and 2nd-order accurate approximation methods to approximate the first-order time derivative at initial time, have been recorded in Table 3.25. The time step was set as $\Delta t = 0.142$. The results verify the effect that higher-order approximation of the first-order time derivative at initial time has on the whole solution. Additionally, the results given in Table 3.25 show the capability of the Cartesian cut-stencil FDM to solve the second-order wave equation on irregular shaped domains.

Order used for $\frac{\partial \emptyset}{\partial t}\big|_{t_0}$	Relative error (%)	
	Avg.	Max.
1st-order	3.12747	11.49735
2nd-order	0.11337	0.47351

Table 3.25: Comparison of relative error at t = 1.42 for Problem 11.2 (wave equation, irregular shaped domain

3.6   Chapter Summary

Cartesian cut-stencil FDM solutions to the unsteady and steady convection-diffusion equations have been presented in this chapter. The main purpose of this chapter was to use the method of manufactured solutions (MMS) to verify the cut-stencil formulations and implementation of the various approximations developed in Chapter 2.

The verification of the cut-stencil formulations and corresponding computer coding was carried out by comparing the cut-stencil FDM solutions to exact solutions for a variety of manufactured equations. The cut-stencil FDM solutions on rectangular domains were presented to verify the real order of accuracy of each formulation. A systematic grid refinement study along with the RMS error for each grid was employed to confirm the real order of accuracy. Solution of the convection-diffusion equation in irregular shaped domains exhibited the capabilities of the cut-stencil FDM to solve PDEs in any type of complex domain. The solutions for a number of problems were presented for a non-uniform mesh, in domains much more complicated than rectangles and with different types of boundary conditions, i.e., Dirichlet or Neumann conditions.

It was confirmed that the 2nd-order 5-point stencil formulation retained this order as the real order of accuracy. The higher-order formulations showed different real order of accuracy depending on the type of boundary condition, order of approximation employed to approximate Neumann conditions and the order of approximation of derivatives at the endpoints of the computational stencil. HO cut-stencil FDM solutions to a sample problem, with Neumann conditions approximated by 2nd-, 3rd- and 4th-order accuracy, were discussed. The higher-order approximation of the Neumann condition shows that order of accuracy higher than 3rd and 4th can be captured using HO cut-stencil FDM2 when 3rd- and 4th-order accurate approximations were employed to approximate the Neumann condition.

The effect of central or upwind differencing of convective terms on the real order of accuracy was discussed and illustrated through several examples. Also, for most cases, the maximum local absolute truncation error (|LTE|) was presented for each grid size which demonstrated the potential of the Cartesian cut-stencil FDM to calculate high-fidelity solutions of very complicated PDEs in any type of domain and quantitatively assess the numerical error.

For the unsteady problems, the validity of suggested stability criteria and level of accuracy for the cut-stencil FDM solutions were studied through solution of manufactured unsteady diffusion equations in regular and irregular shaped domains. Similarly, these features were also discussed for the solution of the model second-order wave equation.

CHAPTER 4

CARTESIAN CUT-STENCIL FDM SOLUTIONS to SOLID MECHANICS and HEAT TRANSFER PROBLEMS

4.1 Objective of the Chapter

The sample problems discussed in Chapter 3 demonstrated the capabilities and potential of the Cartesian cut-stencil FDM to solve PDEs on regular and irregular domains for manufactured problems which may not define any real physical problem. The aim of this chapter is to discuss and solve a number of PDEs which model real phenomenon in science and engineering. In the event that the analytical solution is not available for a specific problem, the cut-stencil FD solution is compared to other numerical results obtained from commercial software. The cut-stencil FD solution to some basic problems of advanced elasticity that are associated with solid mechanics and problems in heat transfer are considered in this chapter.

The problems of solid mechanics, e.g. in civil engineering, fracture mechanics and contact problems of solid bodies, have been widely analyzed and solved for several decades by applying the finite element method (FEM). This numerical method is the most popular approach in these fields [136, 137, 138]. The specific advantage of FEM for problems in solid mechanics field arises from the fact that FEM can easily be applied to complex domains, e.g. with curved boundaries. However the TFDM, as mentioned in Chapter 1, has a serious restriction in that it cannot easily accommodate a complex and irregular domain. The sample problems discussed in Chapter 3 were selected to provide proof that, in spite of the straightforward formulation and coding procedure of the cut-stencil FDM, it is able to solve PDEs on complex and irregular shaped domains.

The main body of this chapter covers some basic PDEs in advanced elasticity and heat transfer and the Cartesian cut-stencil FDM solutions to the governing equations are presented in the context of some numerical examples.

Due to the developing nature of the cut-stencil method/algorithm, which is the main focus of this research, only the 2nd-order 5-point cut-stencil solution scheme for steady problems and FTCS formulation for unsteady problems will be discussed through this chapter. Higher-order solutions of these problems, in either space or time, are left as the future research.

4.2 Application of Cut-Stencil FDM in Elasticity

The Saint-Venant's torsional problem for a bar with elliptical cross-section, as a classical problem in the field of elasticity, is discussed in this section. The torsional problem can be stated by the use of Prandtl's stress function [139]. The cut-stencil FDM formulation and solution for Prandtl's stress function for torsion of an irregular shaped cross-section, e.g. elliptical cross-section of bar are considered, as well as the solution for the stress function for bending of a cantilever beam with the same cross-section.

4.2.1 Stress Function of Torsion for Straight Bars

Consider a uniform cylindrical bar of an arbitrary cross-section that is fixed at plane $z = 0$, as depicted in Figure 4.1. It is assumed that the bar is subjected to no body and external forces on its

lateral surfaces. The bar is twisted by a couple in the plane $z = l$ and the moment of the couple is directed along the axis of the bar.
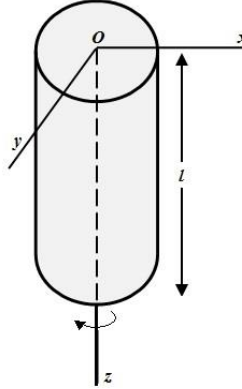
Figure 4:1: Cylindrical bar subjected to torsional torque

The deformation of the twisted shaft, according to Saint-Venant's assumptions, includes rotations and warping of the cross-section. The displacement of any point in the xy-plane corresponding to the rotation of the cross-section can be defined by $u = -\theta_z y$ and $v = -\theta_z x$ where u and v represent the displacement along x and y axes, respectively, and θ_z is the angle of rotation of the cross -section at distance z from the origin. The parameter ψ is considered as function of x and y to define the warping (ω) of the cross-section by $\omega = \theta\psi(x, y)$ where θ is angle of twist of the bar. It can be shown that, to satisfy the equilibrium equation, the function $\psi(x, y)$ should satisfy the Laplace equation

$$\frac{\partial^2 \psi}{\partial x^2} + \frac{\partial^2 \psi}{\partial y^2} = 0 \qquad (4.1.1)$$

Considering the fact that the system of stresses must satisfy the boundary conditions of the equilibrium equation on the lateral surface of the cross-section, along with some mathematical manipulations, will lead to expressions for the shearing stresses τ_{xz} and τ_{yz}:

$$\tau_{xz} = \frac{\partial \emptyset}{\partial y} ; \tau_{yz} = -\frac{\partial \emptyset}{\partial y} \qquad (4.1.2)$$

where $\emptyset(x, y)$ is called the Prandtl's stress function. This function satisfies Poisson's equation given in equation (4.1.3), in which the constant G is called the "modulus of elasticity in shear" or the "modulus of rigidity".

$$\frac{\partial^2 \emptyset}{\partial x^2} + \frac{\partial^2 \emptyset}{\partial y^2} = F = -2G\theta \qquad (4.1.3)$$

The boundary conditions for the equilibrium equation declares that the stress function must be constant along the boundary of the solid bar cross-section. This condition is normally stated as $\psi(x, y) = 0$ along the boundary of the cross-section and this will be used in the following discussion. The derivation procedure and comprehensive concepts of the stress function for torsion have been stated in mathematical and theoretical elasticity texts such as [140, 141] and

also in numerical studies [142]. The discussion above has been adopted from these references or similar texts.

If the boundary of the cross-section, as shown in Figure 4.2, is defined by the equation of an ellipse, that is $\frac{x^2}{a^2} + \frac{y^2}{b^2} - 1 = 0$, one can prove that equation (4.1.3) can be satisfied by taking the function in equation (4.1.4) as Prandtl's stress function. Equation (4.1.4) also satisfies the boundary conditions of the equilibrium equation and is equal to zero along the boundary.
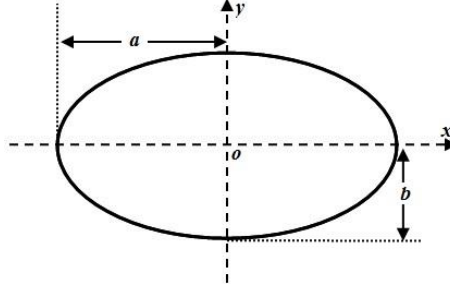
Figure 4.2: Illustration of elliptical cross-section of a bar

$$\phi = \frac{a^2 b^2 F}{2(a^2 + b^2)} \left(\frac{x^2}{a^2} + \frac{y^2}{b^2} - 1 \right) \tag{4.1.4}$$

The mapped form of equation (4.1.3) under the transformation equation $x = x(\xi)$ and $y = y(\eta)$ introduced by equations (2.4) is given in equation (4.2.1). Central differencing for the derivatives in equation (4.2.1), at point P of the computational stencil, gives the 2nd-order accurate approximation for equation (4.2.1), which has been written in equation (4.2.2).

$$\frac{1}{(x')^2} \frac{\partial^2 \phi}{\partial \xi^2} - \frac{x''}{(x')^3} \frac{\partial \phi}{\partial \xi} + \frac{1}{(y')^2} \frac{\partial^2 \phi}{\partial \eta^2} - \frac{y''}{(y')^3} \frac{\partial \phi}{\partial \eta} = F \tag{4.2.1}$$

$$\frac{1}{(x_P')^2} [\phi_w - 2\phi_P + \phi_e] - \frac{x_P''}{2(x_P')^3} [\phi_e - \phi_w]$$
$$+ \frac{1}{(y_P')^2} [\phi_s - 2\phi_P + \phi_n] - \frac{y_P''}{2(y_P')^3} [\phi_n - \phi_s] = F \tag{4.2.2}$$

The irregularity of the domain causes creation of irregular boundary nodes on the boundary. This type of node is created even if a uniform Cartesian grid is designed to mesh this cross-section, as seen for the grids depicted in Figure 4.3. The unique localized one-dimensional mappings used in the cut-stencil FDM provides the facility to treat these boundary nodes and offers a fully 2nd-order accurate solution, even for a non-uniform mesh, as illustrated in Chapter 3.

The cut-stencil solution of equation (4.1.3) with $F = -1$, by taking $a = 5$ and $b = 2.5$ for the elliptical cross-section shown in Figure 4.2, is reported in Table 4.1. A number of Cartesian grids were constructed for this problem, as indicated by the corresponding numbers of nodes in Table 4.1. Schematics of a grid of 54 nodes for the full elliptical cross-section and a grid of 38 nodes for the half cross-section are illustrated in Figure 4.3. Several regular and irregular types of boundary nodes and the corresponding cut stencils are clearly seen along the boundaries.
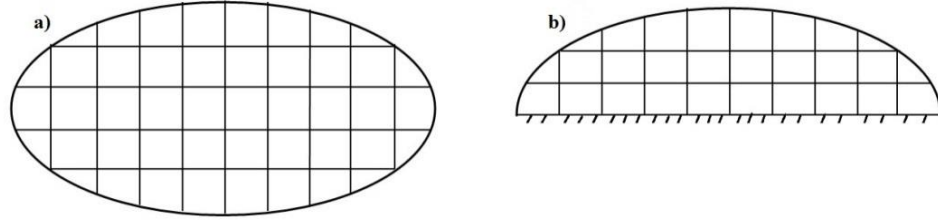
Figure 4.3: Schematic of grids used for elliptical cross-section, a) grid of 54 nodes, b) grid of 38 nodes

The symmetry of the elliptical cross-section provides the opportunity to impose Neumann boundary conditions on the major and minor axes. To do this, the half and quarter elliptical cross-sections were chosen, as depicted in Figure 4.4, and Neumann conditions taken from the exact solution were imposed on the south boundary corresponding to $y = 0$ for one case, the west boundary corresponding to $x = 0$ for another case, as well as on both south and west boundaries.
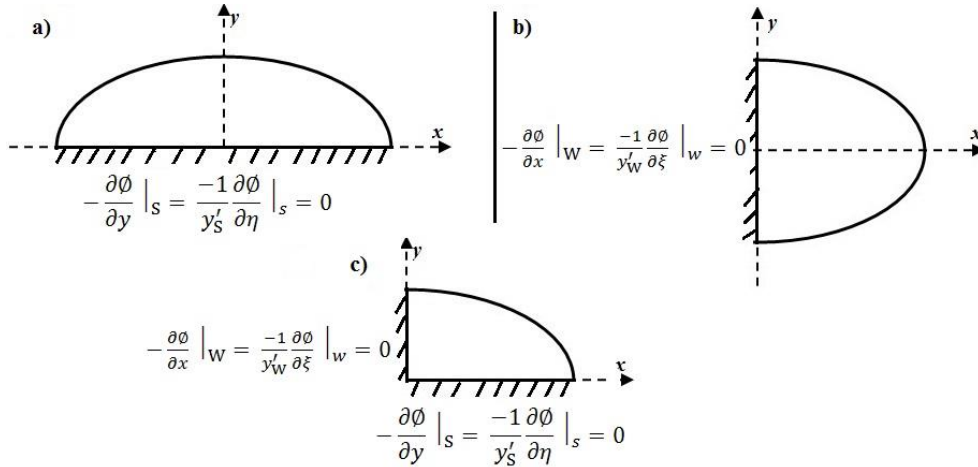
Figure 4.4: Illustration of half and quarter elliptical cross-sections with Neumann condition imposed, a) south, b) west, c) south and west boundaries

Boundary condition	# of nodes	Rel. error at internal nodes (%)		Rel. error at boundary nodes (%)	
		Avg.	Max.	Avg.	Max.
Dirichlet (full domain)	54	0.80437	2.89997	-	-
	97	0.19255	0.98111	-	-
Neumann (south - half domain)	38	0.44322	0.92870	0.28950	0.34655
Neumann (west - half domain)	38	0.20448	0.32780	0.16137	0.32780
Neumann (south & west – quarter domain)	21	0.41934	0.91663	0.30808	0.47767

Table 4.1: Relative error for cut-stencil solution to Prandtl's stress function for torsion of a bar with elliptical cross-section

The data in Table 4.1 shows good agreement of the cut-stencil FD solution with the exact solution of Prandtl's stress function for torsion of an elliptical cross-section. Grid refinement for the case

of Dirichlet boundary conditions demonstrates that the error decreases as the number of grid points increases. The cases with imposed Neumann conditions on the boundaries confirms the accuracy of the differencing formula for this type of boundary, as already discussed for the manufactured problems, for this type of real engineering application.

4.2.2   Stress Function for Bending of Bars

In the case when a bar is bent in one of its principal planes and subjected to two equal and opposite couples at the ends, only the normal stress parallel to the axis of the bar will be non-zero [140]. Figure 4.5 displays a cantilever beam with constant cross-section of arbitrary shape while a force of magnitude P is applied at the end and parallel to one of the principal axes of the bar cross-section. In case of pure bending, the normal stress is calculated by $\sigma_z = -\frac{P(l-z)x}{I}$ where I is the moment of inertia of the cross-section.
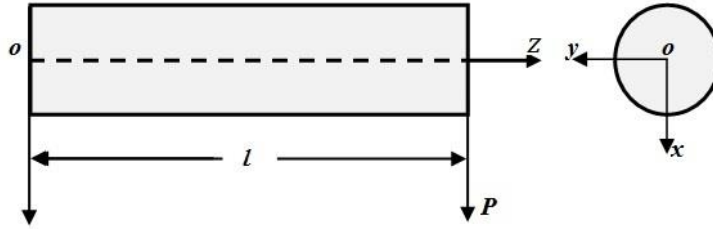
Figure 4.5: Illustration of cantilever beam under bending moment at the end

It can be shown that the three components of stresses σ_z, τ_{xz} and τ_{yz} are non-zero. Taking this assumption along with neglecting body forces, one can conclude from the equilibrium equation that these stresses are not dependent on z, i.e. they are the same in all cross-sections of the bar. The compatibility equations are cast in the form $\nabla^2 \tau_{yz} = 0$ and $\nabla^2 \tau_{xz} = -\frac{P}{I(1+\vartheta)}$ in which ϑ is Poisson's ratio. Therefore, the solution of bending of a prismatic cantilever beam requires finding functions of x and y which satisfy the equilibrium equation, the boundary conditions and the reduced form of compatibility equations [140].

The solution procedure benefits from the definition of the stress function $\emptyset(x, y)$. The stress function can be determined from the equilibrium equations, which are satisfied by taking τ_{xz} and τ_{yz} as:

$$\tau_{xz} = \frac{\partial \emptyset}{\partial y} - \frac{Px^2}{2I} + f(y) \tag{4.3.1.1}$$

$$\tau_{yz} = -\frac{\partial \emptyset}{\partial x} \tag{4.3.1.2}$$

where $f(y)$ is only a function of y. These determined forms of τ_{xz} and τ_{yz} are substituted in the compatibility equations and, taking zero for the constant of integration, it can be shown that the stress function is governed by the Poisson equation

$$\frac{\partial^2 \emptyset}{\partial x^2} + \frac{\partial^2 \emptyset}{\partial y^2} = \frac{\vartheta}{1+\vartheta}\frac{Py}{I} - \frac{df}{dy} \tag{4.3.2}$$

Function f is determined from the boundary conditions and, similar to the case of stress function for torsion, ϕ is constant along the boundary and normally set as zero. For the case of an elliptical cross-section with boundary equation $\frac{x^2}{a^2} + \frac{y^2}{b^2} - 1 = 0$, the function $f(y)$ can be chosen as in equation (4.3.3) to satisfy the boundary conditions of the equilibrium equation. Substituting $f(y)$ in equation (4.3.2) gives the Poisson equation (4.3.4) for the stress function of bending for the bar of elliptical cross-section:

$$f(y) = -\frac{P}{2I}\left(\frac{a^2}{b^2}y^2 - a^2\right) \tag{4.3.3}$$

$$\frac{\partial^2 \emptyset}{\partial x^2} + \frac{\partial^2 \emptyset}{\partial y^2} = \frac{Py}{I}\left(\frac{a^2}{b^2} + \frac{\vartheta}{1+\vartheta}\right) \tag{4.3.4}$$

The analytical solution of equation (4.3.4), along with the condition of $\phi = 0$ at the boundary, yields the stress function

$$\phi = \frac{(1+\vartheta)a^2 + \vartheta b^2}{2(1+\vartheta)(3a^2 + b^2)}\frac{P}{I}\left(x^2 + \frac{a^2}{b^2}y^2 - a^2\right)y \tag{4.3.5}$$

On the computational 5-point stencil, the mapped form of equation (4.3.4) and its corresponding discrete form, using 3-point central differencing of first and second derivatives at point P, are given by:

$$\frac{1}{(x')^2}\frac{\partial^2 \emptyset}{\partial \xi^2} - \frac{x''}{(x')^3}\frac{\partial \emptyset}{\partial \xi} + \frac{1}{(y')^2}\frac{\partial^2 \emptyset}{\partial \eta^2} - \frac{y''}{(y')^3}\frac{\partial \emptyset}{\partial \eta} = \frac{Py}{I}\left(\frac{a^2}{b^2} + \frac{\vartheta}{1+\vartheta}\right) \tag{4.4.1}$$

$$\frac{1}{(x_P')^2}[\phi_w - 2\phi_P + \phi_e] - \frac{x_P''}{2(x_P')^3}[\phi_e - \phi_w]$$

$$+ \frac{1}{(y_P')^2}[\phi_s - 2\phi_P + \phi_n] - \frac{y_P''}{2(y_P')^3}[\phi_n - \phi_s] = \frac{Py_P}{I}\left(\frac{a^2}{b^2} + \frac{\vartheta}{1+\vartheta}\right) \tag{4.4.2}$$

The results for the bending stress function of a bar of elliptical cross-section with $a = 5$, $b = 2.5$ and $\vartheta = 0.35$ $P = 1000$, are reported in Table 4.2. For those cases involving Neumann boundary conditions, the value of the normal derivative of the stress function was taken from equation (4.3.5).The Neumann condition is imposed on the north boundary, corresponding to the line $x= 0$ (referring to Figure 4.5) where the lower half of the ellipse was taken as the domain of the problem. Comparison of results for cases with Neumann condition on south and north boundaries verifies the symmetry of the solution captured by the cut-stencil solution procedure and confirms the accuracy of the calculations and the corresponding code.

Boundary condition	# of nodes	Abs. error at internal nodes		Abs. error at boundary nodes	
		Avg.	Max.	Avg.	Max.
Dirichlet (full domain)	54	0.13689	0.35617	-	-
	97	0.05499	0.18960	-	-
Neumann (south – half domain)	38	0.07609	0.17225	0.10204	0.22966
Neumann (west – half domain)	38	1.12580	2.22102	4.67888	5.43839
	54	0.54749	1.31315	1.91955	2.30357
Neumann (north – half domain)	38	0.07609	0.17225	0.10204	0.22966

Table 4.2: Absolute error for cut-stencil solution of Prandtl's stress function for bending of a bar with elliptical cross-section beam

4.3   Application of Cut-Stencil FDM to Heat Transfer Problems on Regular and Irregular Shaped Domains

A large number of research studies have been done to consider heat transfer and related subjects due to its wide range of applications in several areas of engineering and science [97, 143, 144, 145, 146]. The complexity of heat transfer phenomena and the various geometries studied precludes the development of analytical solutions for these problems, so numerical methods must be applied to solve such heat transfer problems.

The cut-stencil FDM, which has been shown to accurately solve PDEs in irregular shaped domains, can be used to solve heat transfer problems in any type of domain. For this purpose, the cut-stencil solution of steady and unsteady conduction heat transfer will be discussed in the following sub-sections. The cut-stencil FDM results are compared to the exact analytical solution, if available, or to the results from commercial software.

4.3.1   Steady Conduction Heat Transfer in a Rectangular Domain

The Laplace equation (4.5.1) is a model for steady state 2-D heat conduction provided the thermal conductivity is assumed to be constant and no heat is generated in the domain.

$$\frac{\partial^2 T}{\partial x^2} + \frac{\partial^2 T}{\partial y^2} = 0 \qquad (4.5.1)$$

The analytical solution of equation (4.5.1) can be derived using the separation of variable technique for limited cases of boundary conditions on a rectangular domain. It is assumed that the temperature $T(x, y)$ can be written as the product of two functions, one depending only on x and the other depending only on y. The rectangular plate shown in Figure 4.6 is considered with three sides of the plate maintained at constant temperature T_1 and the fourth side held at T_2.
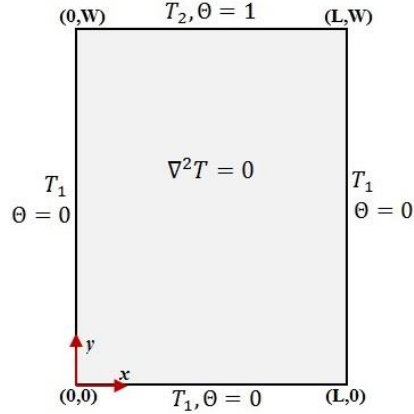
Figure 4.6: Two dimensional steady conduction heat transfer in a rectangular plate

The non-dimensional variable Θ, defined by

$$\Theta = \frac{T - T_1}{T_2 - T_1} \tag{4.5.2}$$

also satisfies the Laplace equation and holds the temperature between 0 and 1. The boundary conditions for this variable are described in Figure 4.6.

One can seek a solution of Θ as the product of two functions, i.e., $\Theta(x, y) = X(x)Y(y)$. Using this form of function, the governing equation can be separated as:

$$-\frac{1}{X}\frac{\partial^2 X}{\partial x^2} = \frac{1}{Y}\frac{\partial^2 Y}{\partial y^2} = \lambda^2 \tag{4.5.3.1}$$

where λ is a constant. The general solutions of these two ordinary differential equations are:

$$X = A_1 \cos(\lambda x) + A_2 \sin(\lambda x) \tag{4.5.3.1}$$
$$Y = B_1 e^{\lambda y} + B_2 e^{-\lambda y} \tag{4.5.3.2}$$

and the function Θ is given by the product

$$\Theta = (A_1 \cos(\lambda x) + A_2 \sin(\lambda x))(B_1 e^{\lambda y} + B_2 e^{-\lambda y}) \tag{4.5.4.1}$$

The proposed form of Θ in equation (4.5.4.1) must satisfy the boundary conditions shown in Figure 4.6, yielding the values of the coefficients A_1, A_2, B_1 and B_2. Replacing these coefficients in equation (4.5.4.1), along with some mathematical concepts such as the property of orthogonal functions or expansion of unity in a Fourier series, determines the final form of Θ as a convergent infinite series, as written in equation (4.5.4.2). Detail for this solution technique has been discussed in most heat transfer text books such as [147, 148].

$$\Theta = \frac{2}{\pi} \sum_{n=1}^{\infty} \frac{(-1)^{n+1} + 1}{n} \sin\left(\frac{n\pi x}{L}\right) \frac{\sinh(n\pi y/L)}{\sinh(n\pi W/L)} \tag{4.5.4.2}$$

The cut-stencil solution of the steady heat conduction in a rectangular plate with L = W = 1, and with boundary conditions $T_1 = 300$ and $T_2 = 310$, as displayed in Figure 4.6, is presented and the results are compared to exact solution (4.5.4.2) and two commercial software. A Cartesian grid of 81 nodes was designed to solve this problem by the cut-stencil FDM. Finite volume and finite element grids with the same number of nodes were also constructed for ANSYS FLUENT as a finite volume FV-based solver and ANSYS Mechanical as a finite element FE-based solver. Figure 4.7 shows a plot of the numerical solutions at internal nodes versus the corresponding number of nodes which are listed in Table 4.3.
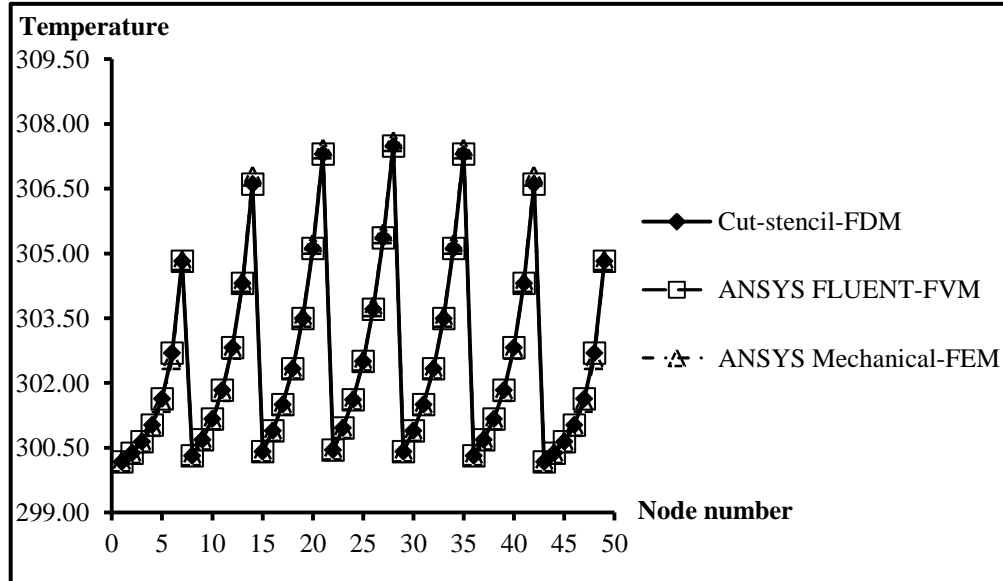
Figure 4.7: Comparison of cut-stencil FDM with FVM and FEM for 2-D steady conduction heat transfer in a rectangular plate

Figure 4.7 demonstrates that there is good agreement between the cut-stencil FDM solution and that obtained from FVM and FEM. Figure 4.7 gives a qualitative comparison of the different numerical methods while the value of temperature at each node predicted by each of the three numerical methods are given in Table 4.3, along with the analytical solution at each of these nodes, calculated from the first nine terms of the series (4.5.4.2). It is evident from this table that the cut-stencil FD method provides the same level of accuracy as the well-established FV and FE methods.

| Node | Coordinate | | FDM* | FVM** | FEM*** | Analytical |
no.	x	y	cut-stencil	ANSYS FLUENT	ANSYS Mechanical	solution
1	0.125	0.125	300.17	300.17	300.17	300.17
2	0.125	0.25	300.38	300.38	300.36	300.37
3	0.125	0.375	300.64	300.64	300.62	300.63
4	0.125	0.5	301.03	301.03	300.99	301.01
5	0.125	0.625	301.64	301.64	301.55	301.59
6	0.125	0.75	302.69	302.69	302.54	302.63
7	0.125	0.875	304.83	304.83	304.83	304.85
8	0.25	0.125	300.32	300.32	300.31	300.31
9	0.25	0.25	300.69	300.69	300.67	300.68
10	0.25	0.375	301.17	301.17	301.14	301.15
11	0.25	0.5	301.84	301.84	301.80	301.82
12	0.25	0.625	302.82	302.82	302.78	302.80
13	0.25	0.75	304.31	304.31	304.33	304.32
14	0.25	0.875	306.61	306.61	306.79	306.68
15	0.375	0.125	300.42	300.42	300.40	300.41
16	0.375	0.25	300.89	300.89	300.87	300.88
17	0.375	0.375	301.50	301.50	301.48	301.49
18	0.375	0.5	302.33	302.33	302.32	302.33
19	0.375	0.625	303.50	303.50	303.52	303.51
20	0.375	0.75	305.12	305.12	305.21	305.16
21	0.375	0.875	307.31	307.31	307.42	307.36
22	0.5	0.125	300.45	300.45	300.44	300.44
23	0.5	0.25	300.96	300.96	300.94	300.95
24	0.5	0.375	301.62	301.62	301.60	301.61
25	0.5	0.5	302.50	302.50	302.50	302.50
26	0.5	0.625	303.71	303.71	303.76	303.73
27	0.5	0.75	305.36	305.36	305.45	305.41
28	0.5	0.875	307.49	307.49	307.59	307.55
29	0.625	0.125	300.42	300.42	300.4	300.41
30	0.625	0.25	300.89	300.89	300.87	300.88
31	0.625	0.375	301.50	301.50	301.48	301.49
32	0.625	0.5	302.33	302.33	302.32	302.33
33	0.625	0.625	303.50	303.50	303.52	303.51
34	0.625	0.75	305.12	305.12	305.21	305.16
35	0.625	0.875	307.31	307.31	307.42	307.36
36	0.75	0.125	300.32	300.32	300.31	300.31
37	0.75	0.25	300.69	300.69	300.67	300.68
38	0.75	0.375	301.17	301.17	301.14	301.15
39	0.75	0.5	301.84	301.84	301.80	301.82
40	0.75	0.625	302.82	302.82	302.78	302.80
41	0.75	0.75	304.31	304.31	304.33	304.32
42	0.75	0.875	306.61	306.61	306.79	306.68
43	0.875	0.125	300.17	300.17	300.17	300.17
44	0.875	0.25	300.38	300.38	300.36	300.37
45	0.875	0.375	300.64	300.64	300.62	300.63
46	0.875	0.5	301.03	301.03	300.99	301.01
47	0.875	0.625	301.64	301.64	301.55	301.59
48	0.875	0.75	302.69	302.69	302.54	302.63
49	0.875	0.875	304.83	304.83	304.83	304.85

*: Cut-stencil FD method, **: Finite volume method,***: Finite element method

Table 4.3: Numerical and analytical solution for 2-D steady conduction heat transfer in rectangular plate

4.3.2   Steady Conduction Heat Transfer in an Irregular Domain

The cut-stencil solution of 2-dimensional steady conduction heat transfer in an irregular shaped domain, as shown in Figure 4.8, is considered in this sub-section. The dimensions of the domain and the temperature boundary condition for each wall are given in the figure. The homogeneous Neumann boundary condition, which simulates an insulated wall, is imposed on the east boundary that corresponds to the vertical line $x = 1$.
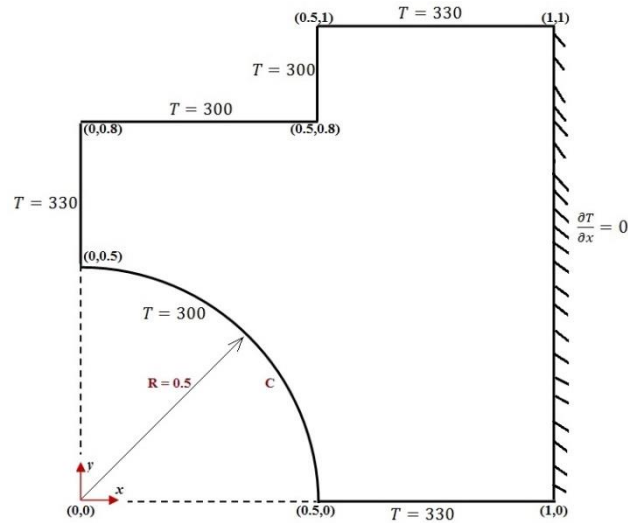
Figure 4.8: Irregular shaped domain used for steady conduction heat transfer

A Cartesian grid of 93 active nodes was constructed to solve the Laplace equation (4.5.1) for this heat transfer problem and the solution has been compared with FVM results obtained from ANSYS FLUENT. The Cartesian grid created a number of regular and irregular boundary nodes on the curve boundary of the domain shown in Figure 4.8. A combination of triangular and quadrilateral cells is used to design the mesh for the FVM analysis. A triangular mesh was used in the zone located between $0 \leq x < 0.5$ and quadrilateral cells were used for $0.5 \leq x \leq 1$, creating a mesh of 91 nodes for the ANSYS FLUENT simulation.

Table 4.4 indicates the value of temperature at a number of internal nodes and Neumann boundary nodes located along east boundary. The comparison of these results verifies good agreement between the cut-stencil FD solution and values of temperature taken from popular CFD commercial software. In particular, the results in Table 4.4 confirm the accuracy of the proposed 2nd-order one-sided differencing scheme for boundary nodes with a Neumann condition.

Coordinate		FDM	FVM	Coordinate		FDM	FVM
x	y	cut-stencil	ANSYS FLUENT	x	y	cut-stencil	ANSYS FLUENT
0.1	0.5	305.628	306.927	0.5	0.2	305.750	300.246
0.1	0.6	313.682	314.398	0.5	0.3	305.856	304.851
0.1	0.7	312.322	312.413	0.6	0.1	318.232	316.621
0.2	0.5	303.376	301.435	0.6	0.9	315.534	315.869
0.2	0.6	306.779	307.523	0.8	0.3	317.957	317.493
0.2	0.7	305.607	304.781	1	0.1	326.078	325.817
0.3	0.5	303.039	302.749	1	0.2	322.630	322.257
0.3	0.6	304.452	303.945	1	0.3	320.011	319.667
0.3	0.7	303.324	303.014	1	0.4	318.372	318.136
0.4	0.4	302.699	302.781	1	0.5	317.752	317.642
0.4	0.5	304.326	304.554	1	0.6	318.171	318.161
0.4	0.6	304.666	304.721	1	0.7	319.671	319.699
0.4	0.7	303.239	303.343	1	0.8	322.275	322.277
0.5	0.1	306.863	300.496	1	0.9	325.852	325.820

Table 4.4: Comparison of cut-stencil FDM and FVM for solution of steady conduction heat transfer in an irregular domain

Contours of isothermal lines in the zone $0.6 \leq x \leq 0.9$ of the irregular shaped domain in Figure 4.8 are presented in Figure 4.9 for both the cut-stencil FDM and ANSYS FLUENT's FV solution. This figure shows that these two methods predict the same temperature distribution in this region of the domain.

This sample heat transfer problem has shown the capability of the Cartesian cut-stencil FD algorithm/method to solve heat transfer problems on irregular shaped domains. This FD scheme can solve PDEs on the cut stencils associated with nodes which are located near the boundaries of the domain without any special formulation at these nodes and, consequently, the programming does not become complicated.
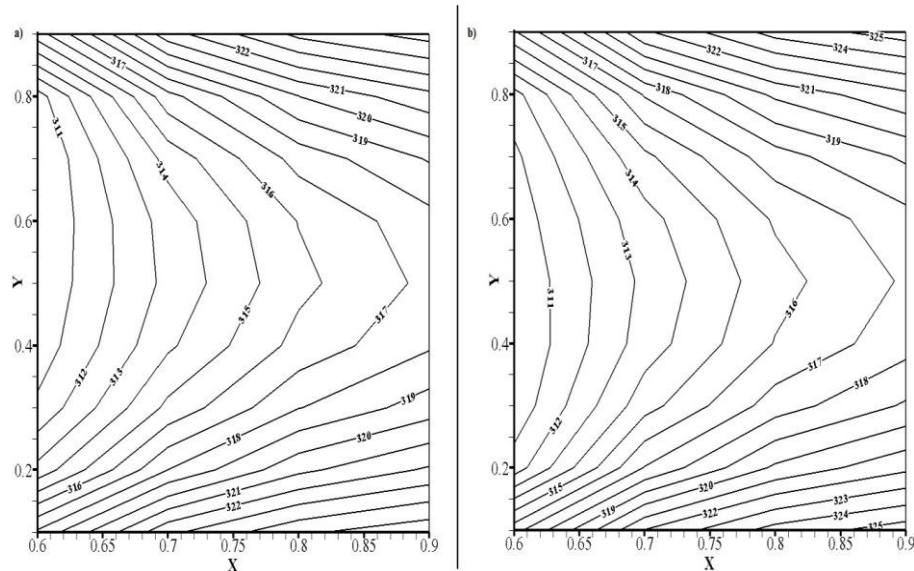
Figure 4.9: Contours of isothermal lines in zone $0.6 \leq x \leq 0.9$ of irregular shaped domain, a) cut-stencil FDM, b) ANSYS FLUENT FVM

4.3.3 Unsteady Heat Conduction in a Rectangular Domain

The governing equation for 2-D transient heat conduction, assuming constant material property and no heat generation, is given by equation (4.6.1), in which v is introduced as thermal diffusivity. The analytical solution for this equation can be derived only for some limited cases under specific initial and boundary conditions and for regular domains.

$$\frac{\partial T}{\partial t} = v \left(\frac{\partial^2 T}{\partial x^2} + \frac{\partial^2 T}{\partial y^2} \right) \tag{4.6.1}$$

The mapped and discrete forms of equation (4.6.1) at node P of an arbitrary 5-point stencil were introduced in equations (2.52.1) and (2.52.2) in which the terms RHS and RHS_P^n are considered as zero.

At first, the FTCS cut-stencil solution to equation (4.6.1) is presented for the rectangular domain shown in Figure 4.10, with temperature boundary conditions as prescribed. The thermal diffusivity and the initial temperature (at initial time t_0 (s)) are specified as $v = 11.234E - 5 \text{ m}^2/\text{s}$ and $T_0 = 0°\text{C}$, respectively. This transient problem with the same initial and boundary conditions as well as thermal diffusivity and dimensions was solved in Hoffmann's textbook using TFDM [17].
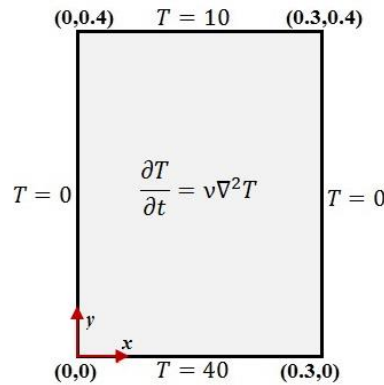
Figure 4.10: Schematic of rectangular domain used for comparison of cut-stencil FDM and TFDM solutions to transient heat conduction

A uniform Cartesian grid of 1271 nodes with $\Delta x = \Delta y = 0.01$, or $x' = y' = 0.01$ in terms of the metrics of transformation, was designed for studying this problem. This is the same as the grid defined by Hoffmann for the TFD study. The maximum allowable time step to satisfy the stability criteria, as discussed in Chapter 2, is $\Delta t_{Max.} = 0.2225$ (s). The time step taken in the TFD calculation was $\Delta t = 0.2$ (s) which is also used in the cut-stencil FD scheme. Table 4.5 reports the predicted value of temperature at a number of internal nodes at two different times $t = 10$ (s) and $t = 40$ (s). The cut-stencil solution to this transient heat transfer problem agrees well with the TFD solution at these two available time steps. The stability criteria proposed in Chapter 2 which provides a stable solution is also in good agreement with the suggested maximum allowable time step by TFDM.

Coordinate		$t = 10\ (s)$		$t = 40\ (s)$	
x	y	Cut-stencil FDM	TFDM (Hoffmann)	Cut-stencil FDM	TFDM (Hoffmann)
0.05	0.01	32.381	32.381	34.224	34.224
	0.05	10.051	10.051	16.765	16.765
	0.10	1.116	1.116	6.505	6.505
	0.20	0.001	0.001	0.808	0.808
	0.25	0.012	0.012	0.711	0.711
	0.35	2.513	2.513	4.195	4.195
	0.39	8.095	8.095	8.556	8.556
0.10	0.01	33.311	33.311	36.143	36.143
	0.05	11.657	11.657	22.039	22.039
	0.10	1.394	1.394	9.898	9.898
	0.20	0.001	0.001	1.336	1.336
	0.25	0.015	0.015	1.155	1.155
	0.35	2.914	2.914	5.516	5.516
	0.39	8.328	8.328	9.036	9.036
0.15	0.01	33.351	33.351	36.436	36.436
	0.05	11.750	11.750	23.096	23.096
	0.10	1.415	1.415	10.798	10.798
	0.20	0.001	0.001	1.508	1.508
	0.25	0.015	0.015	1.294	1.294
	0.35	2.938	2.938	5.781	5.781
	0.39	8.338	8.338	9.110	9.110
0.20	0.01	33.311	33.311	36.143	36.143
	0.05	11.657	11.657	22.039	22.039
	0.10	1.394	1.394	9.898	9.898
	0.20	0.001	0.001	1.336	1.336
	0.25	0.015	0.015	1.155	1.155
	0.35	2.914	2.914	5.516	5.516
	0.39	8.328	8.328	9.036	9.036
0.25	0.01	32.381	32.381	34.224	34.224
	0.05	10.051	10.051	16.765	16.765
	0.10	1.116	1.116	6.505	6.505
	0.20	0.001	0.001	0.808	0.808
	0.25	0.012	0.012	0.711	0.711
	0.35	2.513	2.513	4.195	4.195
	0.39	8.095	8.095	8.556	8.556

Table 4.5: Comparison of cut-stencil FDM and TFDM for solution of unsteady conduction heat transfer in a rectangular domain

The analytical solution for the steady-state condition of this transient heat transfer problem is given by [17]:

$$T = 2 * 40 \sum_{n=1}^{\infty} \frac{1-\cos(n\pi)}{n\pi} \sin\left(\frac{n\pi x}{0.3}\right) \frac{\sinh\left(\frac{n\pi(0.4-y)}{0.3}\right)}{\sinh\left(\frac{0.4n\pi}{0.3}\right)} + 2$$

$$* 10 \sum_{n=1}^{\infty} \frac{1-\cos(n\pi)}{n\pi} \sin\left(\frac{n\pi x}{0.3}\right) \frac{\sinh\left(\frac{n\pi y}{0.3}\right)}{\sinh\left(\frac{0.4n\pi}{0.3}\right)}$$

(4.6.2)

For the purpose of our discussion, the solution is said to be steady when for all nodes, the total of the absolute difference of temperature between one time level and the next is less than 0.01. The total difference of temperature between $t = 410.4\ (s)$ and $t = 410.6\ (s)$ is equal to 0.02, while for time between $t = 410.6\ (s)$ and $t = 410.8\ (s)$ and between $t = 410.8\ (s)$ and $t = 411\ (s)$, this difference is equal to 0.01. So, one can say that the solution reaches to steady-state condition at about $t = 410.8\ (s)$.

Cut-stencil FDM and TFDM solutions at steady-state condition for the transient conduction problem in Figure 4.10 are compared to the analytical solution (4.6.2) in Table 4.6.

Coordinate		Cut-stencil FDM	TFDM (Hoffmann)	Analytical solution (Hoffmann)	Coordinate		Cut-stencil FDM	TFDM (Hoffmann)	Analytical solution (Hoffmann)
x	y				x	y			
0.05	0.01	34.693	34.693	34.961	0.15	0.25	6.145	6.145	6.145
0.05	0.02	29.800	29.800	29.898	0.15	0.35	7.648	7.648	7.652
0.05	0.05	18.935	18.935	18.937	0.15	0.38	8.998	8.998	8.996
0.05	0.10	9.934	9.934	9.921	0.15	0.39	9.495	9.495	9.457
0.05	0.25	3.142	3.142	3.140	0.20	0.01	36.954	36.954	37.038
0.05	0.35	5.131	5.131	5.131	0.20	0.02	33.964	33.964	33.989
0.05	0.38	7.603	7.603	7.627	0.20	0.05	25.788	25.788	25.809
0.05	0.39	8.749	8.749	8.816	0.20	0.10	15.822	15.822	15.827
0.10	0.01	36.954	36.954	37.038	0.20	0.25	5.360	5.360	5.359
0.10	0.02	33.964	33.964	33.989	0.20	0.35	7.134	7.134	7.139
0.10	0.05	25.788	25.788	25.809	0.20	0.38	8.756	8.756	8.762
0.10	0.10	15.822	15.822	15.827	0.20	0.39	9.370	9.370	9.391
0.10	0.25	5.360	5.360	5.359	0.25	0.01	34.693	34.693	34.961
0.10	0.35	7.134	7.134	7.139	0.25	0.02	29.800	29.800	29.898
0.10	0.38	8.756	8.756	8.762	0.25	0.05	18.935	18.935	18.937
0.10	0.39	9.370	9.370	9.391	0.25	0.10	9.934	9.934	9.921
0.15	0.01	37.371	37.371	37.221	0.25	0.25	3.142	3.142	3.140
0.15	0.02	34.772	34.772	34.763	0.25	0.35	5.131	5.131	5.131
0.15	0.05	27.419	27.419	27.436	0.25	0.38	7.603	7.603	7.627
0.15	0.10	17.630	17.630	17.641	0.25	0.39	8.749	8.749	8.816

Table 4.6: Comparison of cut-stencil FDM and TFDM steady-state solution of the transient conduction heat transfer with analytical solution

The comparison of results in Table 4.6 confirms the good agreement between both numerical methods and the analytical solution. The average and maximum absolute difference between the cut-stencil FD solution and the analytical solution are 0.038 and 0.268, respectively.

4.3.4   Unsteady Heat Conduction in an Irregular Domain

In this final example, the unsteady conduction heat transfer problem is simulated in the irregular shaped domain depicted in Figure 4.11. The cut-stencil FD solution is compared to a FV solution

using the commercial software ANSYS FLUENT. The thermal diffusivity v in equation (4.6.1) is taken as $11.105E - 3$ m^2/s and $T_0 = 273\ K$ is the value of temperature at initial time. A uniform Cartesian grid comprised of 100 nodes was used for the cut-stencil FD solution, while a mesh system including triangular and quadrilateral cells, totalling 101 nodes, was designed to conduct the FV analysis. The maximum allowable time step, by taking into account that $x' = y' = 0.1$ for this case, is about $0.225\ (s)$.
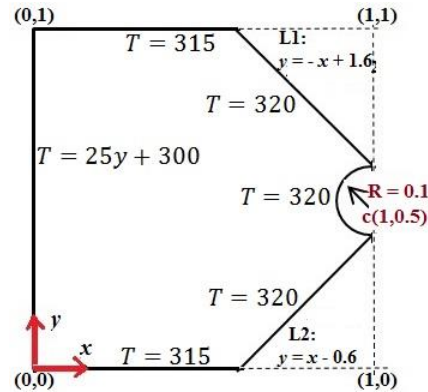
Figure 4.11: Irregular shaped domain used for unsteady conduction heat transfer

The temperature (in degrees kelvin) at the circular and angular cut boundaries of the domain in Figure 4.11 is kept constant, similar to the condition for the south and north boundaries. However, the temperature along the west boundary of the domain, corresponding to the line $x = 0$, is varied linearly with the y coordinate. The comparison of the values of temperature resulting from the cut-stencil FD and commercial software FV methods, at $t = 2$ (s), is reported in Table 4.7.

Coordinate		FDM	FVM	Coordinate		FDM	FVM
x	y	cut-stencil	ANSYS FLUENT	x	y	cut-stencil	ANSYS FLUENT
0.1	0.1	304.866	303.982	0.5	0.9	303.281	303.789
0.1	0.3	298.156	296.620	0.6	0.3	290.643	291.770
0.1	0.9	312.559	311.548	0.6	0.4	285.516	286.481
0.2	0.1	303.610	302.428	0.6	0.7	290.223	291.742
0.2	0.4	288.266	287.327	0.7	0.2	308.891	308.098
0.2	0.8	298.977	297.323	0.7	0.4	294.066	293.599
0.3	0.2	292.061	290.925	0.7	0.6	293.890	293.508
0.3	0.3	285.390	284.770	0.7	0.8	308.648	308.291
0.3	0.9	303.288	302.357	0.8	0.3	310.562	308.967
0.4	0.1	302.078	301.437	0.8	0.4	305.301	303.814
0.4	0.3	283.623	283.591	0.8	0.6	305.201	304.530
0.4	0.6	279.563	280.346	0.8	0.7	310.454	309.945
0.5	0.2	293.217	292.957	0.9	0.4	316.004	316.834
0.5	0.8	292.846	293.142	0.9	0.6	315.982	317.038

Table 4.7: Comparison of cut-stencil FDM and FVM for solution of unsteady conduction heat transfer in an irregular domain at $t = 2$ (s)

The results in Table 4.7 reveal good agreement between the solution from the cut-stencil FDM and the FVM. The average and maximum absolute difference for all the internal nodes are

0.95856 and 3.01582, respectively. The values of temperature along the horizontal mid-line of the domain ($y = 0.5$), are plotted in Figure 4.12 for both the cut-stencil FDM and FVM.
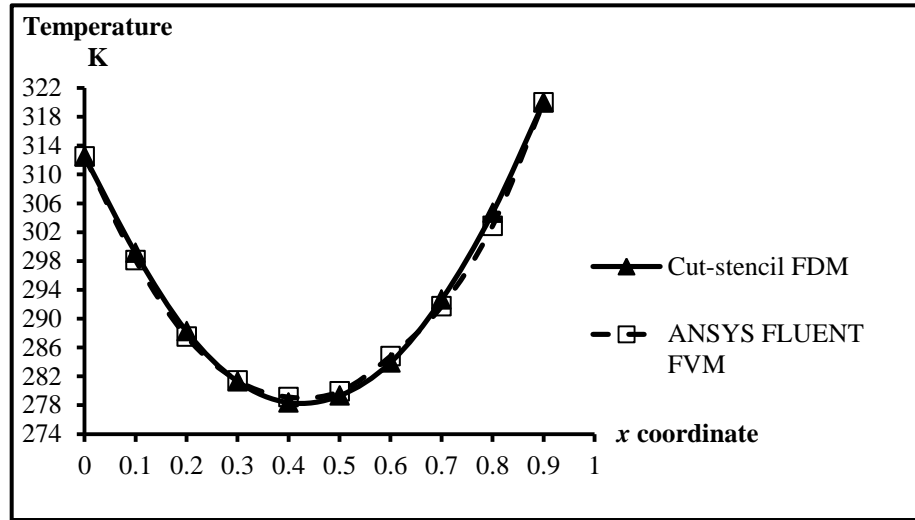
Figure 4.12: Comparison of cut-stencil FDM and FVM for temperature along the line $y = 0.5$ in an irregular domain at $t = 2$ (s)

4.4   Chapter Summary

The application of the Cartesian cut-stencil FDM for a number of real engineering problems was addressed in this chapter through the solution to some boundary value problems in advanced elasticity and heat transfer. Apart from verification for formulations and coding, results of this chapter show the broad capabilities of the cut-stencil FDM to solve PDEs that are commonly encountered in many fields of science and engineering.

The cut-stencil FDM solutions for the stress function of torsion and bending for a bar were obtained and results were compared to the analytical solutions. Neumann boundary conditions taken from the analytical solution were applied along the symmetry lines of domains studied. The results confirmed the accuracy of formulations used for treatment of Neumann boundary conditions which may be defined for real engineering problems.

The solution of steady and unsteady heat conduction on regular and irregular complex domains were considered in this chapter. The results were compared with available analytical solutions or to simulation results from commercial software. For one of the cases studied, the cut-stencil solution was compared to two common commercial FV-based and FE-based packages and good agreement was observed between the results. The simulations included heat conduction in a domain with a Neumann boundary condition, which may interpreted as an insulated wall, and for a wall with variable temperature.

CHAPTER 5

CUT-STENCIL FD FORMULATION for THE SOLUTION of LID-DRIVEN CAVITY FLOW

5.1   Objective of the Chapter

The material in previous chapters examined fundamental concepts of the Cartesian cut-stencil finite difference algorithm/formulations and corresponding results for some mathematical sample problems and some engineering problems from advanced elasticity and heat transfer fields. This chapter discusses implementation of the cut-stencil method for lid-driven cavity flow. As one of the most popular benchmark problems in the area of fluid mechanics, the 2-D lid-driven cavity flow has been studied widely in the field of fluid mechanics [149] and researchers have used this problem to test different numerical methodologies e.g. FDM [150], FVM [151], FEM [152] or the Lattice Boltzmann method [153]. Several significant numerical studies will be referenced in this chapter and used for verification purposes. From the mathematical point-of-view, the cavity flow problem exhibits the most difficult numerical challenges of solving PDEs; highly non-linear governing equations, convection-diffusion type of transport equations, strongly coupled system of PDEs and lack of appropriate boundary conditions. These complex mathematical features are due to the complex physics associated with this flow, such as strong vortices and flow separation and reattachment. Numerical solutions of this problem must be able to predict the strength and location of vortices appearing at the corners of the cavity. Hence, this test problem has often been employed to verify and test the accuracy of new numerical schemes.

The formulation and implementation of the cut-stencil FDM to 2-D steady lid-driven cavity flow on rectangular and non-rectangular domains, e.g., skewed quadrilateral and triangular cross-sections, will be considered in this chapter for different values of Reynolds numbers. Due to the lack of a general analytical solution, results are compared to similar numerical studies for this benchmark problem.

5.2   Primitive Variable Formulation of the Navier-Stokes Equations

The equations of fluid motion can be derived from conservation principles for mass, linear momentum and energy, associated with continuity, Newton's second law and the first law of thermodynamics, respectively. The resulting system of equations is called the Navier-Stokes equations [17].

For an incompressible flow, the energy equation can be decoupled from the system of equations. Then, the Navier-Stokes equations for 2-D steady incompressible laminar flow in Cartesian coordinates (X, Y), in dimensional and non-conservative form, are:

$$\frac{\partial \mathcal{U}}{\partial X} + \frac{\partial \mathcal{V}}{\partial Y} = 0 \tag{5.1.1}$$

$$\mathcal{U}\frac{\partial \mathcal{U}}{\partial X} + \mathcal{V}\frac{\partial \mathcal{U}}{\partial Y} + \frac{1}{\rho}\frac{\partial \mathtt{p}}{\partial X} = \vartheta\left(\frac{\partial^2 \mathcal{U}}{\partial X^2} + \frac{\partial^2 \mathcal{U}}{\partial Y^2}\right) \tag{5.1.2}$$

$$\mathcal{U}\frac{\partial \mathcal{V}}{\partial X} + \mathcal{V}\frac{\partial \mathcal{V}}{\partial Y} + \frac{1}{\rho}\frac{\partial \mathtt{p}}{\partial Y} = \vartheta\left(\frac{\partial^2 \mathcal{V}}{\partial X^2} + \frac{\partial^2 \mathcal{V}}{\partial Y^2}\right) \tag{5.1.3}$$

where $\mathcal{U}$, $\mathcal{V}$, ρ, p and ϑ denote X and Y-components of velocity, density, pressure and kinematic viscosity of the fluid, respectively. Additionally, for a 2-D incompressible flow, the streamfunction Ψ and the Z-component Ω_z of the vorticity vector, in a Cartesian coordinate system, are defined as

$$\frac{\partial \Psi}{\partial Y} = \mathcal{U} \tag{5.2.1}$$

$$\frac{\partial \Psi}{\partial X} = -\mathcal{V} \tag{5.2.2}$$

$$\Omega_z = \left(\frac{\partial \mathcal{V}}{\partial X} - \frac{\partial \mathcal{U}}{\partial Y} \right) \tag{5.2.3}$$

5.3   Streamfunction-Vorticity Equations

The streamfunction-vorticity formulation of the Navier-Stokes equations is obtained by differentiating the momentum equations (5.1.2) and (5.1.3) with respect to Y and X, respectively, and subtracting the resulting equations to eliminate the pressure.

The non-dimensional form of streamfunction and vorticity are defined as $\psi = \frac{\Psi}{U_{ref} L_c}$ and $\omega = \frac{\Omega_z L_c}{U_{ref}}$, respectively, where L_c is a characteristic length and U_{ref} is a reference velocity. The components of velocity, similarly, can be stated in non-dimensional form and related to ψ by defining $u = \frac{\mathcal{U}}{U_{ref}} = \frac{\partial \psi}{\partial y}$ and $v = \frac{\mathcal{V}}{U_{ref}} = -\frac{\partial \psi}{\partial x}$, where $x = X/L_c$, $y = Y/L_c$. Thus, the non-dimensional and non-conservative form of the governing equations for streamfunction and vorticity, in Cartesian coordinates, can be expressed as:

$$\frac{\partial^2 \psi}{\partial x^2} + \frac{\partial^2 \psi}{\partial y^2} = -\omega \tag{5.3.1}$$

$$u \frac{\partial \omega}{\partial x} + v \frac{\partial \omega}{\partial y} = \frac{1}{Re} \left(\frac{\partial^2 \omega}{\partial x^2} + \frac{\partial^2 \omega}{\partial y^2} \right) \tag{5.3.2}$$

where $Re = \frac{U_{ref} L_c}{\vartheta}$ is the Reynolds number. One can see that, using the streamfunction-vorticity definition, the Navier-Stokes equations are split into a convection-diffusion transport equation for vorticity and a Poisson equation for streamfunction. One of the advantages of this formulation is that the pressure has been eliminated from the calculation, but can be determined from a Poisson equation once the velocity field has been obtained from (5.3.1) and (5.3.2).

5.4   Mapped Form of Streamfunction-Vorticity Equations and Boundary Conditions for Lid-Driven Cavity Flow

The mapped form of the non-dimensional streamfunction-vorticity equations under the transformation $x = x(\xi)$, $y = y(\eta)$, which were introduced in equation (2.4) and illustrated in Figure 2.2, are given by:

$$\frac{1}{(x')^2}\frac{\partial^2\psi}{\partial\xi^2}-\frac{x''}{(x')^3}\frac{\partial\psi}{\partial\xi}+\frac{1}{(y')^2}\frac{\partial^2\psi}{\partial\eta^2}-\frac{y''}{(y')^3}\frac{\partial\psi}{\partial\eta}=-\omega \tag{5.4.1}$$

$$\frac{-1}{Re}\left(\frac{1}{(x')^2}\frac{\partial^2\omega}{\partial\xi^2}-\frac{x''}{(x')^3}\frac{\partial\omega}{\partial\xi}+\frac{1}{(y')^2}\frac{\partial^2\omega}{\partial\eta^2}-\frac{y''}{(y')^3}\frac{\partial\omega}{\partial\eta}\right)+\frac{u}{x'}\frac{\partial\omega}{\partial\xi}$$
$$+\frac{v}{y'}\frac{\partial\omega}{\partial\eta}=0 \tag{5.4.2}$$

Now consider a rectangular cavity of width L and height H, with the top wall ($Y = H$, $0 \leq X \leq L$) sliding in the X direction with velocity U_{lid}. The typical boundary conditions for viscous flow at a solid wall (or boundary) are described by the physical requirements of no-slip and no-penetration, meaning that both the tangential and normal components of fluid velocity must agree with the same components of the wall motion. The values of velocity components are set as zero for stationary walls while, for a moving wall, the no-slip and no-penetration conditions are the governing boundary conditions [130, 154, 155]. This implies that, if the moving wall of the cavity is the top wall and is parallel to the X-axis, the X component on the wall velocity provides the prescribed value U_{lid}, which is normally considered as $u = 1$ for the non-dimensional form, i.e., the reference velocity is taken as U_{lid}. The normal component of velocity (v) is equal to zero on the moving wall. Since the velocity components are related to derivatives of the streamfunction, the velocity boundary conditions (in non-dimensional variables) lead to a Neumann condition for ψ, i.e., $\frac{\partial\psi}{\partial n} = 0$ on the walls, where n represents the normal direction to the wall at each point. Along the walls, the streamfunction can be taken as an arbitrary constant which is usually set equal to zero. The boundary conditions on vorticity can be defined by applying equation (5.3.1) on the boundaries, producing Dirichlet boundary conditions for ω. Similar approaches for definition of boundary conditions for lid-driven cavity flow, as discussed herein, have been addressed and used widely in other numerical studies [156-159]. Figure 5.1 provides a schematic of the boundary conditions used for the lid-driven cavity flow problem in the non-dimensional $x - y$ coordinate system.
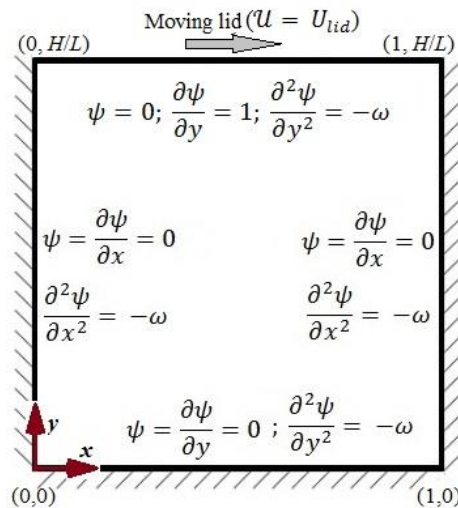
Figure 5.1: Schematic of the boundary conditions used for the lid-driven cavity flow

For cavity flow, the non-dimensional parameter Reynolds number is defined by $Re = \frac{U_{lid}L}{\vartheta}$ where the characteristic length L_c is the width L of the cavity.

5.4.1   2nd-Order Discretization of Streamfunction-Vorticity Equations

Initially, the 5-point 2nd-order cut-stencil FD formulation is used to approximate equations (5.4.1) and (5.4.2) in difference form. The second-order derivatives in equations (5.4.1) and (5.4.2) are approximated by 3-point central differencing, while either upwind or central differencing is used to approximate the derivatives in the convective terms in equation (5.4.2) depending on Reynolds number. The formulations associated with upwind discretization of the convective terms in the model convection-diffusion equation were discussed in Chapter 2. In the event that the convection terms of equations (5.4.1) are approximated by 2nd-order differences, the discrete approximation of the streamfunction-vorticity equations (5.4.1) and (5.4.2) at point P of an arbitrary 5-point computational stencil are:

$$\frac{\psi_w - 2\psi_P + \psi_e}{(x'_P)^2} - \frac{x''_P}{(x'_P)^3}\frac{\psi_e - \psi_w}{2} + \frac{\psi_s - 2\psi_P + \psi_n}{(y'_P)^2} - \frac{y''_P}{(y'_P)^3}\frac{\psi_n - \psi_s}{2} = -\omega_P \qquad (5.5.1)$$

$$\frac{-1}{Re}\left(\frac{\omega_w - 2\omega_P + \omega_e}{(x'_P)^2} - \frac{x''_P}{(x'_P)^3}\frac{\omega_e - \omega_w}{2} + \frac{\omega_s - 2\omega_P + \omega_n}{(y'_P)^2} - \frac{y''_P}{(y'_P)^3}\frac{\omega_n - \omega_s}{2}\right)$$
$$+ u_P\left(\frac{\omega_e - \omega_w}{2x'_P}\right) + v_P\left(\frac{\omega_n - \omega_s}{2y'_P}\right) = 0 \qquad (5.5.2)$$

The condition for switching to any upwind schemes, i.e., backward or forward discretization, for convection terms is based on the sign of velocity components at point P. The discretization of equation (5.4.2), using the cut-stencil FD formulation and applying upwind differencing for convective terms, is addressed in equation (5.5.3). The parameters k and l take values 0 or 1, based on the sign of u_P and v_P, to switch from backward to forward differencing or vice versa. For example, if at any solution iteration the sign of u_P is positive, the value of k will be equal to zero and the corresponding convective term is approximated by $u_P\frac{\omega_P - \omega_w}{x'_P}$. In event of negative u_P, the value of k will be equal to one and the corresponding convective term is approximated by $u_P\frac{\omega_e - \omega_P}{x'_P}$. Hence, in both cases of $k = 0$ or 1, the differencing scheme is associated with backward or forward differencing, respectively, which represents a 1st-order accurate approximation. The same conditions can be imagined for the value of l, which will be equal to 0 or 1 depending on the sign of v_P. Thus, the discrete approximation of the flow equations with upwinding for the convective terms is:

$$\frac{-1}{Re}\left(\frac{\omega_w - 2\omega_P + \omega_e}{(x'_P)^2} - \frac{x''_P}{(x'_P)^3}\frac{\omega_e - \omega_w}{2} + \frac{\omega_s - 2\omega_P + \omega_n}{(y'_P)^2} - \frac{y''_P}{(y'_P)^3}\frac{\omega_n - \omega_s}{2}\right) +$$
$$u_P\left(\frac{(-1)^k\omega_P - (1-k)\omega_w + k\omega_e}{x'_P}\right) + v_P\left(\frac{(-1)^l\omega_P - (1-l)\omega_s + l\omega_n}{y'_P}\right) = 0 \qquad (5.5.3)$$

5.4.2 Higher-Order (HO) Discretization of Streamfunction-Vorticity Equations

Higher-order discretization schemes for the streamfunction-vorticity formulation of the Navier-Stokes equations have been reported in literature. For example, Erturk [160] compared wide and compact 4th-order schemes. The higher-order compact FD formulations, generally, have been developed using a nine-point stencil, as depicted in Figure 5.2. Some examples of this type of methodology for streamfunction-vorticity formulation of Navier-Stokes equation can be seen in [158, 161, 162, 163]. The stencil shown in Figure 5.2 encounters difficulty to treat a cut stencil if a Cartesian grid is used and a number of different types of stencils must be defined depending on the location of central point of the stencil, say node (i, j), relative to the boundaries. Hence, with a Cartesian grid, the stencil shown in Figure 5.2 is more applicable for a regular type of domain, e.g. the cavity flow problem in a rectangle. Nevertheless, this stencil has been used to construct higher-order differencing of the streamfunction-vorticity form of the Navier-Stokes equations on irregular shaped domains in [162], for a constricted channel using a non-orthogonal grid. However, this condition needs 2-D transformation functions $x = x(\xi, \eta)$ and $y = y(\xi, \eta)$ which makes the transformation procedure much more complicated compared to the 1-D mapping functions used in the Cartesian cut-stencil FDM.
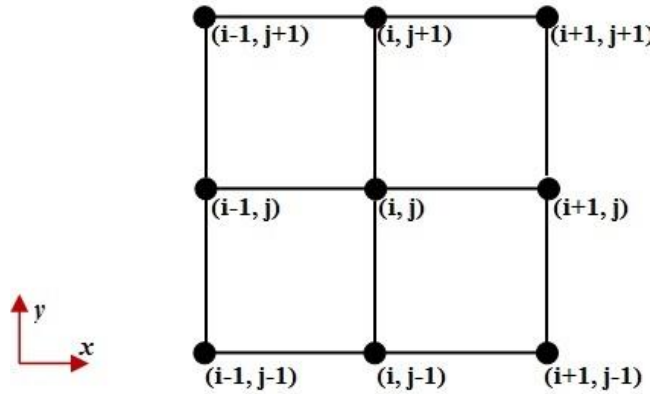
Figure 5.2: Illustration of 9-point stencil normally used for HO schemes in streamfunction-vorticity formulation e.g. [158, 162]

The higher-order formulations of the cut-stencil FDM, introduced in Chapter 2 and referred to as HO cut-stencil FDM1 and HO cut-stencil FDM2, can be used to construct the higher-order methods for the streamfunction-vorticity equations. The first and second derivatives in equations (5.4.1) and (5.4.2) can be approximated by the compact Padé-Hermitian finite differencing technique.

5.4.2.1 Higher-Order Cut-Stencil Finite Differencing Method 1 (HO Cut-Stencil FDM1) for Streamfunction-Vorticity Equations

The HO cut-stencil FDM1 formulation of equations (5.4.1) and (5.4.2), at point P of an arbitrary 5-point computational stencil, are given in equations (5.6.1) and (5.6.2), respectively. The scheme used in equation (2.41) for approximation of the first and second derivatives in the HO-FDM1 formulation, has been used in these equations. Equation (5.6.2) is obtained when the central difference approximation is applied for the derivatives in the convective terms.

$$\frac{1}{(x_P')^2}\left[\frac{6\psi_w - 12\psi_P + 6\psi_e}{5} - \frac{1}{10}\left(\frac{\partial^2\psi}{\partial\xi^2}\Big|_w + \frac{\partial^2\psi}{\partial\xi^2}\Big|_e\right)\right] - \frac{x_P''}{(x_P')^3}\left[\frac{3\psi_e - 3\psi_w}{4} - \frac{1}{4}\left(\frac{\partial\psi}{\partial\xi}\Big|_w + \frac{\partial\psi}{\partial\xi}\Big|_e\right)\right]$$
$$+ \frac{1}{(y_P')^2}\left[\frac{6\psi_s - 12\psi_P + 6\psi_n}{5} - \frac{1}{10}\left(\frac{\partial^2\psi}{\partial\eta^2}\Big|_s + \frac{\partial^2\psi}{\partial\eta^2}\Big|_n\right)\right] - \frac{y_P''}{(y_P')^3}\left[\frac{3\psi_n - 3\psi_s}{4} - \frac{1}{4}\left(\frac{\partial\psi}{\partial\eta}\Big|_s + \frac{\partial\psi}{\partial\eta}\Big|_n\right)\right] = -\omega_P \tag{5.6.1}$$

$$\frac{-1}{Re}\left\{\frac{1}{(x_P')^2}\left[\frac{6\omega_w - 12\omega_P + 6\omega_e}{5} - \frac{1}{10}\left(\frac{\partial^2\omega}{\partial\xi^2}\Big|_w + \frac{\partial^2\omega}{\partial\xi^2}\Big|_e\right)\right] - \frac{x_P''}{(x_P')^3}\left[\frac{3\omega_e - 3\omega_w}{4} - \frac{1}{4}\left(\frac{\partial\omega}{\partial\xi}\Big|_w + \frac{\partial\omega}{\partial\xi}\Big|_e\right)\right] +\right.$$
$$\left.\frac{1}{(y_P')^2}\left[\frac{6\omega_s - 12\omega_P + 6\omega_n}{5} - \frac{1}{10}\left(\frac{\partial^2\omega}{\partial\eta^2}\Big|_s + \frac{\partial^2\omega}{\partial\eta^2}\Big|_n\right)\right] - \frac{y_P''}{(y_P')^3}\left[\frac{3\omega_n - 3\omega_s}{4} - \frac{1}{4}\left(\frac{\partial\omega}{\partial\eta}\Big|_s + \frac{\partial\omega}{\partial\eta}\Big|_n\right)\right]\right\} + \tag{5.6.2}$$
$$\frac{u_P}{x_P'}\left[\frac{3\omega_e - 3\omega_w}{4} - \frac{1}{4}\left(\frac{\partial\omega}{\partial\xi}\Big|_w + \frac{\partial\omega}{\partial\xi}\Big|_e\right)\right] + \frac{v_P}{y_P'}\left[\frac{3\omega_n - 3\omega_s}{4} - \frac{1}{4}\left(\frac{\partial\omega}{\partial\eta}\Big|_s + \frac{\partial\omega}{\partial\eta}\Big|_n\right)\right] = 0$$

As explained in Chapter 2, all derivatives at endpoints of a 5-point stencil appearing in equation (5.6.1) and (5.6.2), are approximated by a central or one-sided 2nd-order approximation. However if both endpoints w and e or s and n are located on the boundary, a one-sided 1st-order accurate approximation is used for evaluation of the second derivatives at corresponding endpoint. This situation was depicted in Figure 2.26. The global order of accuracy associated with the convective term approximations in (5.6.2) is 4th-order, while these terms are approximated to 2nd-order of accuracy when the central scheme in equation (5.5.2) is used.

The HO upwind discretization of the convective terms in equation (5.5.3), when the HO cut-stencil FDM1 formulation is applied to construct the higher-order differencing, is illustrated in equation (5.6.3). The methodology for approximation of derivatives at endpoints in equation (5.6.3) is the same as the procedure explained above.

$$\frac{-1}{Re}\left\{\frac{1}{(x_P')^2}\left[\frac{6\omega_w - 12\omega_P + 6\omega_e}{5} - \frac{1}{10}\left(\frac{\partial^2\omega}{\partial\xi^2}\Big|_w + \frac{\partial^2\omega}{\partial\xi^2}\Big|_e\right)\right] - \frac{x_P''}{(x_P')^3}\left[\frac{3\omega_e - 3\omega_w}{4} - \frac{1}{4}\left(\frac{\partial\omega}{\partial\xi}\Big|_w +\right.\right.\right.$$
$$\left.\left.\frac{\partial\omega}{\partial\xi}\Big|_e\right)\right] + \frac{1}{(y_P')^2}\left[\frac{6\omega_s - 12\omega_P + 6\omega_n}{5} - \frac{1}{10}\left(\frac{\partial^2\omega}{\partial\eta^2}\Big|_s + \frac{\partial^2\omega}{\partial\eta^2}\Big|_n\right)\right] - \frac{y_P''}{(y_P')^3}\left[\frac{3\omega_n - 3\omega_s}{4} - \frac{1}{4}\left(\frac{\partial\omega}{\partial\eta}\Big|_s +\right.\right.$$
$$\left.\left.\left.\frac{\partial\omega}{\partial\eta}\Big|_n\right)\right]\right\} + \frac{u_P}{x_P'}\left[\frac{1+k}{2}\left(2\omega_P - 2\omega_w - \frac{\partial\omega}{\partial\xi}\Big|_w\right) + \frac{1-k}{2}\left(2\omega_e - 2\omega_P - \frac{\partial\omega}{\partial\xi}\Big|_e\right)\right] + \tag{5.6.3}$$
$$\frac{v_P}{y_P'}\left[\frac{1+l}{2}\left(2\omega_P - 2\omega_s - \frac{\partial\omega}{\partial\xi}\Big|_s\right) + \frac{1-l}{2}\left(2\omega_n - 2\omega_P - \frac{\partial\omega}{\partial\xi}\Big|_n\right)\right] = 0$$

The values of parameters k and l in equations (5.6.3) are set as 1 or -1 based on the sign of u_P and v_P to construct backward or forward differencing schemes for the HO formulation, respectively. The convective terms are approximated by one-sided 2nd-order accurate formulas for equation (5.6.3) while the same terms are approximated by 1st-order accurate expressions in equation (5.5.3).

5.4.2.2 Higher-Order Cut-Stencil Finite Differencing Method 2 (HO Cut-Stencil FDM2) for Streamfunction-Vorticity Equations

The equations for streamfunction and vorticity, equations (5.4.1) and (5.4.2), can also be evaluated using the HO cut-stencil FDM2 formulation that was discussed in Chapter 2 for the convection-diffusion model equation, e.g. equation (2.43). In this case, discretization of equations (5.4.1) and (5.4.2), using HO cut-stencil FDM2 formulation with central differencing to approximate the convective terms of equation (5.4.2), yields:

$$\frac{1}{(x'_P)^2}\left[(2\psi_w - 4\psi_P + 2\psi_e) + \frac{1}{2}\left(\frac{\partial\psi}{\partial\xi}\Big|_w - \frac{\partial\psi}{\partial\xi}\Big|_e\right)\right] - \frac{x''_P}{(x'_P)^3}\left[\frac{3\psi_e - 3\psi_w}{4} - \frac{1}{4}\left(\frac{\partial\psi}{\partial\xi}\Big|_w + \frac{\partial\psi}{\partial\xi}\Big|_e\right)\right]$$

$$+ \frac{1}{(y'_P)^2}\left[(2\psi_s - 4\psi_P + 2\psi_n) + \frac{1}{2}\left(\frac{\partial\psi}{\partial\eta}\Big|_s - \frac{\partial\psi}{\partial\eta}\Big|_n\right)\right] - \frac{y''_P}{(y'_P)^3}\left[\frac{3\psi_n - 3\psi_s}{4} - \frac{1}{4}\left(\frac{\partial\psi}{\partial\eta}\Big|_s + \frac{\partial\psi}{\partial\eta}\Big|_n\right)\right] = \omega_P \tag{5.7.1}$$

$$\frac{-1}{Re}\left\{\frac{1}{(x'_P)^2}\left[(2\omega_w - 4\omega_P + 2\omega_e) + \frac{1}{2}\left(\frac{\partial\omega}{\partial\xi}\Big|_w - \frac{\partial\omega}{\partial\xi}\Big|_e\right)\right] - \frac{x''_P}{(x'_P)^3}\left[\frac{3\omega_e - 3\omega_w}{4} - \frac{1}{4}\left(\frac{\partial\omega}{\partial\xi}\Big|_w + \frac{\partial\omega}{\partial\xi}\Big|_e\right)\right] + \right.$$

$$\left. \frac{1}{(y'_P)^2}\left[(2\omega_s - 4\omega_P + 2\omega_n) + \frac{1}{2}\left(\frac{\partial\omega}{\partial\eta}\Big|_s - \frac{\partial\omega}{\partial\eta}\Big|_n\right)\right] - \frac{y''_P}{(y'_P)^3}\left[\frac{3\omega_n - 3\omega_s}{4} - \frac{1}{4}\left(\frac{\partial\omega}{\partial\eta}\Big|_s + \frac{\partial\omega}{\partial\eta}\Big|_n\right)\right]\right\} + $$

$$\frac{u_P}{x'_P}\left[\frac{3\omega_e - 3\omega_w}{4} - \frac{1}{4}\left(\frac{\partial\omega}{\partial\xi}\Big|_w + \frac{\partial\omega}{\partial\xi}\Big|_e\right)\right] + \frac{v_P}{y'_P}\left[\frac{3\omega_n - 3\omega_s}{4} - \frac{1}{4}\left(\frac{\partial\omega}{\partial\eta}\Big|_s + \frac{\partial\omega}{\partial\eta}\Big|_n\right)\right] = 0 \tag{5.7.2}$$

Referring to the discussion of HO cut-stencil FDM2 in Chapter 2, all the first derivatives in equations (5.7.1) and (5.7.2) at endpoints of the 5-point stencil are approximated by either central, one-sided or upwind 4th, 3rd or 2nd-order accurate differencing depending on the location of point P relative to the boundaries. Samples of the situations for these orders of accuracy were shown in Figures 2.27 and 2.28. The global order of accuracy of HO-FDM2 for the discretization of the convective terms in equation (5.7.2) is 4th-order.

Upwind discretization of the convective terms in equation (5.4.2) using HO cut-stencil FDM2 to approximate the derivatives produces equation (5.7.3). Approximation of first derivatives at stencil endpoints is the same as for FDM1.

$$\frac{-1}{Re}\left\{\frac{1}{(x'_P)^2}\left[(2\omega_w - 4\omega_P + 2\omega_e) + \frac{1}{2}\left(\frac{\partial\omega}{\partial\xi}\Big|_w - \frac{\partial\omega}{\partial\xi}\Big|_e\right)\right] - \frac{x''_P}{(x'_P)^3}\left[\frac{3\omega_e - 3\omega_w}{4} - \frac{1}{4}\left(\frac{\partial\omega}{\partial\xi}\Big|_w + \right.\right.\right.$$

$$\left. \frac{\partial\omega}{\partial\xi}\Big|_e\right)\right] + \frac{1}{(y'_P)^2}\left[(2\omega_s - 4\omega_P + 2\omega_n) + \frac{1}{2}\left(\frac{\partial\omega}{\partial\eta}\Big|_s - \frac{\partial\omega}{\partial\eta}\Big|_n\right)\right] - \frac{y''_P}{(y'_P)^3}\left[\frac{3\omega_n - 3\omega_s}{4} - \right.$$

$$\left.\left. \frac{1}{4}\left(\frac{\partial\omega}{\partial\eta}\Big|_s + \frac{\partial\omega}{\partial\eta}\Big|_n\right)\right]\right\} + \frac{u_P}{x'_P}\left[\frac{1+k}{2}\left(2\omega_P - 2\omega_w - \frac{\partial\omega}{\partial\xi}\Big|_w\right) + \frac{1-k}{2}\left(2\omega_e - 2\omega_P - \frac{\partial\omega}{\partial\xi}\Big|_e\right)\right] + $$

$$\frac{v_P}{y'_P}\left[\frac{1+l}{2}\left(2\omega_P - 2\omega_s - \frac{\partial\omega}{\partial\xi}\Big|_s\right) + \frac{1-l}{2}\left(2\omega_n - 2\omega_P - \frac{\partial\omega}{\partial\xi}\Big|_n\right)\right] = 0 \tag{5.7.3}$$

The values of k and l in equation (5.7.3) are decided to be 1 or -1 based on the sign of u_P and v_P, determining whether HO backward to forward differencing of the convective terms is used at point P at each iteration. This formulation provides the condition of globally 2nd-order upwind approximation for the convective terms.

5.4.3 Vorticity Boundary Condition Approximation

The boundary condition for vorticity has been a topic of much debate and finite difference derivations of this subject date back to the 1930s [164]. Thom [165,166] proposed the 1st-order accurate approximation formula $\omega_s = \frac{2(\psi_{s+1} - \psi_s)}{(\Delta h)^2}$ for calculation of vorticity (ω_s) on a stationary surface, where ψ_s and ψ_{s+1} stand for streamfunction value on the stationary surface and at the first node at the distance Δh normal to the surface, respectively. A summary of differencing expressions for higher-order accurate approximation of vorticity on the walls has been presented by Orszag and Israeli [167]. Roache [168] has provided details about this issue and analyzed results from the corresponding literature. The idea of no computation or calculation of the vorticity on the surfaces and consequently, no boundary condition for the vorticity, can also be found in numerical studies of the streamfunction-vorticity problem [130, 156, 158, and 169]. The prevailing belief in this category of numerical study of this formulation expresses that no physical

boundary condition is defined for vorticity and consequently, no numerical boundary condition should be imposed on vorticity. This type of study calculates the vorticity at the distance of cell size from the boundary [130], or by shrinking the actual physical domain mostly by the size of one cell [158, 169]. Spotz postulated that the vorticity is generated physically on the walls, so no computation of this parameter on the boundaries is required [130]. However, as mentioned above, a large numbers of studies can be found in which differencing expressions with different order of accuracy similar to Thom's equation were utilized to calculate the vorticity on the boundary walls [149, 170].

In the present study, the vorticity on the boundary walls is computed with different orders of accuracy using the compact finite difference method, accounting for the fact that equation (5.3.1) and its mapped form (5.4.1), are valid on the boundary. It is worth to note, again, that the value of streamfunction ψ has been considered constant on the walls. The vorticity on the wall can be approximated using Taylor's series expansion of streamfunction on the corresponding wall, as detailed below.

To simplify the discussion, consider a boundary wall as shown in Figure 5.3, with boundary node W and uniform grid spacing. The fact that the values of streamfunction at nodes NW, W and SW are all equal to the same constant value leads to $\frac{\partial^2 \psi}{\partial y^2}\big|_W = 0$. Thus, the value of vorticity on the wall is computed from $\omega_W = -\frac{\partial^2 \psi}{\partial x^2}\big|_W$.
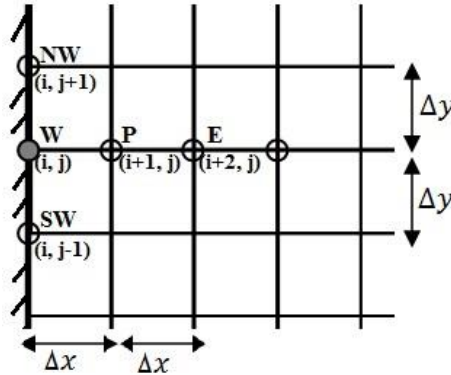
Figure 5.3: Illustration of vorticity computation on a boundary wall

The Taylor's series expansion of the streamfunction ψ at point $(i + 1, j)$ about the point (i, j) in the Cartesian coordinate system and in TFD notation is:

$$\psi_{(i+1,j)} = \psi_{(i,j)} + \Delta x \frac{\partial \psi}{\partial x}\Big|_{(i,j)} + \frac{(\Delta x)^2}{2} \frac{\partial^2 \psi}{\partial x^2}\Big|_{(i,j)} + O(\Delta x)^3 \qquad (5.8.1.1)$$

Rearranging equation (5.8.1.1) gives a 1st-order approximation for the second derivative of ψ with respect to x at the point (i, j),

$$\frac{\partial^2 \psi}{\partial x^2}\Big|_{(i,j)} = \frac{2(\psi_{(i+1,j)} - \psi_{(i,j)})}{(\Delta x)^2} - \frac{2}{(\Delta x)} \frac{\partial \psi}{\partial x}\Big|_{(i,j)} + O(\Delta x) \qquad (5.8.1.2)$$

The second term on the right hand side of equation (5.8.1.2) denotes the v-component of velocity, which is zero for the no-slip condition on stationary walls. At a boundary node on a moving wall,

this term, and a similar term involving $\frac{\partial \psi}{\partial y}$, would be equal to the same velocity component of the moving wall. Thus, for uniform spacing Δx, the vorticity at point (i,j) on the wall, $\omega_W = -\frac{\partial^2 \psi}{\partial x^2}\big|_W$, can be approximated using the 1$^{\text{st}}$-order accurate expression (5.8.1.2).

Using equation (2.3.2) to transform the second derivative, noting that grid spacing on the computational stencil is uniform ($\Delta \xi = 1$) and that $v_W = -\frac{\partial \psi}{\partial x}\big|_w = -\frac{1}{x'_W}\frac{\partial \psi}{\partial \xi}\big|_w$, a 1$^{\text{st}}$-order accurate expression for vorticity on the wall, on the computational stencil, is given as:

$$\omega_w = -\left[\frac{2(\psi_P - \psi_w)}{(x'_W)^2} - \left(\frac{2}{x'_W} + \frac{x''_W}{(x'_W)^2}\right)(-v_W)\right] \qquad (5.8.1.3)$$

If the wall in Figure 5.3 is stationary, the no-slip boundary condition implies that $v_W = 0$ in equation (5.8.1.3). The same procedure as above can be used to write a differencing scheme for computing vorticity at an arbitrary node (i,j) on a horizontal moving wall, depicted in Figure 5.4.
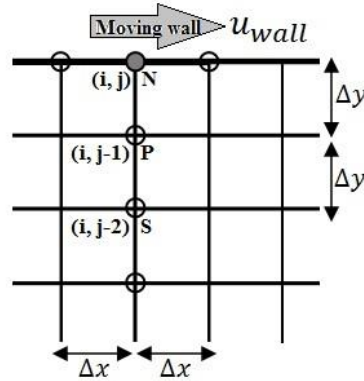
Figure 5.4: Illustration of vorticity computation on a moving boundary wall

The vorticity for this condition, written on the computational stencil, is:

$$\omega_n = -\left[\frac{2(\psi_P - \psi_n)}{(y'_N)^2} + \left(\frac{2}{y'_N} - \frac{y''_N}{(y'_N)^2}\right)(u_{wall})\right] \qquad (5.8.1.4)$$

Both equations (5.8.1.3) and (5.8.1.4) compute the vorticity at boundary nodes by 1$^{\text{st}}$-order accurate approximation. Higher-order accurate approximation can be obtained using compact FDM and the physical relation between streamfunction and components of velocity. This leads to HO formulas for vorticity proposed by Briley [171] by introducing imaginary nodes outside the domain and differentiating cubic splines. Briley's approximation has been used in several numerical studies based on the streamfunction-vorticity formulation, e.g., [168, 170, 172]. For example, using 1-sided compact differencing and the relation between physical parameters and streamfunction, the 2$^{\text{nd}}$-order accurate approximation on the computational stencil for vorticity at boundary nodes W (Figure 5.3) and N (Figure 5.4) are, respectively,

$$\omega_w = -\left[\frac{-7\psi_w + 8\psi_P - \psi_e}{2(x'_W)^2} - \left(\frac{3}{x'_W} + \frac{x''_W}{(x'_W)^2}\right)(-v_W)\right] \qquad (5.8.2.1)$$

$$\omega_n = -\left[\frac{-7\psi_n + 8\psi_P + \psi_s}{2(y_N')^2} + \left(\frac{3}{y_N'} - \frac{y_N''}{(y_N')^2}\right)(u_{wall})\right] \qquad (5.8.2.2)$$

The 2nd-order accurate approximation for calculating vorticity on the walls can also be given by equations (5.8.2.3) and (5.8.2.4) for boundary nodes W and N, in Figures 5.3 and 5.4, respectively. These formulations are even more compact compared to equations (5.8.2.1) and (5.8.2.2). The detailed derivation of these equations is presented in Appendix II.

$$\omega_w = -\left[\frac{-6\psi_w + 6\psi_P}{(x_W')^2} - \left(\frac{4}{x_W'} + \frac{x_W''}{(x_W')^2}\right)(-v_W) - \frac{2}{(x_W')^2}(-x_P'v_P)\right] \qquad (5.8.2.3)$$

$$\omega_n = -\left[\frac{-6\psi_n + 6\psi_P}{(y_N')^2} + \left(\frac{4}{y_N'} - \frac{y_N''}{(y_N')^2}\right)(u_{wall}) + \frac{2}{(y_N')^2}(y_P'u_P)\right] \qquad (5.8.2.4)$$

Implementations of equations (5.8.1.3) to (5.8.2.4) for boundary wall vorticity calculations are discussed through the Cartesian cut-stencil FDM results of the cavity problem.

5.5 Numerical Results of Cut-Stencil FDM for Square Lid-Driven Cavity Flow

The remainder of this chapter will focus on assessing the capabilities and numerical results of the Cartesian cut-stencil FD formulation for the solution of lid-driven cavity flow as a fluid mechanics benchmark problem. The results for each case are compared to numerical results from the literature to verify the methods and formulations that are used in coding of the cut-stencil method.

Figure 5.5 is a schematic of the lid-driven cavity flow problem. For validation purposes, properties such as such strength and locations of streamfunction and vorticity at the primary and secondary vortices, streamfunction and vorticity contours and the plots of velocity components along certain lines, e.g. vertical and horizontal mid-lines, are commonly used for comparison.
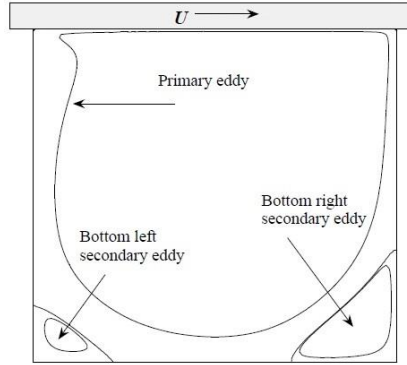
Figure 5.5: Schematic of a lid-driven cavity flow configuration (from Moshkin and Poochinapan [173])

Some results presented in this chapter are obtained from simulations on a non-uniform grid. The clustering function employed to generate the non-uniform grids for the cavity flow in a square domain are discussed in Appendix III.

5.5.1 Numerical Results for 2nd-Order Discretization of Streamfunction-Vorticity Equations

Initially, the 2nd-order accurate discretization method is considered for the solution of lid-driven cavity flow in a square domain. The domain and corresponding boundary conditions were shown in Figure 5.1 in non-dimensional form. The non-dimensional form of the flow equations (5.5.1), (5.5.2) and (5.5.3) are solved for two values of $Re = 100$ and $Re = 1000$.

5.5.1.1 $Re = 100$ with Non-Uniform 129*129 Grid; Boundary Vorticity Approximated by Briley's Formula

Table 5.1 gives the cut-stencil FD results for lid-driven cavity flow at $Re = 100$ when the 2nd-order accurate approximations introduced in equations (5.5.1) and (5.5.2) are used. A non-uniform grid of 129*129 nodes was designed for this case, to match the grid size used by Ghia et al. [150] and Bruneau and Jouron [174] which are used for comparison. The value of Reynolds number for this case is low enough that central differencing for the convective terms can be used. The vorticity on the boundaries is approximated with equations (5.8.2.1) and (5.8.2.2) for the stationary walls and the moving lid, respectively.

The results have been compared with other numerical predictions with the same grid size and good agreement between the cut-stencil solution and other numerical results can be seen from the data reported in Table 5.1. Comparison of vorticity along the moving wall from Ghia's study and the present work shows very good agreement, as observed from the plot in Figure 5.6. The absolute value of ω at point $(0.5, 1)$, which is located on the moving lid, predicted by Ghia et al. [150] and the cut-stencil FD simulations are equal to 6.575 and 6.568, respectively. The velocity at the centre of the cavity is $(-0.209, 0.057)$ from the cut-stencil FD solution and $(-0.206, 0.055)$ from Ghia et al. [150].

$Re = 100$					
Study (Grid)			Ghia et al. [150]	Bruneau and Jouron [174]	Cut-stencil FDM
Primary vortex	Abs. (ψ)		0.1034	0.1026	0.1035
	Location	x	0.6172	0.6172	0.6179
		y	0.7344	0.7344	0.7363
	Abs. (ω)		3.16646	N.A.	3.17681
B.L* vortex	Abs. (ψ)		1.75E-6	1.63E-6	1.79E-6
	Location	x	0.0313	0.0313	0.0350
		y	0.0391	0.0391	0.0350
	Abs. (ω)		1.555E-2	N.A.	1.589E-2
B.R** vortex	Abs. (ψ)		1.25E-5	1.23E-5	1.25E-5
	Location	x	0.9453	0.9453	0.9425
		y	0.0625	0.0625	0.0625
	Abs. (ω)		3.307E-2	N.A.	3.622E-2
*: Bottom left, **: Bottom right					

Table 5.1: Comparison of 2nd-order accurate cut-stencil solution to results of Ghia et al. [150] and Bruneau and Jouron [174] for lid-driven cavity flow at $Re = 100$ with non-uniform grid size of 129*129
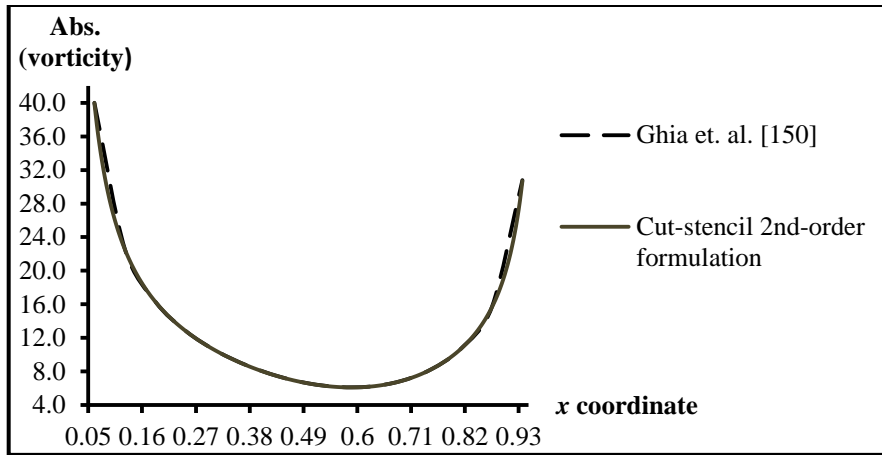
Figure 5.6: Comparison of vorticity along moving wall from 2nd-order cut-stencil FD formulation and Ghia et al. [150] ($Re = 100$, 129*129 grid)

The contours of streamfunction and vorticity obtained from the 2nd-order accurate cut-stencil FDM with non-uniform grid of size 129*129 are shown in Figures 5.7 and 5.8, respectively. Both of these contour plots compare well, quantitatively and qualitatively, with those reported in other studies [150, 153].
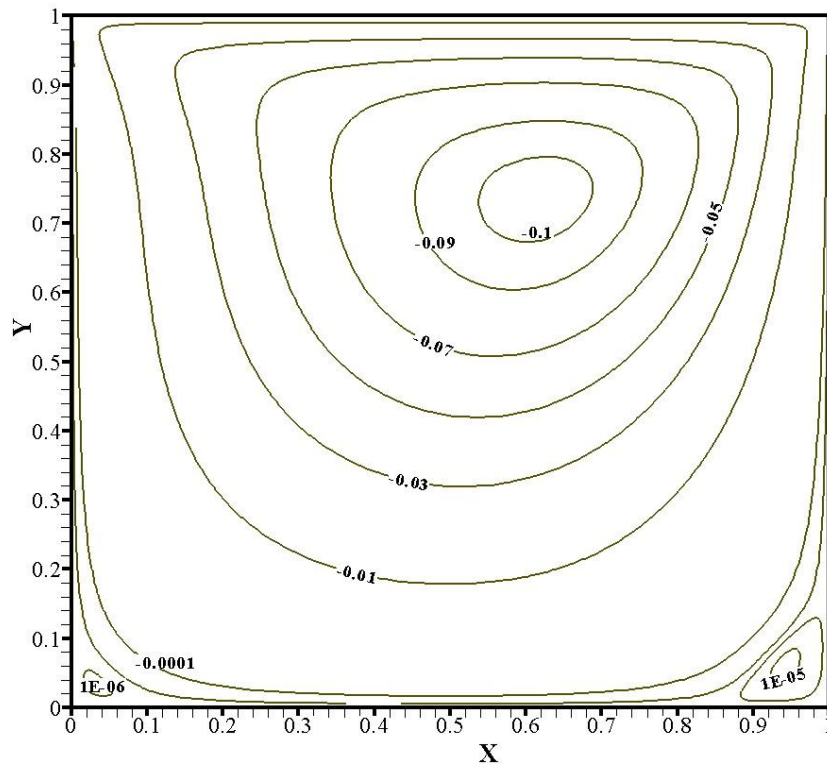
Figure 5.7: Streamfunction contours of 2nd-order cut-stencil FD solution ($Re = 100$, non-uniform 129*129 grid)
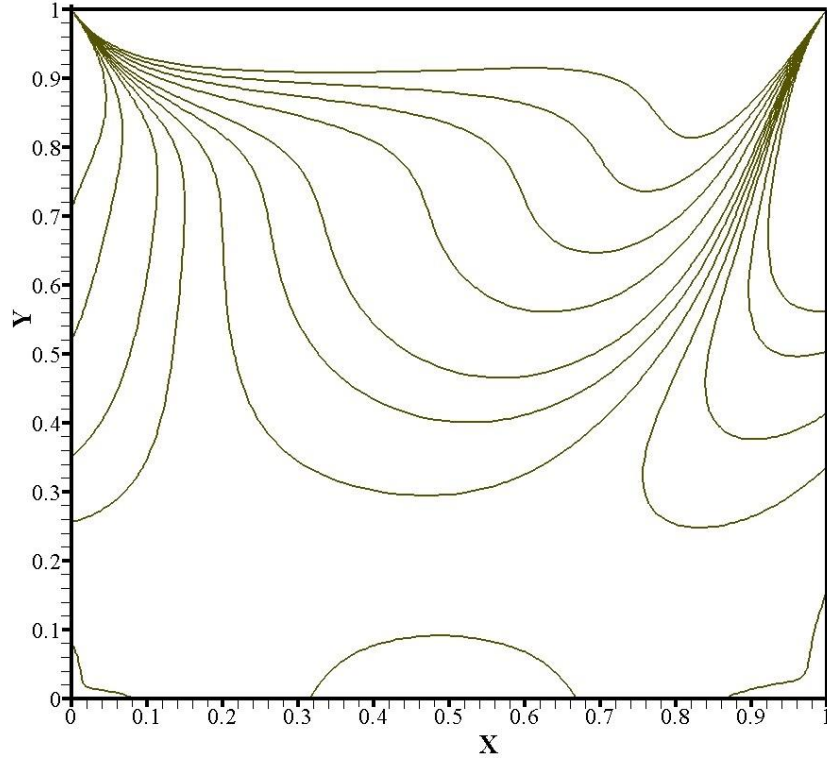
Figure 5.8: Vorticity contours of 2nd-order cut-stencil FD solution ($Re = 100$, non- uniform 129*129 grid)

5.5.1.2 $Re = 1000$ with Non-Uniform 129*129 Grid; Boundary Vorticity Approximated by Briley's Formula

A non-uniform Cartesian grid of 129*129 nodes is used to solve lid-driven cavity flow using the 2nd-order formulation of the cut-stencil FDM, for $Re = 1000$. Initially equations (5.5.1) and (5.5.2) were applied for this case using the Point-Jacobi scheme, which was the iterative method used for most of the previous simulations presented in this thesis. Like the $Re = 100$ case, vorticity on the boundaries is approximated with equations (5.8.2.1) and (5.8.2.2) for the stationary walls and moving lid, respectively. Since the Reynolds number in this case is relatively high, central differencing of the convective terms causes numerical instability and the simulation diverges.

Convergent computations for this case can be performed by choosing the point successive under-relaxation (SUR) method as the iterative scheme. The computations were repeated with different values of under-relaxation factor (σ) starting from 0.725 since the simulation diverged for $\sigma = 0.75$. The optimum value of σ is that which takes the least computational effort, measured by the number of iterations for each value of under-relaxation factor. The independency of the solution from σ and, consequently, from the number of iterations, is observed by comparing three parameters of the solution, namely, absolute value of ψ at the location of the primary vortex, components of velocity (u, v) at the midpoint ($x = 0.5, y = 0.5$) of the domain and absolute value of ω at location of the bottom left vortex. Table 5.2 reports the values of these flow parameters for each value of under-relaxation factor.

131

σ	Abs. ψ (Primary vortex)	(u, v) (mid-point)	Abs. ω (Bottom left vortex)
0.725	0.1179	(-0.06172,0.02618)	3.503E-1
0.70	0.1179	(-0.06172,0.02618)	3.503E-1
0.60	0.1179	(-0.06170,0.02620)	3.502E-1
0.45	0.1179	(-0.06168,0.02621)	3.502E-1
0.25	0.1179	(-0.06165,0.02622)	3.501E-1

Table 5.2: Independency of solution to relaxation factor σ for 2nd-order accurate solution ($Re = 1000$, non-uniform 129*129 grid)

As seen in Table 5.2, the value of relaxation factor (within the range for convergence) has only negligible effect on the solution. The effect of taken σ on computational effort is shown in Figure 5.9 which confirms 0.725 as the optimal value of σ for this simulation. This value exhibits good agreement with the same parameter for $Re = 1000$ in the literature, such as the values of 0.7 and 0.6 reported by Bruneau and Jouron [174] and Vanka [175], respectively.
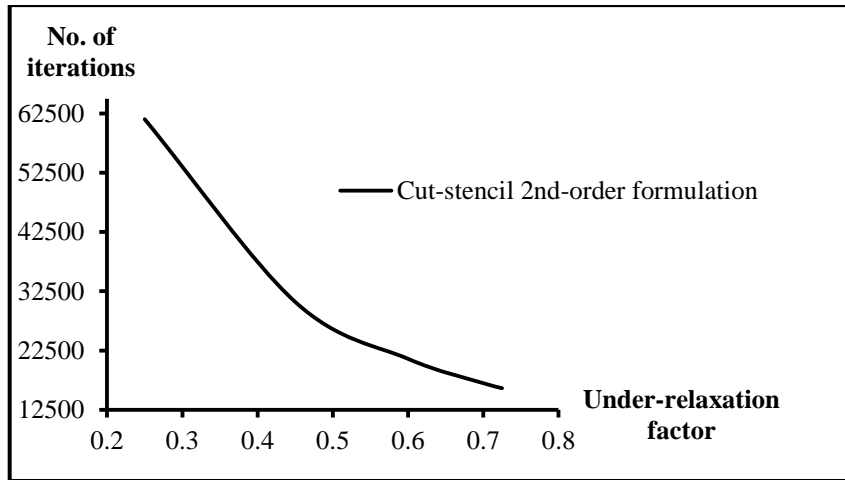
Figure 5.9: Variation of number of iterations with relaxation factor σ for 2nd-order accurate solution ($Re = 1000$, non-uniform 129*129 grid)

The results of the cut-stencil FD method using the SUR iterative scheme (with $\sigma = 0.725$) on a non-uniform 129*129 grid and comparison with a number of published results are summarized in Table 5.3.

$Re = 1000$						
Study (Grid)			Ghia et al. [150] (129*129)	Bruneau and Jouron [174] (256*256)	Goyon [176] (129*129)	Cut-stencil FDM (129*129)
Primary vortex	Abs. (ψ)		0.1179	0.1163	0.1157	0.1179
	Location	x	0.5313	0.5313	0.5312	0.5358
		y	0.5625	0.5586	0.5625	0.5714
	Abs. (ω)		2.04968	N.A.	N.A.	2.05270
B.L.* vortex	Abs. (ψ)		2.31E-4	3.25E-4	2.11E-4	2.30E-4
	Location	x	0.0859	0.0859	0.0859	0.0839
		y	0.0781	0.0820	0.0781	0.0783
	Abs. (ω)		0.36175	N.A.	N.A.	0.35031
B.R.** vortex	Abs. (ψ)		1.75E-3	1.91E-3	1.63E-3	1.71E-3
	Location	x	0.8594	0.8711	0.8671	0.86482
		y	0.1094	0.1094	0.1171	0.11459
	Abs. (ω)		1.15465	N.A.	N.A.	1.12668
*: Bottom left, **: Bottom right						

Table 5.3: Comparison of 2nd-order accurate cut-stencil solution for lid-driven cavity flow ($Re = 1000$, non-uniform 129*129 grid)

The absolute value of vorticity at point (0.5, 1), located on the moving lid, is calculated as 14.8901 in Ghia et al. [150] and as 14.9692 in the present study. Figure 5.10 plots the comparison of vorticity along the moving wall and results of 2nd-order formulation of cut-stencil FDM both for. The velocity (u, v) at the midpoint of the domain is equal to (-0.06172, 0.02618) and (-0.06080, 0.02526) from the cut-stencil FD solution and from Ghia et al. [150], respectively. The contours of streamfunction and vorticity are also shown in Figures 5.11 and 5.12, respectively.
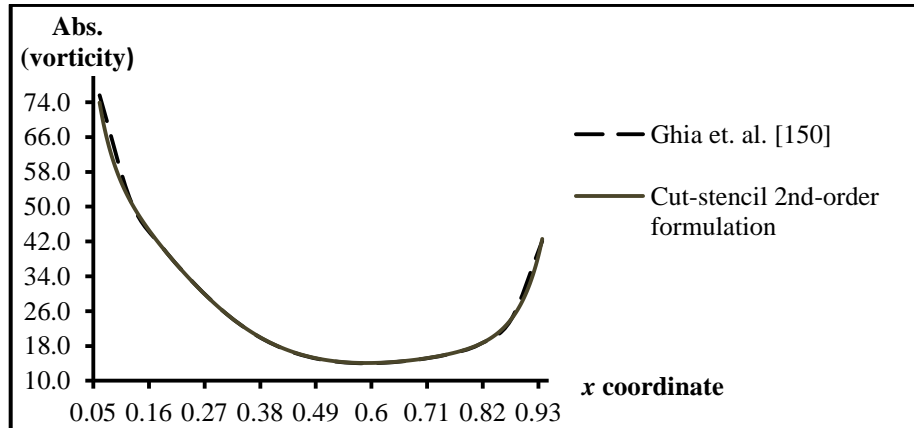
Figure 5.10: Comparison of vorticity along moving wall from 2nd-order cut-stencil FD formulation and Ghia et al. [150] ($Re = 1000$, non-uniform 129*129 grid)

Figure 5.11: Streamfunction contours of 2nd-order cut-stencil FD formulation ($Re = 1000$, non-uniform 129*129 grid)
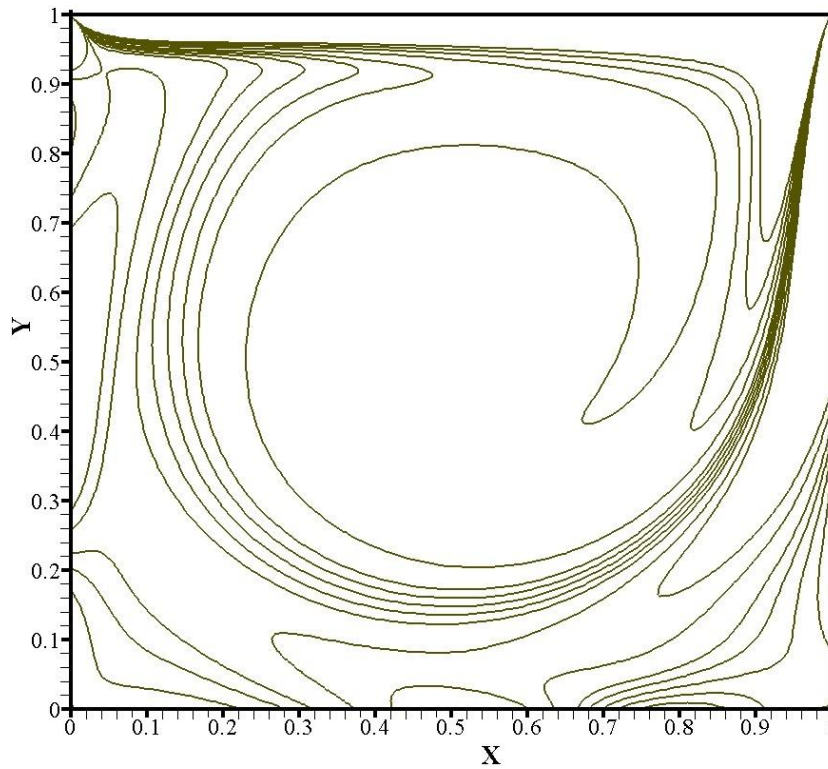
Figure 5.12: Vorticity contours of 2nd-order cut-stencil FD formulation ($Re = 1000$, non-uniform 129*129 grid)

5.5.1.3 $Re = 100$ and $Re = 1000$ with Non-Uniform 129*129 Grid; Boundary Vorticity Approximated by Compact Method

The solution from the 2nd-order formulation of the cut-stencil FDM to lid-driven cavity flow for $Re = 100$ and $Re = 1000$ using Briley's equation [171] for approximation the vorticity on the boundaries, demonstrates the accuracy of this method for this benchmark problem. In this section, the 2nd-order cut-stencil FD formulation is discussed when the vorticity on stationary walls and a moving boundary are approximated by equations (5.8.2.3) and (5.8.2.4), respectively. The purpose of this study is to examine the accuracy of these wall vorticity approximations that are believed to be more applicable for irregular shaped domains since they are more compact than Briley's expression. This study considers Reynolds numbers of $Re = 100$ and $Re = 1000$, with the same non-uniform 129*129 grid as used in previous examples, and the simulation results are revealed in Table 5.4.

Re			100		1000	
Study			Cut-stencil FDM	Ghia et al. [150]	Cut-stencil FDM	Ghia et al. [150]
Primary vortex	Abs. (ψ)		0.1035	0.1034	0.1180	0.1179
	Location	x	0.6179	0.6172	0.5358	0.5313
		y	0.7363	0.7344	0.5714	0.5625
	Abs. (ω)		3.17896	3.16646	2.05399	2.04968
B.L.* vortex	Abs. (ψ)		1.84E-6	1.75E-6	2.32E-4	2.31E-4
	Location	x	0.0350	0.0313	0.0839	0.0859
		y	0.0350	0.0391	0.0783	0.0781
	Abs. (ω)		1.563E-2	1.555E-2	0.35087	0.36175
B.R.** vortex	Abs. (ψ)		1.28E-5	1.25E-5	1.71E-3	1.75E-3
	Location	x	0.9425	0.9453	0.8648	0.8594
		y	0.0625	0.0625	0.1146	0.1094
	Abs. (ω)		3.574E-2	3.307E-2	1.12679	1.15465
*: Bottom left, **: Bottom right						

Table 5.4: Comparisons of 2nd-order accurate cut-stencil solution to lid-driven cavity flow using compact method for vorticity approximation on boundaries to results of Ghia et al. [150] ($Re = 100, 1000$)

Comparison of the results reported in Table 5.4 and the results in Tables 5.1 and 5.3 exhibits the good agreement between the solutions obtained using Briley's approximation [171] for the wall vorticity and the compact scheme, Figures 5.13 and 5.14 illustrate the vorticity along the moving wall, resulting from both wall vorticity approximation methods, for $Re = 100$ and $Re = 1000$, respectively. As Figures 5.13 and 5.14 indicate, no meaningful difference is observed for the vorticity approximation using these two methods.
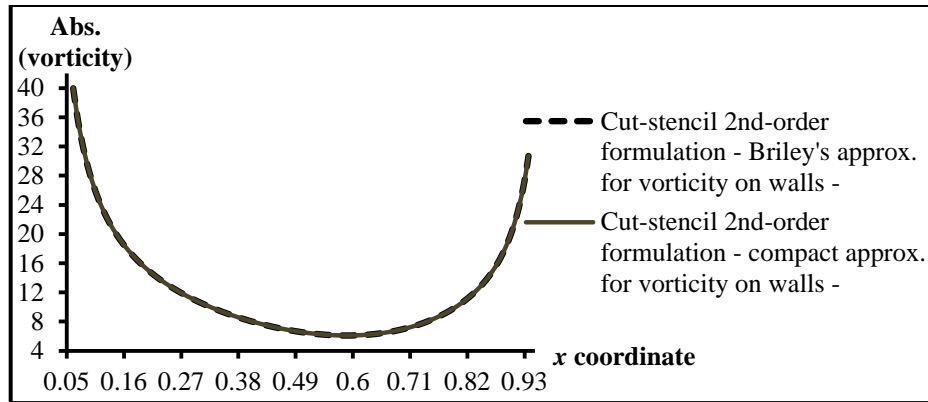
Figure 5.13: Comparison of vorticity along moving wall, approximated by Briley [171] and compact methods ($Re = 100$)
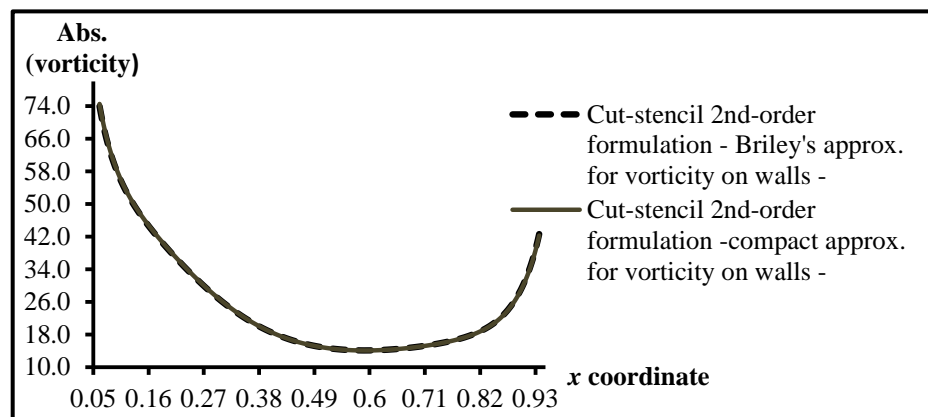
Figure 5.14: Comparison of vorticity along moving wall, approximated by Briley [171] and compact methods ($Re = 1000$)

5.5.2   Higher-Order Cut-Stencil FD Solution to Lid-Driven Flow in a Square Cavity

The solutions from higher-order formulations of the cut-stencil FDM for the lid-driven cavity flow are considered for $Re = 100, 400$ and 1000. The verification of the proposed higher-order formulas introduced in equations (5.6) and (5.7) is associated with demonstrating the capability of these higher-order formulations to accurately capture the flow features and quantitative parameters with a coarser mesh compared to that used for the 2nd-order accurate schemes. Also, the higher-order cut-stencil FDM solutions will be compared to solutions from some higher-order formulations in the literature.

In the following sections, HO cut-stencil FDM1 and HO cut-stencil FDM2 refer to discretization of the streamfunction-vorticity equations on the computational stencil using equations (5.6.1) to (5.6.3) and (5.7.1) to (5.7.3), respectively.

5.5.2.1 Results of Higher-Order Discretization ($Re = 100$)

Table 5.5 reveals the comparison of the higher-order cut-stencil FD solution to lid-driven flow on a square cavity to other numerical studies for $Re = 100$. A non-uniform grid of 41*41 nodes was used to compute the data shown in Table 5.5. The HO cut-stencil FDM1 and HO cut-stencil

136

FDM2 both exhibit good agreement with literature for the value of streamfunction at the primary vortex. Comparison of the data for the bottom left and right vortices to Ghia et al. [150], Gupta and Kalita [161] and Pandit [177] indicates that the higher-order cut-stencil methods yield more accurate solutions, and that HO cut-stencil FDM2 shows more precise data in comparison with Ghia et al. [150].

$Re = 100$						
Study (Grid)			Gupta and Kalita [161] (41*41)	Pandit [177] (41*41)	Cut-stencil HO-FDM1 (41*41)	Cut-stencil HO-FDM2 (41*41)
Primary vortex	Abs. (ψ)		0.103	0.104	0.103	0.103
	Location	x	0.6125	0.6184	0.6133	0.6133
		y	0.7375	0.7273	0.7501	0.7501
	Abs. (ω)		N.A.	N.A.	3.20415	3.19331
B.L.* vortex	Abs. (ψ)		1.83E-6	2.28E-6	1.78E-6	1.72E-6
	Location	x	0.0375	0.0316	0.0333	0.0333
		y	0.0375	0.0439	0.0333	0.0333
	Abs. (ω)		N.A.	N.A.	1.370E-2	1.350E-2
B.R.** vortex	Abs. (ψ)		1.45E-5	1.60E-5	1.33E-5	1.22E-5
	Location	x	0.9375	0.9425	0.9376	0.9376
		y	0.0625	0.0575	0.0625	0.0625
	Abs. (ω)		N.A.	N.A.	3.991E-2	4.020E-2
*: Bottom left, **: Bottom right						

Table 5.5: Comparison of higher-order cut-stencil solutions for lid-driven cavity flow ($Re = 100$, non-uniform 41*41 grid)

The components of velocity at the centre of the domain were obtained as $(-0.20838, 0.05574)$ and $(-0.20726, 0.05578)$ from the solutions of HO cut-stencil FDM1 and HO cut-stencil FDM2, respectively, which are in good agreement with the value $(-0.20581, 0.05454)$ from Ghia et al. [150]. The sum of relative errors of the velocity components compared to reported data in [150] are 3.45% and 2.98% for HO cut-stencil FDM1 and HO cut-stencil FDM2, respectively. Table 5.6 gives the data from the 2nd-order cut-stencil solution with grid sizes relatively coarser than the previous study (129*129 nodes) for $Re = 100$, to show the fundamental accuracy of the cut-stencil FDM. Also, data for one finer mesh than previously used for the higher-order cut-stencil FDMs recorded in Table 5.5 are reported in Table 5.6 to show the grid convergence for these solutions. All the grids for the results in Table 5.6 are non-uniform. The 2nd-order data in this table shows close values of key quantities compared to those reported in Table 5.1. The 2nd-order solution for grid size of 81*81 nodes is almost the same as the solution with 129*129 nodes in Table 5.1, which indicates mesh independency of the solution. The higher-order solutions obtained from the two grids of 41*41 and 51*51 nodes provide further evidence of grid independence. Figure 5.15 demonstrates the variation of vorticity along the moving wall and compares this parameter with data from Ghia et al. [150]. This plot suggests that Briley's formula [171] for vorticity approximation on walls can match accuracy with the higher-order cut-stencil schemes. Quantitatively, the absolute of vorticity at the centre of the moving wall ($x = 0.5, y = 1$) with a grid size of 41*41 nodes are 6.52285 and 6.54359 from HO cut-stencil FDM1 and HO cut-stencil FDM2, respectively, in comparison with the value 6.57451 in Ghia et al. [150].

Re = 100			2nd-order cut-stencil (41*41)	2nd-order cut-stencil (51*51)	2nd-order cut-stencil (81*81)	Cut-stencil HO-FDM1 (51*51)	Cut-stencil HO-FDM2 (51*51)
Study (Grid)							
Primary vortex	Abs. (ψ)		0.1024	0.1028	0.1032	0.1035	0.1033
	Location	x	0.61332	0.6207	0.6133	0.6207	0.6207
		y	0.75008	0.7311	0.7343	0.7311	0.7311
	Abs. (ω)		3.15676	3.16327	3.13028	3.19442	3.18636
B.L.* vortex	Abs. (ψ)		1.76E-6	1.77E-6	1.79E-6	1.77E-6	1.73E-6
	Location	x	0.0333	0.0360	0.0333	0.0360	0.0360
		y	0.0333	0.0360	0.0333	0.0360	0.0360
	Abs. (ω)		1.306E-2	1.677E-2	1.340E-2	1.728E-2	1.712E-2
B.R.** vortex	Abs. (ψ)		1.12E-5	1.21E-5	1.24E-5	1.31E-5	1.26E-5
	Location	x	0.9376	0.9407	0.9454	0.9407	0.9407
		y	0.0625	0.0593	0.0625	0.0593	0.0593
	Abs. (ω)		4.121E-2	3.501E-2	3.308E-2	3.416E-2	3.437E-2
*: Bottom left, **: Bottom right							

Table 5.6: 2nd-order and higher-order cut-stencil solutions for lid-driven cavity flow ($Re = 100$, different non-uniform grid sizes)
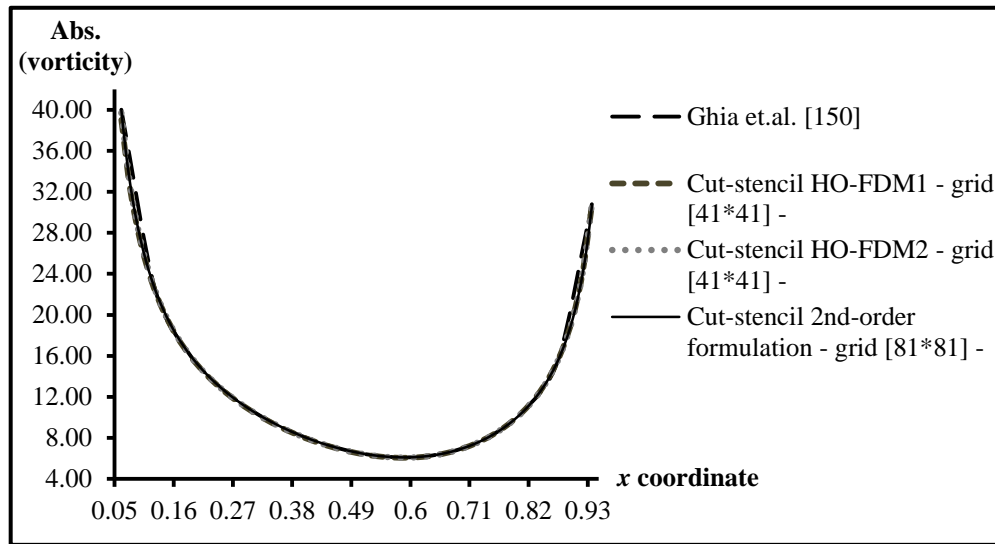
Figure 5.15: Comparison of vorticity along the moving wall from 2nd-order and higher-order cut-stencil FD solutions ($Re = 100$)

The contours of streamfunction and vorticity of HO cut-stencil FDM1 and HO cut-stencil FDM2 solutions, on a grid size of 41*41 nodes, are shown in Figures 5.16 to 5.19. These figures exhibit good agreement with contours of the 2nd-order cut-stencil solution on a grid size of 129*129, as shown in Figures 5.7 and 5.8, and with the contours produced by other numerical studies.
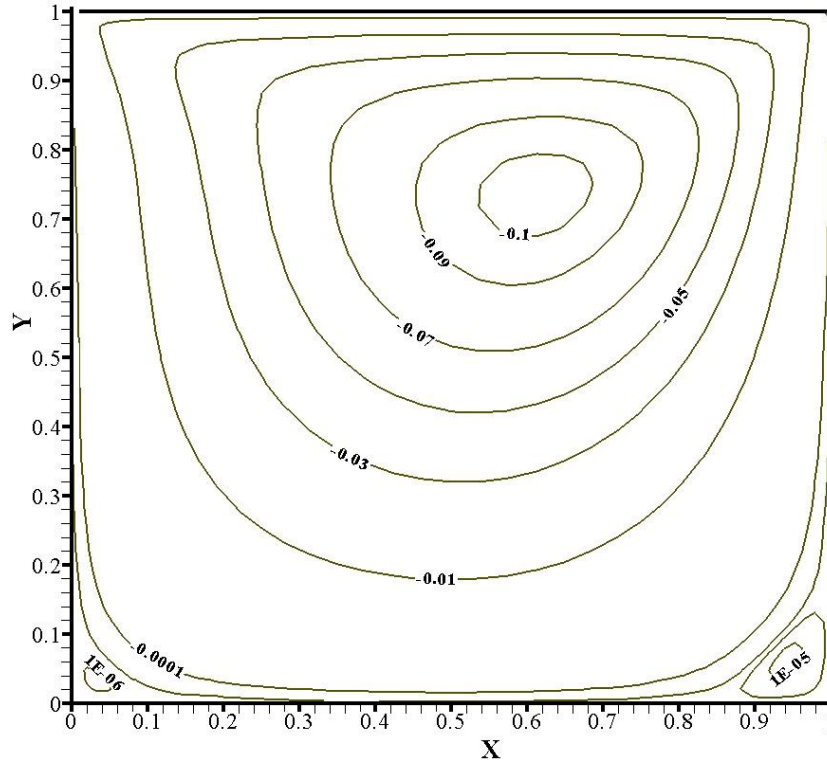
Figure 5.16: Streamfunction contours of cut-stencil HO-FDM1 formulation ($Re = 100$, non-uniform grid of 41*41 nodes)
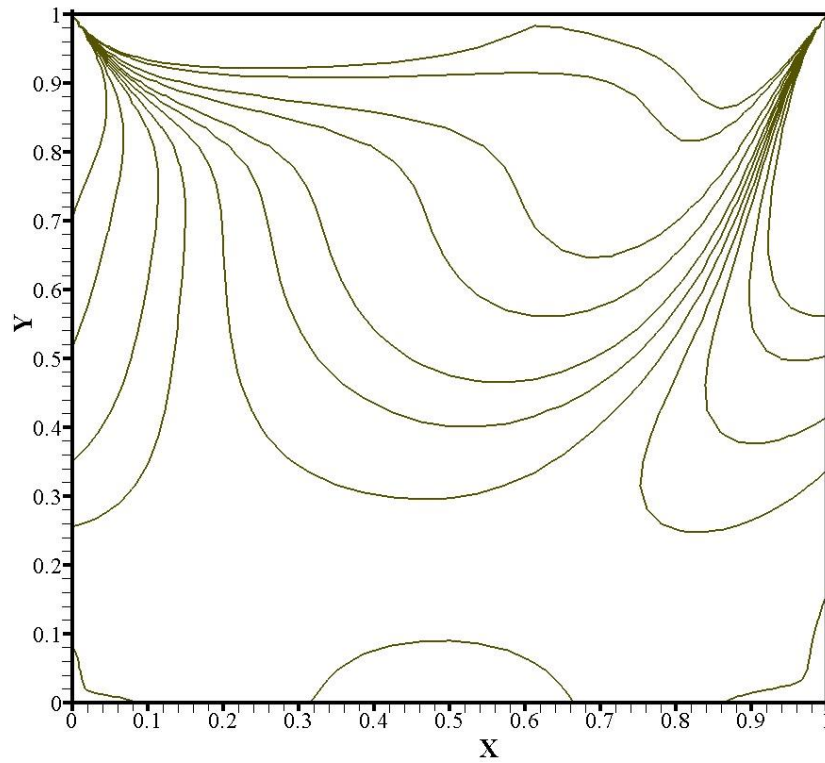
Figure 5.17: Vorticity contours of cut-stencil HO-FDM1 formulation ($Re = 100$, non-uniform grid of 41*41 nodes)
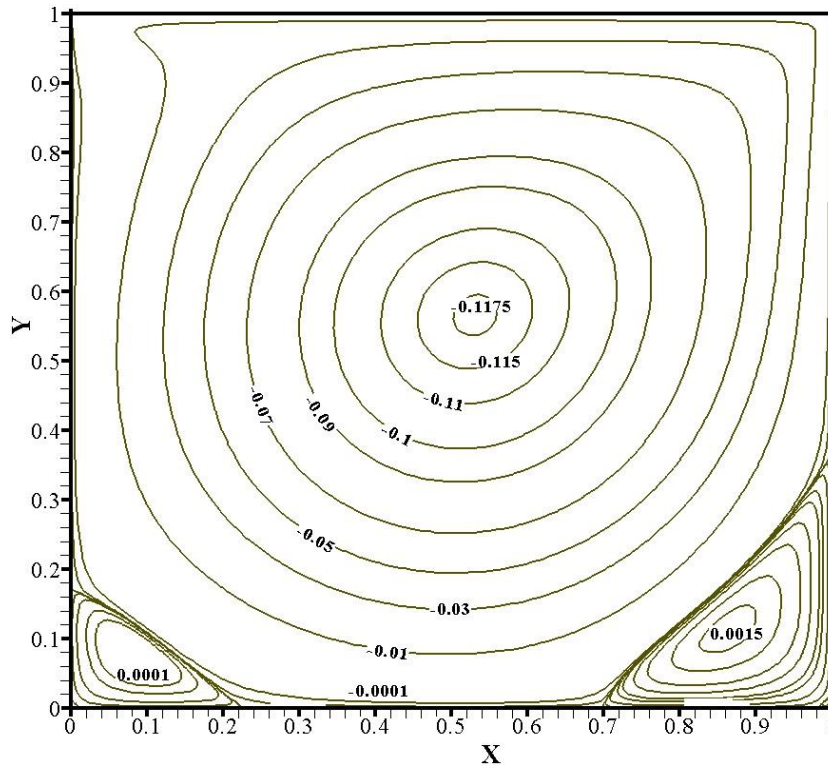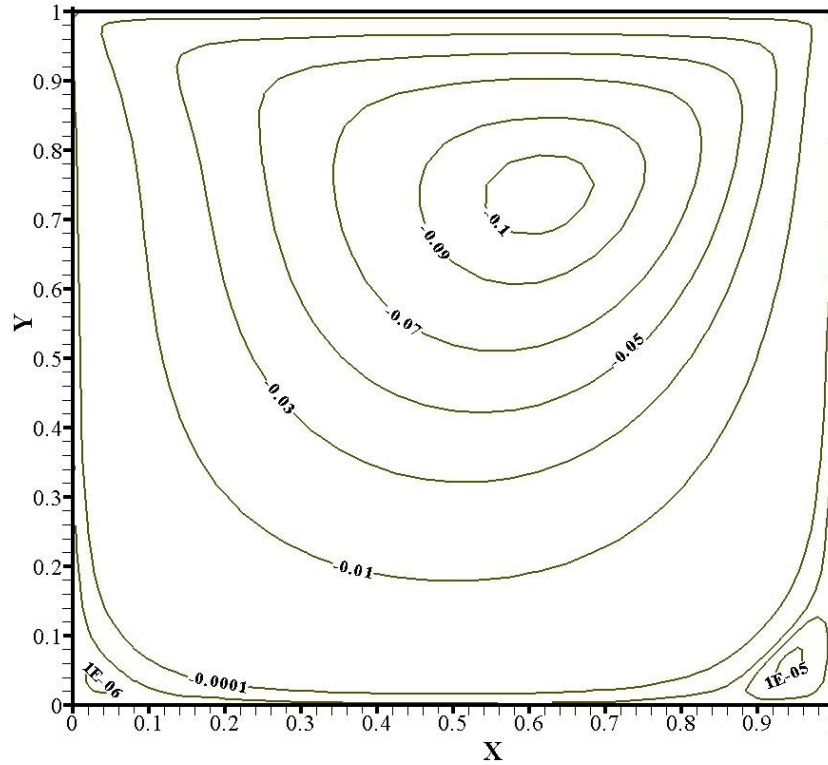
Figure 5.18: Streamfunction contours of cut-stencil HO-FDM2 formulation ($Re = 100$, non-uniform grid of 41*41 nodes)
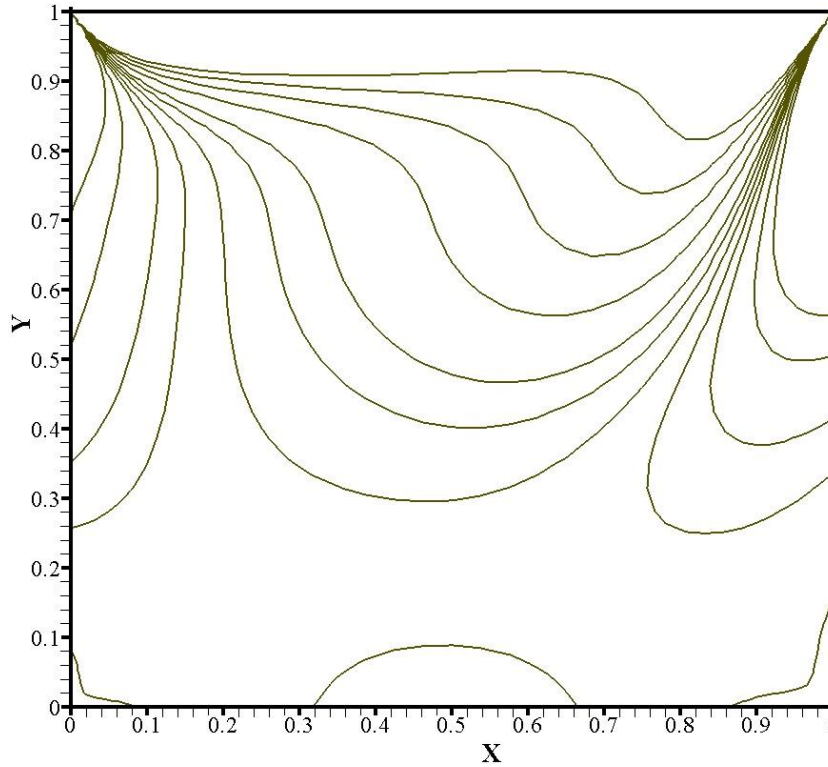
Figure 5.19: Vorticity contours of cut-stencil HO-FDM2 formulation ($Re = 100$, non-uniform grid of 41*41 nodes)

5.5.2.2 Results for 2nd-Order and Higher-Order Discretizations ($Re = 400$)

The cut-stencil FD solutions for $Re = 400$ using 2nd-order and higher-order schemes are compared to other available numerical data in this section. The 2nd-order cut-stencil FD solutions at $Re = 400$ for several non-uniform Cartesian grids are reported in Table 5.7, along with other 2nd-order accurate solutions and a mesh-free smooth particle hydrodynamics solution. The cut-stencil FD solutions in Table 5.7 signify good agreement even for the coarsest mesh size (81*81 grid) compared to other available data, especially in comparison with the generally regarded most reliable study [150]. The difference between the cut-stencil solution and other numerical data becomes smaller as the grid size increases for almost all key features of the solutions. Comparison of the cut-stencil FD solutions between grid size of 101*101 nodes and grid size of 129*129 nodes demonstrates that the differences of strength of vorticity in the primary vortex and the bottom left and right vortices are negligible, a sign of grid independency of the solution.

$Re = 400$								
Study (Grid)			Ghia et al. [150] (129*129)	Schreiber and Keller [178] (141*141)	Khorasan-izade and Sousa [179] MFM[i]	2nd-order cut-stencil FDM (81*81)	2nd-order cut-stencil FDM (101*101)	2nd-order cut-stencil FDM (129*129)
Primary vortex	Abs. (ψ)		0.1139	0.1130	0.1088	0.1128	0.1132	0.1135
	Location	x	0.5547	0.5571	0.5568	0.5572	0.5610	0.5596
		y	0.6055	0.6071	0.6066	0.6133	0.6059	0.6064
	Abs. (ω)		2.29469	2.28100	2.2793	2.27841	2.27985	2.28453
B.L.* vortex	Abs. (ψ)		1.42E-5	1.45E5	9.42E-6	1.37E-5	1.40E-5	1.41E-5
	Location	x	0.0508	0.0500	0.0692	0.0546	0.0531	0.052698
		y	0.0469	0.0429	0.0422	0.0471	0.0471	0.048051
	Abs. (ω)		5.697E-2	4.710E-2	5.514E-2	6.232E-2	6.040E-2	6.206E-2
B.R.** vortex	Abs. (ψ)		6.42E-4	6.44E-4	5.89E-4	6.28E-4	6.34E-4	6.39E-4
	Location	x	0.8906	0.8857	0.8815	0.8814	0.8814	0.8854
		y	0.1250	0.1143	0.1262	0.1186	0.1186	0.1213
	Abs. (ω)		4.335E-1	3.940E-1	4.232E-1	4.445E-1	4.479E-1	4.418E-1
*: Bottom left, **: Bottom right, (i): Mesh-free method								

Table 5.7: 2nd-order cut-stencil solutions and comparison to literature for lid-driven cavity flow ($Re = 400$, different non-uniform grids)

The velocity components at the midpoint of the domain were calculated from the cut-stencil FD solutions for grid sizes of 81*81, 101*101 and 129*129, yielding values of $(-0.11594, 0.05307)$, $(-0.11562, 0.05271)$ and $(-0.11541, 0.05246)$, respectively. The relative errors between these values and that of Ghia et al. [150] are 3.35%, 2.38% and 1.71%, respectively. Additionally, the absolute value of vorticity at the centre of the sliding lid ($x = 0.5, y = 1$) is equal to 10.17987, 10.12931 and 10.09345 from the cut-stencil solutions on these same grids, producing relative errors of 1.25%, 0.75% and 0.39%, confirming correctness of the vorticity approximation formula for this moderate value of Reynolds number. Comparison of the vorticity along the moving wall from the solution on 129*129 nodes with Ghia et al, [150] is plotted in Figure 5.20. All the data from this analysis provides further evidence of the precision of the formulations and programming approach of the 2nd-order cut-stencil FDM.
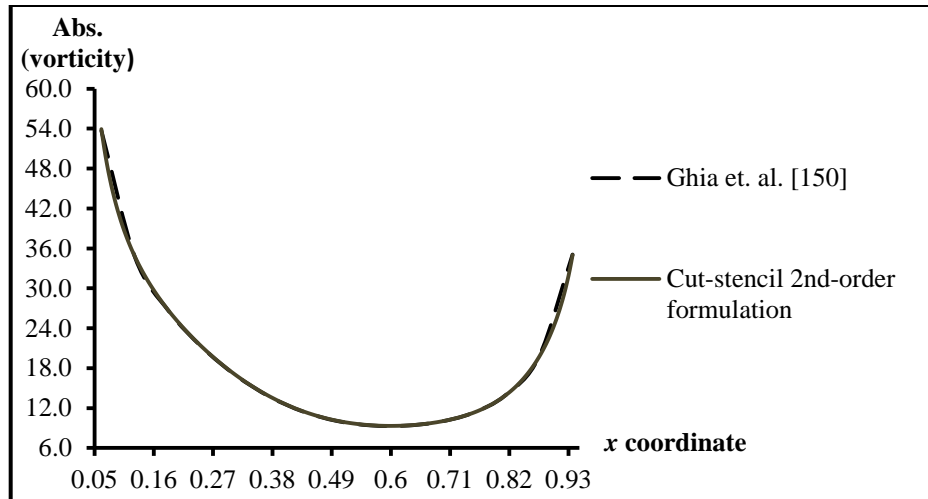
Figure 5.20: Comparison of vorticity along moving wall from 2nd-order cut-stencil FD formulation to Ghia et al. [150] ($Re = 400$, non-uniform 129*129 grid)

The contours of streamfunctions and vorticity for the 2nd-order cut-stencil solution at $Re = 400$ are depicted in Figures 5.21 and 5.22, based on a grid size of 129*129 nodes.

Figure 5.21: Streamfunction contours of 2nd-order cut-stencil FD formulation ($Re = 400$, non-uniform 129*129 grid)
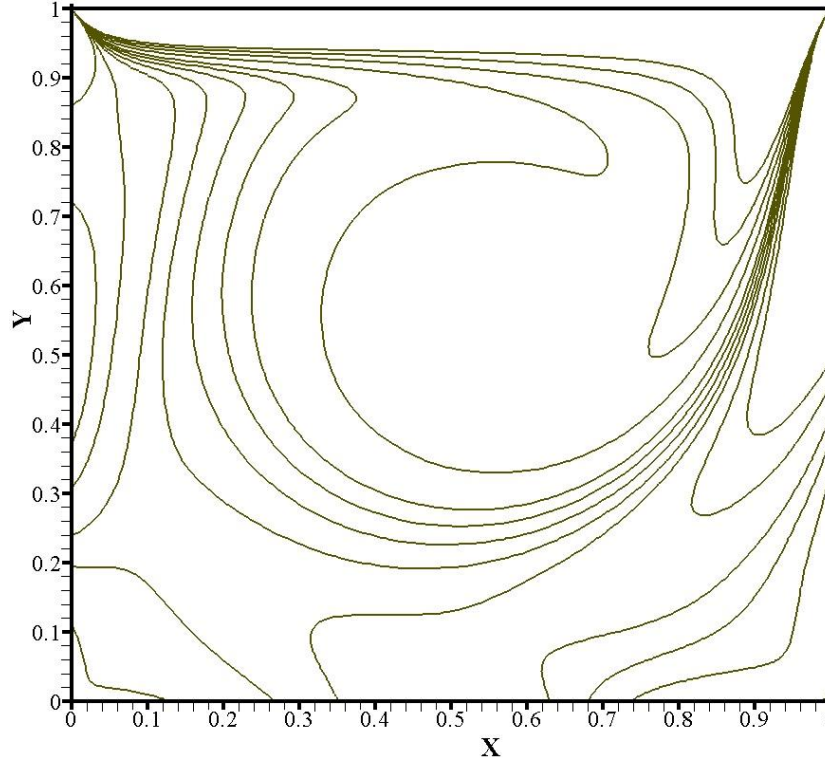
Figure 5.22: Vorticity contours of 2nd-order cut-stencil FD formulation ($Re = 400$, non-uniform 129*129 grid)

The data from the HO cut-stencil FDM1 and HO cut-stencil FDM2 solutions using two non-uniform grids of sizes 65*65 and 81*81 nodes, and comparison with other available higher-order solutions for lid-driven cavity flow on a square at $Re = 400$ are reported here. The initial simulation, which used HO-FDM1 with Point-Jacobi as the iterative scheme and central differencing for the convective terms, failed to converge. Possible reasons of this condition in convective-dominated flows have been pointed out in the literature, along with different answers to resolve this issue, as discussed in Chapter 2, e.g. [56] and in other research [180, 181,182]. But, the HO cut-stencil FDM1 formulation with Point-Jacobi method and using the upwind higher-order compact discretization method in equation (5.6.3) to approximate the convective terms, gives the key features of the solution as indicated in Table 5.8 for a non-uniform grid of size 65*65 nodes.

$Re = 400$				
		Primary vortex	B.L.* vortex	B.R.** vortex
Abs. (ψ)		0.1154	1.44E-5	7.10E-4
Location	x	0.5477	0.0527	0.8787
	y	0.5948	0.0436	0.1213
Abs. (ω)		2.33753	5.461E-2	4.758E-1
*: Bottom left, **: Bottom right				

Table 5.8: HO-FDM1 solution to lid-driven cavity flow on a square using higher-order compact upwind scheme for approximation of convective terms ($Re = 400$, non-uniform 65*65 grid)

Although comparison of data in Table 5.8 to other researchers' results [150, 177] shows good agreement for most key features of this case, the streamfunction at the centre of the bottom right vortex is not very accurate. To resolve this problem, the HO cut-stencil FDM1 formulation is tested on the same grid size when the point successive under-relaxation (SUR) method is chosen as the iterative scheme. Numerical tests show that this iterative method converges with higher-order central differencing of the convective terms when the under-relaxation factor (σ) is chosen below 0.85. The solution is shown to be independent of σ by comparing three parameters of the solutions, the value of ψ at the location of the primary vortex, components of velocity at midpoint of the domain and absolute value of ω at location of bottom left vortex. Table 5.9 reports the values of these parameters for each value of under-relaxation factor.

σ	Abs. ψ (Primary vortex)	(u, v) (midpoint)	Abs. ω (Bottom left vortex)
0.850	0.1143	(-0.11621,0.05122)	5.368E-2
0.825	0.1143	(-0.11623,0.05123)	5.367E-2
0.800	0.1143	(-0.11623,0.05123)	5.367E-2
0.750	0.1143	(-0.11623,0.05123)	5.367E-2
0.725	0.1143	(-0.11623,0.05123)	5.367E-2
0.685	0.1143	(-0.11623,0.05123)	5.367E-2

Table 5.9: Independency of solution to relaxation factor σ for HO-FDM1 ($Re = 400$, non-uniform 65*65 grid)

The optimum value of σ is determined by considering the number of iterations for each under-relaxation factor as the variation of iterations versus σ is demonstrated in Figure 5.23. The optimum value of σ is found to be 0.825, requiring the minimum number of iterations to complete the solution.

Figure 5.23: Variation of number of iterations with relaxation factor σ for HO-FDM1 solution ($Re = 400$, non-uniform 65*65 grid)

The HO-FDM1 formulation with a non-uniform grid of 81*81 nodes suffers from divergence if Point-Jacobi and higher-order central differencing are used. This issue, similar to the grid size of 65*65 nodes for the same formulation, is resolved when the upwind higher-order compact

discretization method in equation (5.6.3) is used to approximate the convective terms. The results for this case are summarized in Table 5.10.

$Re = 400$				
		Primary vortex	B.L.* vortex	B.R.** vortex
Abs. (ψ)		0.1150	1.45E-5	6.86E-4
Location	x	0.5572	0.0546	0.8814
	y	0.6133	0.0471	0.1186
Abs. (ω)		2.31252	6.529E-2	4.491E-1
*: Bottom left, **: Bottom right				

Table 5.10: Solution for HO-FDM1 formulation to lid-driven cavity flow on a square using higher-order compact upwind scheme for approximation of convective terms ($Re = 400$, non-uniform 81*81 grid)

The HO-FDM1 solution for $Re = 400$, along with central higher-order compact approximation for convective terms, for a non-uniform grid of 81*81 nodes, can be obtained when SUR is used as the iterative scheme. The optimum value of σ for this case is found as 0.98.

The issue of divergence of the Point-Jacobi method when the central higher-order compact scheme is used to approximate convective terms does not occur when the HO-FDM2 formulation is used for both non-uniform grid sizes of 65*65 and 81*81 nodes. The higher-order solutions for lid-driven cavity flow in a square, for $Re = 400$, from both HO cut-stencil FD formulations and from other numerical studies are reported in Table 5.11. The HO-FDM1 solutions in Table 5.11 are obtained from the SUR iterative method along with central higher-order compact approximation for convective terms, with $\sigma = 0.825$ and $\sigma = 0.98$ for the non-uniform grids of 65*65 and 81*81 nodes, respectively.

$Re = 400$								
Study (Grid)			Gupta and Kalita [161] (81*81)	Pandit [177] (61*61)	Cut-stencil HO-FDM1		Cut-stencil HO-FDM2	
					(65*65)	(81*81)	(65*65)	(81*81)
Primary vortex	Abs. (ψ)		0.113	0.114	0.114	0.114	0.114	0.114
	Location	x	0.5500	0.5532	0.5477	0.5572	0.5477	0.5572
		y	0.6125	0.6055	0.5948	0.6133	0.5948	0.6133
	Abs. (ω)		N.A.	N.A.	2.31378	2.29800	2.30684	2.29282
B.L* vortex	Abs. (ψ)		1.30E-5	1.49E-5	1.43E-5	1.43E-5	1.40E-5	1.41E-5
	Location	x	0.0500	0.0528	0.0527	0.0546	0.0527	0.0546
		y	0.0500	0.0439	0.0436	0.0471	0.0436	0.0471
	Abs. (ω)		N.A.	N.A.	5.367E-2	6.432E-2	5.288E-2	6.367E-2
B.R** vortex	Abs. (ψ)		6.48E-4	6.35E-5	6.67E-4	6.60E-4	6.51E-4	6.49E-4
	Location	x	0.8875	0.8908	0.8787	0.8814	0.8787	0.8814
		y	0.1250	0.1384	0.1213	0.1186	0.1213	0.1186
	Abs. (ω)		N.A.	N.A.	4.817E-1	4.511E-1	4.789E-1	4.492E-1
*: Bottom left, **: Bottom right								

Table 5.11: Higher-order cut-stencil FD solutions for lid-driven cavity flow ($Re = 400$, different non-uniform grids)

Initially, the results of HO-FDM1 shown in Tables 5.9 to 5.11 reveal better agreement with other numerical solutions for data in Table 5.11. This close agreement is due to the higher-order accurate differencing used to approximate the convective terms, since the formal order of

accuracy for the approximation of the convective terms are 4th and 2nd-order for equations (5.6.2) and (5.6.3), respectively. Comparisons of both cut-stencil higher-order formulations exhibit no meaningful difference between the key features of the solution for each grid size, except for the value of ψ at the bottom right vortex, where HO-FDM2 predicts a value that is closer to the results reported in Table 5.11 and to Ghia et al. [150]. HO-FDM2 also gives a value closer to Ghia et al. [150] for ψ at the bottom left vortex with a non-uniform grid of 65*65 nodes compared to the predictions of Gupta and Kalita [161] and Pandit [177] which use 81*81 and 61*61 nodes, respectively.

More quantitative confirmation of the higher-order accuracy of HO-FDM1 and HO-FDM2 for $Re = 400$ is provided by comparison of the components of velocity at the centre of the domain and the vorticity at the midpoint of the moving wall with Ghia et al [150]. This comparison is presented in Table 5.12.

Study (Grid)	Ghia et al. [150] (129*129)	Cut-stencil HO-FDM1		Cut-stencil HO-FDM2	
		(65*65)	(81*81)	(65*65)	(81*81)
(u, v) at midpoint* of domain	(-0.11477, 0.05186)	(-0.11623, 0.05123)	(-0.11579, 0.05152)	(-0.11633, 0.05198)	(-0.11589, 0.05202)
Abs. (ω) at midpoint** of moving wall	10.0542	9.9356	9.9702	10.0171	10.0239
*: $(x = 0.5, y = 0.5)$, **: $(x = 0.5, y = 1)$					

Table 5.12: Comparison of velocity components at midpoint of domain and vorticity at midpoint of moving wall for HO cut-stencil FD solutions with Ghia et al. [150] ($Re = 400$)

The contours of streamfunction and vorticity for the higher-order cut-stencil solutions are shown in Figures 5.24 to 5.27, for a non-uniform grid of 81*81 nodes. The comparison of contours from HO-FDM1 and HO-FDM2 to the contours of the 2nd-order cut-stencil method that were presented in Figures 5.21 and 5.22 for 129*129 nodes, tells same qualitative accuracy captured by relatively coarser mesh from higher order solutions.
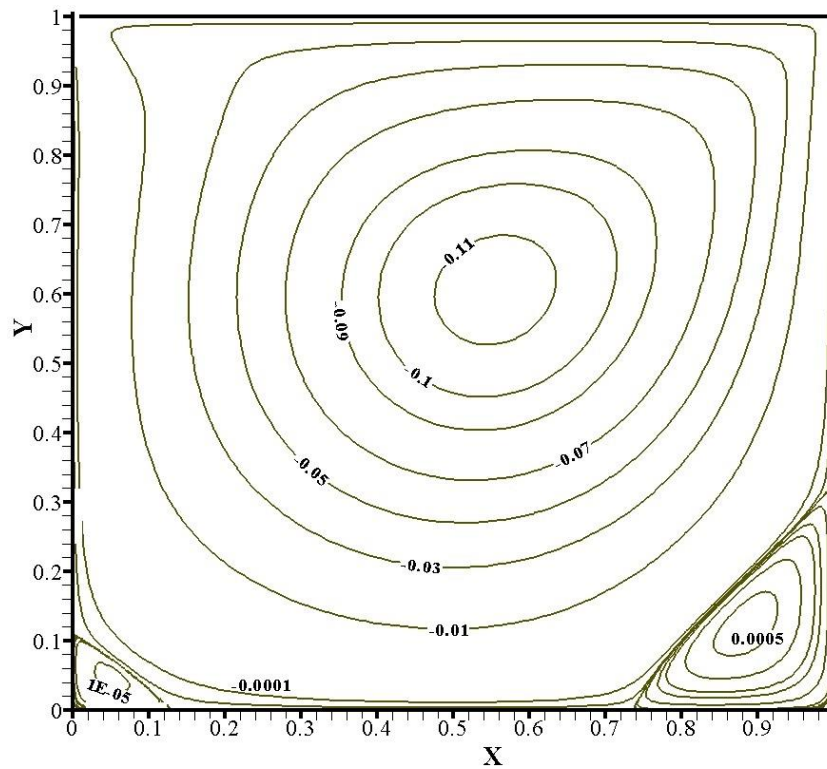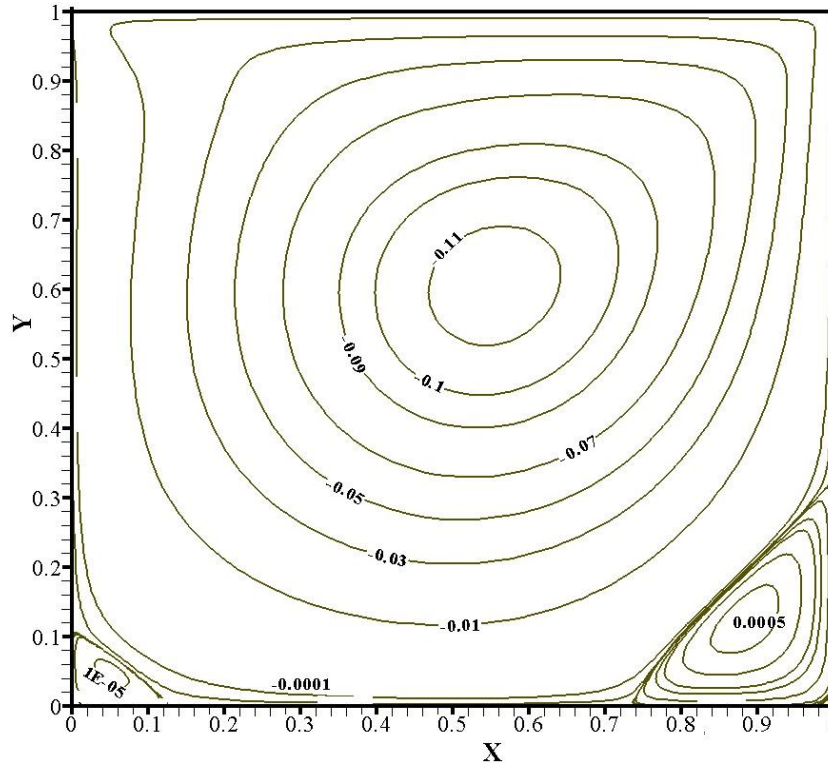
Figure 5.24: Streamfunction contours of HO-FDM1 solution ($Re = 400$, non-uniform 81*81 grid)
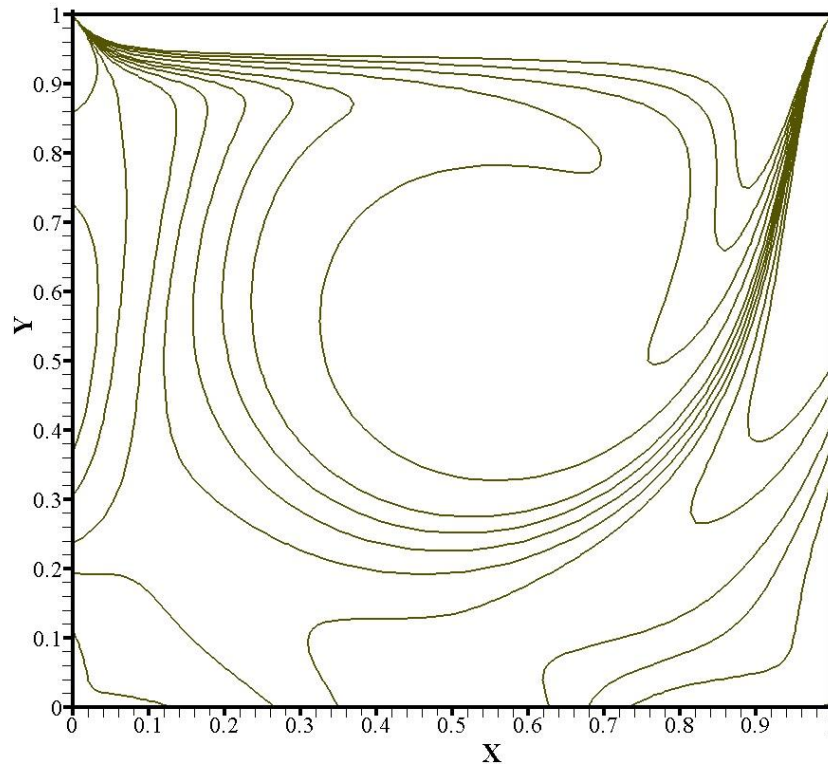
Figure 5.25: Vorticity contours of HO-FDM1 solution ($Re = 400$, non-uniform 81*81 grid)
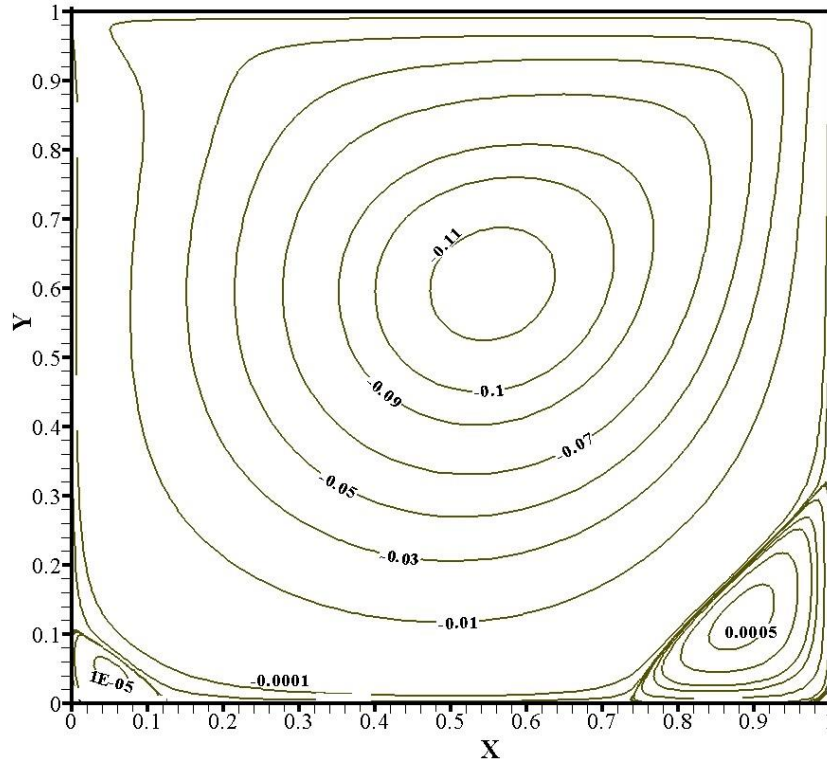
Figure 5.26: Streamfunction contours of HO-FDM2 solution ($Re = 400$, non-uniform 81*81 grid)
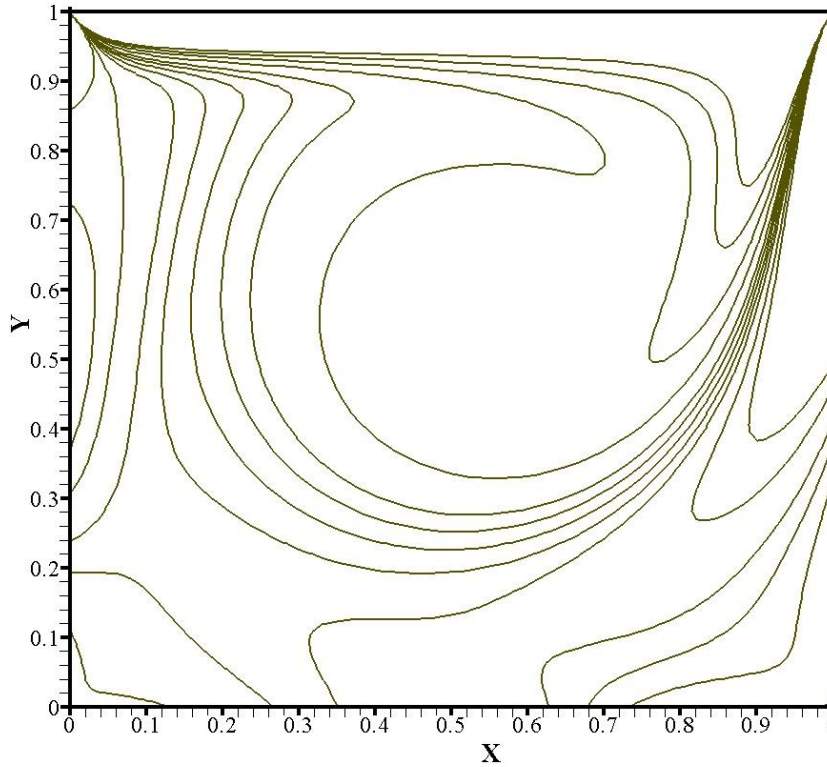
Figure 5.27: Vorticity contours of HO-FDM2 solution ($Re = 400$, non-uniform 81*81 grid)

5.5.2.3 Results of Higher-Order Discretization ($Re = 1000$)

The 2nd-order cut-stencil solution for $Re = 1000$ using a grid size of 129*129 was presented in section 5.5.1.2 and the corresponding results were used for overall validation of the cut-stencil FD formulation for the cavity flow problem.

The higher-order formulations (5.6) and (5.7) are implemented for $Re = 1000$ in this section and compared to other available higher-order numerical results.

The initial computations using higher-order central difference approximation of the convective terms for two grids of 65*65 and 81*81 nodes, for both HO cut-stencil FD formulations, failed to converge. Results for the higher-order formulations, using higher-order upwind approximations of the convective terms are summarized in Table 5.13.

$Re = 1000$			Cut-stencil HO-FDM1		Cut-stencil HO-FDM2
Study (Grid)			(65*65)	(81*81)	(81*81)
Primary vortex	Abs. (ψ)		0.1214	0.1207	0.1222
	Location	x	0.5239	0.5382	0.5191
		y	0.5713	0.5761	0.5572
	Abs. (ω)		2.14188	2.11547	2.13616
B.L.* vortex	Abs. (ψ)		2.18E-4	2.27E-4	2.41E-4
	Location	x	0.0839	0.0794	0.0794
		y	0.0728	0.0794	0.0794
	Abs. (ω)		3.195E-1	3.455E-1	3.542E-1
B.R.** vortex	Abs. (ψ)		1.94E-3	1.87E-3	1.87E-3
	Location	x	0.8501	0.8590	0.8590
		y	0.1081	0.1186	0.1081
	Abs. (ω)		1.138	1.198	1.112
*: Bottom left, **: Bottom right					

Table 5.13: Solutions of HO cut-stencil formulations for lid-driven cavity flow on a square using higher-order compact upwind scheme for approximation of convective terms ($Re = 1000$, non-uniform grid)

The SUR method was used to perform the computations for the higher-order FDMs and similar to previous Reynolds numbers, the optimum value of the relaxation factor σ can be defined for each grid size and each higher-order formulation. HO-FDM1 for a non-uniform grid size of 65*65 nodes failed to converge for values of σ greater than or equal to 0.325. The variation of number of iterations versus the value of σ starting from 0.30 is shown in Figure 5.28, indicating that the minimum computational effort is obtained by choosing $\sigma = 0.30$. Table 5.14 examines the independency of the solution from the value of σ for a non-uniform grid of 65*65 nodes, by reporting the same three features of the solution used for the analysis for other values of Re.
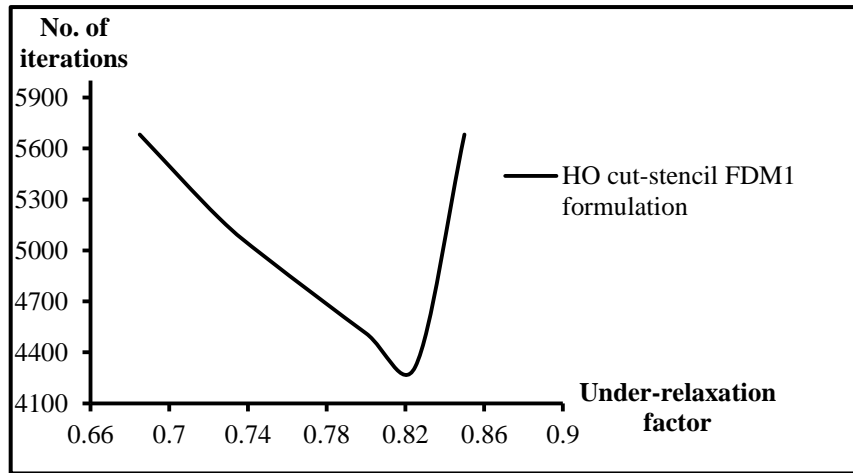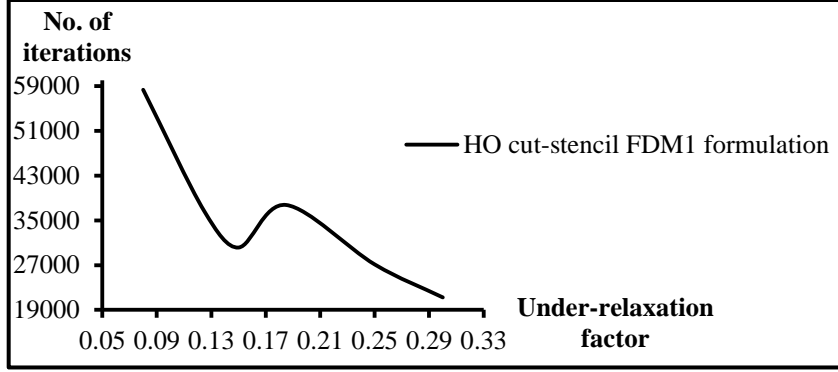
Figure 5.28: Variation number of iterations with relaxation factor σ for HO-FDM1 solution ($Re = 1000$, non-uniform 65*65 grid)

$Re = 1000$			
σ	Abs. ψ (Primary vortex)	(u, v) (mid-point)	Abs. ω (B.L vortex)
0.300	0.1195	(-0.06361, 0.02442)	3.209E-1
0.250	0.1195	(-0.06361, 0.02442)	3.210E-1
0.185	0.1195	(-0.06361, 0.02442)	3.210E-1
0.150	0.1194	(-0.06300, 0.02457)	3.216E-1
0.125	0.1194	(-0.06299,0.02457)	3.215E-1
0.080	0.1194	(-0.06298,0.02458)	3.215E-1

Table 5.14: Independency of solution to relaxation factor σ for HO-FDM1 solution ($Re = 1000$, non-uniform 65*65 grid)

The minimum computational effort for the HO-FDM2 solution on a non-uniform grid of 65*65 nodes, using SUR as the iterative scheme and higher-order central compact approximation of the convective terms, is achieved by taking $\sigma = 0.3$. The higher-order computations diverged for any value of $\sigma \geq 0.45$. The variation of the number of iterations versus the value of σ is depicted in Figure 5.29. The independency of the HO-FDM2 solution from the number of iterations is verified by the data reported in Table 5.15. The optimum value for σ for this grid size for both cut-stencil higher-order formulations can be taken as 0.3.
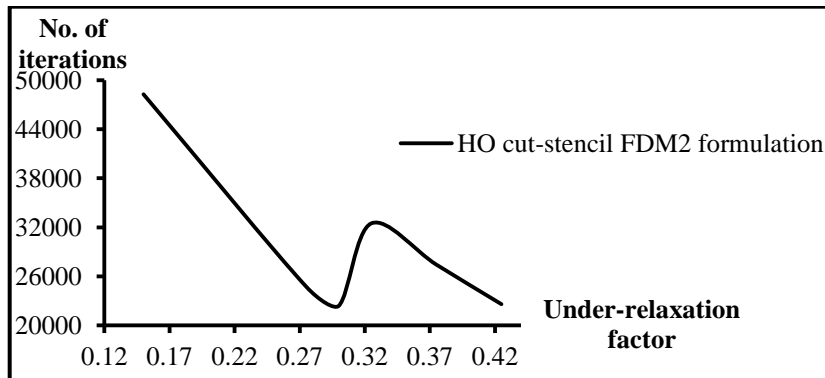
Figure 5.29: Variation number of iterations with relaxation factor σ for HO-FDM2 solution ($Re = 1000$, non-uniform 65*65 grid)

Table 5.15 records the data to verify the independency of the solution from the value of the relaxation factor for HO-FDM2, with the same key features of the solution as used previously, e.g. in Table 5.14. The optimum value of σ for the non-uniform grid of 65*65 nodes takes the same value of 0.3 for both cut-stencil HO formulations.

| σ | $Re = 1000$ | | |
	Abs. ψ (Primary vortex)	(u, v) (midpoint)	Abs. ω (B.L. vortex)
0.425	0.1185	(-0.06306, 0.02516)	3.139E-1
0.375	0.1185	(-0.06306, 0.02516)	3.139E-1
0.325	0.1185	(-0.06306, 0.02516)	3.139E-1
0.300	0.1184	(-0.06227, 0.02520)	3.161E-1
0.275	0.1184	(-0.06227, 0.02520)	3.161E-1
0.150	0.1184	(-0.06224, 0.02522)	3.159E-1

Table 5.15: Independency of solution to relaxation factor σ for HO-FDM2 solution ($Re = 1000$, non-uniform 65*65 grid)

Higher-order central differencing of the convective terms using HO-FDM1 and a non-uniform 81*81 grid converges for values of σ less than 0.375 and the computational cost is minimum by taking $\sigma = 0.35$, as shown in Figure 5.30. The data in Table 5.16 shows that the solution is independent of the values of σ for this grid size.
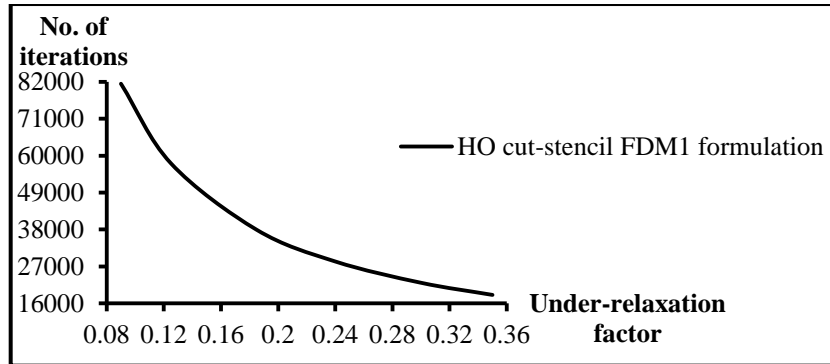
Figure 5.30: Variation number of iterations with relaxation factor σ for HO-FDM1 solution ($Re = 1000$, non-uniform 81*81 grid)

σ	Abs. ψ (Primary vortex)	(u, v) (mid-point)	Abs. ω (B.L vortex)
0.350	0.1192	(-0.06249,0.02503)	3.432E-1
0.300	0.1192	(-0.06249,0.02504)	3.431E-1
0.240	0.1192	(-0.06246,0.02505)	3.431E-1
0.185	0.1192	(-0.06245,0.02505)	3.430E-1
0.125	0.1192	(-0.06243,0.02506)	3.430E-1
0.090	0.1192	(-0.06243,0.02507)	3.429E-1

Table 5.16: Independency of solution to relaxation factor σ for HO-FDM1 solution ($Re = 1000$, non-uniform 81*81 grid)

Choosing a value of σ greater or equal to 0.55 leads to divergence for the HO-FDM2 formulation, for a non-uniform grid of 81*81 nodes, when central higher-order differencing is used to

approximate the convective terms. The variation of the number of iterations versus σ for the HO-FDM2 solution on this non-uniform grid is plotted in Figure 5.31. The number of iterations reaches a minimum when the value of σ is taken as 0.465. The data in Table 5.17 addresses the independency of the solution from σ.
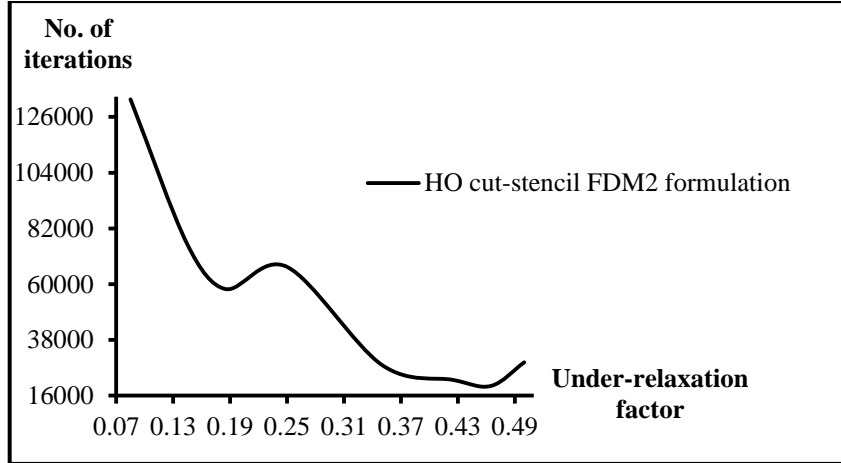
Figure 5.31: Variation number of iterations with relaxation factor σ for HO-FDM2 solution ($Re = 1000$, non-uniform 81*81 grid)

σ	Abs. ψ (Primary vortex)	(u, v) (midpoint)	Abs. ω (B.L. vortex)
0.500	0.1186	(-0.06271,0.02538)	3.370E-1
0.465	0.1185	(-0.06180,0.02527)	3.415E-1
0.425	0.1185	(-0.06179,0.02528)	3.414E-1
0.350	0.1185	(-0.06177,0.02529)	3.413E-1
0.250	0.1186	(-0.06271,0.02538)	3.370E-1
0.185	0.1185	(-0.06173,0.02532)	3.411E-1
0.145	0.1185	(-0.06173,0.02532)	3.411E-1
0.085	0.1185	(-0.06172,0.02533)	3.410E-1

Table 5.17: Independency of solution to relaxation factor σ for HO-FDM2 solution ($Re = 1000$, non-uniform 81*81 grid)

Some published higher-order (mostly 4th-order) results for lid-driven cavity flow at $Re = 1000$ are summarized in Table 5.18. These results are compared with solutions of the cut-stencil higher-order formulations. All the cut-stencil FDM results reported in Table 5.18 are from simulations carried out using the optimum σ of each method and corresponding mesh size.

Comparing the cut-stencil FD solutions in Tables 5.13 and 5.18 shows that the results given in Table 5.18 are closer to the results from other numerical methods, especially with the benchmark results of Ghia et al. [150]. This observation can be seen clearly for the values of streamfunction in the primary, bottom left and right vortices, demonstrating the effect of the proposed higher-order approximations for convective terms (equations (5.6.2) or (5.7.2)) as used for the data reported in Table 5.18. In other words, for these higher-order schemes, the suggested higher-order central differencing to approximate convective terms can be applied even for relatively high Reynolds number.

Study (Grid)	Primary vortex			B.L.* vortex			B.R.** vortex		
	Abs. (ψ)	Location (x,y)	Abs. (ω)	Abs. (ψ)	Location (x,y)	Abs. (ω)	Abs. (ψ)	Location (x,y)	Abs. (ω)
Gupta and Kalita [161] (81*81)	0.117	(0.5250, 0.5625)	N. A.	2.02 E-4	(0.0875, 0.0750)	N. A.	1.70 E-3	(0.8625, 0.1125)	N. A.
Pandit [177] (61*61)	0.118	(0.5266, (0.5532)	N. A.	2.31 E-4	(0.0840, 0.0840)	N. A.	1.72 E-3	(0.8577, 0.1092)	N. A.
Nishida and Satofuka [183] (65*65)	0.118	(0.5313, 0.5625)	2.05692	2.24 E-4	(0.0781, 0.0781)	3.134 E-1	1.67 E-3	(0.8594, 0.1094)	1.125
Nishida and Satofuka [183] (129*129)	0.119	(0.5313, 0.5625)	2.06616	2.32 E-4	(0.0859, 0.0781)	3.671 E-1	1.72 E-3	(0.8594, 0.1094)	1.144
Cut-stencil HO-FDM1 (65*65)	0.120	(0.5239, 0.5714)	2.08386	2.30 E-4	(0.0839, 0.0728)	3.209 E-1	1.81 E-3	(0.8648, 0.1213)	1.175
Cut-stencil HO-FDM1 (81*81)	0.119	(0.5382, 0.5572)	2.07696	2.35 E-4	(0.0794, 0.0794)	3.432 E-1	1.78 E-3	(0.8590, 0.1081)	1.121
Cut-stencil HO-FDM2 (65*65)	0.118	(0.5239, 0.5714)	2.06372	2.30 E-4	(0.0839, 0.0728)	3.161 E-1	1.76 E-3	(0.8648, 0.1081)	1.031
Cut-stencil HO-FDM2 (81*81)	0.119	(0.5382, 0.5572)	2.06270	2.33 E-4	(0.0794, 0.0794)	3.415 E-1	1.74 E-3	(0.8590, 0.1081)	1.127
*: Bottom left, **: Bottom right									

Table 5.18: HO cut-stencil FD solutions and comparison to other HO solutions for lid-driven cavity flow ($Re = 1000$, different non-uniform grids)

Comparison of cut-stencil solutions in Table 5.18 to studies of Gupta and Kalita [161], Pandit [177], Nishida and Satofuka [183] with grid size of 129*129 and Ghia et al. [150] indicate close agreement for almost all key features of the solution, except for the value of streamfunction at the bottom right vortex predicted by HO-FDM1 with a non-uniform 65*65 grid. This issue has been resolved by the HO-FDM2 solution with the same grid or by HO-FDM1 formulation with a finer grid (81*81 nodes). The more accurate solution can be obtained by HO-FDM2, even with a coarser mesh, which originates from the more accurate approximation of derivatives at endpoints of the 5-point stencil, as discussed in Chapter 2. Analysis of other numerical results reveals that the higher-order solution in [161] was not able to capture the streamfunction value at the bottom left corner as accurately as other studies. Furthermore, the streamfunction values at both corner vortices reported in [183] with a 65*65 grid are somewhat different from other studies, such as [149], [150] and [177]. Comparison of velocity from HO-FDM1 and HO-FDM2 at the centre of the domain and vorticity at the midpoint of the moving wall to data of Ghia et al. [150] is exhibited in Table 5.19. A relative difference of 7.95% for velocity components from HO-FDM1 with a non-uniform 65*65 grid is reduced to 2.66% for the same grid when HO-FDM2 is applied. A similar reduction in relative difference is seen for vorticity at the midpoint of the moving wall, from 2.87% for HO-FDM1 with the non-uniform 65*65 grid to 0.87% for HO-FDM2 with the same grid size. Generally speaking, the data in Table 5.19 indicates good quantitative agreement

between both cut-stencil FD higher-order formulations for $Re = 1000$, while the precision of HO-FDM2 predicts slightly more accurate results compared to Ghia et al. [150]. It should be noted that the higher-order results in Table 5.19 correspond to coarser non-uniform grids than used by Ghia et al. [150]. Furthermore, the HO-FDM2 predictions are closer to Ghia's than HO-FDM1 due to the implementation of more accurate approximations of the derivatives at the endpoints of the stencil in the HO-FDM2 formulation. The plot in Figure 5.32 also demonstrates the qualitative comparison of vorticity along the moving wall to Ghia et al. [150] for $Re = 1000$, verifying the accuracy of the approximation for vorticity for this rather high value of Reynolds number. The coarser grid sizes used for the higher-order cut-stencil solutions produces good agreement with the Ghia et al. data, where a relatively finer mesh has been used to predict the values of vorticity along the moving wall.

Study (Grid)	Ghia et al. [150] (129*129)	Cut-stencil HO-FDM1		Cut-stencil HO-FDM2	
		(65*65)	(81*81)	(65*65)	(81*81)
(u, v) at midpoint* of domain	(-0.06080, 0.02526)	(-0.06361, 0.02442)	(-0.06249, 0.02503)	(-0.06227, 0.02520)	(-0.06180, 0.02527)
Abs. (ω) at midpoint** of moving wall	14.8901	14.4625	14.5943	14.7604	14.7827
*: $(x = 0.5, y = 0.5)$, **: $(x = 0.5, y = 1)$					

Table 5.19: Comparison of velocity components at midpoint of the domain and vorticity at midpoint of the moving wall for HO cut-stencil FD solutions with Ghia et al. [150] ($Re = 1000$)
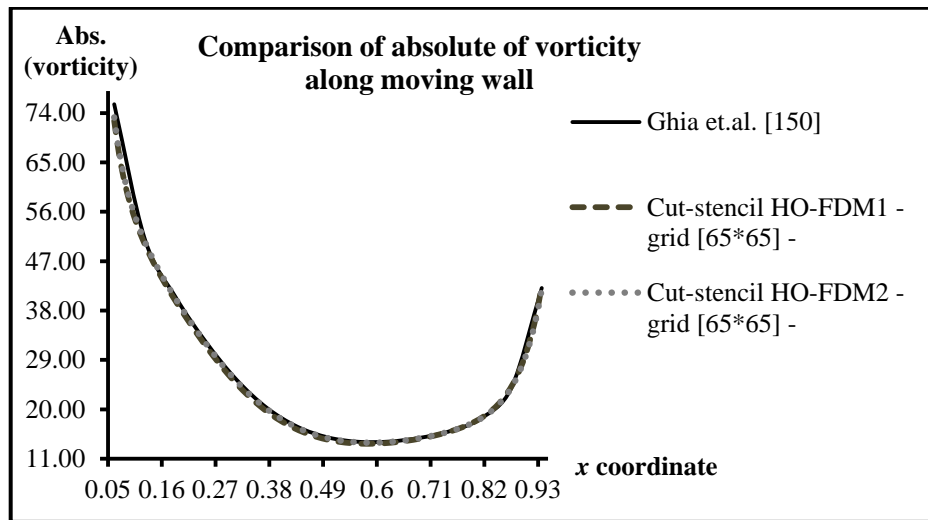
Figure 5.32: Comparison of vorticity along the moving wall from HO cut-stencil FD solutions to Ghia et al. [150] ($Re = 1000$)

The streamfunction and vorticity contours for both higher-order cut-stencil FD solutions with the non-uniform 65*65 grid are shown in Figures 5.33 to 5.36, providing a good qualitative comparison between the higher-order solutions, the results from other numerical studies and the 2nd-order solution of the present study, depicted in Figures 5.11 and 5.12.

154
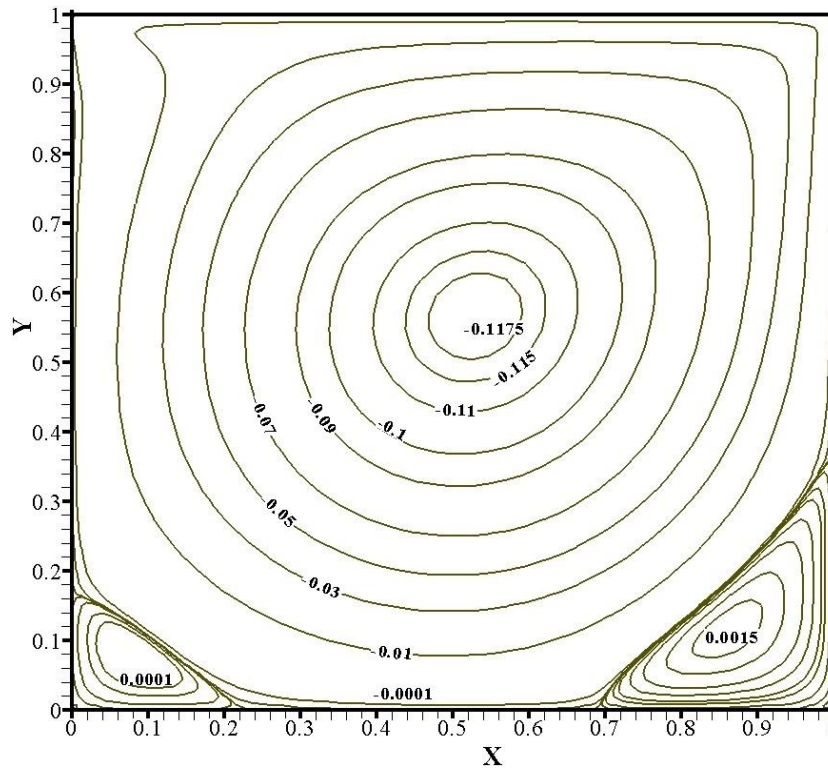
Figure 5.33: Streamfunction contours of HO-FDM1 formulation ($Re = 1000$, non-uniform 65*65 grid)
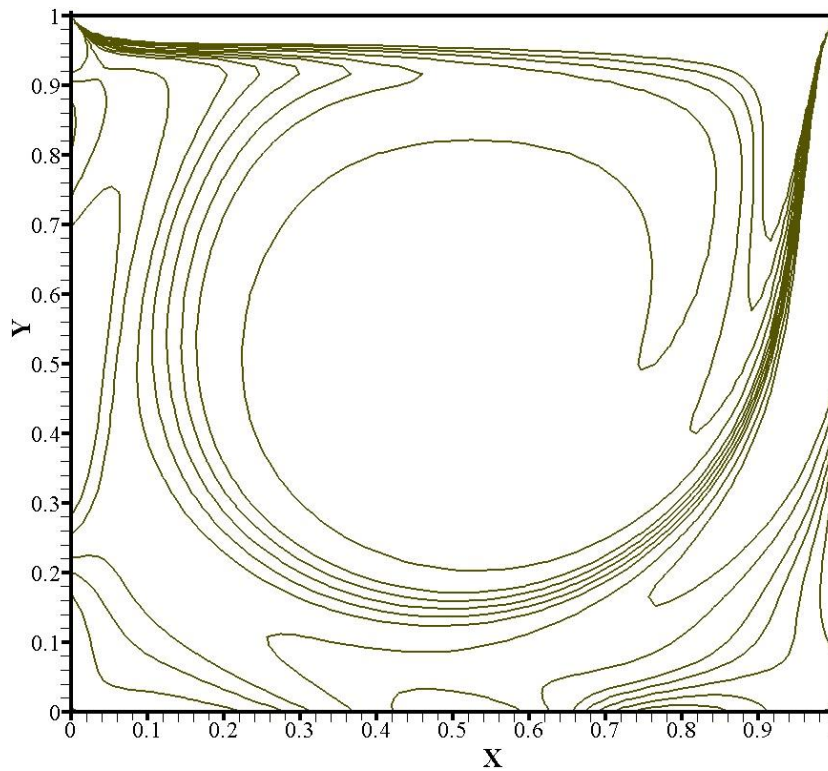
Figure 5.34: Vorticity contours of HO-FDM1 formulation ($Re = 1000$, non-uniform 65*65 grid)
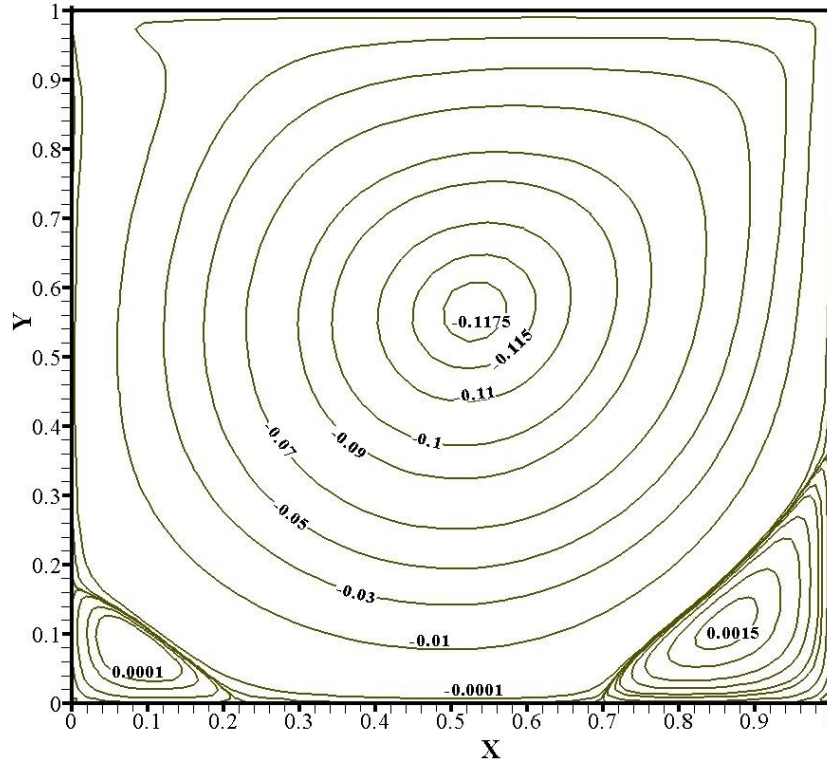
Figure 5.35: Streamfunction contours of HO-FDM2 formulation ($Re = 1000$, non-uniform 65*65 grid)
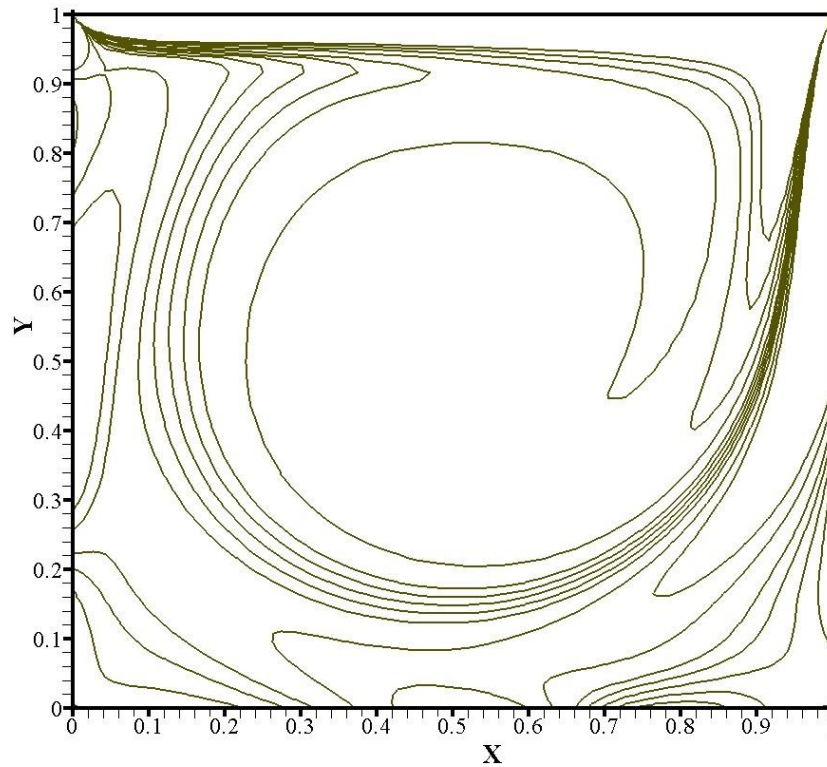
Figure 5.36: Vorticity contours of HO-FDM2 formulation ($Re = 1000$, non-uniform 65*65 grid)

Key features of the 2nd-order cut-stencil solution to lid-driven cavity flow on a square with $Re = 1000$ have been discussed in section 5.5.1.2, and comparisons have been made with the results from other researchers using roughly the same grid of 129*129 nodes. Tables 5.3 and 5.4 show that there is little difference between the Briley and compact 2nd-order approximations for the wall vorticity. In fact, the 2nd-order cut-stencil method provides a solution that is in good agreement with other results obtained on much finer grids. This is illustrated in Table 5.20 by using a non-uniform grid of 101*101 nodes and comparing to other methods of the same order on grids as fine as 601*601 [184]. Central differencing with 2nd-order accuracy for the convective terms is possible with the cut-stencil method if SUR is chosen as the iterative scheme. The optimum value of the relaxation factor σ is found to be 0.6. For any values of σ equal or higher than 0.625, the solution diverges for this case study. Since the results of Ghia et al. [150] are regarded as the benchmark, their data has been repeated in Table 5.12 for a more convenient comparison.

Study (Grid)			Ghia et al. [150] (129*129)	Schreiber and Keller [178] (141*141)	Erturk et al. [184] (601*601)	2nd-order cut-stencil (101*101)
Primary vortex	Abs. (ψ)		0.1179	0.1160	0.1188	0.1174
	Location	x	0.5313	0.5286	0.5300	0.5306
		y	0.5625	0.5643	0.5650	0.5610
	Abs. (ω)		2.04968	2.02600	2.06553	2.04487
B.L.* vortex	Abs. (ψ)		2.31E-4	2.17E-4	2.33E-4	2.25E-4
	Location	x	0.0859	0.0857	0.0833	0.0794
		y	0.0781	0.0714	0.0783	0.0794
	Abs. (ω)		3.618E-1	3.020E-1	3.535E-1	3.276E-1
B.R.** vortex	Abs. (ψ)		1.75E-3	1.70E-3	1.73E-3	1.70E-3
	Location	x	0.8594	0.8643	0.8633	0.8637
		y	0.1094	0.1071	0.1117	0.1102
	Abs. (ω)		1.15465	0.9990	1.11551	1.079
*: Bottom left, **: Bottom right						

Table 5.20: Comparison of 2nd-order accurate cut-stencil solution to other studies for lid-driven cavity flow ($Re = 1000$, non-uniform 101*101 grid)

Analysis of the data in Table 5.20 suggests that the 2nd-order accurate formulation of the cut-stencil FDM is capable of producing almost the same values for key features of the solution as those reported in the literature using relatively finer meshes. Most results of the 2nd-order cut-stencil method are in better agreement with Ghia et al. [150] than other reported results, e.g. [178, 184] that were generated using a finer mesh. The accuracy of the 2nd-order accurate formulation of the cut-stencil FDM can be further supported by comparison with data from Bruneau and Saad [185], as given in Table 5.21. It is worthwhile to note that Bruneau and Saad [185] has employed a 3rd-order accurate upwind scheme for approximation of the convective terms with the cavity lid sliding right to left, as well as using a much finer mesh as indicated in Table 5.21.

Study (Grid)	Ghia et al. [150] (129*129)	Bruneau and Saad [185] (1024*1024)	2nd-order cut-stencil (101*101)
(u, v) at midpoint* of domain	(-0.06068, 0.02526)	(0.06205, 0.02580)	(-0.06184, 0.02631)
Abs. (ω) at midpoint* of domain	N.A.	2.0669	2.0439
Abs. (ω) at midpoint** of moving wall	14.8901	N.A.	15.0852
*: $(x = 0.5, y = 0.5)$, **: $(x = 0.5, y = 1)$			

Table 5.21: Comparison of vorticity and velocity components at midpoint of domain and vorticity at midpoint of moving wall ($Re = 1000$)

5.6   Cut-Stencil FDM Solution of Lid-Driven Cavity Flow in Irregular Shaped Domains

The remainder of this chapter is devoted to application of the cut-stencil FDM for lid-driven cavity flow in several irregular domains. Typically, these irregular domains contain cut stencils which are created by intersection of the grid lines and the boundaries of the domain of interest. The domains include skewed, triangular and L-shaped cavities found in other numerical studies which are used here to verify the solutions obtained by the Cartesian cut-stencil methods.

5.6.1   Cut-Stencil FD Solution for the Lid-Driven Skewed Cavity Flow

The schematic of the skewed lid-driven cavity flow is depicted in Figure 5.37. Two skew angles, $\alpha = 45°$ and $\alpha = 135°,$ are considered. This flow problem has been studied by several researchers using different numerical methods. For example, Oosterlee et al. [186] proposed the solution for this problem with FVM using general curvilinear coordinates and Erturk and Dursun [187] solved skewed cavity flow with FDM and in general curvilinear coordinates with a non-orthogonal skewed grid system. Erturk and Dursun [187] applied 2-D transformation functions, as discussed in Chapter 1, to map a non-orthogonal grid in the physical domain to an orthogonal uniform mesh in the computational domain. This approach causes more complexity in the transformed governing equations compared to the Cartesian grid system with the 1-D transformation functions used in the cut-stencil FDM.

The vorticity along the skewed walls is approximated with 1st-order of accuracy, details of which are provided in Appendix IV. The vorticity along the regular boundaries (aligned with the Cartesian axes) are approximated with 2nd-order of accuracy using equations (5.8.2.3) or (5.8.2.4) which have been shown to have the same accuracy as Briley's formulation [171] for lid-driven cavity in a square domain. However, equations (5.8.2.3) and (5.8.2.4) are even more compact and this condition is a necessary key feature in complex domains, especially for the internal nodes located adjacent to the sloped or skewed boundaries.
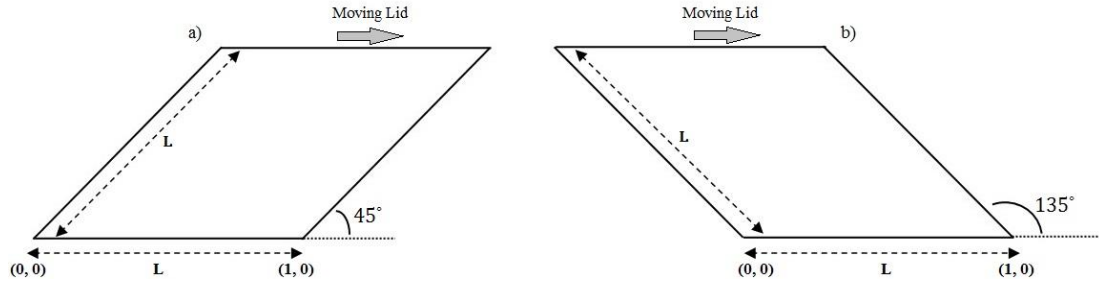
Figure 5.37: Schematic of domain for skewed lid-driven cavity, a) $\alpha = 45°$ and b) $\alpha = 135°$

The Reynolds number is defined by taking L and U_{Lid} as the characteristic length and velocity, to retain consistency with other numerical studies. The flow field in a skewed cavity exhibits a large vertical motion in the central or upper part of the cavity and, depending on Reynolds number, other smaller vortices in the upper and/or lower parts of the cavity.

The 2nd-order and higher-order results of the cut-stencil FD formulations for the case of $\alpha = 45°$ and $Re = 100$ are compared to results from other numerical studies in Table 5.22. In Table 5.22, vortex centre refers to the locations with maximum and minimum streamfunction values, which are reported in absolute format to keep consistency for all reported results. Examination of the data reported in Table 5.22 reveals that all cut-stencil FD results are in good agreement with other numerical studies, while the cut-stencil FDM predicts these solutions on a relatively coarser mesh. Due to the small value of Reynolds number for this case, no significant differences are observed between cut-stencil 2nd-order accurate solutions and higher-order formulations. The same observation can be made for the cut-stencil FDMs for cavity flow in a unit square domain in Table 5.6. The comparison of these key features for the two grid sizes used for the cut-stencil FD solution, verifies the grid independence since no significant changes are observed between the results.

Study (Grid)	Properties of vortex centre-1			Properties of vortex centre-2		
	Abs. (ψ)	Location (x,y)	Abs. (ω)	Abs. (ψ)	Location (x,y)	Abs. (ω)
Oosterlee et al. [186] (256*256)	7.0238E-2	(1.1100, 0.5469)	N.A.	3.69E-5	(0.3390, 0.1409)	N.A.
Erturk and Dursun [187] (513*513)	7.0232E-2	(1.1119, 0.5455)	4.615	3.67E-5	(0.3392, 0.1422)	1.825E-2
Demirdzic et al. [188] (320*320)	7.0226E-2	(1.1100, 0.5464)	N.A.	3.68E-5	(0.3387, 0.1431)	N.A.
Shkyar and Arbel [189] (320*320)	7.0129E-2	(1.1146, 0.5458)	N.A.	3.93E-5	(0.3208, 0.1989)	N.A.
2nd-order cut-stencil (1189*)	6.8618E-2	(1.1250, 0.5500)	4.919	3.81E-5	(0.3500, 0.1250)	1.896E-2
Cut-stencil HO-FDM1 (1189*)	6.9654E-2	(1.1000, 0.5500)	4.789	3.81E-5	(0.3250, 0.1500)	1.652E-2
Cut-stencil HO-FDM2 (1189*)	6.9313E-2	(1.1250, 0.5500)	4.954	3.77E-5	(0.3500, 0.1250)	1.969E-2
2nd-order cut-stencil (4617*)	6.9716E-2	(1.1125, 0.5375)	4.629	3.72E-5	(0.3375, 0.1375)	1.742E-2
Cut-stencil HO-FDM1 (4617*)	7.0052E-2	(1.1000, 0.5375)	4.555	3.73E-5	(0.3375, 0.1375	1.778E-2
Cut-stencil HO-FDM2 (4617*)	6.9945E-2	(1.1000, 0.5375)	4.551	3.73E-5	(0.3375, 0.1375	1.758E-2
*: Number of active nodes						

Table 5.22: Comparison of cut-stencil FD solutions to literature for skewed lid-driven cavity flow ($Re = 100, \alpha = 45°$)

At higher Reynolds numbers the Point-Jacobi iterative scheme fails to converge for all the cut-stencil formulations when the convective terms are approximated by central differences. For such convection-dominated flows, the Point-Jacobi iterations converge if the convective derivatives in the vorticity equation are upwinded which, of course, reduces the overall accuracy of the method. Thus, for $Re = 1000$, the results of upwind discretization in each of the cut-stencil methods are initially considered for the grid size of 4617 active nodes, through the data reported in Table 5.23.

Study (Grid)	Properties of vortex centre-1			Properties of vortex centre-2		
	Abs. (ψ)	Location (x, y)	Abs. (ω)	Abs. (ψ)	Location (x, y)	Abs. (ω)
2nd-order cut-stencil (4617*)	4.1069E-2	(1.3375, 0.5875)	5.660	4.24E-3	(0.7625, 0.3500)	3.577E-1
Cut-stencil HO-FDM1 (4617*)	6.1438E-2	(1.2500, 0.5375)	5.866	9.31E-3	(0.7625, 0.4000)	6.506E-1
Cut-stencil HO-FDM2 (4617*)	5.7905E-2	(1.2750, 0.5500)	6.29109	9.79E-3	(0.7625, 0.4000)	6.556E-1
*: Number of active nodes						

Table 5.23: Cut-stencil FD solutions to skewed lid-driven cavity flow using upwind schemes ($Re = 1000, \alpha = 45°$, 4617 active nodes)

Although the higher-order data in Table 5.23 shows reasonable agreement with other published numerical solutions, especially the HO-FDM2 solution, relatively better agreement can be achieved at this Reynolds number with central differencing of the convective terms. Iterative convergence with central differencing of the convective terms is achieved by using SUR. To achieve this purpose, the optimum SUR factor, which corresponds to the minimum computational effort, is determined for each formulation and grid size. This procedure is carried out by changing σ in a range whose upper limit is the border between divergence and the converged solution. The independency of the solution on the value of σ is investigated by comparison of two key features of the solution, as illustrated in Table 5.24 for the 2nd-order cut-stencil FD formulation for a mesh with 18193 active nodes.

σ	ψ vortex centre-1	ω vortex centre-2
0.890	5.1531E-2	6.216E-1
0.800	5.1531E-2	6.216E-1
0.700	5.1531E-2	6.216E-1
0.580	5.1531E-2	6.216E-1
0.500	5.1531E-2	6.216E-1

Table 5.24: Independency of skewed cavity solution to relaxation factor σ for 2nd-order cut-stencil formulation ($Re = 1000, \alpha = 45°$, 18193 active nodes)

The results in Tables 5.23 and 5.25 indicate that better agreement between the present cut-stencil solutions and other numerical results when central differencing is used for the convective derivatives for each formulation. Also, the capability of the higher-order formulations to produce values closer to those from other numerical studies is more obvious for this higher value of Reynolds number and, between the two higher-order cut-stencil FD formulations, HO-FDM2 appears to yield slightly better agreement with other data. Additionally, the Point-Jacobi method converges for HO-FDM2 on a finer mesh (18193 nodes) with central differencing of the convective terms, as recorded in Table 5.25. Results for the skewed cavity flow at $Re = 1000$ and with $\alpha = 45°$ are summarized and compared with numerical results of other researchers in Table 5.25.

Study (Grid)	Properties of vortex centre-1			Properties of vortex centre-2		
	Abs. (ψ)	Location (x,y)	Abs. (ω)	Abs. (ψ)	Location (x,y)	Abs. (ω)
Oosterlee et al. [186] (256*256)	5.3523E-2	(1.3128, 0.5745)	N.A.	1.0039E-2	(0.7775, 0.4005)	N.A.
Erturk and Dursun [187] (513*513)	5.3423E-2	(1.3148, 0.5745)	6.955	1.0024E-2	(0.7780, 0.3991)	6.269E-1
Demirdzic et al [188] (320*320)	5.3507E-2	(1.3130, 0.5740)	N.A.	1.0039E-2	(0.7766, 0.3985)	N.A.
Shklyar and Arbel [189] (320*320)	5.2553E-2	(1.3120, 0.5745)	N.A.	1.0039E-2	(0.7766, 0.3985)	N.A.
Louaked et al. [190] (120*120)	5.4690E-2	(1.3100, 0.5700)	N.A.	1.0170E-2	(0.7760, 0.3980)	N.A.
2nd-order cut-stencil (4617*)	4.6779E-2 $(0.400 \leq \sigma \leq 0.660)^{\text{i}}$ $(\sigma_{\text{Opt.}} = 0.565)^{\text{ii}}$	(1.3500, 0.5875)	7.961	9.45E-3	(0.7875, 0.3875)	5.756E-1
Cut-stencil HO-FDM1 (4617*)	5.6464E-2 $(0.450 \leq \sigma \leq 0.550)$ $(\sigma_{\text{Opt.}} = 0.512)$	(1.2875, 0.5625)	6.510	1.01E-2	(0.7750, 0.4000)	6.454E-1
Cut-stencil HO-FDM2 (4617*)	5.3191E-2 $(0.470 \leq \sigma \leq 0.656)$ $(\sigma_{\text{Opt.}} = 0.656)$	(1.3125, 0.5625)	6.992	1.01E-2	(0.7750, 0.4000)	6.404E-1
2nd-order cut-stencil (18193*)	5.1531E-2 $(0.500 \leq \sigma \leq 0.890)$ $(\sigma_{\text{Opt.}} = 0.890)$	(1.3186, 0.5750)	7.214	9.87E-3	(0.7750, 0.3938)	6.216E-1
Cut-stencil HO-FDM1 (18193*)	5.4278E-2 $(0.650 \leq \sigma \leq 0.840)$ $(\sigma_{\text{Opt.}} = 0.830)$	(1.3000, 0.5625)	6.849	1.00E-2	(0.7688, 0.3938)	6.389E-1
Cut-stencil HO-FDM2 (18193*)	5.3438E-2	(1.3063, 0.5688)	6.968	1.00E-2	(0.7750, 0.3938)	6.270E-1
*: Number of active nodes						
(i): Study range of under-relaxation factor, (ii): Optimum value of under-relaxation factor						

Table 5.25: Comparison of cut-stencil FD solutions for skewed lid-driven cavity flow ($Re = 1000, \alpha = 45°$)

The contours of streamfunction from the cut-stencil HO-FDM2 fine mesh solutions to the skewed cavity problem, for both Reynolds numbers of 100 and 1000, are depicted in Figures 5.38 and 5.39, respectively. The contours of streamfunction show good qualitative agreement with those from other numerical studies, such as [187, 188].

Figure 5.38: Streamfunction contours of HO-FDM2 formulation for skewed lid-driven cavity
($Re = 100$, $\alpha = 45°$, 4617 active nodes)

Figure 5.39: Streamfunction contours of HO-FDM2 formulation for skewed lid-driven cavity
($Re = 1000$, $\alpha = 45°$, 18193 active nodes)

A similar analysis as above can be conducted for skewed cavity flow with a skew angle of $\alpha = 135°$. The results for cut-stencil FD formulations and comparison to numerical results by Erturk

and Dursun [187] for $Re = 100$ are reported in Table 5.26. Again, there are no significant changes between the results of different cut-stencil FD formulations. Comparison between the solutions of the same formulation for the two grids listed in Figure 5.26 reveals the grid independence since the changes in all the key features of the solution are negligible. Additionally, the results of the present study show good agreement with those of Erturk and Dursun [187], whose solution was carried out with a relatively finer mesh.

Study (Grid)	Properties of vortex centre-1			Properties of vortex centre-2		
	Abs. (ψ)	Location (x, y)	Abs. ω	Abs. (ψ)	Location (x, y)	Abs. (ω)
Erturk and Dursun [187] (513*513)	8.3704E-2	(0.1055, 0.4999)	4.065	1.08E-4	(0.6708, 0.1436)	5.742E-2
2nd-order cut-stencil (4617*)	8.3509E-2	(0.1125, 0.4875)	4.011	1.10E-4	(0.6750, 0.1375)	5.635E-2
Cut-stencil HO-FDM1 (4617*)	8.3503E-2	(0.1125, 0.4875)	4.017	1.07E-4	(0.6750, 0.1375)	5.707E-2
Cut-stencil HO-FDM2 (4617*)	8.3541E-2	(0.1125, 0.4875)	4.018	1.08E-4	(0.6750, 0.1375)	5.693E-2
2nd-order cut-stencil (18193*)	8.3623E-2	(0.1125, 0.4938)	4.081	1.07E-4	(0.6750, 0.1438)	5.861E-2
Cut-stencil HO-FDM1 (18193*)	8.3611E-2	(0.1125, 0.4938)	4.083	1.07E-4	(0.6750, 0.1438)	5.878E-2
Cut-stencil HO-FDM2 (18193*)	8.3620E-2	(0.1125, 0.4938)	4.083	1.07E-4	(0.6750, 0.1438)	5.874E-2
*: Number of active nodes						

Table 5.26: Comparison of cut-stencil FD solutions to Erturk and Dursun [187] for skewed lid-driven cavity flow ($Re = 100, \alpha = 135°$)

The solutions for skew angle of 135° for $Re = 1000$ are summarized in Tables 5.27-5.29. Since central differencing of the convective terms leads to divergence with the Point-Jacobi method, the results of upwind discretization for each formulation of the cut-stencil FDM, with a mesh of 4617 active nodes, are presented in Table 5.27.

Study (Grid)	Properties of vortex centre-1			Properties of vortex centre-2		
	Abs. (ψ)	Location (x, y)	Abs. (ω)	Abs. (ψ)	Location (x, y)	Abs. (ω)
2nd-order cut-stencil (4617*)	7.4631E-2	(0.1375, 0.4000)	2.516	2.07E-3	(0.5625, 0.1500)	7.197E-1
Cut-stencil HO-FDM1 (4617*)	9.6500E-2	(0.1625, 0.3750)	3.036	3.04E-3	(0.6000, 0.1375)	1.106
Cut-stencil HO-FDM2 (4617*)	9.4886E-2	(0.1500, 0.3875)	3.003	3.29E-3	(0.5875, 0.1500)	1.134
*: Number of active nodes						

Table 5.27: Cut-stencil FD solutions for skewed lid-driven cavity flow using upwind schemes for approximation of convective terms for ($Re = 1000$, $\alpha = 135°$, 4617 active nodes)

SUR iterations converge for all the cut-stencils formulations discussed in this thesis when central differencing is employed for $Re = 1000$. As an example of the independency of the solution on the under-relaxation factor, two key features of the cut-stencil HO-FDM1 solution and corresponding σ, for mesh of 18193 active nodes, are reported in Table 5.28.

σ	ψ (vortex centre-1)	ω (vortex centre-2)
0.815	9.3817E-2	1.237
0.785	9.3817E-2	1.237
0.765	9.3817E-2	1.237
0.680	9.3817E-2	1.237
0.600	9.3817E-2	1.237

Table 5.28: Independency of skewed cavity solution to relaxation factor σ for cut-stencil HO-FDM1 formulation ($Re = 1000$, $\alpha = 135°$, 18193 active nodes)

The results of different cut-stencil FD formulations, when central differencing is applied to discretize the convective terms and SUR is used as the iterative scheme to solve the finite difference equations, are given in Table 5.29. The range of variation of σ that is studied for each formulation and the optimum value of σ are stated in the table, and it is further noted that central differencing of the convective terms along with the Point-Jacobi iterative scheme can be employed for the HO-FDM2 formulation with the finer mesh of 18193 nodes.

Analysis of the data in Tables 5.27 and 5.29 shows that, for 4617 active nodes, discretizing the convective derivatives with central differencing yields better agreement with the numerical data of Erturk and Dursun [187] than upwind discretization of the convective terms. The data in Table 5.29 demonstrates that the higher-order cut-stencil formulations produce accurate results for almost all key features of the solution, particularly for the coarser mesh. This supports the idea that the higher-order formulations have the capability to generate accurate results even by employing coarse meshes. Between the two proposed cut-stencil higher-order formulations, the HO-FDM2 formulation shows greater capability to capture the key features more accurately compared to the HO-FDM1 formulation.

Study (Grid)	Properties of vortex centre-1			Properties of vortex centre-2		
	Abs. (ψ)	Location (x, y)	Abs. (ω)	Abs. (ψ)	Location (x, y)	Abs. (ω)
Erturk and Dursun [187] (513*513)	9.3512E-2	(0.1390, 0.3922)	2.992	3.78E-3	(0.5554, 0.1478)	1.197
2nd-order cut-stencil (4617*)	9.4407E-2 $(0.425 \leq \sigma \leq 0.570)^{i}$ $(\sigma_{Opt.} = 0.570)^{ii}$	(0.1375, 0.3875)	3.109	4.30E-3	(0.5375, 0.1500)	1.349
Cut-stencil HO-FDM1 (4617*)	9.4753E-2 $(0.380 \leq \sigma \leq 0.515)$ $(\sigma_{Opt.} = 0.515)$	(0.1500, 0.3875)	3.003	3.50E-3	(0.5750, 0.1375)	1.262
Cut-stencil HO-FDM2 (4617*)	9.4036E-2 $(0.525 \leq \sigma \leq 0.785)$ $(\sigma_{Opt.} = 0.785)$	(0.1500, 0.3875)	3.013	3.69E-3	(0.5625, 0.1375)	1.279
2nd-order cut-stencil (18193*)	9.3445E-2 $(0.550 \leq \sigma \leq 0.840)$ $(\sigma_{Opt.} = 0.840)$	(0.1438, 0.3875)	3.025	3.85E-3	(0.5563, 0.1500)	1.220
Cut-stencil HO-FDM1 (18193*)	9.3817E-2 $(0.600 \leq \sigma \leq 0.815)$ $(\sigma_{Opt.} = 0.765)$	(0.1438, 0.3875)	3.010	3.66E-3	(0.5625, 0.1438)	1.237
Cut-stencil HO-FDM2 (18193*)	9.3774E-2	(0.1438, 0.3875)	3.017	3.73E-3	(0.5625, 0.1438)	1.200
*: Number of active nodes (i): Study range of under-relaxation factor, (ii): Optimum value of under-relaxation factor						

Table 5.29: Comparison of cut-stencil FD solutions with Erturk and Dursun [187] for skewed lid-driven cavity flow ($Re = 1000$, $\alpha = 135°$)

The contours of streamfunction of the cut-stencil HO-FDM2 solution for both $Re = 100$ and $Re = 1000$ for $\alpha = 135°$ using the finer mesh of 18193 active nodes are plotted in Figures 5.40 and 5.41, respectively. The quantitative and qualitative comparison of the aforementioned contours to available plots from Erturk and Dursun [187], show more evidence of the accuracy of the methods and algorithms developed in this research, particularly noting that the data in [187] has been obtained with a much finer mesh (~ 260,000) than those used in present study.
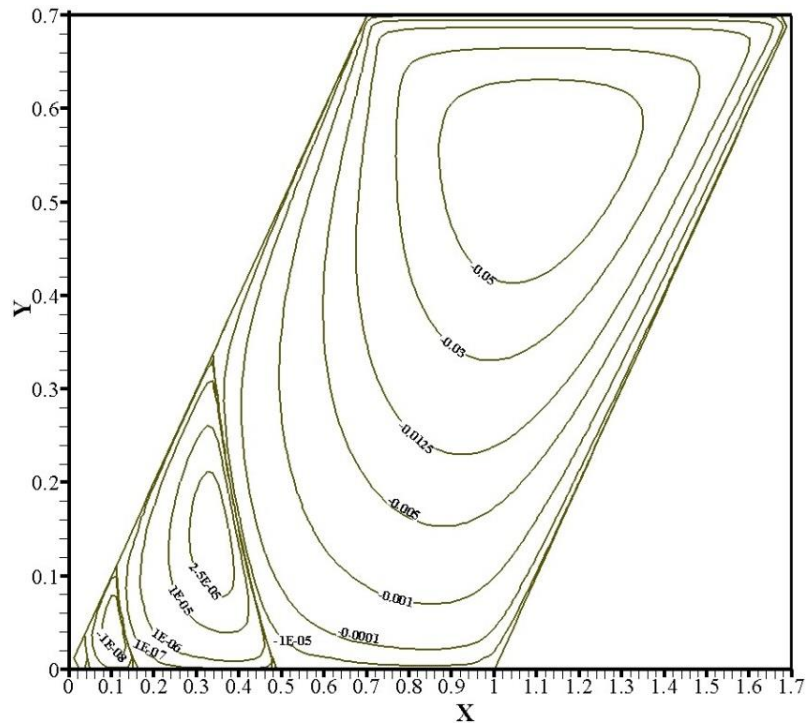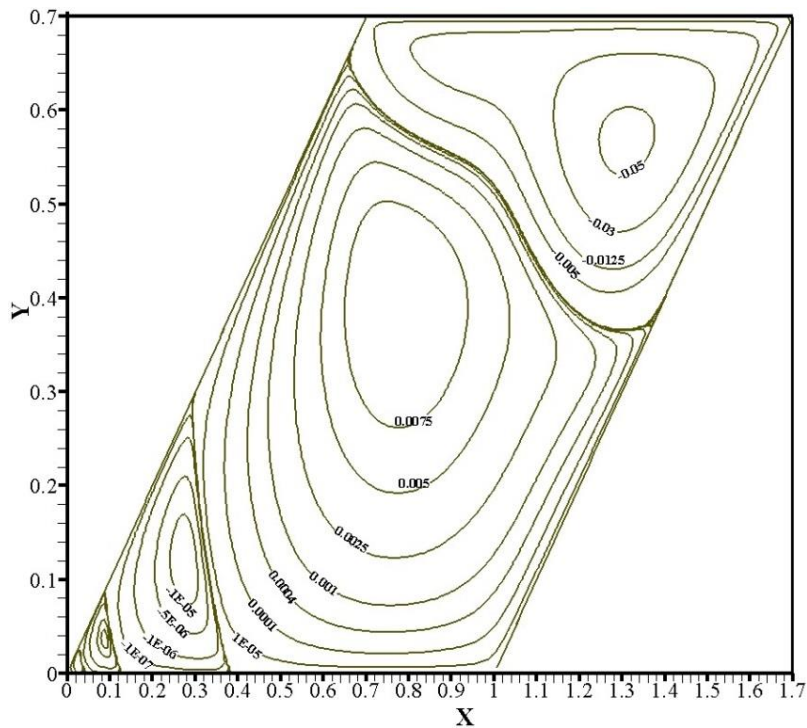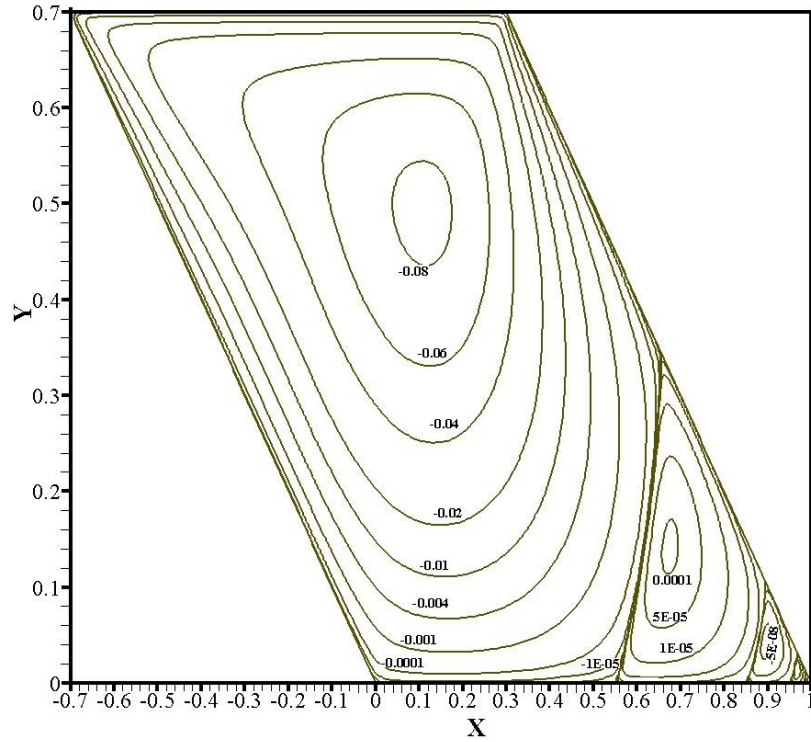
Figure 5.40: Streamfunction contours of HO-FDM2 solution for skewed lid-driven cavity ($Re = 100$, $\alpha = 135°$, 18193 active nodes)
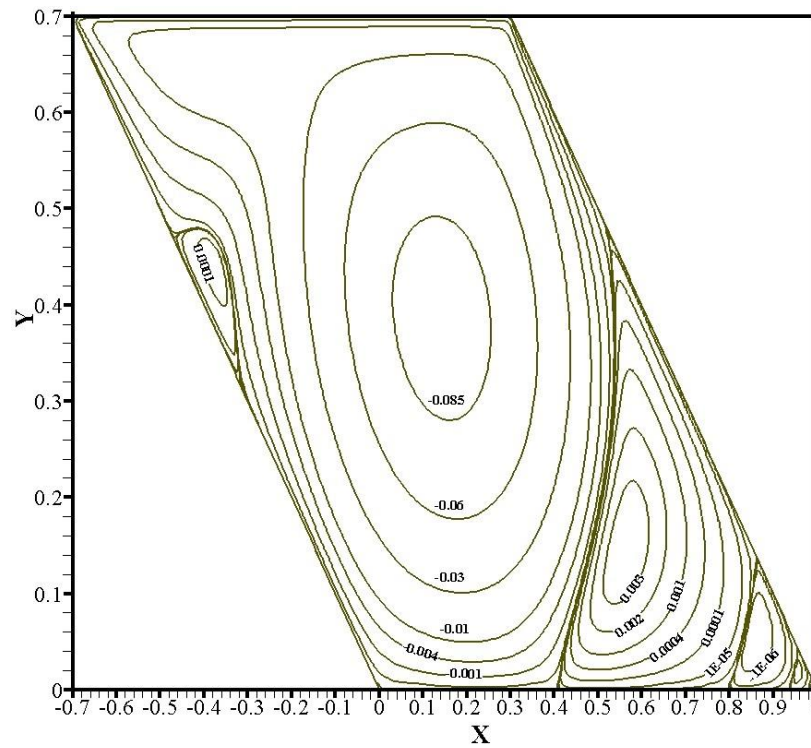
Figure 5.41: Streamfunction contours of HO-FDM2 solution for skewed lid-driven cavity ($Re = 1000$, $\alpha = 135°$, 18193 active nodes)

5.6.2 Cut-Stencil FD Solution for Lid-Driven Right-Side and Left-Side Aligned Right Triangular Cavity Flow

The cut-stencil solutions to lid-driven cavity flow for the domains shown in Figure 5.42 are considered in this section, to investigate the capability of the cut-stencil FDM for solution of fluid flow problems in any irregular shaped domains. The definition of Reynolds number uses L as the characteristic length and U_{Lid} as the characteristic velocity.
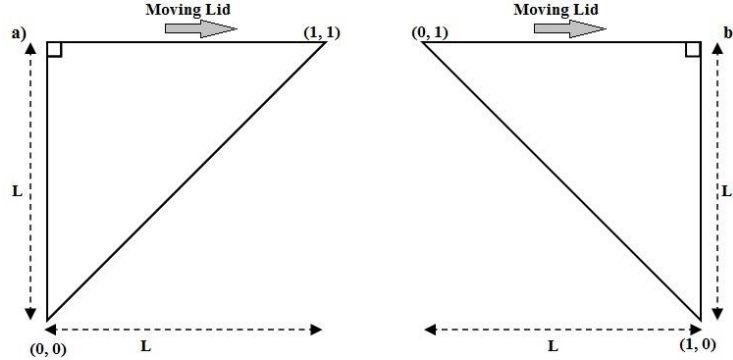
Figure 5.42: Schematic of isosceles right triangular domains, a) left-side aligned, and b) right-side aligned

Erturk and Gokcol [191] have considered 2-D incompressible cavity flow inside different triangular cross-sections including those depicted in Figure 5.42. Their study [191] used FDM and a general arbitrary triangle, as the physical domain, was mapped to an isosceles right triangle as the computational domain. The mapping function used in [191] is solely applicable to carry out the transformation for triangular domains. The solution of lid-driven cavity flow for different cross-sections, such as cavity flow in skewed or trapezoidal or triangular cross-sections, has been mostly presented in numerical studies using FVM, such as [182]. However, in case of employing FDM, different mapping functions can be defined for each geometry, e.g. [187, 191, 192]. Additionally, semi 2-D transformation functions in [191] produced cross derivatives in the mapped form of the streamfunction-vorticity equations and made it more complex and hence more difficult to discretize. It is important to note that in this research and thesis, the mapping process is performed with same transformation functions for every geometrical cross-section, which also generates the mapped form of the governing equation(s) in relatively simple form. The flows inside the triangular cavities shown in Figure 5.42 have also been studied using other numerical schemes such as FEM [193] and the Lattice Boltzmann method (LBM) [194].

Table 5.30 looks at the cut-stencil FD solution for lid-driven flow in the triangular cavity illustrated in Figure 5.42(a), and presents a comparison to a number of available numerical studies, for $Re = 500$.

Study (Grid)	Properties of primary vortex centre		
	Abs. (ψ)	Location (x, y)	Abs. (ω)
Erturk and Gokcol [191] (512*512)/2	0.06065	(0.5469, 0.8496)	5.737
Ahmed and Kuhlmann [193] (100 subspaces)	0.06072	(0.5486, 0.08482)	5.759
Munir et al. [194] (300*300)	N.A.	(0.5550, 0.8500)	N.A.
2nd-order cut-stencil (2145*)	0.05584 $(0.600 \leq \sigma \leq 0.830)^{i}$ $(\sigma_{Opt.} = 0.830)^{ii}$	(0.5781, 0.8594)	6.215
Cut-stencil HO-FDM1 (2145*)	0.06213 $(0.600 \leq \sigma \leq 0.830)$ $(\sigma_{Opt.} = 0.825)$	(0.5313, 0.8438)	5.534
Cut-stencil HO-FDM2 (2145*)	0.06010	(0.5469, 0.8438)	5.824
2nd-order cut-stencil (3321*)	0.05674	(0.5625, 0.8500)	5.783
Cut-stencil HO-FDM1 (3321*)	0.06167 $(0.650 \leq \sigma \leq 0.940)$ $(\sigma_{Opt.} = 0.940)$	(0.5375, 0.8500)	5.552
Cut-stencil HO-FDM2 (3321*)	0.06045	(0.5500, 0.8500)	5.754
2nd-order cut-stencil (5151*)	0.05858	(0.5600, 0.8500)	5.986
Cut-stencil HO-FDM1 (5151*)	0.06140	(0.5400, 8500)	5.605
Cut-stencil HO-FDM2 (5151*)	0.06132	(0.5400, 8500)	5.515
*: Number of active nodes			
(i): Study range of under-relaxation factor, (ii): Optimum value of under-relaxation factor			

Table 5.30: Comparison of cut-stencil FD solutions for lid-driven cavity flow in a left-side aligned right triangle ($Re = 500$)

Examination of the cut-stencil FD data given in table 5.30 shows good agreement of the higher-order cut-stencil FD formulations with numerical data reported in [191, 193, 194], which are obtained with much finer grids. The relative differences of ψ and ω at the primary vortex between HO-FDM2 and the data of Erturk and Gokcol [191] are equal to 0.91% and 1.52%, respectively, for the mesh of 2145 active nodes. These differences are 3.41% and 4.34% for the 2nd-order cut-stencil FD formulation on a mesh of 5151 active nodes. This provides strong evidence that the cut-stencil FD methods, especially the higher-order methods, can accurately

simulate complex flow phenomena on a coarse mesh, in addition to a similar observation based on previous results for irregular shaped domains.

The results of the cut-stencil FDM for cavity flow inside the triangular cross-section shown in Figure 5.42(a) for $Re = 1000$, as well as comparison to other numerical studies, are presented through the data in Table 5.31.

Study (Grid)	Properties of primary vortex center		
	Abs. (ψ)	Location (x, y)	Abs. (ω)
Erturk and Gokcol [191] (512*512)/2	0.05306	(0.6094, 0.8691)	7.022
Ahmed and Kuhlmann [193] (100 subspaces)	0.05325	(0.6081, 0.8678)	6.997
Munir et al. [194] (300*300)	N.A.	(0.6050, 0.8650)	N.A.
2nd-order cut-stencil (3321*)	0.04647 $(0.350 \leq \sigma \leq 0.575)^{i}$ $(\sigma_{Opt.} = 0.575)^{ii}$	(0.6500, 0.8875)	8.036
Cut-stencil HO-FDM1 (3321*)	0.05614 $(0.325 \leq \sigma \leq 0.515)$ $(\sigma_{Opt.} = 0.515)$	(0.5875, 0.8625)	6.565
Cut-stencil HO-FDM2 (3321*)	0.05291 $(0.470 \leq \sigma \leq 0.665)$ $(\sigma_{Opt.} = 0.665)$	(0.6125, 0.8625)	7.051
2nd-order cut-stencil (5151*)	0.04865 $(0.425 \leq \sigma \leq 0.665)$ $(\sigma_{Opt.} = 0.665)$	(0.6400, 0.8800)	7.669
Cut-stencil HO-FDM1 (5151*)	0.05510 $(0.400 \leq \sigma \leq 0.600)$ $(\sigma_{Opt.} = 0.600)$	(0.6000, 0.8600)	6.703
Cut-stencil HO-FDM2 (5151*)	0.05305 $(0.400 \leq \sigma \leq 0.700)$ $(\sigma_{Opt.} = 0.700)$	(0.6100, 0.8700)	7.032
2nd-order cut-stencil (8001*)	0.05014 $(0.550 \leq \sigma \leq 0.790)$ $(\sigma_{Opt.} = 0.790)$	(0.6320, 0.8800)	7.389
Cut-stencil HO-FDM1 (8001*)	0.05449 $(0.475 \leq \sigma \leq 0.700)$ $(\sigma_{Opt.} = 0.700)$	(0.6000, 8640)	6.813
Cut-stencil HO-FDM2 (8001*)	0.05310 $(0.600 \leq \sigma \leq 0.725)$ $(\sigma_{Opt.} = 0.725)$	(0.6080, 8720)	7.015
*: Number of active nodes (i): Study range of under-relaxation factor, (ii): Optimum value of under-relaxation factor			

Table 5.31: Comparison of cut-stencil FD solutions for lid-driven cavity flow in a left-side aligned right triangle ($Re = 1000$)

The data, as reported in Table 5.31, shows that there is good agreement between cut-stencil HO-FDM1 solutions and data from other numerical work for all grid sizes studied. There is even

better agreement in the event that cut-stencil HO-FDM2 is employed. The relative difference of ψ and ω at the primary vortex between the HO-FDM2 results and reported data in [191] can be seen as 0.28% and 0.41%, respectively, for the coarser mesh studied in Table 5.31. These values are equal 5.50% and 5.23% for ψ and ω at the primary vortex, respectively, when the 2nd-order cut-stencil formulation is employed on the finer grid (8001 active nodes). This shows that in irregular shaped domains, even when the Reynolds number increases, more accurate solutions can be obtained by apply the higher-order formulations. Additionally, the benefit of central differencing of the convective terms can be achieved by employing SUR as the iterative method when necessary. This supports the proposition that the cut-stencil FDM is a powerful new numerical formulation with known features of traditional well-established numerical methods and, even though it is a pure finite difference method, it can be used to solve complex PDEs in irregular shaped domains.

Figure 5.43 illustrates the contours of streamfunction for $Re = 500$ and $Re = 1000$, for lid-driven cavity flow in a left-side aligned right triangle employing cut-stencil HO-FDM2 and using the finer grid size studied for each Reynolds number.

Figure 5.43: Streamfunction contours for HO-FDM2 formulation for left-side aligned right triangle lid-driven cavity, a) $Re = 500$ with grid of 5151 active nodes, b) $Re = 1000$ with grid of 8001 active nodes

The results of cut-stencil FDM solutions for lid-driven cavity flow in a right-side aligned right triangle cross-section for $Re = 500$ and other available numerical data are reported in Table 5.32. Analysis of the data in Table 5.32 reveals good agreement between the cut-stencil FDM solutions and other numerical data from [191, 193], for all cut-stencil FD formulations, while all the grids used in the present study are coarser than the ones used by other researchers. Also, the agreement is even better when higher-order formulations of the cut-stencil FDM are employed.

Study (Grid)	Properties of primary vortex centre		
	Abs. (ψ)	Location (x, y)	Abs. (ω)
Erturk and Gokcol [191] (512*512)/2	0.08106	(0.7070, 0.7676)	4.121
Munir et al. [194] (300*300)	N.A.	(0.7100, 0.7650)	N.A.
2nd-order cut-stencil (2145*)	0.07729 $(0.380 \leq \sigma \leq 0.580)^i$ $(\sigma_{Opt.} = 0.580)^{ii}$	(0.7031, 0.7656)	4.051
Cut-stencil HO-FDM1 (2145*)	0.08132 $(0.350 \leq \sigma \leq 0.520)$ $(\sigma_{Opt.} = 0.520)$	(0.7031, 0.7656)	4.184
Cut-stencil HO-FDM2 (2145*)	0.08154 $(0.365 \leq \sigma \leq 0.570)$ $(\sigma_{Opt.} = 0.550)$	(0.7031, 0.7656)	4.182
2nd-order cut-stencil (3321*)	0.07856 $(0.585 \leq \sigma \leq 0.750)$ $(\sigma_{Opt.} = 0.750)$	(0.7125, 0.7750)	4.015
Cut-stencil HO-FDM1 (3321*)	0.08092 $(0.625 \leq \sigma \leq 0.727)$ $(\sigma_{Opt.} = 0.727)$	(0.7125, 0.7750)	4.107
Cut-stencil HO-FDM2 (3321*)	0.08064	(0.7125, 0.7750)	4.116
2nd-order cut-stencil (5151*)	0.07951	(0.7100, 0.7700)	4.052
Cut-stencil HO-FDM1 (5151*)	0.08098 $(0.750 \leq \sigma \leq 0.940)$ $(\sigma_{Opt.} = 0.940)$	(0.7100, 0.7700)	4.110
Cut-stencil HO-FDM2 (5151*)	0.08082	(0.7100, 0.7700)	4.104
*: Number of active nodes (i): Study range of under-relaxation factor, (ii): Optimum value of under-relaxation factor			

Table 5.32: Comparison of cut-stencil FD solutions for lid-driven cavity flow in a right-side aligned right triangle ($Re = 500$)

The solution of lid-driven cavity flow inside the right-side aligned right triangle for $Re = 1000$ is presented in Table 5.33. The relative difference for streamfunction and vorticity of the 2nd-order cut-stencil FD solution compared to the same data in [191] are 2.68% and 2.30%, respectively, for the finest mesh shown in Table 5.33. These differences are reduced to 0.13% and 0.26% for streamfunction and vorticity, respectively, in the event of applying cut-stencil HO-FDM1 for the same mesh. This comparison shows only 0.03% and 0.12% of relative differences for streamfunction and vorticity, respectively, for the cut-stencil HO-FDM2 solution. Although the Reynolds number is increased, the methods of the present study are able to generate accurate solutions for lid-driven cavity flow with the cross-section depicted in Figure 5.42(b), while the

finest mesh used in Table 5.33 is much coarser than the ones employed in other numerical studies. It is worthwhile, again, to point out that despite the different cross-sections used for reporting data in Tables 5.30-5.33, the transformation functions and mapping methodology are the same for all irregular domains, as discussed in Chapter 2.

Study (Grid)	Properties of primary vortex centre		
	Abs. (ψ)	Location (x, y)	Abs. (ω)
Erturk and Gokcol [191] (512*512/2)	0.08318	(0.6992, 0.7559)	3.925
Munir et al. [194] (300*300)	N.A.	(0.7000, 0.7550)	N.A.
2nd-order cut-stencil (4186*)	0.07939 $(0.225 \leq \sigma \leq 0.374)^{i}$ $(\sigma_{Opt.} = 0.374)^{ii}$	(0.7000, 0.7556)	3.785
Cut-stencil HO-FDM1 (4186*)	0.08415 $(0.180 \leq \sigma \leq 0.280)$ $(\sigma_{Opt.} = 0.280)$	(0.7000, 0.7556)	3.994
Cut-stencil HO-FDM2 (4186*)	0.08453 $(0.060 \leq \sigma \leq 0.165)$ $(\sigma_{Opt.} = 0.144)$	(0.7000, 0.7556)	3.994
2nd-order cut-stencil (5151*)	0.07992 $(0.300 \leq \sigma \leq 0.427)$ $(\sigma_{Opt.} = 0.427)$	(0.7000, 0.7600)	3.802
Cut-stencil HO-FDM1 (5151*)	0.08372 $(0.225 \leq \sigma \leq 0.340)$ $(\sigma_{Opt.} = 0.325)$	(0.7000, 0.7600)	3.972
Cut-stencil HO-FDM2 (5151*)	0.08385 $(0.100 \leq \sigma \leq 0.290)$ $(\sigma_{Opt.} = 0.275)$	(0.7000, 0.7600)	3.967
2nd-order cut-stencil (8001*)	0.08095 $(0.400 \leq \sigma \leq 0.560)$ $(\sigma_{Opt.} = 0.560)$	(0.7040, 0.7600)	3.835
Cut-stencil HO-FDM1 (8001*)	0.08329 $(0.350 \leq \sigma \leq 0.510)$ $(\sigma_{Opt.} = 0.510)$	(0.6960, 0.7520)	3.935
Cut-stencil HO-FDM2 (8001*)	0.08316 $(0.340 \leq \sigma \leq 0.432)$ $(\sigma_{Opt.} = 0.400)$	(0.7040, 0.7520)	3.930
*: Number of active nodes (i): Study range of under-relaxation factor, (ii): Optimum value of under-relaxation factor			

Table 5.33: Comparison of cut-stencil FD solutions to literature for lid-driven cavity flow in a right-side aligned right triangle at $Re = 1000$

The contours of streamfunction for $Re = 500$ and $Re = 1000$, for lid-driven cavity flow in a right-side aligned right triangle employing cut-stencil HO-FDM2 and using the finest grid size studied for each Reynolds number, are presented in Figure 5.44.
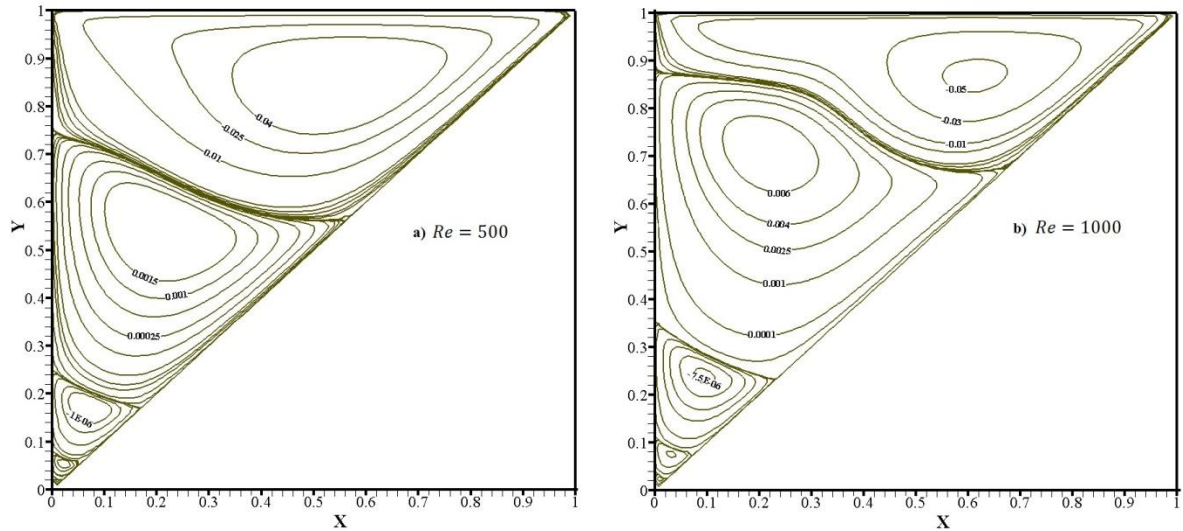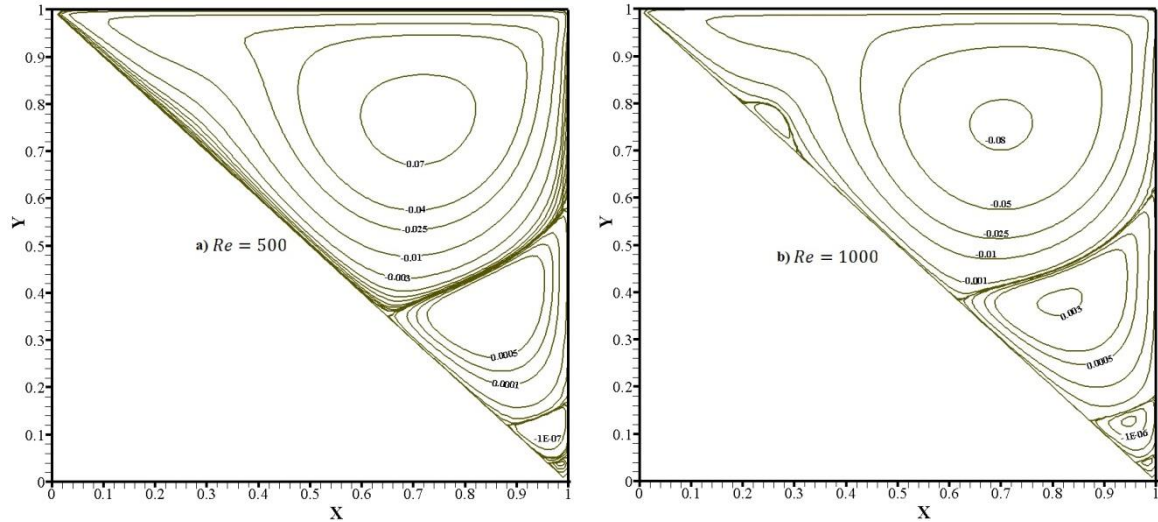
Figure 5.44: Streamfunction contours for HO-FDM2 formulation for right-side aligned right triangle lid-driven cavity, a) $Re = 500$ with grid of 5151 active nodes, b) $Re = 1000$ with grid of 8001 active nodes

5.6.3   Cut-Stencil FD Solution for Lid-Driven L-Shaped Cavity Flow

Cut-stencil FD solution to lid-driven cavity flow in the L-shaped domain depicted in Figure 5.45 is investigated in this section. The lid-driven cavity flow in an L-shaped domain has been addressed in other numerical studies to verify domain decomposition methods [186, 195], as well as checking discretization techniques [186]. The characteristic length is defined by L and U_{Lid} is taken as the characteristic velocity.
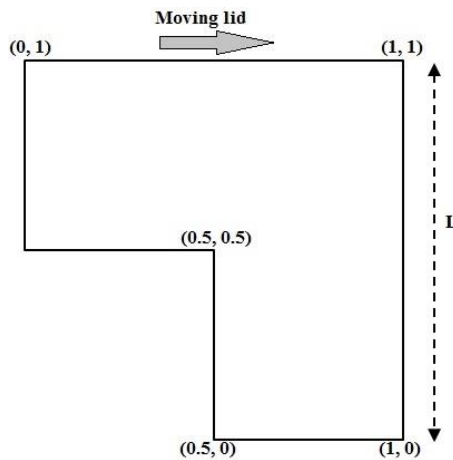
Figure 5.45: Schematic of L-shaped domain

Table 5.34 reports the cut-stencil FD solutions for lid-driven cavity flow in the L-shaped domain and makes comparison to available solutions in literature for $Re = 1000$. The same transformation functions and mapping procedure that have been used for other irregular shaped domains is employed for the L-shaped domain. This point, again, confirms the generality of the Cartesian cut-stencil FD procedure to solve PDEs in any type of domain without requiring any changes in the mapping procedure.

174

Basically, three primary vortices occur at $Re = 1000$ in the L-shape domain, as also tabulated by Oosterlee et al. [186]. One of the extrema of streamfunction occurs in the region $x < 0.5$ and another extrema occurs in the region $x > 0.5$. The absolute value of streamfunction and vorticity at the three primary vortices are given in Table 5.33 along with the coordinates of each. The finest mesh in numerical study [186] is the grid of 512*512 nodes, but independency of the solution from the grids used can be observed between the grids of 256*256 and 512*512 nodes. So, the key features of the solution on the grid of 256*256 nodes in [186] are shown in Table 5.33. Additionally, four grid sizes, varying from 1.25E5 to 8.00E6 are employed in [196] but due to negligible difference between reported key features of each mesh, the available key features of the coarse mesh are given in Table 5.34. The central differencing of convective terms has been employed using the SUR iterative method.

Study (Grid)	Properties of primary vortex centre								
	Min. (ψ)			Extrema (ψ) ($x < 0.5$)			Extrema (ψ) ($x > 0.5$)		
	Abs. (ψ)	Location (x, y)	Abs. (ω)	Abs. (ψ)	Location (x, y)	Abs. (ω)	Abs. (ψ)	Location (x, y)	Abs. (ω)
Oosterlee et al. [186] (256*256)	0.08539	(0.6947, 0.7488)	N.A.	6.20 E-3	(0.1819, 0.7505)	N.A.	6.25 E-3	(0.6877, 0.3069)	N.A.
Ahusborde and Glockner [196] (125000*)	N.A.	(0.6944, 0.7511)	3.877	N.A.	(0.1842, 0.7508)	1.211	N.A.	(0.6874, 0.3094)	9.61 E-1
2nd-order cut-stencil (12545**)	0.08377 ($0.485 \leq \sigma \leq 0.600$)^i ($\sigma_{Opt.} = 0.575$)^{ii}	(0.6953, 0.7500)	3.767	5.87 E-3	(0.1797, 0.7500)	1.130	5.95 E-3	(0.6875, 0.3047)	9.16 E-1
Cut-stencil HO-FDM1 (12545**)	0.08592 ($0.485 \leq \sigma \leq 0.590$) ($\sigma_{Opt.} = 0.590$)	(0.6875, 0.7500)	3.862	6.16 E-3	(0.1797, 0.7500)	1.187	6.34 E-3	(0.6875, 0.3047)	9.48 E-1
Cut-stencil HO-FDM2 (12545**)	0.08576 ($0.460 \leq \sigma \leq 0.570$) ($\sigma_{Opt.} = 0.569$)	(0.6875, 0.7500)	3.852	6.15 E-3	(0.1797, 0.7500)	1.175	6.30 E-3	(0.6875, 0.3047)	9.48 E-1
2nd-order cut-stencil (19521**)	0.08441 ($0.670 \leq \sigma \leq 0.775$) ($\sigma_{Opt.} = 0.775$)	(0.6938, 0.7500)	3.799	6.04 E-3	(0.1813, 0.7500)	1.153	6.07 E-3	(0.6875, 0.3063)	9.35 E-1
Cut-stencil HO-FDM1 (19521**)	0.08580 ($0.670 \leq \sigma \leq 0.780$) ($\sigma_{Opt.} = 0.780$)	(0.6938, 0.7500)	3.861	6.21 E-3	(0.1813, 0.7500)	1.189	6.32 E-3	(0.6875, 0.3063)	9.56 E-1
Cut-stencil HO-FDM2 (19521**)	0.08566 ($0.785 \leq \sigma \leq 0.885$) ($\sigma_{Opt.} = 0.850$)	(0.6938, 0.7500)	3.849	6.21 E-3	(0.1813, 0.7500)	1.183	6.27 E-3	(0.6875, 0.3063)	9.54 E-1
*: Number of nodes, **: Number of active nodes									
(i): Study range of under-relaxation factor, (ii): Optimum value of under-relaxation factor									

Table 5.34: Comparison of cut-stencil FD solutions for lid-driven cavity flow in an L-shaped domain ($Re = 1000$)

Comparison of the 2nd-order cut-stencil FD solutions and other published numerical results show good agreement for the key features of the solution, where previous numerical studies have used much finer meshes than those in the present research work. The finer meshes used with the cut-stencil FD methods gives 1.15% relative difference for the minimum value of ψ compared to the value in [186]. This difference reaches to 1.90% when the grid of 12545 active nodes is employed. Same comparison of the extrema of ψ, in the region $x < 0.5$, gives the reduction of 8.39% to 2.58% for the grids of 12545 and 19251 nodes, respectively, for the 2nd-order cut-stencil FD solution.

The sum of relative differences for minimum and extremes of ψ in the present study, compared to the same values in [186], gives 15.08%, 2.71% and 2.08% for 2nd-order, HO-FDM1 and HO-FDM2, respectively, for the grid of 12545 active nodes. These differences are reduced to 6.61%, 1.75% and 0.79%, respectively, when the grid of 19521 active nodes is employed. One can see that, regardless of the good accuracy for all cut-stencil formulations of the present study, the higher-order methods can predict accurate solutions on the grid of 12545 active nodes since the solution on the finer grid, for the same methods, just verifies the independency of the solution from the grid size. The solution of the 2nd-order formulation of cut-stencil FDM shows significant changes in the key features of the solutions, especially in the extrema of ψ in region $x < 0.5$ that implies that the grid of 19521 active nodes or even a finer grid can generate the solution of the 2nd-order formulation. The contours of streamfunction for cut-stencil HO-FDM2 solution for lid-driven cavity flow in an L-shaped domain, using the grid of 12545 active nodes, is plotted in Figure 5.46.
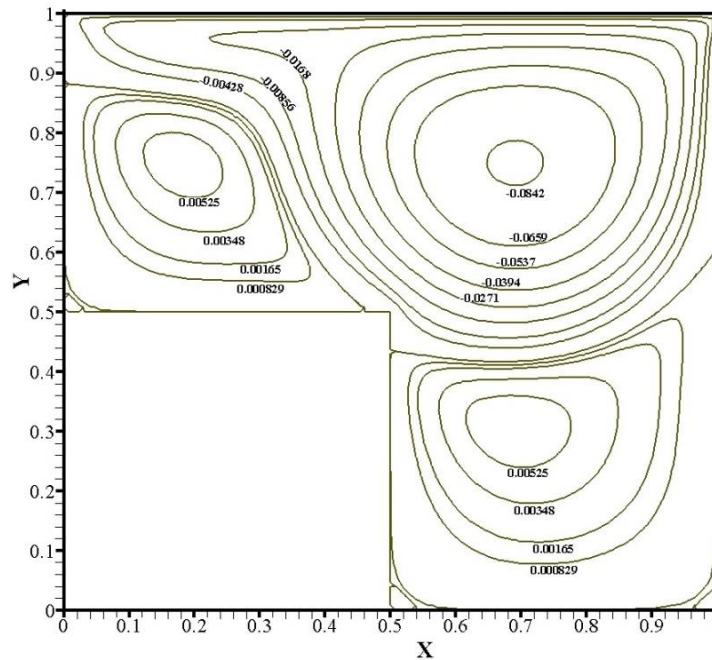
Figure 5.46: Streamfunction contours of HO-FDM2 solution to lid-driven cavity flow in L-shaped domain ($Re = 1000$, 12545 active nodes)

5.7   Chapter Summary

The simulation of lid-driven cavity flow, as a fluid flow benchmark problem, was explored in this chapter using the Cartesian cut-stencil FDM. The 2nd-order accurate formulation of the cut-stencil FDM was initially solved for Reynolds numbers of 100 and 1000, and compared to other available numerical results for the same size grid. This step confirmed that the cut-stencil formulations can be applied to coupled sets of non-linear PDEs to solve complex fluid flows such as those described by the streamfunction-vorticity equations. Good agreement with relatively fine mesh results from the literature was obtained using a coarser mesh when the 2nd-order accurate cut-stencil formulation was employed. Higher-order formulations of the cut-stencil FDM were tested, initially in a regular square domain, for streamfunction-vorticity equations and results were compared to higher-order results in other numerical studies. Solutions using both HO cut-stencil FDM1 and FDM2 show good agreement with data from other researchers. All the grids for the unit square cavity were designed to be non-uniform with the nodes clustered near the walls.

The Cartesian cut-stencil FDM solution of the streamfunction-vorticity equations in several irregular shaped domains was also presented in this chapter. Unlike other finite difference studies for irregular shaped domains, the Cartesian cut-stencil FDM does not require specialized grid generation for each different geometry of the domain. For all the domains, the quadratic transformation functions introduced in Chapter 2 provide the computational stencil on which the numerical solution algorithm is based. The 2nd-order accurate formulation of the cut-stencil FDM showed good agreement with previously published results, even with relatively coarser meshes. This agreement is improved in the event of employing higher-order formulations.

The Point-Jacobi method was chosen as the default iterative scheme and, for cases when the flow problem was dominated by convection, central differencing of the convective terms led to divergence of the iterations. Upwinding schemes for each cut-stencil FDM were able to resolve this issue and provide a converged solution for convective-dominant flow. Additionally, the SUR iterative formulation for streamfunction and vorticity equations gave a converged solution for central differencing of the convective terms which yielded more accurate results compared to the lower order upwind approximation.

CHAPTER 6

CONCLUDING REMARKS and RECOMMENDATIONS for FUTURE WORKS

6.1 Summary and Concluding Remarks

The development of a new formulation and numerical algorithm for the solution of partial differential equations (PDEs), referred to as the Cartesian cut-stencil finite difference method (FDM), are the principal themes of this thesis. Generally, any numerical method to solve PDEs should have several key features, including ease of implementation, ability to produce accurate solutions and capability of application to any type of complex domain. Most researchers regard the first two characteristics to be more closely associated with the finite difference method, while other numerical schemes such as the finite volume method (FVM) and finite element method (FEM) cover the last feature. The Cartesian cut-stencil FDM proposed in this thesis exhibits all the desirable features to solve PDEs from many areas of engineering and science, modeling a variety of physics on any type of domain, while at the same time being very simple to formulate.

A summary of the Cartesian cut-stencil FDM and its special features that have been investigated in this thesis are:

- This thesis is the first comprehensive research using this new cut-stencil numerical method and due to the programme-based nature of the research, the verification of the codes and formulations was considered as one of the main aims of the thesis. Verification was carried out by comparing the cut-stencil results with the exact solution of a number of manufactured problems.
- The Cartesian cut-stencil FDM uses a unique localized mapping of each 5-point stencil in the physical domain to a generic uniform computational stencil. The 1-D quadratic transformation functions make the form of the mapped governing equations relatively simple compared to the complicated form of the same equations when 2-D transformation functions are used, as is the case if numerical grid generation is necessary to achieve finite difference solutions in a complex domain.
- The Cartesian cut-stencil method, even when dealing with highly complex domains, does not require any formal or classical grid generation techniques. The localized mapping of each physical stencil, regardless of uniform or non-uniform arm lengths, eliminates the grid generation aspect of the solution process.
- No special formulation is needed when the physical stencil is cut by a boundary, so the same mapping procedure is carried out for cut stencils as well as uncut stencils. This feature makes the cut-stencil method easy to programme, regardless of the complexity of the solution domain.
- The details of boundary node treatment, in particular, in the event of Neumann boundary conditions, are presented. One-sided 2nd-order accurate approximation of the Neumann boundary condition is the basic differencing method to evaluate the solution at boundary nodes. Higher-order accurate approximations for this type of node are also feasible and details and corresponding results are presented in this thesis.

- Formulations of the unsteady convection-diffusion and wave equations are studied using a forward in time and central in space (FTCS) scheme and stability requirements are developed and tested.
- The Cartesian cut-stencil FDM can be combined with the higher-order compact Padé-Hermitian method to produce higher-order schemes for the numerical solution of PDEs. It is shown that the higher-order formulations can significantly reduce the demand on computational resources and time to achieve a desired level of accuracy.
- The details of formulations for one-sided 3rd-order and 4th-order accurate approximations of the derivative at Neumann boundary nodes, using the same 5-point stencil as the 2nd-order accurate approximation, are developed and numerical tests show the potential of the Cartesian cut-stencil FDM to approximate the unknown values at boundary nodes with the same global order of accuracy as internal nodes.
- Another advantage of the Cartesian cut-stencil FDM is the availability of the local truncation error (LTE). LTE provides a reliable measure of the numerical accuracy and can be used for mesh adaption. The simple formulation of the Cartesian cut-stencil FDM makes it possible to easily calculate the complex mathematical expression of LTE at each point in the domain of interest.
- The Cartesian cut-stencil FD solution of lid-driven cavity flow problem, as a benchmark problem in the field of fluid flow, is discussed in Chapter 5. The solutions of 2nd-order and higher-order formulations are obtained for different values of Reynolds number in a square cavity as well as a number of irregular shaped domains. The results show good agreement compared to other reported results.

The characteristics of the Cartesian cut-stencil FDM, as summarized above, illustrate the ability of the method to yield high-fidelity solutions of PDEs in irregular shaped domain and from many fields of science and engineering. The method exhibits many desirable features demonstrated in commercial simulation packages which are based on FVM and FEM. This dissertation demonstrates that the Cartesian cut-stencil FDM can be considered as a viable alternative to commercial packages for the solution of complex physics-based phenomena in complicated domains.

6.2   Recommendations for Future Work

Some recommendations to continue this research are:

- Due to the 3-dimensional nature of most engineering problems or physical phenomenon, a 3-D version of the Cartesian cut-stencil FDM can be regarded as one of the most important steps in the future of this research. The idea of 1-D quadratic transformation functions can be easily defined for each direction on a 3-D physical stencil. To accomplish this purpose, the Cartesian grid software needs to be updated to provide all the requirements of a 3-D version of the code.

- The possibility of implementing other differencing schemes for the unsteady formulation, particularly for temporal discretization, is another potential option to solve unsteady PDEs in regular or irregular shaped domains with higher accuracy.
- Putting additional effort to resolve the issues with cut stencils of the 5+4-point stencil formulation, as mentioned in Chapter 2, may lead to differencing schemes with order of accuracy higher than methods used in this thesis. A hybrid formulation could be developed in which the 5+4-point formulation is employed for the solution for PDEs on stencils when none of their arms are cut, while other higher-order formulations discussed in this thesis are applied for the stencils with boundary cuts.
- Studying the combination of the Cartesian cut-stencil FD formulation with other higher-order compact Padé-Hermitian methods, e.g. globally 6th-order accurate approximation of first and second derivatives, will lead to more accurate solutions of PDEs.
- 2nd-order and higher-order Cartesian cut-stencil FD schemes can be formulated and tested for flows with high gradient regions such as turbulent flows, or for flows with strong discontinuities, e.g. shock waves in compressible flow.

The simple formulation of the Cartesian cut-stencil FD and ease of writing the differencing formulas using this method can provide the condition to solve PDEs in two mediums, simultaneously. Examples of this type of phenomenon can be seen in fluid-solid interaction or conjugate heat transfer problems. The complexity of the domains for each of the mediums does not create any limitations for this method.

REFERENCES

[1] A. Gilat and V. Subramaniam. *Numerical Methods for Engineering and Scientists: An Introduction with Applications Using MATLAB*. John Wiley & Sons, Inc., USA, 2008.

[2] D.M. Causon and C.G. Mingham. *Introductory Finite Difference Methods for PDEs*. Free ebook at bookboon.com, Copyright Ventus Publishing ApS, 2010.

[3] J.N. Reddy. *An Introduction to the Finite Element Method*. McGraw-Hill, Inc., USA, 1984.

[4] P.S. Jensen. Finite difference techniques for variable grids. *Journal of Computers & Structures*, 2: 17-29, 1972.

[5] C. Fischer, G. Nanz and S. Selberherr. Finite difference, boundary-fitted grid generation for arbitrarily shaped two-dimensional simulation areas. *Journal of Computer Methods in Applied Mechanics and Engineering*, 110: 17-24, 1993.

[6] J. Blazek. *Computational Fluid Dynamics: Principles and Applications*. 1st Edition, Elsevier Science Ltd., UK, 2001.

[7] E.A. Fadlun, R. Verzicco, P. Orlandi and J. Mohd-Yusof. Combined immersed-boundary finite-difference methods for three-dimensional complex flow simulations. *Journal of Computational Physics*, 161: 35–60, 2000.

[8] J. Nordström, J. Gong, E. van der Weide and M. Svärd. A stable and conservative high order multi-block method for the compressible Navier–Stokes equations. *Journal of Computational Physics*, 228: 9020–9035, 2009.

[9] T. Sumi, T. Kurotaki and J. Hiyama. Generalized characteristic interface conditions for high-order multi-block computation. *International Journal of Computational Fluid Dynamics*, 21: 335–350, 2007.

[10] F. Pascal and J-M. Ghidaglia. Footbridge between finite volumes and finite elements with applications to CFD. *International Journal for Numerical Methods in Fluids*, 37: 951–986, 2001.

[11] J.F. Wendt (editor) with contributions by J.D. Anderson Jr., J. Degroote, G. Degrez, E. Dick, R. Grundmann and J. Vierendeels. *Computational Fluid Dynamics, An Introduction*. 3rd Edition, Springer-Verlag, Berlin, Heidelberg, 2009.

[12] F. Bassi and S. Rebay. High-order accurate discontinuous finite element solution of the 2D Euler equations. *Journal of Computational Physics*, 138: 251–285, 1997.

[13] H. Yoshioka, K. Unami and M. Fujihara. A finite element/volume method model of the depth-averaged horizontally 2D shallow water equations. *International Journal for Numerical Methods in Fluids*, 75: 23–41, 2014.

[14] S. Aliabadia, C. Bigler, E. Yilmaza, S. Pallea and B. Soni. Hybrid finite element/volume method for 3D incompressible flows with heat transfer. *International Journal of Computational Fluid Dynamics*, 25: 175–189, 2011.

[15] P. Wapperom and M.F. Webster. A second-order hybrid finite-element/volume method for viscoelastic flows. *Journal of Non-Newtonian Fluid Mechanics*, 79: 405-431, 1998.

[16] G.D. Smith. *Numerical Solution of Partial Differential Equations: Finite Difference Methods*. 3rd Edition, Oxford University Press Inc., New York, USA, 2004.

[17] K.A. Hoffmann and S.T. Chiang. *Computational Fluid Dynamics*. Vol. 1, 4th Edition, Engineering Education System, Kansas, USA, 2004

[18] L.M. Leslie and B.J. McAvaney. Comparative test off direct and iterative methods for solving Helmholtz-type equations. *Journal of Monthly Weather Review*, 101: 235-239, 1973.

[19] W.L. Wood. *Introduction to Numerical Methods for Water Resources*. Oxford University Press Inc., New York, USA, 1993.

[20] S.D. Conte and C. de Boor. *Elementary Numerical Analysis: An Algorithmic Approach*. McGraw-Hill, Inc., USA, 1980.

[21] I.B. Kalambi. A comparison of three iterative methods for the solution of linear equations. *Journal of Applied Sciences and Environmental Management*, 12: 53 - 55, 2008.

[22] Y. Saad and H.A. van der Vorst. Iterative solution of linear systems in the 20th century. *Journal of Computational and Applied Mathematics*, 123: 1-33, 2000.

[23] J.K. Reid. A method for finding the optimum successive over-relaxation parameter. *The Computer Journal*, 9: 200-2004, 1966.

[24] X.I.A. Yang and R. Mittal. Acceleration of the Jacobi iterative method by factors exceeding 100 using scheduled relaxation. *Journal of Computational Physics*, 274: 695–708, 2014.

[25] P.R. Eiseman. Grid generation for fluid mechanics computations. *Annual Review of Fluid Mechanics*, 17: 487-522, 1985.

[26] A. Khamayseh and C.W. Mastin. Computational conformal mapping for surface grid generation. *Journal of Computational Physics*, 123: 394–401, 1996.

[27] P.M. Bagade, Y.G. Bhumkar and T.K. Sengupta. An improved orthogonal grid generation method for solving flows past highly cambered aerofoils with and without roughness elements. *Journal of Computers & Fluids*, 103: 275–289, 2014.

[28] J.F. Thompson. Grid generation techniques in computational fluid dynamics. *AIAA Journal*, 22: 1505-1523, 1984.

[29] M.A. Akinlar, S. Salako and G. Liao. A method for orthogonal grid generation. *Journal of General Mathematics Notes*, 3: 55-72, 2011.

[30] J.F. Thompson, B.K. Soni and N.P. Weatherill. *Handbook of Grid Generation*. CRC Press LLC, USA, 1999.

[31] M.T. Nair and T.K. Sengupta. Orthogonal grid generation for Navier–Stokes computations. *International Journal for Numerical Methods in Fluids*, 28: 215–224, 1998.

[32] G. Ryskin and L.G. Leal. Orthogonal mapping. *Journal of Computational Physics*, 50: 71–100, 1983.

[33] R. Duraiswami and A. Prosperetti. Orthogonal mapping in two dimensions. *Journal of Computational Physics*, 98: 254-268, 1992.

[34] H.J. Oh and I.S. Kang. A non-iterative scheme for orthogonal grid generation with control function and specified boundary correspondence on three sides. *Journal of Computational Physics*, 112: 138-148, 1994.

[35] S. Kawata, N. Takura and Y. Manabe. Grid generation with orthogonality and uniformity of line-spacing changing ratio. *Computer Physics Communications*, 94: 19-24, 1996.

[36] H. Johansen and P. Colella. A Cartesian grid embedded boundary method for Poisson's equation on irregular domains. *Journal of Computational Physics*, 147: 60–85, 1998.

[37] R.B. Pember, John B. Bell, P. Colella, W.Y. Crutchfield and M.L. Welcome. An adaptive Cartesian grid method for unsteady compressible flow in irregular regions. *Journal of Computational Physics*, 120: 278-304, 1995.

[38] T. Ye, R. Mittal, H.S. Udaykumar and W. Shyy. An accurate Cartesian grid method for viscous incompressible flows with complex immersed boundaries. *Journal of Computational Physics*, 156: 209–240, 1999.

[39] M.W. Johnson. A novel Cartesian CFD cut cell approach. *Computers & Fluids*, 79: 105–119, 2013.

[40] K. Morinishi. A finite difference solution of the Euler equations on non-body-fitted Cartesian grids. *Computers & Fluids*, 21: 331–344, 1992.

[41] K.A. Hoffmann and S.T. Chiang. *Computational Fluid Dynamics*. Vol. 2, 4th Edition, Engineering Education System, Kansas, USA, 2004.

[42] H.K. Versteeg and W. Malalasekera. *An Introduction to Computational Fluid Dynamics: the Finite Volume Method.* Pearson Education Limited, UK, 2007.

[43] G.E. Forsythe and W.R. Wasow. *Finite-Difference Methods for Partial Differential Equations*. Wiley, New York, 1960.

[44] S.V. Patankar. *Numerical Heat Transfer and Fluid Flow.* Series in Computational Methods in Mechanics and Thermal Sciences. Hemisphere Publ. Corp., USA, 1980.

[45] L.F. Richardson. The approximate arithmetical solution by finite differences of physical problems involving differential equations, with an application to the stresses in a masonry dam. *Proc. Roy. Soc. London A: Mathematical, Physical and Engineering Sciences,* 83: 335-336, 1910.

[46] M. Turner, R. Clough, H. Martin and L. Topp. Stiffness and deflection analysis of complex structures. *Journal of Aerospace Science,* 23: 805-823, 1956.

[47] R.W. Clough. The finite element method in plane strain analysis. *Journal of Struct. Div. ASCE, Proc. 2nd Conf. on Electronic Computation,* pp. 345-378, 1960.

[48] P.F.A. Mancera and R. Hunt. Fourth order method for solving the Navier-Stokes equations in a constricting channel. *International Journal for Numerical Methods in Fluids*, 25: 1119-1135, 1997.

[49] M. Lakner and I. Plazl. The finite differences method for solving systems on irregular shapes. *Journal of Computers and Chemical Engineering*, 32: 2891–2896, 2008.

[50] Y. Satô and K. Harumi. A method for determining the eigenfrequency of a mechanical system by simulation. *Journal of Computational Physics*, 9: 194-206, 1972.

[51] V.C. Mariani and A.T. Prata. A Eulerian-Lagrangian method applied to fluid flow in lid-driven cavities with irregular bottom walls. *Numerical Heat Transfer, Part B*, 53: 206–233, 2008.

[52] B. Koren. Upwind discretization of the steady Navier–Stokes equations. *International Journal for Numerical Methods in Fluids*, 11: 99-117, 1990.

[53] B. Zogheib and R.M. Barron. Velocity–pressure coupling in finite difference formulations for the Navier–Stokes equations. *International Journal for Numerical Methods in Fluids*, 65: 1096–1114, 2011.

[54] S.E. Rogers and D. Kwak. An upwind-differencing scheme for the incompressible Navier-Stokes equations. NASA Technical Memorandum 101051, 1988.

[55] T. Timin and N. Esmail. A comparative study of central and upwind difference schemes using the primitive variables. *International Journal for Numerical Methods in Fluids*, 3: 295-305, 1983.

[56] W. Shyy. A study of finite difference approximations to steady-state, convection-dominated flow problems. *Journal of Computational Physics*, 57: 415-438, 1985.

[57] T.J. Chung. *Computational Fluid Dynamics*. Cambridge University Press, United Kingdom, 2002.

[58] B. Bradie. *A Friendly Introduction to Numerical Analysis*. Pearson Education, Inc., New Jersey, USA, 2006.

[59] R. Hixon. Prefactored small-stencil compact schemes. *Journal of Computational Physics*, 165: 522-541, 2000.

[60] R.K. Shukla and X. Zhong. Derivation of high-order compact finite difference schemes for non-uniform grid using polynomial interpolation. *Journal of Computational Physics*, 204: 404-429, 2005.

[61] D. Liu, W. Kuang and A. Tangborn. High-order compact implicit difference methods for parabolic equations in geodynamo simulation. *Hindawi Publishing Corporation Advances in Mathematical Physics*, Article ID 568296: 23 pages, 2009.

[62] J.S. Shang. High-order compact-difference schemes for time-dependent Maxwell equations. *Journal of Computational Physics*, 153: 312-333, 1999.

[63] J. Zhang. Multigrid method and fourth-order compact scheme for 2d Poisson equation with unequal mesh-size discretization. *Journal of Computational Physics*, 179: 170-179, 2002.

[64] K. Mahesh. A family of high order finite difference schemes with good spectral resolution. *Journal of Computational Physics*, 145: 332-358, 1998.

[65] W.F. Spotz and G.F. Carey. Higher-order compact scheme for the steady stream-function vorticity equations. *International Journal of Numerical Methods in Engineering*, 38: 3497-3512, 1995.

[66] Y. Adams. Highly accurate compact implicit methods and boundary conditions. *Journal of Computational Physics*, 24: 10-22, 1977.

[67] Y. Adams. A Hermitian finite difference method for the solution of parabolic equations. *Journal of Computers & Mathematics with Applications*, 1: 393-406, 1975.

[68] P.C. Chu and C. Fan. A three-point six order staggered combined compact difference scheme. *Journal of Mathematical and Computer Modelling*, 32: 323-340, 2000.

[69] S. Ghader, A. Ghasemi, M.R. Banazadeh and D. Mansoury. High-order compact scheme for Boussinesq equations: Implementation and numerical boundary condition issue. *International Journal for Numerical Methods in Fluids*, 69: 590-605, 2012.

[70] L. Gamet, F. Ducros, F. Nicoud and T. Poinsot. Compact finite diffrence schemes on non-uniform meshes. Application to direct numerical simulation of compressible flows. *International Journal for Numerical Methods in Fluids*, 29: 159-191, 1999.

[71] S. Abarbanel and A. Kumar. Compact high-order schemes for the Euler equations. *Journal of Scientific Computing*, 3: 275-288, 1988.

[72] R.S. Hirsh. Higher order accurate difference solutions of fluid mechanics problems by a compact differencing technique. *Journal of Computational Physics*, 19: 90-109, 1975.

[73] M. Venutelli. New optimized fourth-order compact finite difference scheme for wave propagation phenomena. *Journal of Applied Numerical Mathematics*, 87: 53-73, 2015.

[74] S.K. Lele. Compact finite difference schemes with spectral-like resolution. *Journal of Computational Physics*, 103: 16-42, 1992.

[75] J.A. Ekaterinaris. High-order accurate, low numerical diffusion methods for aerodynamics. *Progress in Aerospace Sciences*, 41: 192–300, 2005

[76] P.C. Chu and C. Fan. A three-point combined compact difference scheme. *Journal of Computational Physics*, 140: 370-399, 1998.

[77] J.H. Ferziger and M. Perić. *Computational Methods for Fluid Dynamics*. 3rd Edition, Springer-Verlag, Berlin, Heidelberg, New York, 1999.

[78] P.M. Gresho and R.L. Lee. Don't suppress the wiggles-They're telling you something. *Journal of Computers & Fluids*, 9: 255-263, 1981.

[79] F. Ali and D.F. Mayers. Error in the upwind differencing of the convection-diffusion equation. *Journal of Computational and Applied Mathematics*, 58: 201-224, 1995.

[80] S.M. Choo and S.K. Chung. High-order perturbation-difference scheme for a convection-diffusion problem. *Journal of Computer Methods in Applied Mechanics and Engineering*, 190: 721-732, 2000.

[81] B.P. Leonard. Stable and accurate convective modelling procedure based on quadratic upstream interpolation. *Journal of Computer Methods in Applied Mechanics and Engineering*, 19: 59-98, 1979.

[82] R.C. Swanson and E. Turkel. On central-difference and upwind schemes. *Journal of Computational Physics*, 101: 292–306, 1992.

[83] E. Sousa. High-order methods and numerical boundary conditions. *Journal of Computer Methods in Applied Mechanics and Engineering*, 196: 4444 – 4457, 2007.

[84] B. Gustafsson. The convergence rate for difference approximations to mixed initial boundary value problems. *Journal of Mathematics of Computation*, 29: 396-406, 1975.

[85] M.H. Carpenter, D. Gottlieb and S. Abarbanel. The stability of numerical boundary treatments for compact high-order finite difference schemes. *Journal of Computational Physics*, 108: 272-295, 1993.

[86] X. Zhong. High-order finite-difference schemes for numerical simulation of hypersonic boundary-layer transition. *Journal of Computational Physics,* 144: 662–709, 1998.

[87] M.H. Carpenter, D. Gottlieb and S. Abarbanel. Stable and accurate boundary treatments for compact, high-order finite-difference schemes. *Journal of Applied Numerical Mathematics*, 12: 55-87, 1993.

[88] W. Shen, C. Zhang and J. Zhang. Relaxation method for unsteady convection–diffusion equations. *Journal of Computers and Mathematics with Applications*, 61: 908–920, 2011.

[89] H. Fasel. Investigation of the stability of boundary layers by a finite-difference model of the Navier-Stokes equations. *Journal of Fluid Mechanics*, 78: 355-383, 1976.

[90] Y. Zang, R.L. Street and J.R. Koseff. A non-staggered grid, fractional method for time-dependent incompressible Navier-Stokes equations in curvilinear coordinates. *Journal of Computational Physics*, 114: 18-33, 1994.

[91] H. Johnston and J. Liu. Finite difference schemes for incompressible flow based on local pressure boundary conditions. *Journal of Computational Physics*, 180: 120-154, 2002.

[92] W. Liao. A compact high-order finite difference method for unsteady convection-diffusion equation. *International Journal for Computational Methods in Engineering Science and Mechanics*, 13:135–145, 2012.

[93] H.W. Sun and L.Z. Li. A CCD–ADI method for unsteady convection–diffusion equations. *Journal of Computer Physics Communications*, 185: 790–797, 2014.

[94] K.E. Torrance. Comparison of finite-difference computations of natural convection. *Journal of Research of the National Bureau of Standards - B. Mathematical Sciences*, 72B: 281-301, 1968.

[95] S.F. Radwan. Comparison of higher-order accurate schemes for solving the two-dimensional unsteady Burgers'equation. *Journal of Computational and Applied Mathematics*, 174: 383–397, 2005.

[96] R.S. Bernard. A MacCormack scheme for incompressible flow. *Journal of Computers and Mathematics with Applications*, 24: 151-168, 1992.

[97] J. Thibault. Comparison of nine three-dimensional numerical methods for the solution of the heat diffusion equation. *Journal of Numerical Heat Transfer*, 8: 281-298, 1985.

[98] R.M. Clancy. A note on finite differencing of the advection-diffusion equation. *Journal of Monthly Weather Review*, 109: 1807-1809, 1981.

[99] J.M. Beckers. Analytical linear numerical stability conditions for an anistropic three-dimensional advection-diffusion equation. *SIAM Journal on Numerical Analysis*, 29: 701-713,1992.

[100] A. Rigal. Stability analysis of finite difference schemes for two-dimensional advection-diffusion problems. *International Journal For Numerical Methods in Fluids*, 13: 579-597, 1991.

[101] T.F. Chan. Stability analysis of finite difference schemes for the advection-diffusion equation. *SIAM Journal on Numerical Analysis*, 21: 272-284, 1984.

[102] H.D. Thompson, B.W. Webb and J.D. Hoffmann. The cell Reynolds number myth. *International Journal For Numerical Methods in Fluids*, 5: 305-310, 1985.

[103] S. Biringen. A note on the numerical stability of the convection-diffusion equation. *Journal of Computational and Applied Mathematics*, 7: 17-20, 1981.

[104] G.W. Wei. Vibration analysis by discrete singular convolution. *Journal of Sound and Vibration*, 244: 535-553, 2001.

[105] A. Novais and L.T. Santos. 2.5D finite-difference solution of the acoustic wave equation. *Geophysical Prospecting*, 53: 523-531, 2005

[106] L. Eça and M. Hoekstra, A. Hay and D. Pelletier. A manufactured solution for a two-dimensional steady wall-bounded incompressible turbulent flow. *International Journal of Computational Fluid Dynamics*, 21: 175–188, 2007.

[107] P.J. Roache. Code verification by the method of manufactured solutions. *ASME*, *Journal of Fluids Engineering*, 124: 4-10, 2002.

[108] L.A. Petri, P. Sartori, J.K. Rogenski and L.F. de Souza. Verification and validation of a direct numerical simulation code. *Journal of Computer Methods in Applied Mechanics and Engineering*, 291: 266-279, 2015.

[109] K. Salari and P. Knupp. Code verification by the method of manufactured solutions. *SAND 2000-1444*, *Sandia National Laboratories*, 124 pages, 2000.

[110] C.J. Roy, C.C. Nelson, T.M. Smith and C.C. Ober. Verification of Euler/Navier–Stokes codes using the method of manufactured solution. *International Journal for Numerical Methods in Fluids*, 44: 599–620, 2004.

[111] S.P. Veluri, C.J. Roy and E.A. Luke. Comprehensive code verification techniques for finite volume CFD codes. *Journal of Computers & Fluids*, 70: 59-72, 2012.

[112] S. Étienne, A. Garon and D. Pelletier. Some manufactured solutions for verification of fluid-structure interaction codes. *Journal of Computers and Structures*, 106–107: 56–67, 2012.

[113] J.M. Vedovoto, A. da S. Neto, A. Mura and L.F.F. da Silva. Application of the method of manufactured solutions to the verification of a pressure-based finite-volume numerical scheme. *Journal of Computers & Fluids*, 51: 85-99, 2011.

[114] L. Eça and M. Hoekstra. Evaluation of numerical error estimation based on grid refinement studies with the method of the manufactured solutions. *Journal of Computers & Fluids*, 38: 1580-1591, 2009.

[115]   W.L. Oberkampf and F.G. Blottner. Issues in computational fluid dynamics code verification and validation, *AIAA Journal*, 36: 687-695, 1998.

[116]   C.J. Roy. Grid convergence error analysis for mixed-order numerical schemes, *AIAA Journal*, 41: 595-604, 2003.

[117]   L. Shunn and F. Ham. Method of manufactured solutions applied to variable-density flow solvers. *Annual Research Briefs*, *Center for Turbulence Research*, 155-168, Stanford, CA, 2007.

[118]   L. Eça, M. Hoekstra, A. Hay and D. Pelletier. On the construction of manufactured solutions for one and two-equation eddy-viscosity models. *International Journal for Numerical Methods in Fluids*, 54: 119–154, 2007.

[119]   L. Eça, M. Hoekstra, A. Hay and D. Pelletier. Verification of RANS solvers with manufactured solutions. *Journal of Engineering with Computers*, 23: 253–270, 2007.

[120]   C.J. Roy, T.M. Smith, and C.C. Ober. Verification of a compressible CFD code using the method of manufactured solutions. *AIAA Paper 2002-3110*, 2002.

[121] J.C. Tannehill, D.A. Anderson, R.H. Pletcher, *Computational Fluid Mechanics and Heat Transfer*, 2nd Edition, Taylor & Francis, USA, 1997.

[122] D.S. McRae. r-Refinement grid adaptation algorithms and issues. *Journal of Computer Methods in Applied Mechanics and Engineering*, 189: 1161-1182, 2000.

[123] N.K. Yamaleev. Minimization of the truncation error by grid adaptation. *Journal of Computational Physics*, 170: 459–497, 2001.

[124] F. Fraysse, E. Valero and J. Ponsín. Comparison of mesh adaptation using the adjoint methodology and truncation error estimates. *AIAA Journal*, 50: 1920-1932, 2012.

[125] E.M. Hirthe and T. Graf. Non-iterative adaptive time-stepping scheme with temporal truncation error control for simulating variable-density flow. *Advances in Water Resources*, 49: 46–55, 2012.

[126] W.L. Oberkampf, S.M. DeLand, B.M. Rutherford, K.V. Diegert and K.F. Alvin. Error and uncertainty in modeling and simulation. *Journal of Reliability Engineering & System Safety*, 75: 333-357, 2002.

[127] M.D. Salas and H.L. Atkins. On problems associated with grid convergence of functionals. *Journal of Computers & Fluids*, 38:1445–1454, 2009.

[128] Z. Gong, C. Lu and H. Huang. Accuracy analysis of immersed boundary method using method of manufactured solutions. *Journal of Applied Mathematics and Mechanics (English Edition),* 31: 1197–1208, 2010.

[129] P.J. Roache. Quantification of uncertainty in computational fluid dynamics. *Annual Review of Fluid Mechanics*, 29: 123-160, 1997.

[130] W.F. Spotz. Accuracy and performance of numerical wall boundary conditions for steady, 2D, incompressible streamfunction vorticity. *International Journal for Numerical Methods in Fluids*, 28: 737–757, 1998.

[131] C.J. Roy. Review of code and solution verification procedures for computational simulation. *Journal of Computational Physics*, 205: 131–156, 2005.

[132] M. Arad, G. Ben-Dor and A. Yakhot. High-order-accurate discretization of a second-order equation with discontinuous coefficients. *Journal of Applied Mathematical Modelling*, 22: 69-79, 1998

[133] M.D. Salas. Some observations on grid convergence. *Journal of Computers & Fluids*, 35: 688–692, 2006.

[134] S. Karaa and J. Zhang. Analysis of stationary iterative methods for the discrete convection–diffusion equation with a 9-point compact scheme. *Journal of Computational and Applied Mathematics*, 154: 447–476, 2003.

[135] M.M. Gupta, R.P. Manohar and J.W. Stephenson. A single cell high order scheme for the convection-diffusion equation with variable coefficients. *International Journal for Numerical Methods in Fluids*, 4: 641-651, 1984.

[136] D. Hu, Y. Wang, G.R. Liu, T. Li, X. Han and Y.T. Gu. A sub-domain smoothed Galerkin method for solid mechanics problems. *International Journal for Numerical Methods in Engineering*, 98:781–798, 2014.

[137] E.F. Rybicki and M.F. Kanninen. A finite element calculation of stress intensity factors by a modified crack closure integral. *Journal of Engineering Fracture Mechanics*, 9: 931–938, 1977.

[138] S.K. Chan and I.S. Tura. A finite element method for contact problems of solid bodies - Part I. Theory and validation. *International Journal of Mechanical Sciences*, 13: 615–625, 1971.

188

[139] I. Ecsedi. Some analytical solutions for Saint-Venant torsion of non-homogeneous cylindrical bars. *European Journal of Mechanics A/Solids*, 28: 985–990, 2009.

[140] S.P. Timoshenko and J.N. Goodier. *Theory of Elasticity*. 3rd Edition, McGraw-Hill Book Company, Inc., USA, 1970.

[141] I.S. Sokolnikoff. *Mathematical Theory of Elasticity*. 2nd Edition, McGraw-Hill Book Company, Inc., USA, 1956.

[142] J.F. Ely and O.C. Zienkiewicz. Torsion of compound bars: a relaxation solution. *International Journal of Mechanical Sciences*, 1: 356-365, 1960.

[143] K.H. Sun, D.L. Pyle, A.D. Fitt, C.P. Please, M.J. Baines and N. Hall-Taylor. Numerical study of 2D heat transfer in a scraped surface heat exchanger. *Journal of Computers & Fluids*, 33:869–880, 2004.

[144] F. Agyenim, N. Hewitt, P. Eames and M. Smyth. A review of materials, heat transfer and phase change problem formulation for latent heat thermal energy storage systems (LHTESS). *Journal of Renewable and Sustainable Energy Reviews*, 14: 615–628, 2010.

[145]   J. Kim and H. Choi. An immersed-boundary finite-volume method for simulation of heat transfer in complex geometries. *KSME International Journal*, 18: 1026-1035, 2004.

[146]   J. Mazumder and W.M. Steen. Heat transfer model for cw laser material processing. *Journal of Applied Physics*, 51:941-947, 1980.

[147]   T.L. Bergman, A.S. Lavine, F.P. Incropera and D.P. Dewitt. *Fundamentals of Heat and Mass Transfer*. 7th Edition, John Wiley & Sons, Inc., USA, 2011.

[148]   L.C. Thomas. *Heat Transfer*. Prentice-Hall, Inc., USA, 1992.

[149] E. Erturk. Discussions on driven cavity flow. *International Journal for Numerical Methods in Fluids*, 60: 275–294, 2009.

[150] U. Ghia, K.N. Ghia and C.T. Shin. High-Re solutions for incompressible flow using the Navier-Stokes equations and a multigrid method. *Journal of Computational Physics*, 48: 387-411, 1982.

[151] M. Sahin and R.G. Owens. A novel fully implicit finite volume method applied to the lid-driven cavity problem—Part I: High Reynolds number flow calculations. *International Journal for Numerical Methods in Fluids*, 42: 57–77, 2003.

[152] E. Barragy and G.F. Carey. Stream function-vorticity driven cavity solution using *p* finite elements. *Journal of Computers & Fluids*, 26: 453-468, 1997.

[153] S. Hou, Q. Zou, S. Chen, G. Doolen, A.C. Cogley. Simulation of cavity flow by the Lattice Boltzmann method. *Journal of Computational Physics*, 118: 329-347, 1995.

[154] B.E. Griffith. An accurate and efficient method for the incompressible Navier–Stokes equations using the projection method as a preconditioner. *Journal of Computational Physics*, 228: 7565–7595, 2009.

[155] P.M. Gresho and R.L. Sani. *Incompressible Flow and the Finite Element Method, Vol. 2: Isothermal Laminar Flow*, John Wiley & Sons Ltd, England, 2000.

[156] P. M. Gresho. Incompressible fluid dynamics: some fundamental formulation issues. *Annual Review Fluid Mechanics*, 23: 413-53, 1991.

[157] S.C.R. Dennis and J.D. Hudson. Compact h^4 finite-difference approximations to operators of Navier-Stokes type. *Journal of Computational Physics*, 85: 390-416, 1989.

[158] M. Li, T. Tang and B. Fornberg. A compact fourth-order finite difference scheme for the steady incompressible Navier-Stokes equations. *International Journal for Numerical Methods in Fluids*, 20: 1137-1151, 1995.

[159] H.F. Oztop and I. Dagtekin. Mixed convection in two-sided lid-driven differentially heated square cavity. *International Journal of Heat and Mass Transfer*, 47: 1761–1769, 2004.

[160] E. Erturk. Comparison of wide and compact fourth-order formulations of the Navier–Stokes equations. *International Journal for Numerical Methods in Fluids*, 60: 992–1010, 2009.

[161] M.M. Gupta and J.C. Kalita. A new paradigm for solving Navier–Stokes equations: streamfunction–velocity formulation. *Journal of Computational Physics*, 207: 52–68, 2005.

[162] S.K. Pandit, J.C. Kalita and D.C. Dalal. A fourth-order accurate compact scheme for the solution of steady Navier–Stokes equations on non-uniform grids. *Journal of Computers & Fluids*, 37: 121–134, 2008.

[163] M. Ben-Artzi, J.P. Croisille and D. Fishelov. A high order compact scheme for the pure-streamfunction formulation of the Navier-Stokes equations. *Journal of Scientific Computing*, 42: 216–250, 2010.

[164] W. E and J-G. Liu. Vorticity boundary condition and related issues for finite difference schemes. *Journal of Computational Physics*, 124:368–382, 1996.

[165] A. Thom. An investigation of fluid flow in two dimensions. *Reports and Memoranda*, No. 1194 Aeronautical Research Committee, London, England, 1928.

[166] A. Thom. Flow past circular cylinders at low speeds. *Proceedings of the Royal Society of London. Series A*, 141: 651-669, 1933.

[167] S.A. Orszag and M. Israeli. Numerical simulation of viscous incompressible flows. *Annual Review Fluid Mechanics*, 6: 281-318, 1974.

[168] P.J. Roache. *Fundamentals of Computational Fluid Dynamics*. Hermosa Publishers, New Mexico, USA, 1998.

[169] H.H. Yang. The computational boundary methods for solving the incompressible flows. *Applied Mathematics Letters*, 6: 3-7, 1993.

[170] A.S. Benjamin and V.E. Denny. On the convergence of numerical solutions for 2-D flows in a cavity at large Re. *Journal of Computational Physics*, 33: 340-358, 1979.

[171] W.R. Briley. A numerical study of laminar separation bubbles using the Navier-Stokes equations. *Journal of Fluid Mechanics*, 47: 713-736, 1971.

[172] M.M. Gupta. High accuracy solutions of incompressible Navier–Stokes equations. *Journal of Computational Physics*, 93: 343-359, 1991.

[173]   N.P. Moshkin and K. Poochinapan. Novel finite difference scheme for the numerical solution of two-dimensional incompressible Navier-Stokes equations. *International Journal of Numerical Analysis and Modeling*, 7: 321–329, 2010.

[174]   C-H. Bruneau and C. Jouron. An efficient scheme for solving steady incompressible Navier-Stokes equations. *Journal of Computational Physics*, 89: 389-413, 1990.

[175]   S.P. Vanka. Block-implicit multigrid solution of Navier-Stokes equations in primitive variables. *Journal of Computational Physics*, 65: 138-158, 1986.

[176]   O. Goyon. High-Reynolds number solutions of Navier-Stokes equations using incremental unknowns. *Journal of Computer Methods in Applied Mechanics and Engineering*, 130: 319-335, 1996.

[177]   S.K. Pandit. On the use of compact streamfunction-velocity formulation of steady Navier-Stokes equations on geometries beyond rectangular. *Journal of Scientific Computing*, 36: 219-242, 2008.

[178]   R. Schreiber and H.B. Keller. Driven cavity flows by efficient numerical techniques. *Journal of Computational Physics*, 49: 310-333, 1983.

[179]   S. Khorasanizade and J.M.M. Sousa. A detailed study of lid-driven cavity flow at moderate Reynolds numbers using incompressible SPH. *International Journal for Numerical Methods in Fluids*, 76: 653-668, 2014.

[180]   B. Yu, W.Q. Tao, D.S. Zhang and Q.W. Wang. Discussion on numerical stability and boundedness of convective discretized scheme. *Numerical Heat Transfer, Part B*, 40: 343-365, 2001.

[181]   Y. Wang and K. Hutter. Comparisons of numerical methods with respect to convectively dominated problems. *International Journal for Numerical Methods in Fluids*, 37: 721–745, 2001.

[182]   S.B. Paramane and A. Sharma. Consistent implementation and comparison of FOU, CD, SOU, and QUICK convection schemes on square, skew, trapezoidal, and triangular lid-driven cavity flow. *Numerical Heat Transfer, Part B*, 54: 84–102, 2008

[183]   H. Nishida and N. Satofuka. Higher-order solutions of square driven cavity flow using a variable-order multi-grid method. *International Journal for Numerical Methods in Engineering*, 34: 637-653, 1992.

[184]   E. Erturk, T.C. Corke and C. Gökçöl. Numerical solutions of 2-D steady incompressible driven cavity flow at high Reynolds numbers. *International Journal for Numerical Methods in Fluids*, 48: 747–774, 2005.

[185]   C-H. Bruneau and M. Saad. The 2D lid-driven cavity problem revisited. *Journal of Computers & Fluids*, 35: 326–348, 2006.

[186]   C.W. Oosterlee, P. Wesseling, A. Segal and E. Brakkee. Benchmark solutions for the incompressible Navier–Stokes equations in general co-ordinates on staggered grids. *International Journal for Numerical Methods in Fluids*, 17: 301-321, 1993.

[187]   E. Erturk and B. Dursun. Numerical solutions of 2-D steady incompressible flow in a driven skewed cavity. *ZAMM - Journal of Applied Mathematics and Mechanics*, 87: 377-392, 2007.

[188]   I. Demirdžić, Ž. Lilek and M. Perić. Fluid flow and heat transfer test problems for non-orthogonal grids: bench-mark solutions. *International Journal for Numerical Methods in Fluids*, 15: 329-354, 1992.

[189]   A. Shklyar and A. Arbel. Numerical method for calculation of the incompressible flow in general curvilinear co-ordinates with double staggered grid. *International Journal for Numerical Methods in Fluids*, 41: 1273–1294, 2003.

[190]   M. Louaked, L. Hanich and K.D. Nguyen. An efficient finite difference technique for computing incompressible viscous flows. *International Journal for Numerical Methods in Fluids*, 25: 1057-1082, 1997.

[191]   E. Erturk1 and O. Gokcol. Fine grid numerical solutions of triangular cavity flow. *The European Physical Journal Applied Physics*, 38: 97-105, 2007.

[192]   W.D. McQuain, C.J. Ribbens, C.-Y. Wang and L.T. Watson. Steady viscous flow in a trapezoidal cavity. *Journal of Computers & Fluids*, 23: 613-626, 1994.

[193]   M. Ahmed and H.C. Kuhlmann. Flow instability in triangular lid-driven cavities with wall motion away from a rectangular corner. *Fluid Dyn. Res.*, 44: (21pp) 025501, 2012.

[194]   F.A. Munir, N.A. Che Sidik, M.I. Mohd. Azmi and M.R. Mohamad Zin. Application of Lattice Boltzmann method in predicting flow of shear driven cavities. *Journal of Mechanical Engineering and Technology*, 3: 55-70, 2011.

[195]   C.Y. Perng and R.L. Street. A coupled multigrid-domain-splitting technique for simulating incompressible lows in geometrically complex domains. *International Journal for Numerical Methods in Fluids*, 13: 269-286, 1991.

[196]   E. Ahusborde and S. Glockner. 2D block-structured mesh partitioner for accurate flow simulations on non-rectangular geometries. *Journal of Computers & Fluids*, 43: 2–13, 2011.

[197]   J.A. Stratton. *Electromagnetic Theory*. IEEE Press, John Wiley & Sons, Inc. Publication, USA, 2007.

[198]   Z. Li and C. Wang. A fast finite difference method for solving Navier-Stokes equations on irregular domains. *Journal of Communications in Mathematical Sciences*, 1: 181-197, 2003.

APPENDIX I: SUMMARY OF MANUFACTURED PROBLEMS

Problem #	Section #	Equation used	Domain studied	Type of BCs	Cut-stencil FD scheme used
1	3.5.1	Poisson	Square	Dirichlet	2nd-order
2	3.5.2	Poisson	Square	(1) Neumann	2nd-order
3	3.5.3	Poisson	Square	(2) Neumann	2nd-order
4	3.5.4	Convection-diffusion	Rectangular	Dirichlet or Neumann	2nd-order
5	3.5.5	Laplace	Irregular	Dirichlet or Neumann	2nd-order
6	3.5.6	Convection-diffusion	Irregular	Dirichlet or Neumann	2nd-order
7	3.5.7	Poisson	Rectangular	Dirichlet or Neumann	2nd-order & 5+4-point stencil
8.1	3.5.8	Poisson	Rectangular	Dirichlet	HO-FDM1
8.2	3.5.8	Diffusion	Irregular (triangular)	Dirichle	2nd-order & HO-FDM1
8.3	3.5.8	Convection-diffusion	Irregular	Dirichlet or Neumann	2nd-order & HO-FDM1
9.1	3.5.9	Diffusion	Square	Dirichlet	2nd-order & HO-FDM2
9.2	3.5.9	Diffusion	Irregular (triangular)	Dirichlet	HO-FDM2
9.3	3.5.9	Convection-diffusion	Irregular	Dirichlet or Neumann	2nd-order & HO-FDM1 & 2
9.4	3.5.9	Diffusion	Square	Neumann	2nd-order & HO-FDM1 & 2
10.1	3.5.10	Unsteady diffusion	Square	-	FTCS
10.2	3.5.10	Unsteady diffusion	Irregular	-	FTCS
11.1	3.5.11	Second-order wave equation	Square	-	Cut-stencil FDM
11.2	3.5.11	Second-order wave equation	Irregular	-	Cut-stencil FDM

Table A.I.1: Summary of manufactured problems studied in Chapter 3

APPENDIX II: DERIVATION of 2nd-ORDER ACCURATE APPROXIMATION for VORTICITY on a STRAIGHT WALL

A.II.1 Derivation of Briley's Formulation

An approximation for the second derivative of streamfunction ψ along the y direction at node (i,j) on a horizontal wall can be derived for a uniform grid depicted in Figure A.II.1.
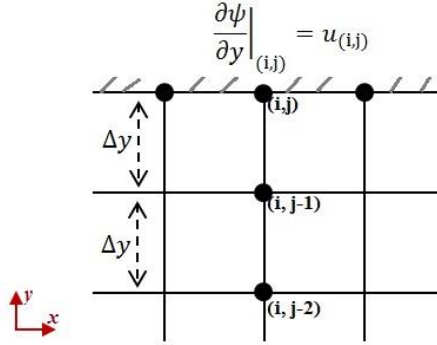

Figure A.II.1: Schematic of uniform grid near a boundary node used to derive the approximation of Briley [171]

A 3-point one-sided difference approximation for $\left.\frac{\partial^2\psi}{\partial y^2}\right|_{(i,j)}$ can be expressed as:

$$\left.\frac{\partial^2\psi}{\partial y^2}\right|_{(i,j)} + a_1\psi_{(i,j)} + a_2\psi_{(i,j-1)} + a_3\psi_{(i,j-2)} + a_4\left.\frac{\partial\psi}{\partial y}\right|_{(i,j)} = O(\Delta y^k) \qquad \text{(A.II.1)}$$

The coefficients a_j (j = 1,2,3,4) and k are calculated from Taylor's series expansions about point (i,j) and in the y direction, which can be conveniently tabulated using Table A.II.1.

	$\psi_{(i,j)}$	$\left.\frac{\partial\psi}{\partial y}\right|_{(i,j)}$	$\left.\frac{\partial^2\psi}{\partial y^2}\right|_{(i,j)}$	$\left.\frac{\partial^3\psi}{\partial y^3}\right|_{(i,j)}$	$\left.\frac{\partial^4\psi}{\partial y^4}\right|_{(i,j)}$
$\left.\frac{\partial^2\psi}{\partial y^2}\right|_{(i,j)}$	0	0	1	0	0
$a_1\psi_{(i,j)}$	a_1	0	0	0	0
$a_2\psi_{(i,j-1)}$	a_2	$a_2(-\Delta y)$	$a_2(\Delta y)^2/2!$	$a_2(-\Delta y)^3/3!$	$a_2(\Delta y)^4/4!$
$a_3\psi_{(i,j-2)}$	a_3	$a_3(-2\Delta y)$	$a_3(2\Delta y)^2/2!$	$a_3(-2\Delta y)^3/3!$	$a_3(2\Delta y)^4/4!$
$a_4\left.\frac{\partial\psi}{\partial y}\right|_{(i,j)}$	0	a_4	0	0	0
Σ	0	0	0	0	$O(\Delta y^k)$

Table A.II.1: Taylor's series expansions used to derive Briley's equation to approximate the wall vorticity

The four coefficients a_j (j = 1,2,3,4) are calculated from the system of four linear equations formed by summing the 2nd to 5th columns of Table A.II.1 to zero, giving the value of these coefficients:

$$a_1 = 7/2(\Delta y)^2, \quad a_2 = -4/(\Delta y)^2, \quad a_3 = 1/2(\Delta y)^2, \quad a_4 = -3/4(\Delta y) \qquad \text{(A.II.2)}$$

Using the coefficients listed in (A.II.2), and evaluating the coefficient of $\left.\dfrac{\partial^4 \emptyset}{\partial y^4}\right|_{(i,j)}$ in the 6th column

yields the explicit expression for the 2nd-order accurate approximation for $\left.\dfrac{\partial^2 \emptyset}{\partial y^2}\right|_{(i,j)}$:

$$\left.\frac{\partial^2 \psi}{\partial y^2}\right|_{(i,j)} = \frac{-7\psi_{(i,j)} + 8\psi_{(i,j-1)} - \psi_{(i,j-2)}}{2(\Delta y)^2} + \frac{3}{(\Delta y)}\left.\frac{\partial \psi}{\partial y}\right|_{(i,j)} + O(\Delta y^2) \qquad \text{(A.II.3)}$$

For the lid-driven cavity problem the term $\left.\dfrac{\partial \psi}{\partial y}\right|_{(i,j)}$ has the physical meaning of non-dimensional u

component of velocity $u_{(i,j)}$ which is equal to 0 or 1 on a stationary or moving wall, respectively. The cut-stencil FD format of equation A.II.3, at the north endpoint of the 5-point stencil, is given in (5.8.2.2).

A.II.2 Derivation of a Compact 2nd-Order Formulation

Similar to the above, an alternative 2nd-order expression to approximate vorticity on the wall can be obtained. This is accomplished by assuming that the second derivative of ψ along the y direction at node (i,j) on the wall can be written in terms of ψ values at (i,j) and (i,j-1), i.e.,

$$\left.\frac{\partial^2 \psi}{\partial y^2}\right|_{(i,j)} + b_1\psi_{(i,j)} + b_2\psi_{(i,j-1)} + b_3\left.\frac{\partial \psi}{\partial y}\right|_{(i,j)} + b_4\left.\frac{\partial \psi}{\partial y}\right|_{(i,j-1)} = O(\Delta y^k) \qquad \text{(A.II.4)}$$

The coefficients b_m (m = 1,2,3,4) and k are calculated from Taylor's series expansions about point (i,j) and in the y direction. Table A.II.2 records the details of the mathematical manipulations.

	$\psi_{(i,j)}$	$\left.\dfrac{\partial \psi}{\partial y}\right\|_{(i,j)}$	$\left.\dfrac{\partial^2 \psi}{\partial y^2}\right\|_{(i,j)}$	$\left.\dfrac{\partial^3 \psi}{\partial y^3}\right\|_{(i,j)}$	$\left.\dfrac{\partial^4 \psi}{\partial y^4}\right\|_{(i,j)}$
$\left.\dfrac{\partial^2 \psi}{\partial y^2}\right\|_{(i,j)}$	0	0	1	0	0
$b_1\psi_{(i,j)}$	b_1	0	0	0	0
$b_2\psi_{(i,j-1)}$	b_2	$b_2(-\Delta y)$	$b_2(\Delta y)^2/2!$	$b_2(-\Delta y)^3/3!$	$b_2(\Delta y)^4/4!$
$b_3\left.\dfrac{\partial \psi}{\partial y}\right\|_{(i,j)}$	0	b_3	0	0	0
$b_4\left.\dfrac{\partial \psi}{\partial y}\right\|_{(i,j-1)}$	0	b_4	$b_4(-\Delta y)$	$b_4(\Delta y)^2/2!$	$b_4(-\Delta y)^3/3!$
Σ	0	0	0	0	$O(\Delta y^k)$

Table A.II.2: Taylor's series expansions used to derive the 2nd-order accurate approximation of the wall vorticity in the compact finite difference method

Solution of the four linear equations formed by summing the 2nd to 5th columns of Table A.II.2 to zero, leads to the value of the coefficients b_m as:

$$b_1 = 6/(\Delta y)^2, \qquad b_2 = -6/(\Delta y)^2, \qquad b_3 = -4/(\Delta y), \qquad b_4 = -2/(\Delta y) \qquad \text{(A.II.5)}$$

Using the coefficients listed in (A.II.5), an explicit expression for the 2nd-order accurate approximation for $\left.\dfrac{\partial^2 \emptyset}{\partial y^2}\right|_{(i,j)}$, is:

$$\left.\frac{\partial^2 \psi}{\partial y^2}\right|_{(i,j)} = \frac{-6\psi_{(i,j)} + 6\psi_{(i,j-1)}}{(\Delta y)^2} + \frac{4}{(\Delta y)}\left.\frac{\partial \psi}{\partial y}\right|_{(i,j)} + \frac{2}{(\Delta y)}\left.\frac{\partial \psi}{\partial y}\right|_{(i,j-1)} + O(\Delta y^2) \qquad \text{(A.II.6)}$$

As mentioned above, for the lid-driven cavity flow problem $\left.\dfrac{\partial \psi}{\partial y}\right|_{(i,j)}$ is 0 or 1. In this approximation, $\left.\dfrac{\partial \psi}{\partial y}\right|_{(i,j-1)}$ is the u component of velocity at the internal node (i,j-1) adjacent to the wall. The mapped form of equation (A.II.6), in the cut-stencil FD notation, for the north endpoint of the 5-point stencil is given by equation (5.8.2.4).

APPENDIX III: CLUSTERING FUNCTION for NON-UNIFORM GRID GENERATION for LID-DRIVEN CAVITY FLOW in SQUARE DOMAIN

The non-uniform grid, as utilized for the cases of lid-driven cavity flow in unit the square domain, was designed by clustering toward $x = 0$, $x = 1$ and similarly towards $y = 0, y = 1$. The clustering function δ, e.g. for the x direction, is defined as:

$$\delta(x) = \frac{1}{2} + \frac{1}{2}\left[\frac{ln\left|\frac{B - 1 + 2x}{B + 1 - 2x}\right|}{ln\left|\frac{B + 1}{B - 1}\right|}\right] \tag{A.III.1}$$

where $1 < B < 2$. The parameter B controls the clustering rate. As $B \rightarrow 1$ clustering increases at the endpoints and, for all cases of non-uniform domain, as studied in Chapter 5, $B = 1.15$. Solving (A.III.1) for $x(\delta)$ gives:

$$x(\delta) = \frac{1}{2}\left[\frac{(B + 1)^{2\delta} - (B - 1)^{2\delta}}{(B + 1)^{2\delta - 1} + (B - 1)^{2\delta - 1}}\right] \tag{A.III.2}$$

It should be noted that $0 \leq \delta \leq 1$ which leads to $0 \leq x \leq 1$. A sample of nodes' distribution from equation (A.III.2), for 51 total nodes, is presented in Figure A.III.1.
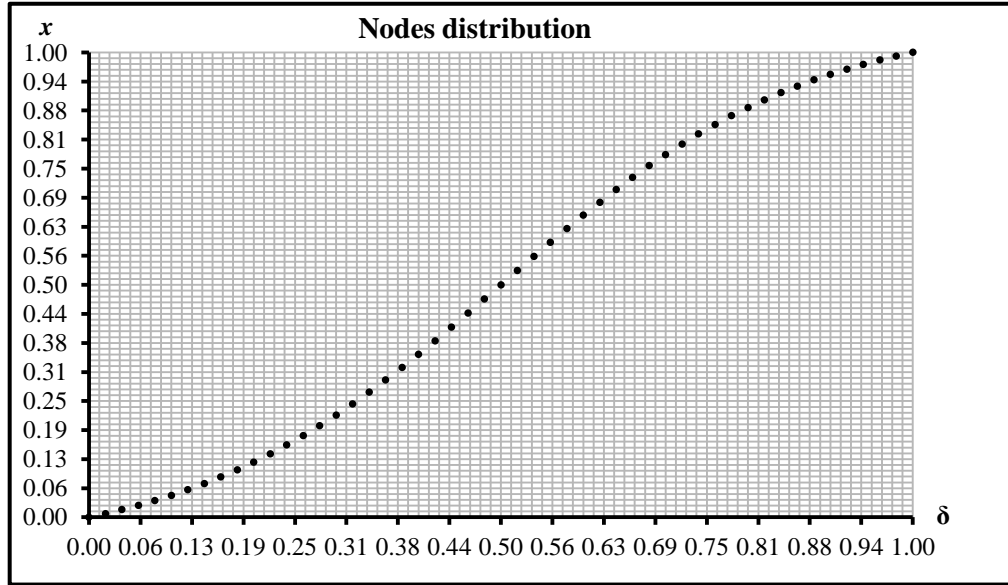

Figure A.III.1: Schematic of nodes distribution using clustering function (total number of nodes = 51 and $B = 1.15$)

Also, the expressions for $\Delta\delta$ and Δx are defined by:

$$\Delta\delta = \frac{2B}{ln\left|\frac{B + 1}{B - 1}\right|}\frac{\Delta x}{[B^2 - (1 - 2x)^2]} \tag{A.III.3}$$

$$\Delta x = \frac{ln\left|\frac{B + 1}{B - 1}\right|}{2B}[B^2 - (1 - 2x)^2]\Delta\delta \tag{A.III.4}$$

A similar methodology, as above, is employed for clustering the grid in y direction. The schematic of a sample of a non-uniform grid in the unit square, using 129*129 grid nodes, is depicted in Figure A.III.2.
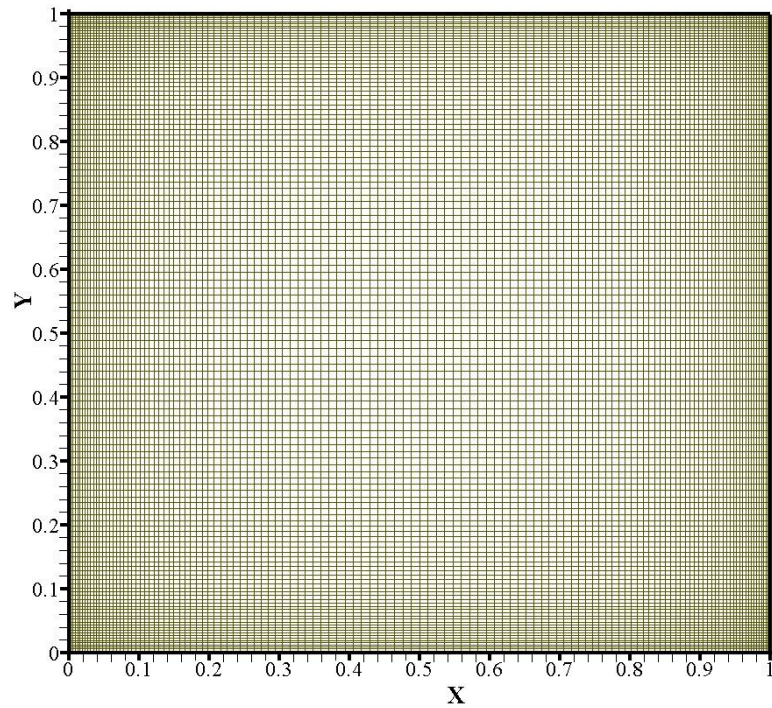

Figure A.III.2: Schematic of non-uniform grid on unit square domain (used for lid-driven cavity flow in Chapter 5)

APPENDIX IV: VORTICITY EVALUATION on SLOPED or CURVED WALLS

First, the procedure to calculate the vorticity at point W on an arbitrary wall, illustrated by the dashed curve in Figure A.IV.1, is presented. The orthogonal coordinate system aligned along the tangential direction (t) and normal direction (n) is constructed as shown in Figure A.IV.1. The orthogonal (x, y) coordinate system is also assumed to have its origin located at W, while θ introduces the angle between the x axis and tangential direction at point W.
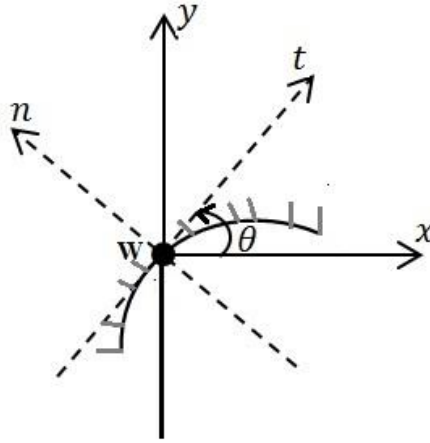

Figure A.IV.1: Schematic of orthogonal coordinate systems defined at a boundary point on an arbitrary wall

Since the (t, n) system is simply a rotation of the (x, y) system through the angle θ, the derivatives of ψ in these two systems are related by

$$\overrightarrow{\nabla \psi}(x, y) = \left(\cos(\theta)\frac{\partial \psi}{\partial t} + \sin(\theta)\frac{\partial \psi}{\partial n}\right)\hat{\imath} + \left(-\sin(\theta)\frac{\partial \psi}{\partial t} + \cos(\theta)\frac{\partial \psi}{\partial n}\right)\hat{\jmath} \qquad \text{(A.IV.1)}$$

The invariant property of the Laplacian operator with respect to orthogonal coordinate systems [197, 198] yields:

$$\frac{\partial^2 \psi}{\partial x^2} + \frac{\partial^2 \psi}{\partial y^2} = \frac{\partial^2 \psi}{\partial t^2} + \frac{\partial^2 \psi}{\partial n^2} \qquad \text{(A.IV.2)}$$

The second derivative of ψ with respect to x and y are written as:

$$\frac{\partial^2 \psi}{\partial x^2} = \frac{\partial}{\partial x}\left(\frac{\partial \psi}{\partial x}\right) = \left(\cos(\theta)\frac{\partial}{\partial t} + \sin(\theta)\frac{\partial}{\partial n}\right)\left(\cos(\theta)\frac{\partial \psi}{\partial t} + \sin(\theta)\frac{\partial \psi}{\partial n}\right)$$
$$= \left(cos(\theta)\right)^2 \frac{\partial^2 \psi}{\partial t^2} + \left(sin(\theta)\right)^2 \frac{\partial^2 \psi}{\partial n^2} + 2cos(\theta)sin(\theta)\frac{\partial^2 \psi}{\partial t \partial n} \qquad \text{(A.IV.3)}$$

$$\frac{\partial^2 \psi}{\partial y^2} = \frac{\partial}{\partial y}\left(\frac{\partial \psi}{\partial y}\right) = \left(-\sin(\theta)\frac{\partial}{\partial t} + \cos(\theta)\frac{\partial}{\partial n}\right)\left(-\sin(\theta)\frac{\partial \psi}{\partial t} + \cos(\theta)\frac{\partial \psi}{\partial n}\right)$$
$$= \left(sin(\theta)\right)^2 \frac{\partial^2 \psi}{\partial t^2} + \left(cos(\theta)\right)^2 \frac{\partial^2 \psi}{\partial n^2} - 2cos(\theta)sin(\theta)\frac{\partial^2 \psi}{\partial t \partial n} \qquad \text{(A.IV.4)}$$

Since the no-slip condition on the wall implies that $\frac{\partial^2 \psi}{\partial t^2} = 0$ and the no-penetration condition

leads to $\frac{\partial^2 \psi}{\partial t \partial n} = 0$, on the wall, equations (A.IV.3) and (A.IV.4) reduced to the following equations, respectively:

$$\left.\frac{\partial^2 \psi}{\partial x^2}\right|_W = \left(sin(\theta)\right)^2 \left.\frac{\partial^2 \psi}{\partial n^2}\right|_W \tag{A.IV.5}$$

$$\left.\frac{\partial^2 \psi}{\partial y^2}\right|_W = \left(cos(\theta)\right)^2 \left.\frac{\partial^2 \psi}{\partial n^2}\right|_W \tag{A.IV.6}$$

Therefore, the vorticity at point W on the wall (ω_W) can be written as:

$$\omega_W = -\left.\frac{\partial^2 \psi}{\partial n^2}\right|_W = -\frac{1}{2}\left[\left(\frac{1}{sin(\theta)}\right)^2 \frac{\partial^2 \psi}{\partial x^2} + \left(\frac{1}{cos(\theta)}\right)^2 \frac{\partial^2 \psi}{\partial y^2}\right]_W \tag{A.IV.7}$$

An approximation of the second derivative of ψ at node (i,j), shown in Figure A.IV.2, assuming a uniform grid, can be expressed by:

$$\left.\frac{\partial^2 \psi}{\partial x^2}\right|_{(i,j)} + a_1 \psi_{(i,j)} + a_2 \psi_{(i+1,j)} + a_3 \left.\frac{\partial \psi}{\partial x}\right|_{(i,j)} = O(\Delta x^k) \tag{A.IV.8}$$
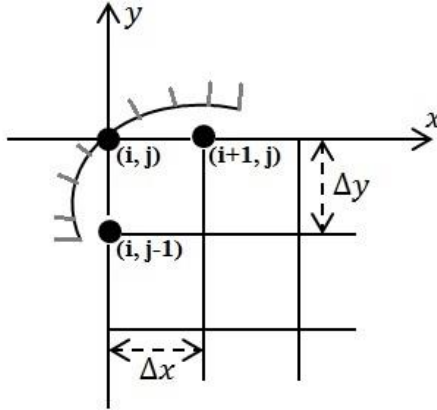

Figure A.IV.2: Schematic of uniform grid near a boundary node on an arbitrary wall

Using Taylor's series about (i,j), similar to procedures of the compact differencing method, yields a 1st-order accurate approximation of $\left.\frac{\partial^2 \psi}{\partial x^2}\right|_{(i,j)}$:

$$\left.\frac{\partial^2 \psi}{\partial x^2}\right|_{(i,j)} = \frac{-2\psi_{(i,j)} + 2\psi_{(i+1,j)}}{(\Delta x)^2} - \frac{2}{(\Delta x)} \left.\frac{\partial \psi}{\partial x}\right|_{(i,j)} + O(\Delta x^1) \tag{A.IV.9}$$

Similarly, a 1st-order accurate approximation of $\left.\frac{\partial^2 \psi}{\partial y^2}\right|_{(i,j)}$ can be stated as:

$$\left.\frac{\partial^2 \psi}{\partial y^2}\right|_{(i,j)} = \frac{-2\psi_{(i,j)} + 2\psi_{(i,j-1)}}{(\Delta y)^2} + \frac{2}{(\Delta y)}\left.\frac{\partial \psi}{\partial y}\right|_{(i,j)} + O(\Delta y^1) \qquad \text{(A.IV.10)}$$

The terms $\left.\frac{\partial \psi}{\partial x}\right|_{(i,j)}$ and $\left.\frac{\partial \psi}{\partial y}\right|_{(i,j)}$ are zero in the event of a stationary wall. Noting the fact that nodes W and (i,j) in Figures A.IV.1 and A.IV.2 denote the same point, the differencing approximations in equations (A.IV.9) and (A.IV.10) can be used in (A.IV.7) and gives:

$$\omega_W = -\left.\frac{\partial^2 \psi}{\partial n^2}\right|_W = -\frac{1}{2}\left[\left(\frac{1}{sin(\theta)}\right)^2 \frac{-2\psi_{(i,j)} + 2\psi_{(i+1,j)}}{(\Delta x)^2} + \left(\frac{1}{cos(\theta)}\right)^2 \frac{-2\psi_{(i,j)} + 2\psi_{(i,j-1)}}{(\Delta y)^2}\right]_W \qquad \text{(A.IV.11)}$$

Roache [168] has proposed a similar result in the case when $\theta = 45°$ (see [168], p. 158).
Figure A.IV.3 shows physical stencils near a boundary node WN located on an arbitrary wall. The boundary node WN is simultaneously the west node of the 5-point physical stencil centred at node P_1 and the north node of the 5-point physical stencil centred at node P_2.
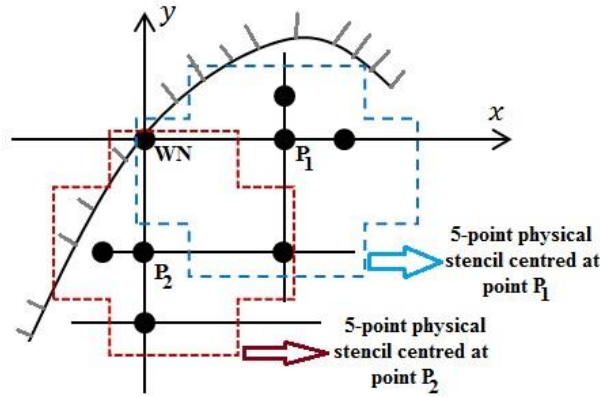

Figure A.IV.3: Schematic of physical stencils with boundary endpoint on an arbitrary wall

The 1st-order accurate approximation of vorticity at boundary node WN on an arbitrary stationary wall in the cut-stencil FD notation on the computational stencil, is

$$\omega_{wn} = -\frac{1}{2}\left[\left(\frac{1}{sin(\theta)}\right)^2 \frac{-2\psi_{wn} + 2\psi_{P_1}}{(x'_{WN})^2} + \left(\frac{1}{cos(\theta)}\right)^2 \frac{-2\psi_{wn} + 2\psi_{P_2}}{(y'_{WN})^2}\right] \qquad \text{(A.IV.12)}$$

where all the terms including $\frac{1}{x'_{WN}}\left.\frac{\partial \psi}{\partial \xi}\right|_{wn}$ and $\frac{1}{y'_{WN}}\left.\frac{\partial \psi}{\partial \eta}\right|_{wn}$ are set to zero since these terms are the velocity components at a stationary wall node.

VITA AUCTORIS

Name:	Mohammadali Esmaeilzadeh
Year of Birth:	1978
Place of Birth:	Iran
Education:	University of Mazandaran, Babol, Iran, B.Sc. in Mechanical Engineering, 2002
	University of Semnan, Semnan, Iran, M.Sc. in Mechanical Engineering, 2005
	University of Windsor, Windsor, Canada, M.Eng. in Mechanical Engineering, 2012
	University of Windsor, Windsor, Canada, Ph.D. in Mechanical Engineering, 2016